Université du Québec
à Rimouski

TREMPE AU LASER

Analyse numérique et expérimentale de l'effet du durcissement au laser sur les propriétés mécaniques en statique et en fatigue de l'acier AISI 4340

Mémoire présenté
dans le cadre du programme de maîtrise en ingénierie
en vue de l'obtention du grade de maître ès sciences appliquées (M.Sc.A.)

PAR

© RACHID FAKIR

Mars 2019

Composition du jury :

Adrian Ilinca, Président du jury, Université du Québec à Rimouski

Noureddine Barka, Directeur de recherche, Université du Québec à Rimouski

Jean Brousseau, Codirecteur de recherche, Université du Québec à Rimouski

Lorraine Blais, Examinatrice externe, Solutions Novika

Dépôt initial le 15 janvier 2019 Dépôt final le 04 mars 2019

REMERCIEMENTS

Tout d'abord, je tiens à exprimer ma reconnaissance et ma profonde gratitude à mon directeur de recherche, le professeur Noureddine Barka, de m'avoir encadré, orienté, aidé et conseillé à chaque moment important de ce projet de recherche. Merci Noureddine, car sans votre soutien éclairé et permanent, ce mémoire de recherche n'aurait pas atteint sa forme actuelle.

Je tiens également à remercier mon codirecteur de recherche, le professeur Jean Brousseau, pour ses judicieux conseils, pour le temps consacré à la lecture et aux réunions qui ont rythmé les différentes étapes de mon mémoire. Les discussions que nous avons partagées ont permis d'orienter mon travail d'une manière pertinente et ce projet n'aurait pas réussi sans votre aide ponctuelle.

Je remercie le personnel du département de mathématiques, informatique et de génie de l'UQAR, tout particulièrement Suzie, Karel, Vianney, R. Lafrance, Dany, Jean-Charles et R. Lepage pour leurs conseils, patiences, amabilités, et appui fourni.

Je remercie également toute l'équipe de Bombardier Transport et de Solutions Novika, tout particulièrement Gabriel, Mathieu, Gaston et Lorraine qui ont contribué au succès de mon stage, grâce à leur accueil, leur esprit d'équipe et leur confiance qui m'a permis de m'accomplir totalement dans mes missions.

J'aimerais aussi remercier chaleureusement ma compagne, mes parents, et mes proches pour leur support inestimable.

Finalement, un grand merci à tous les amis et collègues pour les bons moments simples qui sont devenus inoubliables grâce à vous.

RÉSUMÉ

Le durcissement au laser en surface est de plus en plus utilisé par l'industrie du transport civil et militaire pour l'amélioration de la dureté, la résistance à l'usure, la résistance mécanique en statique et en fatigue des composantes structurelles tout en conservant indemnes les propriétés de la masse telle que la ténacité et la ductilité. La maîtrise de ce procédé nécessite une connaissance précise des facteurs physiques qui influencent la réponse du procédé telles que le type du matériau, le fini de surface, le coefficient d'absorption, la puissance laser, l'angle d'incidence du faisceau laser et la vitesse de déplacement de la tache focale.

En ayant pour but le développement des techniques de prédiction de la profondeur durcie, et des propriétés mécaniques en statique et en fatigue d'un cylindre en acier AISI 4340 en haute vitesse de rotation, cette recherche répond à six objectifs particuliers :

- Analyse des propriétés mécaniques de l'acier AISI 4340 traité thermiquement dans la masse en utilisant un four de laboratoire et refroidi dans trois fluides différents.

- Analyse numérique par la méthode des différences finies (MDF) et validation expérimentale, du durcissement au laser en un point stationnaire (sans vitesse de balayage) d'un cylindre d'acier AISI 4340 en rotation.

- Investigation numérique MDF du durcissement au laser d'une éprouvette cylindrique en acier AISI 4340, en introduisant le déplacement du faisceau laser au niveau des conditions aux limites.

- Analyse numérique par la méthode des éléments finis (MEF) et validation expérimentale, de la variation du profil de dureté dans le cas d'une trempe au laser (puissance constante) appliquée à des éprouvettes cylindriques en acier AISI 4340.

- Optimisation de la profondeur durcie d'un cylindre en acier AISI 4340 par la méthode des éléments finis (FEM) et des tests expérimentaux, au moyen d'un contrôle actif des paramètres laser.

- Analyse du comportement mécanique en statique et en fatigue d'éprouvettes cylindriques normalisées (ASTM E8) en acier AISI 4340 durcies au laser.

L'approche d'analyse de la distribution de la température a été développée sous le logiciel MATLAB pour une discrétisation des équations différentielles en différences finies, a été validée par le logiciel COMOSL et par des tests expérimentaux en laboratoire. L'approche d'analyse de la variation des propriétés mécaniques en statique et en fatigue, en fonction des paramètres de durcissement au laser est fondée sur un plan d'expérience DOE et une analyse de variance corrélée avec la puissance de prédiction des réseaux de neurones.

L'approche proposée a permis, de mettre en évidence les variations du coefficient d'absorption en fonction des conditions d'opération, d'analyser la dynamique des échanges thermiques au moyen des nombres adimensionnels, de confirmer la robustesse de la prédiction numérique du profil de température versus la profondeur durcie, et finalement de proposer un modèle robuste de prédiction des propriétés mécaniques en statique et en fatigue avec un écart relatif de moins de 10%.

Finalement, nous montrons qu'il est possible d'uniformiser le profil de dureté par un asservissement des paramètres de durcissement au laser. Et que la trempe autogène peut améliorer de 20 à 40% la limite d'endurance en fatigue pour des spécimens de diamètre de 9 à 10 mm.

Mots clés : Trempe au laser, bilan des échanges thermiques, modélisation numérique, différences finies et éléments finis, analyse de variance, réseaux de neurones, propriétés mécaniques, résistance en fatigue, AISI 4340.

PUBLICATIONS

Des parties du travail présenté dans ce mémoire de maîtrise ont été publiées ou soumis par les auteurs dans les articles suivants :

- Fakir, R., Barka, N., & Brousseau, J., Mechanical Properties Analysis of 4340 Steel Specimen Heat Treated in Oven and Quenching in Three Different Fluids, Metals and Materials International., 24 (5), 2018, 981–991.

- Fakir, R., Barka, N., & Brousseau, J., Case study of laser hardening process applied to 4340 steel cylindrical specimens using simulation and experimental validation, Case Studies in Thermal Engineering., 11, 2018, 15–25.

- Fakir, R., Barka, N., Brousseau, J., & Caron-Guillemette G., Numerical Investigation by the Finite Difference Method of the Laser Hardening Process Applied to AISI 4340, Journal of Applied Mathematics and Physics., 6 (10), 2018, 2087–2106.

- Fakir, R., Barka, N., Brousseau, J., & Lepage R., Experimental analysis of the hardness profile variation in laser heat treatment applied to 4340 steel cylindrical specimens, Journal of Manufacturing Processes., submitted, 2018.

- Fakir, R., Barka, N., & Brousseau, J., Optimization of the Case Depth of a Cylinder Made With 4340 Steel by a Control of the Laser Heat Treatment Parameters, American Society of Mechanical Engineers, International Design Engineering Technical Conferences and Computers and Information in Engineering Conference., 2018, V01AT02A041–V01AT02A041.

- Fakir, R., Barka, N., Brousseau, J., & Caron-Guillemette G., Analysis of the Mechanical Behavior of AISI 4340 Steel Cylindrical Specimens Heat Treated with Fiber Laser, Journal of Manufacturing Processes., submitted, 2018.

ABSTRACT

The surface laser hardening is increasingly used by the civilian and military transportation industry for improving hardness, wear resistance, the mechanical resistance in static and fatigue of the structural components while keeping intact the properties of the mass such as toughness and ductility. The control of this process requires a precise knowledge of physical factors, that influence the response of the process like the type of material, the surface finish, the absorption coefficient, the laser power, the angle of incidence of the laser beam and the speed of displacement of the focal spot.

With the aim of developing hardened depth prediction techniques, and mechanical properties in static and fatigue of steel AISI 4340, this research meets six specific objectives:

- Analysis of the mechanical properties of AISI 4340 steel heat-treated in the mass, using a laboratory oven, and cooled in three different fluids.
- Numerical analysis by the finite difference method (FDM) and experimental analysis of laser hardening process at a stationary point (without scanning speed) of a cylinder of steel AISI 4340 in rotation.
- FDM numerical investigation of the laser hardening process, of a cylinder in steel AISI 4340, by introducing the displacement parameter of the laser source at the boundary conditions.
- Numerical analysis by the finite element method (FEM) and experimental validation of the variation of the hardness profile in the case of laser hardening (constant power) applied to cylindrical specimens of steel AISI 4340.
- Optimization of the case depth of a steel cylinder AISI 4340 by the finite element method (FEM) and experimental tests by means of an active control of the laser parameters.
- Analysis of mechanical behavior in static and fatigue of standard cylindrical specimens (ASTM E8) in AISI 4340 steel heat-treated by laser.

The analysis approach of the temperature distribution has been developed in the MATLAB software for a discretization of differential equations in finite difference method, and has been validated by the COMSOL software and by experimental tests in the laboratory. The analysis approach of the variation of mechanical properties in static and fatigue, according to the laser hardening parameters is based on a DOE experience plan and an analysis of variance correlated with the predictive power of neural networks.

The proposed approach allowed to highlight the variations of the absorption coefficient according to the operating conditions, to analyze the dynamics of thermal exchanges by means of adimensional numbers, to confirm the robustness of the numerical prediction of the temperature profile versus the case depth, and finally to propose a robust model for predicting mechanical properties in static and fatigue with a relative difference of less than 10%.

Finally, we show that it is possible to regularize the hardness profile by a servo control of the laser hardening parameters. And that autogenous laser quenching can improve the fatigue endurance limit by up to 20-40% for specimens with a diameter of 9 to 10 mm.

Keywords: Laser hardening, balance of thermal exchanges, numerical modeling, finite difference method and finite element method, analysis of variance, neural networks, mechanical properties, fatigue resistance, AISI 4340.

PUBLICATIONS

Parts of the work presented in this thesis have been published or submitted by the authors in the following articles:

- Fakir, R., Barka, N., & Brousseau, J., Mechanical Properties Analysis of 4340 Steel Specimen Heat Treated in Oven and Quenching in Three Different Fluids, Metals and Materials International., 24 (5), 2018, 981–991.

- Fakir, R., Barka, N., & Brousseau, J., Case study of laser hardening process applied to 4340 steel cylindrical specimens using simulation and experimental validation, Case Studies in Thermal Engineering., 11, 2018, 15–25.

- Fakir, R., Barka, N., Brousseau, J., & Caron-Guillemette G. Numerical Investigation by the Finite Difference Method of the Laser Hardening Process Applied to AISI 4340, Journal of Applied Mathematics and Physics., 6 (10), 2018, 2087–2106.

- Fakir, R., Barka, N., Brousseau, J., & Lepage R., Experimental analysis of the hardness profile variation in laser heat treatment applied to 4340 steel cylindrical specimens, Journal of Manufacturing Processes., submitted, 2018.

- Fakir, R., Barka, N., & Brousseau, J., Optimization of the Case Depth of a Cylinder Made With 4340 Steel by a Control of the Laser Heat Treatment Parameters, American Society of Mechanical Engineers, International Design Engineering Technical Conferences and Computers and Information in Engineering Conference., 2018, V01AT02A041–V01AT02A041.

- Fakir, R., Barka, N., Brousseau, J., & Caron-Guillemette G., Analysis of the Mechanical Behavior of AISI 4340 Steel Cylindrical Specimens Heat Treated with Fiber Laser, Journal of Manufacturing Processes., submitted, 2018.

TABLE DES MATIÈRES

LISTE DES TABLEAUX

LISTE DES FIGURES

LISTES DES ACRONYMES, ABRÉVIATIONS, SYMBOLES ET UNITÉS

UQAR	Université du Québec à Rimouski
DMIG	Département de mathématiques, d'informatique et génie
AISI	American Iron and Steel Institute
ASTM	American Society for Testing and Materials
ANOVA	Analyse de variance
DAQ	Boitier d'acquisition (Data Acquisition)
C	Carbone
σ	Constante de Stefan-Boltzmann
CNC	Commande numérique par ordinateur (Computer numerical control)
x	Coordonnée cartésienne - abscisse
y	Coordonnée cartésienne - ordonnée
z	Coordonnée cartésienne - hauteur
S-N	Courbe de Wöhler (Stress vs Number of cycles)
°C	Degré Celsius

HR	Dureté élevée (High hardness region)
HRC	Dureté Rockwell-C
HV	Dureté Vickers
MAE	Erreur absolue moyenne (Mean absolute error)
MRE	Erreur relative moyenne (Mean relative error)
J	Joule
Hz	Hertz
kg	Kilogramme
Laser	Light amplification by stimulated emission of radiation
Ms	Martensite début (start)
MTS	Material Testing Systems
MB	Matériau de base (Material bulk)
MDF	Méthode des différences finies (en anglais FDM)
MEF	Méthode des éléments finis (en anglais FEM)
RSM	Méthode des surfaces de réponses (Response surface methodology)
mm	Millimètre

Ni	Nickel
Bi	Nombre de Biot
Nu	Nombre de Nusselt
Pr	Nombre de Prandtl
Ra_D	Nombre de Rayleigh
DOE	Plan d'expériences (design of experiments)
MLP	Perceptron multicouche (Multilayer perceptron)
R&D	Recherche et développement
TR	Région de transition (Transition region)
MR	Région fusionnée (Melting region)
ANN	Réseau de neurones artificiels (Artificial neural network)
RPM	Rotation par minute
s	Seconde
Ac1	Température de début de formation de l'austénite
Ac3	Température de fin de formation de l'austénite
t	Temps

TTT	Temps - Température - Transformation
3D	Trois dimensions
W	Watt

Nota Béné : Chaque chapitre/article contient sa propre nomenclature, celle-ci se trouve après chaque résumé en anglais (abstract).

INTRODUCTION GÉNÉRALE

1. CONTEXTE ET GÉNÉRALITÉS

Les aciers et les fontes sont essentiellement des alliages de fer et de carbone qui font partie des systèmes d'alliage binaire les plus importants [1]. La teneur en carbone de tous les aciers et de toutes les fontes est généralement inférieure à 6.63%, étant donné qu'au-delà de ce pourcentage se forme la cémentite Fe_3C qui présente une dureté très élevée (dureté Vickers HV = 700 à 800) et une fragilité élevée (allongement à la rupture nul) [2]. La réaction eutectoïde (transformation de phase solide en phase solide qui se déroule à la température Ac3) du système fer-carbone joue un rôle très important dans le traitement thermique des aciers. L'obtention d'un ensemble de caractéristiques mécaniques pour un matériau résulte de l'opération de transformation de phases que déclenchent la réaction eutectoïde et le contrôle de sa vitesse de chauffage et de refroidissement. La vitesse de refroidissement dépend de la conductivité thermique et de la chaleur spécifique de la pièce, de la masse et de la géométrie et également de la capacité de refroidissement du milieu de trempe, celle-ci étant maximale en surface par rapport au cœur de la pièce [3]. La Figure 1 montre de manière sommaire le cycle d'un traitement par trempe suivi d'un traitement par revenu servant à éliminer les contraintes résiduelles et à l'amélioration de la ténacité et de la dureté finale [4].

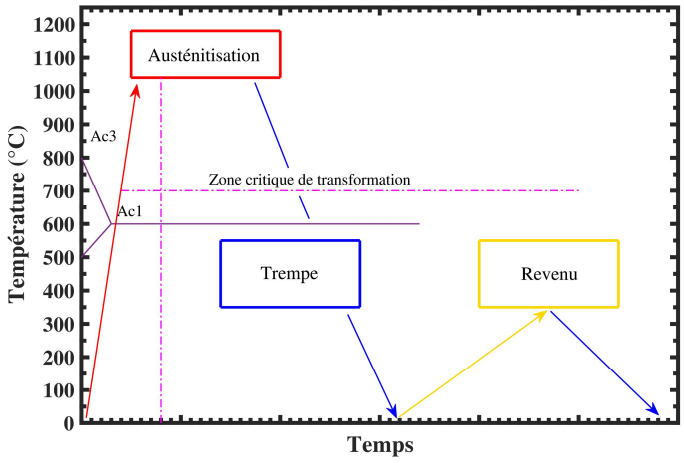

Figure 1 : Cycle de chauffage, de refroidissement et de revenu

Le traitement thermique implique le chauffage de la pièce à des températures élevées (température Ac3 + 50°C environ) suivi d'un refroidissement contrôlé pour en obtenir le résultat désiré, tel que la modification de la dureté, de la ductilité, de la ténacité et de la résistance mécanique du matériau. Les paramètres et les procédés qui peuvent influencer les propriétés matérielles et la composition des pièces métalliques sont le type d'alliage (composition chimique), le mode de chauffage (laser, induction, …), le mode de refroidissement (milieu de trempe), le temps d'exécution du chauffage et du refroidissement, et l'atmosphère de la trempe (humidité, poussière, …) [5].

Généralement les traitements thermiques sont ordonnés en fonction de leur objectif, on peut citer le traitement par homogénéisation qui est réalisé pour égaliser les températures dans l'ensemble d'un alliage, le recuit qui est réalisé pour ramollir les alliages et augmenter leur ductilité, le traitement par détente qui est réalisé pour éliminer les tensions internes à l'intérieur des pièces, le durcissement en surface qui est réalisé pour modifier les propriétés de la couche superficielle, le revenu qui est réalisé pour adoucir les effets de la trempe, et les traitements modifiant la chimie superficielle d'un alliage (cémentation, nitruration, carbonitruration et nitrocarburation) qui permettent de durcir les couches superficielles de la pièce en la plaçant dans une atmosphère gazeuse enrichie en carbone [6]. Les moyens de chauffage à haute énergie, et suivant le type de procédé, permettant d'austénitiser complétement la zone proche de la surface pour en obtenir après refroidissement rapide une région de dureté élevée en fonction de la teneur en carbone de l'alliage, sont nombreux. Le Tableau 1 présente les avantages et les désavantages de la trempe par faisceau laser, par induction, par flamme, et par carburation-nitruration [7].

Toutes les nuances d'acier ferromagnétiques peuvent être chauffées par un des procédés cités ci-haut, mais il convient d'évaluer leur comportement après la trempe. Les aciers les plus couramment utilisées pour fabriquer des composants mécaniques en mouvement se situent entre 0.4 et 0.45 % en teneur du Carbone comme le cas de l'acier AISI 4340 [1]. Grâce à sa forte teneur en nickel, l'acier allié AISI 4340 fait partie de la famille des aciers alliés apte au traitement thermique. On le retrouve dans les arbres à

vilebrequin, les composantes des trains d'atterrissage d'avions (Landing gear), et dans plusieurs autres pièces mécaniques telles que les tiges de piston, les engrenages, les cannelures, les turbines de pompe, les boulons, les arbres de transmission de grand diamètre…, etc.

Tableau 1 : Avantages et désavantages des différentes techniques de durcissement

Avantages et Désavantages	Laser	Induction	Fourneau	Carburation Nitruration
Investissement	😐	😐	😃	😐
Tolérance à la géométrie	😃	😟	😃	😃
Déformation	😃	😃	😣	😣
Trempe en surface	😃	😃	😟	😟
Trempe en profondeur	😐	😃	😃	😃
Précision de traitement	😃	😐	😣	😣
Productivité et rapidité	😃	😃	😐	😐
Énergie et environnement	😃	😃	😐	😟
Contrôle de température	😃	😃	😐	😐
Espace requis et intégration	😃	😃	😟	😟

La trempe de l'acier AISI 4340 consiste à refroidir rapidement la pièce dont la température est supérieure à la température de début de transformation Ac3 (température d'austénitisation), ce qui permet d'augmenter de façon considérable la dureté et la résistance à la traction des matériaux. On note ici que la martensite est la forme la plus dure de ce type d'acier, en effet la trempe martensitique consiste à refroidir rapidement la pièce à une température inférieure à la valeur critique Ms (température de début de transformation martensitique), ce qui provoque un blocage des atomes de carbone du réseau gamma (solution de carbone dans le fer qui favorisent la formation d'austénite entre 914 °C et 1 391 °C) [8]. Ce dernier devient quadratique centré instantanément, qui est une solution solide appelée martensite. Pour les aciers au carbone, on utilise souvent de l'eau comme milieu de trempe, alors que pour les aciers alliés comme l'AISI 4340 on utilise de l'huile de trempe ou un trempant polymère spécial [3].

Par rapport au cout relatif approximatif, qui représente le coût unitaire en masse du matériau divisé par le coût unitaire en masse de l'acier à faible teneur en carbone (même si le prix d'un matériau spécifique variera avec le temps le rapport de prix entre ce matériau et un autre changera probablement plus lentement), l'acier 4340 est maintenant le plus économique et résistant, suivi du composite renforcé de fibres de verre, de l'aluminium 2024-T6, du composite renforcé de fibres de carbone et de l'alliage de titane [1].

2. LE DURCISSEMENT AU LASER

Les procédés laser sont considérés comme des procédés très performants, simples et rapides. La flexibilité et la précision de ces procédés justifient leur utilisation dans la découpe, le soudage, le revêtement, le nettoyage et le traitement thermique en surface [3]. Ces procédés sont exécutés avec rapidité et occasionnent un minimum de déformation et une précision inégalée. La Figure 2 montre une photographie de la cellule laser robotisée de l'UQAR (DMIG) qui est constituée d'un robot FANUC à 6 axes et une tête laser BIMO de HighYag raccordée à une source YLS-3000-ST2 d'une puissance maximale de 3000 W.

Figure 2 : Robot FANUC équipé d'une tête laser HighYag raccordée à une source laser IPG

Les lasers peuvent être aussi bien continus ou pulsés. Dans un laser, l'énergie maximale est limitée par la puissance de la source de pompage, et par le nombre d'atomes qui peuvent être simultanément excités [9]. Lors d'un traitement thermique par laser, le procédé utilise un rayonnement laser de haute intensité pour chauffer rapidement la surface de l'acier dans la région austénitique [10]. En effet, le gradient de température est très

grand, car la vitesse de chauffage est également élevée en raison de la capacité du laser à concentrer une quantité importante de chaleur dans un endroit localisé. Ces conditions permettent de générer une microstructure très fine, homogène et dure [11, 12]. Dans le cas de l'acier 4340, le faisceau laser chauffe localement la surface de la pièce jusqu'à une certaine température d'austénitisation (Ac3) qui est généralement comprise entre 800°C et 1000°C, sans passer la température de fusion du substrat. La chauffe est suivie d'un refroidissement rapide (trempe) afin de former la martensite, qui est la forme la plus dure de ce type d'acier. Ces caractéristiques font que l'acier 4340 est très utilisé dans l'industrie du transport aéronautique, ferroviaire et automobile. Il possède également une forte robustesse et une grande ténacité après un traitement thermique.

Toutefois, malgré les avantages du traitement thermique au laser, le contrôle optimal en termes de profil de dureté et de contraintes résiduelles du procédé reste difficile à atteindre. En effet, plusieurs facteurs physiques influencent les résultats de sortie du procédé comme : le type du matériau, le fini de surface, l'angle d'incidence, le coefficient d'absorption, la vitesse d'avance, la vitesse de rotation et la puissance du laser. La connaissance précise de ces facteurs est capitale pour la réussite du procédé. La Figure 3 montre le mécanisme d'absorption d'une onde électromagnétique laser [13]. Cette dernière constitue le phénomène par lequel un matériau non transparent atténue toute onde électromagnétique le traversant. L'énergie laser absorbée est donc convertie en chaleur sous l'effet de Joule. La valeur du coefficient d'absorption varie d'un matériau à un autre et varie également en fonction de la longueur d'onde pour le même matériau.

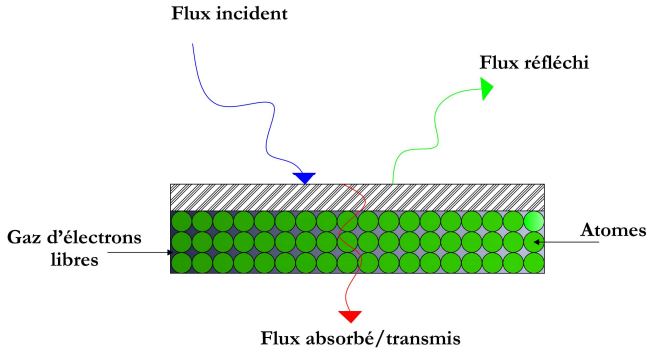

Figure 3 : Bilan global du flux laser incident, réfléchi et transmis dans la pièce

William M. Steen et Jyotirmoy Mazumder ont proposé en 2003, dans le cadre de leur livre Laser Material Processing, une approximation de la valeur du coefficient d'absorption pour les matériaux opaques (Réflectivité = 1 – absorption) en fonction de la longueur d'onde, la température, l'épaisseur de la couche d'oxyde et l'angle d'incidence du faisceau laser [14].

La Figure 4a montre la variation de la réflectivité de l'acier, du nickel, de l'aluminium, et du cuivre en fonction de la longueur d'onde. Quand cette dernière diminue, la capacité d'absorption de la surface augmente. Généralement avec des longueurs d'onde plus courte les photons les plus énergétiques peuvent être absorbés par un plus grand nombre d'électrons liés. Dans le cas de l'acier, on utilise souvent pour favoriser l'absorption de l'énergie laser, une longueur d'onde de 1.07-µm (Laser Fibre) qui correspond à un coefficient d'absorption ~ 40%, comparativement à une longueur d'onde de 10.6-µm (Laser-CO_2) qui correspond à un coefficient d'absorption ~ 18%. La Figure 4b montre la variation de la réflectivité de l'acier, de l'aluminium, et du cuivre en fonction de la température de chauffage. Lorsque la température de la pièce chauffée augmente, le nombre de phonons (quantum d'énergie de vibration dans un solide cristallin) augmente, ce qui entraîne davantage d'échanges d'énergie entre phonons, ainsi les électrons sont plus susceptibles d'interagir avec la zone chauffée de la pièce plutôt que d'osciller et de réirradier. On observe donc une baisse de la réflectivité et une augmentation de l'absorptivité avec une augmentation de la température de certains métaux. La Figure 4c montre la variation de l'absorption de l'acier, pour une longueur d'onde de 10.6-µm et, en fonction de l'épaisseur du film de la couche d'oxyde en surface qui doit être en contact parfait avec la surface. La Figure 4d montre la variation de la réflectivité en fonction de l'angle d'incidence du faisceau laser pour une longueur d'onde de 1.07-µm.

P. Drude a montré en 1922, dans le cadre de son analyse théorique de la réflectivité à partir de considérations atomistiques du flux d'électrons dans un champ rayonnant, que la réflectivité dépend de l'angle d'incidence et du plan de polarisation. Quand le plan de polarisation est dans le plan d'incidence alors le rayon est dit parallèle ("p") et si le rayon

est perpendiculaire au plan d'incidence, on dit qu'il s'agit d'un rayon perpendiculaire ("s"). Tout faisceau n'ayant qu'un seul ou principalement un plan pour le vecteur électrique est appelé un faisceau "polarisé". La plupart des lasers (les lasers d'IPG par exemple) produisent des faisceaux polarisés en raison de la nature du processus d'amplification qui favorise un seul plan [15]. Afin d'éviter les difficultés liées au caractère directionnel d'un procédé utilisant un faisceau polarisé linéairement, ces sources lasers sont généralement dotées d'une polarisation aléatoire ou circulaire.

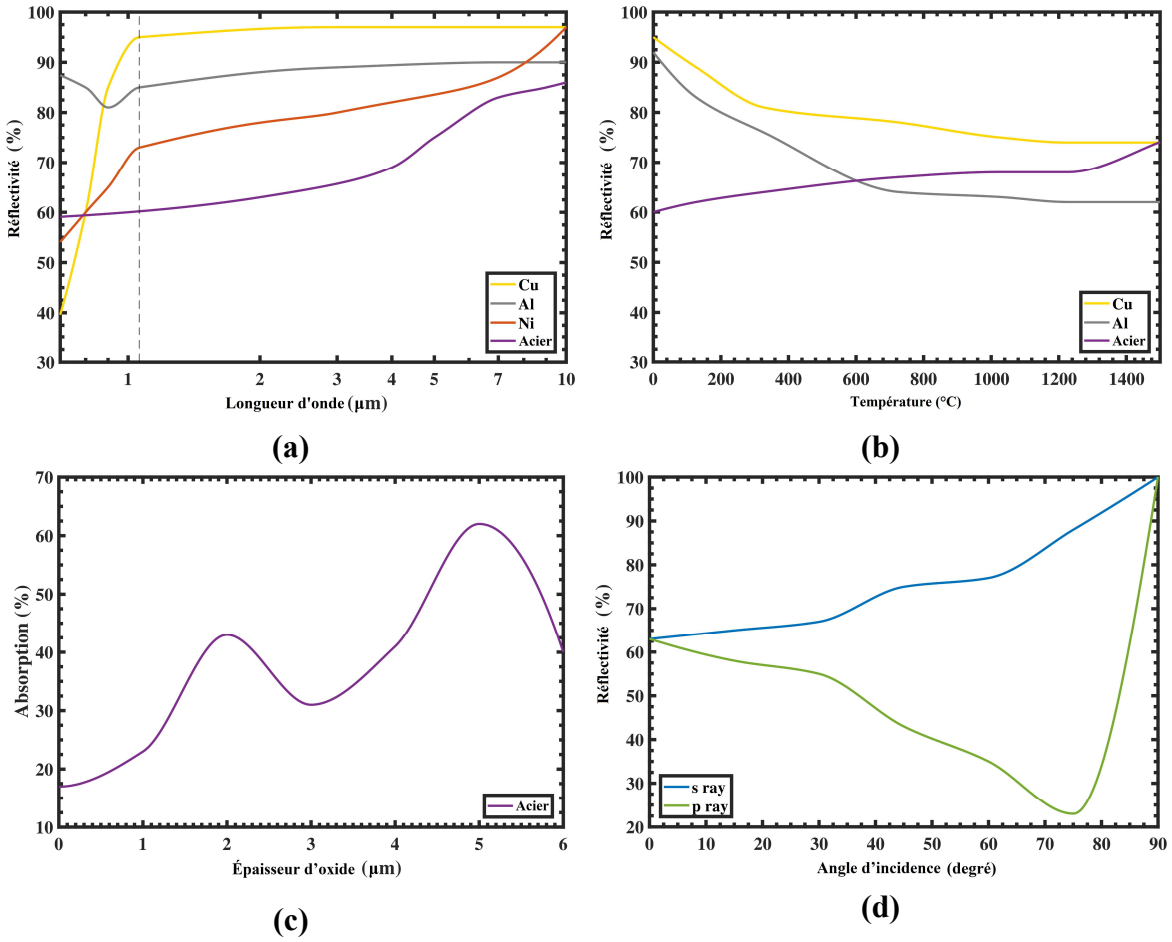

Figure 4 adapté de [14] : Coefficientent d'absorption-réflectivité en fonction de la longueur d'onde (a), de la température de la pièce (b), de l'épaisseur d'oxyde (c), et de l'angle d'incidence (d)

3. PROBLÉMATIQUE

Durant la dernière décennie, plusieurs professionnels de la recherche dans le domaine de la trempe au laser ont réussi à développer des recettes de trempe pour un matériau, une géométrie donnée et sous des conditions d'opération bien spécifiques. Ces recettes portent principalement l'accent sur l'amélioration de la performance des pièces en acier soumises à l'usure telles que les arbres de transmission, les engrenages, les ressorts métalliques, les soupapes, les outils de coupe, etc.

Cependant, il existe divers paramètres qui jouent un rôle important dans la définition de la profondeur de durcissement au laser et qui ne sont pas totalement maitrisés. La prédiction du profil de dureté sur une pièce rectangulaire, ou de géométrie complexe, durcie au laser permet une bonne évaluation des propriétés d'usure et de fatigue. Celle-ci nécessite le développement d'un modèle de couplage du transfert de la chaleur vers le profil de dureté combiné avec une bonne maitrise de la vitesse d'avance du faisceau laser tout en incluant le paramètre d'absorption de l'énergie laser [16]. Le contrôle de la formation inhomogène d'austénite due à des conditions d'austénisation et de trempe localement différente demande un développement numérique et expérimentale (par matériau et par géométrie) pour une fidèle prédiction de l'évolution de la température de début et de fin de la formation de la martensite ainsi que la valeur de la dureté résultante [17]. L'évolution structurelle quant à elle (répartition de la dureté) lors de la trempe au laser de l'acier en géométrie cylindrique par exemple doit tenir compte des paramètres de températures, de la teneur en carbone, des transformations isothermes et non isothermes, de la précipitation des carbures de transition, et de la décomposition de l'austénite retenue [18].

De nombreux modèles intéressants ont été présenté par des groupes de chercheurs pour optimiser les paramètres de traitement au laser sur la base des essais expérimentaux. On peut citer ici l'approche proposée par l'équipe de P. Dinesh en 2012 qui a permis d'obtenir une optimisation du profile de dureté de l'acier EN25, avec une dureté deux fois supérieure à la dureté initiale, en faisant varier la puissance laser et la vitesse de balayage [19]. L'approche proposée par l'équipe de F. Lambiase en 2013 qui consiste en une

méthode de prédiction du durcissement au laser au moyen d'un réseau neurone, d'un composant exposé à une irradiation dans différentes conditions de traitement au laser. Le réseau neurone a permis d'obtenir grâce à un nombre optimal de données, une prédiction de la dureté d'une pièce en un matériaux et à une profondeur donnée [20]. L'approche proposée par l'équipe de S-Y. Lee en 2014 qui consiste à proposer une méthode de résolution des équations de distribution de la température dans une pièce traitée thermiquement au laser, avec une méthode de résolution fondée sur la minimisation de l'erreur quadratique moyenne entre les données expérimentales obtenues et les données estimées de la solution analytique [21]. L'approche proposée par l'équipe de N. Barka en 2015 qui consiste à fournir une approche statistique de prédiction de la profondeur durcie d'un cylindre en acier 4340 traité thermiquement à l'aide d'une source laser 3 kW. Dans ce travail, ils ont supposé que la profondeur durcie est en corrélation avec les paramètres du processus de traitement thermique au laser tels que la puissance laser, la vitesse de balayage du faisceau laser et la vitesse de rotation de la pièce pendant le traitement. En se basant sur la planification d'expérience Taguchi et l'analyse de variance ANOVA, ils ont réussi à montrer les effets, les contributions et l'interaction entre ces paramètres, et à formuler une corrélation empirique capable de prédire la profondeur durcie pour un cylindre d'un diamètre de 10 mm en acier 4340 [22].

Comme il a été rapporté dans les travaux antérieurs, plusieurs approches d'amélioration du comportement mécanique de l'acier par un traitement thermique au laser ont été proposées par des équipes de la R&D. Cependant, la littérature ne rapporte aucune donnée quant à l'apparition d'une variation de la profondeur durcie pour des paramètres de trempe laser fixes (sans l'asservissement des paramètres par un contrôle récurrent). Par ailleurs, il reste encore beaucoup de développement à réaliser afin de rendre les modèles de prédiction plus efficaces et plus performant notamment pour la maitrise des effets des paramètres, pour la maitrise de la variation du profil de dureté dans la même composante, pour l'intégration des effets des propriétés du matériau et leur complexité, et pour répondre aux besoins de l'amélioration des performances mécaniques en fonction de la profondeur durcie.

4. OBJECTIFS

Pour répondre à la complexité de la physique qui entoure le contrôle optimal de la profondeur de transformation eutectoïde des composantes cylindriques. Le but de ce travail de maîtrise est de définir des techniques de contrôle des paramètres du durcissement au laser (puissance laser, et vitesse de rotation du cylindre) par deux approches distinctes ou combinées faisant intervenir la puissance de la simulation numérique et l'approche expérimentale à l'échelle du laboratoire, pour une évaluation des propriétés mécaniques et de la durée de vie d'une éprouvette normalisée traitée thermiquement au laser et soumise à des conditions de chargement en statique et en fatigue.

Le premier objectif est l'étude de la sensibilité du profil de dureté en fonction des paramètres de traitement thermique au laser. Le second objectif est la définition des règles d'extrapolation des résultats numériques et expérimentaux. Et le troisième objectif est l'évaluation des performances mécaniques d'une composante de géométrie cylindrique.

Dans le cadre de ce travail, on a proposé une approche de contrôle des propriétés mécaniques en fonction des paramètres de traitement thermique au laser pour des géométries cylindriques. Les paramètres étudiés sont la vitesse de déplacement de la tache focale et son accélération, la vitesse de rotation de la composante cylindrique, la puissance d'émission de l'énergie laser, le diamètre de la tache focale du faisceau laser, le diamètre de la composante, l'absorption par la surface de l'énergie laser et la dureté initiale de la composante.

L'importante contribution de cette étude est la définition des règles de contrôle (pour des composantes cylindriques) des paramètres de traitement thermique au laser pour une prédiction efficace des propriétés mécaniques (dureté, limite conventionnelle d'élasticité, résistance limite à la traction, allongement à la rupture et limite d'endurance). Pour le développement d'une expertise favorisant l'enrichissement de la base technique de l'ingénierie du traitement thermique au laser des pièces cylindriques. La complexité de ce développement requiert alors la prise en compte du montage expérimental à l'échelle du

laboratoire (cellule laser, machines de métallographie et machines d'évaluation des propriétés mécaniques), pour une validation des recettes (formules et résultats) et des modèles numériques qui sont principalement fondés sur la méthode numérique des différences finies. La méthode des différences finies (MDF) qui remplace les dérivées apparaissant dans le problème continu par des différences divisées ou combinaisons de valeurs ponctuelles de la fonction en un nombre fini de points discrets ou nœuds du maillage, a l'avantage d'être simple d'écriture et moins couteuse en temps de calcul pour des géométries et domaines de calculs simples comme c'est le cas pour des cylindres. La MDF est exploitée pour le contrôle de la répartition du profil de dureté le long d'une ligne du profil radiale. Et l'analyse statistique, fondée sur un plan d'expérience rigoureux (approche de planification de Genichi Taguchi adaptée au comportement mécanique) a été combinée avec la puissance de prédiction des réseaux de neurones pour l'évaluation du comportement mécanique en statique et en fatigue de l'acier allié AISI 4340. Pour produire des courbes de niveau avec des intervalles de réponse variables en fonction des paramètres de traitement thermique au laser, l'analyse expérimentale RSM (méthode des surfaces de réponses) qui est une technique d'analyse statistique est utilisée dans ce travail car elle présente l'avantage d'être facile à appliquer et simple à interpréter.

5. MÉTHODOLOGIE

La première phase de ce travail est consacrée au développement d'une approche prédictive des propriétés mécaniques, en se basant sur une analyse statistique des données expérimentales, d'une éprouvette de géométrie cylindrique en acier 4340 et d'un diamètre de 6 mm, traitée thermiquement dans un four de laboratoire (trempe dans la masse) et refroidie dans trois milieux différents (air, huile de trempe, et l'eau). Les échantillons ont été évalués en essai de dureté et en essai de traction normalisé suivant la norme ASTM E8 [23] pour y accéder à leurs grandeurs caractéristiques dont : le module d'élasticité, la limite conventionnelle d'élasticité, la résistance limite à la traction et la déformation à la rupture. Cette étude permettra d'extraire : les effets, les contributions et l'interaction entre les

facteurs tels que la température de revenu, le temps de revenu et le milieu de refroidissement après traitement thermique.

La deuxième phase est consacrée au développement à l'aide de la méthode des différences finies (MDF) et l'outil MATLAB, d'un modèle numérique sous forme d'un algorithme de prédiction en un point stationnaire (sans vitesse de balayage) de la répartition de la température dans un cylindre en rotation traité thermiquement au laser. Le modèle développé est validé numériquement avec la MEF et le logiciel de simulation numérique COMSOL et expérimentalement à l'aide d'une batterie de tests utilisant une source laser fibre et des échantillons en acier AISI 4340.

La troisième phase de ce travail évoque le développement à l'aide de la méthode des différences finies (FDM) d'un algorithme qui intègre le paramètre déplacement du faisceau laser au niveau des conditions aux limites du processus de durcissement au laser de l'acier AISI 4340. La faisabilité et l'efficacité de l'approche proposée doivent conduire à un modèle mathématique précis et fiable, capable de prédire la distribution de la température dans une pièce cylindrique traitée thermiquement par un faisceau laser en mouvement le long de l'axe longitudinal du cylindre.

La quatrième phase traite l'analyse expérimentale de la variation du profil de dureté le long de l'axe longitudinal du cylindre pour des paramètres fixes de traitement thermique au laser. Cette analyse sera effectuée par l'analyse de variance ANOVA pour en extraire les effets des paramètres sur le processus. Une prédiction de la variation de la profondeur durcie et du profil de dureté par application des réseaux de neurones artificiels sera effectuée afin de proposer une architecture de réseau de neurones artificiels (Artificial Neural Network) pour estimer (prédire) de façon relativement satisfaisante les réponses du modèle en fonction des paramètres de traitement thermique au laser.

La cinquième phase de ce travail propose le développement d'un modèle numérique COMSOL, capable d'optimisation la distribution de la température dans une composante cylindrique en acier AISI 4340, au moyen d'un contrôle récurrent de la puissance laser pour

une homogénéisation de la répartition de la température maximale atteinte en surface, et pour une profondeur durcie uniforme, pour des pièces cylindriques de longueur 50 mm et de diamètre compris entre 16 et 22 mm.

La sixième et dernière phase est consacrée à la réalisation des essais de performance mécanique d'une éprouvette normalisée en acier AISI 4340, pour une prédiction de la durée de vie en sollicitation de traction, par l'utilisation d'un plan d'expérience basé sur une planification Taguchi en ayant comme facteurs : la puissance laser, la vitesse de balayage du faisceau laser, et la contrainte minimale et maximale de la sollicitation sinusoïdale. Cette investigation permettra d'extraire les données nécessaires pour une analyse de variance ANOVA et une estimation du nombre de cycles (durée de vie mécanique) par un polynôme de régression linéaire multiple et par l'emploi de la puissance de prédiction des réseaux de neurones.

6. ORGANISATION DU MÉMOIRE

Le chapitre 1 introduit la trempe au four de l'acier AISI 4340 et analyse ses propriétés mécaniques en fonction de la température du four, le temps de revenu dans le four et le milieu de refroidissement. On retrouve également une technique d'évaluation du pouvoir de refroidissement du milieu de trempe, une présentation ordonnée du plan expérimental et des résultats des essais mécaniques, et finalement une analyse de variance des réponses obtenues en fonction des paramètres de traitement thermique au four. Le chapitre 2 introduit un algorithme numérique de calcul de la distribution de la température pour une composante cylindrique en rotation traitée thermiquement avec un faisceau laser en un point stationnaire. Le chapitre 3 présente une investigation numérique et expérimentale pour compléter l'algorithme développé dans le deuxième chapitre de ce présent mémoire, en introduisant le paramètre déplacement du faisceau laser. Le coefficient de transfert de la chaleur par convection et le coefficient d'absorption du matériau de l'énergie laser, qui sont tous les deux des données indispensables pour l'évaluation du bilan thermique, ont été respectivement approximés par des mesures expérimentales de la température de l'air au voisinage de la composante cylindrique en rotation, au moyen des

mesures de températures en surface à l'aide d'une caméra thermique infrarouge et par des mesures de microdureté. La démarche expérimentale et numérique a été exposée en détail avec les équations de calcul du bilan et les hypothèses de modélisation et de simulation.

Le chapitre 4 vise à montrer l'impact que peut avoir l'emploi de paramètres fixes de durcissement au laser sur la variation de la profondeur durcie et du profil de dureté (région fusionnée, région durcie, région revenue, et région non affectée par le traitement thermique au laser) d'une composante cylindrique traitée thermiquement en surface. Au chapitre 5, nous présentons une technique de contrôle de la variation de la profondeur durcie et du profil de dureté exposée dans le chapitre 4, au moyen de l'ajustement de la puissance du laser. Le chapitre 6 et dernier, relie les principales techniques expérimentales et numériques exposées dans les précédents chapitres pour une analyse des avantages du durcissement au laser sur les propriétés mécaniques en statique et en fatigue d'une éprouvette cylindrique de géométrie normalisée, de diamètre de la partie calibrée de 9 mm, et en acier AISI 4340.

La dernière partie de ce mémoire permet de conclure le travail avec une courte conclusion et un survol des principaux résultats obtenus et quelques recommandations et débouchés potentiels de travail à venir.

Références :

1. William D. Callister, Fundamentals of Materials Science and Engineering: An interactive. John Wiley & Sons, 2001.
2. D. Gandy, Carbon Steel Handbook, March 2007.
3. Totten, George E., Charles E. Bates, and N. A. Clinton. Handbook of quenchants and quenching technology. ASM international, 1993.
4. Guide d'auto-apprentissage pour les opérateurs en traitement thermique. Comité sectoriel de la main-d'œuvre dans la fabrication métallique industrielle (PERFORM). Marché du travail, Québec.
5. Cain T., Hardening, Tempering and Heat Treatment: The Structure of Steel and the Effects of Different Heat Treatments, 1990.
6. S. Fox-Rabinovich, George E. Totten. - Steel Heat Treatment Metallurgy and Technologies-Taylor & Francis, 2007.
7. Les Ateliers Laser Novika, novembre 2018.
8. Avner, Sidney H., Introduction to physical metallurgy, McGraw-Hill, 1974.
9. Michael Bass, Laser Materials Processing, Theory and Practices, Elsevier Science, 1983.
10. Kennedy, E., Byrne, G. and Collins, D.N. (2004) A Review of the Use of High Power Diode Lasers in Surface Hardening. Journal of Materials Processing Technology, 155-156, 1855-1860.
11. Ricciardi, G., Cantello, M. and Micheletti, G.F. (1982) Technological Applications of the Laser Beam in Heat Treatments. CIRP Annals-Manufacturing Technology, 31, 125-130.

12. Lakhkar, R.S., Shin, Y.C. and Krane, M.J.M. (2008) Predictive Modeling of Multi-Track Laser Hardening of AISI 4140 Steel. Materials Science and Engineering A, 480, 209-217.

13. P. Peyre, Les procédés Laser, PIMM, Arts et Métiers - Paris Tech, 2016.

14. William M. Steen PhD, MA, CEng (auth.) Laser Material Processing-Springer London, 2010.

15. Drude P., Theory of optics (English edn). Longmans, Green, New York, 1922.

16. Mazumder, J. Laser heat treatment: the state of the art. JOM, 35(5), 18-26, 1983.

17. T. Mioković, V. Schulze, O. Vöhringer, D. Löhe, Materials Science and Engineering: A, 2006, vol. 435-436, pp. 547-555.

18. Xiaohu Deng, Dongying Ju, Modeling and Simulation of Quenching and Tempering Process in steels, International Federation for Heat Treatment and Surface Engineering 20th Congress Beijing, China, 23-25 October 2012, Physics Procedia 50, 2013, pp. 368-374.

19. Yumen, S. and Mingzhong, H. (2012) Statistical analisys and optimization of process parameters in Ti6A14V. Optics and Laser in Engineering, 50, 985-995.

20. Lambiase, F., Di Ilio, A.M. and Paoletti, A. (2013) Prediction of Laser Hardening by Means of Neural Network. Science Direct, 8th CIRP Conference on Intelligent Computaion in Manufacturing Engineering, 12, 181-186.

21. Sen-Yung Lee, Tsung-Wen Huang, A method for inverse analysis of laser surface heating with experimental data, International Journal of Heat and Mass Transfer 72 (2014) pp. 299-307.

22. N. Barka, A. El Ouafi, Effects of Laser Hardening Process Parameters on Case Depth of 4340 Steel Cylindrical Specimen-A Statistical Analysis, Journal of Surface Engineered Materials and Advanced Technology (2015), vol. 5, pp. 124-135.

23. William M. Steen PhD, MA, CEng (auth.) Laser Material Processing-Springer London (2010).

24. ASTM E8/E8M, Standard test methods for tension testing of metallic materials. ASTM International, West Conshohocken (2009).

CHAPITRE 1

ANALYSE DES PROPRIÉTÉS MÉCANIQUES D'ÉCHANTILLONS EN ACIER AISI 4340 TRAITÉS THERMIQUEMENT DANS UN FOUR ET TREMPÉS DANS TROIS FLUIDES DIFFÉRENTS

Fakir, R., Barka, N., & Brousseau, J.
Université du Québec à Rimouski, Rimouski, Québec, Canada, G5L 3A1

Cet article a été publié dans le journal Metals and Materials International., 24 (5), 2018, 981–991. Son identifiant numérique d'objet (DOI) est : 10.1007/s12540-018-0120-9

Mots clés : Traitement thermique au four · Essai de traction · AISI 4340 · ANOVA · RSM

1.1 RÉSUMÉ EN FRANÇAIS DU PREMIER ARTICLE

Cet article propose une approche statistique pour analyser les propriétés mécaniques d'une éprouvette standard, de géométrie cylindrique et en acier 4340, d'un diamètre de la partie calibrée de 6 mm, traitée thermiquement dans un four de laboratoire et trempée dans trois fluides différents. Les échantillons ont été évalués dans le cadre d'essais de traction standard pour déterminer leurs quantités caractéristiques : dureté, module d'élasticité, limite d'élasticité, résistance limite à la traction et déformation ultime. L'approche proposée est construite progressivement par (i) une présentation du dispositif expérimental, (ii) une présentation du plan expérimental et des résultats des tests mécaniques, (iii) une analyse de variance ANOVA et une représentation des réponses obtenues en utilisant la méthode des surfaces de réponse RSM, et (iv) une analyse des résultats et une discussion. La faisabilité et l'efficacité de l'approche proposée conduisent à un modèle précis et fiable capable de prévoir la variation des propriétés mécaniques, en fonction de la température de revenu, du temps de revenu et de la capacité de refroidissement du milieu de trempe.

Ce premier article, intitulé « *Mechanical Properties Analysis of 4340 Steel Specimen Heat Treated in Oven and Quenching in Three Different Fluids* », fut corédigé par moi-même ainsi que par le professeur Noureddine Barka et le professeur Jean Brousseau. Il fut

accepté pour publication dans sa version finale en 2018 par l'éditeur chef Do Hyang Kim de la revue *Metals and Materials International*. En tant que premier auteur, ma contribution à ce travail fut l'essentiel de la recherche sur l'état de l'art, le développement de la méthode, l'exécution des tests de performance et la rédaction de l'article. Les professeurs Noureddine Barka et Jean Brousseau, second et troisième auteurs, ont participé à définir le projet d'article et ils ont aidé à la recherche sur l'état de l'art, au développement de la méthode ainsi qu'à la révision de l'article.

1.2 TITRE DU PREMIER ARTICLE

Mechanical Properties Analysis of 4340 Steel Specimen Heat Treated in Oven and Quenching in Three Different Fluids.

1.3 ABSTRACT

This paper proposes a statistical approach to analyze the mechanical properties of a standard test specimen, of cylindrical geometry and in steel 4340, with a diameter of 6 mm, heat-treated and quenched in three different fluids. Samples were evaluated in standard tensile test to access their characteristic quantities: hardness, modulus of elasticity, yield strength, tensile strength and ultimate deformation. The proposed approach is gradually being built (a) by a presentation of the experimental device, (b) a presentation of the experimental plan and the results of the mechanical tests, (c) Anova analysis of variance and a representation of the output responses using the RSM response surface method, and (d) an analysis of the results and discussion. The feasibility and effectiveness of the proposed approach leads to a precise and reliable model capable of predicting the variation of mechanical properties, depending on the tempering temperature, the tempering time and the cooling capacity of the quenching medium.

1.4 NOMENCLATURE

Ac_3	*Heating temperature at point A_3, °C*
T	*Oven temperature, °C*
ORT	*Oven residence time, min*
HTC	*Heat Transfer Coefficient, $W.m^{-2}.K^{-1}$*
Ra_D	*Rayleigh number,*
Nu	*Nusselt number,*
Pr	*Prandtl number,*
k	*Thermal conductivity of the material, $W.m^{-1}.K^{-1}$*
T_s	*Surface temperature of the material, °C*
T_∞	*Ambient air temperature, °C*
D	*Diameter of the specimen, mm*
ϑ	*Kinematic viscosity, $m^2.s^{-1}$*
α	*Thermal diffusivity, $m^2.s^{-1}$*
g	*Gravitational acceleration, $m.s^{-2}$*
T_f	*Average temperature between Ts and T_∞, °C*
Bi	*Biot number,*
h	*Thermal transfer coefficient, $W.m^{-2}.K^{-1}$*
C_p	*Specific heat, $J.kg^{-1}.K^{-1}$*
ρ	*Density, $kg.m^{-3}$*
S	*Surface of the sample, m^2*
V	*Volume of the sample, m^3*
Sy	*Offset yield strength, MPa*
Su	*Ultimate tensile strength, MPa*
Er	*Elongation at break, mm/mm*
$\mathcal{H}$	*Hardness, HRC (Rockwell C)*
P	*Prediction polynomial,*

1.5 INTRODUCTION

Alloy steel 4340 is heat treatable steel. When it undergoes a heat treatment it gets a strong robustness, strong toughness, good ductility and immunity against embrittlement [1]. These many qualities allow it to be chosen as a premium alloy in the aviation, marine and automotive industries [2]. It is found in crankshafts of the automotive sector and in the marine environment, in the piston rods, the wheel shafts, aircraft parts, the gears, mechanical parts of boreholes, as well as in several other applications. When heated to a temperature above the Ac_3 austenitization temperature, it changes from a solid phase to another solid with notable mechanical properties [3, 4]. This eutectic reaction plays a very important role in its heat treatment with a maintenance of the shape of its structure, during heating and cooling. Oven heat treatment controls heating and cooling, by acting at the microstructure level of the material, by modifying the mechanical properties, modifying physical properties such as thermal and electrical conductivity and also changing the chemical properties like corrosion resistance [5]. This type of heat treatment consists in varying the temperature of the material while keeping it in the solid state. This time-dependent variation of temperature is called a thermal cycle and consists of a heating at a certain temperature above the Ac_3 temperature, followed by a maintenance of the temperature for a certain time, and finally cooling at a certain speed of well-defined cooling. Cooling is generally done in water, oil or air [6].

Each cooling medium is characterized by a convective heat transfer coefficient, which can be evaluated by empirical correlations. For alloy steel 4340, the rapid cooling of the austenite to a temperature below the critical value Ms causes a fixation of the carbon atoms inserted in the gamma (γ) region. At the atomic scale, the structure becomes quadratically centered instantly. This new solid insertion solution is called martensite and its formation is related to the rate of cooling of the heat-treated material in the oven. The cooling rate must be greater than the critical speed of the martensitic quench which is of the order of 8 $°C.s^{-1}$ for the alloy steel 4340. It is obvious that this condition depends on the thermal conductivity of the metal, the shape and dimensions of the material, and also the

cooling capacity of the quenching medium [7]. In practice, after quenching, samples are returned to the oven in order to eliminate the intermolecular tensions of the rapid cooling which weakens the material. And also to obtain a change in mechanical properties by a change in the microstructure of the material. At the scale of the microstructure, after cooling, a mixture of martensite, residual austenite, bainite and carbides is obtained, while during the tempering this martensite turns into ferrite and the carbides and residual austenite turn into martensite and bainite.

A standard test specimen of a diameter of 6-mm in alloy steel 4340 can be considered as a thin body because it has a Biot number of less than 0.1 (number that compares heat transfer resistances inside and on the surface of the sample). This makes it possible to evaluate the cooling power of the quenching medium by using the approximation of the uniform temperature at any point of the sample. To determine the elastic behavior of a material and to measure its degree of tensile strength one can perform a tensile test which is a physics experiment in a uniaxial stress state. For metallic materials such as 4340 steel, the reference standard for a tensile test is ASTM E8 (Standard test methods for tension testing of metallic materials) which generally defines the shape and dimensions of the specimen, the loading speed and the calibration of the machine [8-10]. This test provides the values of the mechanical properties of a material such as the longitudinal modulus of elasticity, the Poisson's ratio, the yield strength, tensile strength and elongation at break. An empirical correlation between Brinell hardness and Su tensile strength for low-work hardening alloys such as steels, aluminum alloys and titanium alloys was formulated by Datsko et al. in 2001. To estimate the accuracy of the results, Datsko et al. compared the experimental values and the estimated values of Su. The error obtained was weak and did not exceed 10% in most of the prediction cases. It has been shown that this method of predicting the value of Su from the value of hardness is easy to use and can be applied to a wide range of materials [11]. In the field of martensitic quenching, an interesting but untapped prediction using experimental analysis of the mechanical properties of AISI 4340 steel was developed in this study. The proposed approach allows for prediction and control based on oven heat treatment parameters: the variation in mechanical properties (hardness, yield strength,

tensile strength and elongation at break) for a 4340-alloy steel specimen with a cylindrical geometry and a diameter of 6-mm. The approach is built progressively by a presentation of the experimental setup, a presentation of the experimental design and mechanical test results, an Anova variance analysis and a representation of the output responses using the response surface method. RSM, and an analysis of the results and discussion.

1.6 EXPERIMENTAL PROCEDURE

1.6.1 Experimental Setup

The experimental tests were carried out on standard test specimens in 4340 steel and cylindrical geometry, with a diameter of the calibrated portion of 6-mm. Figure 1-1 shows the dimensions of the specimen studied according to ASTM E8.

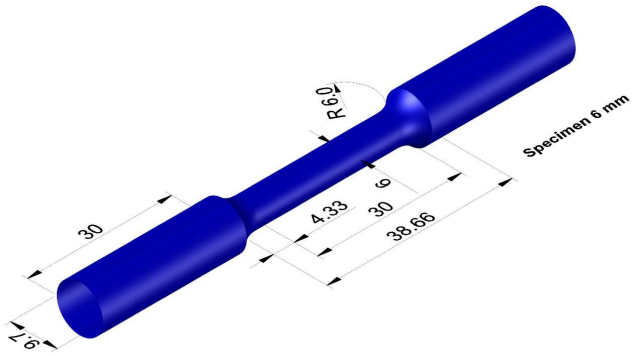

Figure 1-1: 3D visualization of the geometry of the specimen

The samples were prepared, and heat treated in oven. The oven was set at a temperature of 900°C, which is the eutectoid temperature of 4340 alloy steel, before receiving the samples. Once in the oven, the samples remained there for 20-min to reach the austenitic phase, then cooled in groups of three in air, oil and water. After quenching, the samples received a tempering at three different heating temperatures (300, 500 and 650°C) and three different residence time in the oven (30, 60 and 90-min). After the heat treatment in the oven, the samples are carefully prepared, polished and etched using a Nital chemical solution (95% ethanol and 5% nitric acid). The hardness profiles were characterized by microhardness measurements programmed using the Clemex CMT

microhardness machine, and by macrohardness measurements using the Wilson-Rockwell-574 machine, with the Rockwell-C as a unit of measure for hardness.

Subsequently, they were subjected to tensile tests to evaluate their mechanical properties after quenching and tempering. Tensile tests were carried out using a MTS-810 tensile testing machine, which is an automated machine used to develop and qualify the use of materials, with a total load in tension, up to 100-kN. The flexibility of the configuration of this automatic tensile testing machine allows a variety of applications and centralized management of test results using the MTS Test Works program. Once the specimen is in place, a displacement of the span is carried out which has the effect of stretching the specimen, and the force generated by this displacement is measured. The movement is done by a hydraulic piston system and the effort is measured by a force sensor inserted into the load line. The tensile load applied in our experiments was between 28- and 50-kN, with a strain rate of 0.015-min^{-1} [8]. At each increment of load, a measurement is taken by a displacement measuring sensor which makes it possible to accurately evaluate displacements. The test stops at the rupture of the specimen. Figure 1-2 shows the flow chart of the experimental tests.

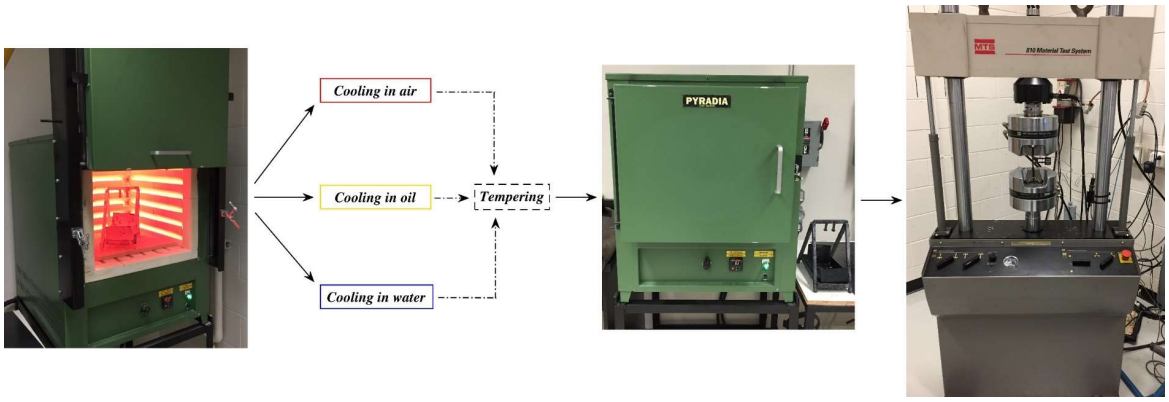

Figure 1-2: Description of the experimental device

1.6.2 Experimental Design

To predict the mechanical properties of a material, using experimental modeling, it is essential to have relevant tests to adequately represent these characteristics according to the

parameters of the test. To obtain results validating a model with as few tests as possible, it is essential to define an ordered sequence of experimental tests using an experimental design. This will collect new information by controlling one or more input parameters. Because of its efficiency and simplicity, factorial design is generally the most commonly used model for selecting values for each factor by simultaneously varying all factors. This type of experiment makes it possible to study the effect of each variable on the process, but with many tests that can then become very large. To avoid having to end up with a considerable number of tests to be carried out, it is essential to determine through a Taguchi experience plan the parameters of the optimal control factors that make the process more robust, more resistant, with a more efficient performance, consistent and statistically significant data in a minimum number of tests [12, 13]. In the case of furnace heat treatment, it is important to avoid the non-transformation of the steel and the melting of the surface layer of the material.

The experimental tests begin by defining the low and combined levels of the three factors used (oven temperature, oven residence time, and cooling medium) to ensure that these conditions are met. Table 1-1 shows the factors and levels used in the planning of experiments. As a result, three factors with three levels are considered. They are continuous and linked to oven tempering temperature (T), residence time (ORT) and convection heat transfer coefficient (HTC). The oven temperature in °C, the residence time in minutes and the coefficient of heat transfer by convection in $W.m^{-2}.K^{-1}$ are considered as input parameters. The design that answers this problem is an L_9 matrix corresponding to nine tests. Each test consists of following the experience methodology detailed in Fig. 1-2. The mechanical properties are determined by examining the tensile test results on the MTS machine (modulus of elasticity, yield strength, tensile strength, and ultimate strain) and examining the cross-sectional area of the samples to determine the average value of the hardness by measuring the microhardness.

Table 1-1: Factors and levels of experience planning

Factors	Levels
Temperature (°C)	300, 500 and 650
Oven Residence Time (min)	30, 60 and 90
Heat Transfer Coefficient ($W.m^{-2}.K^{-1}$)	Air, oil and water

The results obtained from the Taguchi L_9 matrix were exploited using the contributions and the average effects of each factor on the final response. The percentage contribution of a single factor reflects the total variation observed in the experience attributed to this factor, and from the interactions between the factors.

1.6.3 Cooling Rate According to the Quenching Medium

In this study, the coefficient of heat transfer by convection was estimated according to the quench medium and using the empirical correlation formulated by Churchill et al. [14]. This correlation, which is adapted to scientific computing, involves the adimensional number of Nusselt (Eq. 1), Prandtl (Eq. 2) and Rayleigh (Eq. 3). It is valid only for a Rayleigh number less than 10^{12}.

$$\overline{N_{u_D}} = {h.D}/{k} = \left(0.6 + \left(0.387\ {Ra_D}^{1/6} / \left(1 + \left({0.559}/{Pr}\right)^{9/16}\right)^{8/27}\right)\right)^2 \quad (1)$$

The number of Prandtl which characterizes the ratio between the kinematic viscosity ϑ and thermal diffusivity α is given by Eq. (2). The Rayleigh number that characterizes the heat transfer within a fluid, is given by Eq. (3). With T_f the average between the surface temperature of the solid T_s and the initial temperature of the cooling bath T_∞, and D the diameter of the calibrated portion of the sample.

$$Pr = {\vartheta}/{\alpha} \quad (2)$$

$$Ra_D = {g}/{T_f.\vartheta.\alpha}\,(T_s - T_\infty).D^3 \quad (3)$$

Equation (4) presents the adimensional number of Biot. For a specimen of diameter 6-mm and steel AISI 4340, the number Bi < 0.1 therefore we can consider that the body is thermally thin and we can then use the approximation of the uniform temperature to study the evolution over time of temperature.

$$Bi = {}^{h.r}/_{k} \tag{4}$$

Equation (5) presents the thermal balance and Eq. (6) presents the evolution of the sample temperature according to the convective heat transfer coefficient (Eq. 1), the geometric and thermal parameters of the material.

$$h.S.(T_s - T_\infty) = -\rho.C_p.V.{}^{dT_s}/_{dt} \tag{5}$$

$$T_s(t) = (T_i - T_\infty).\exp\left(-{}^{h.S.t}/_{\rho.C_p.V}\right) + T_\infty \tag{6}$$

Figure 1-3a shows the evolution of sample temperature according to time and cooling medium. For 4340 steel, there is a critical fast cooling rate, which gives rise to the formation of a completely martensitic structure, and which is of the order of 8.3°C s−1. We see in Fig. 1-3, by superposition with the 4340-steel cooling curve, that cooling in cold water (29°C.s^{-1}) and in oil (14°C.s^{-1}) will provide a fully martensitic structure. And the cooling in the air blown (3.8°C.s^{-1}) and in the open air (2°C.s^{-1}) will provide a mix between martensite and bainite.

Figure 1-3b shows the value of the average hardness of the samples according to the quenching medium. These values were obtained by measurements of the micro-hardness of the surface at the center of the radial section of the cylinder, by cooling batch, and by repetition (×3) of the tests for a good statistical significance. Austenitization was performed at a temperature of 900°C for a period of 20-min followed by cooling in three different fluids (water, oil and air).

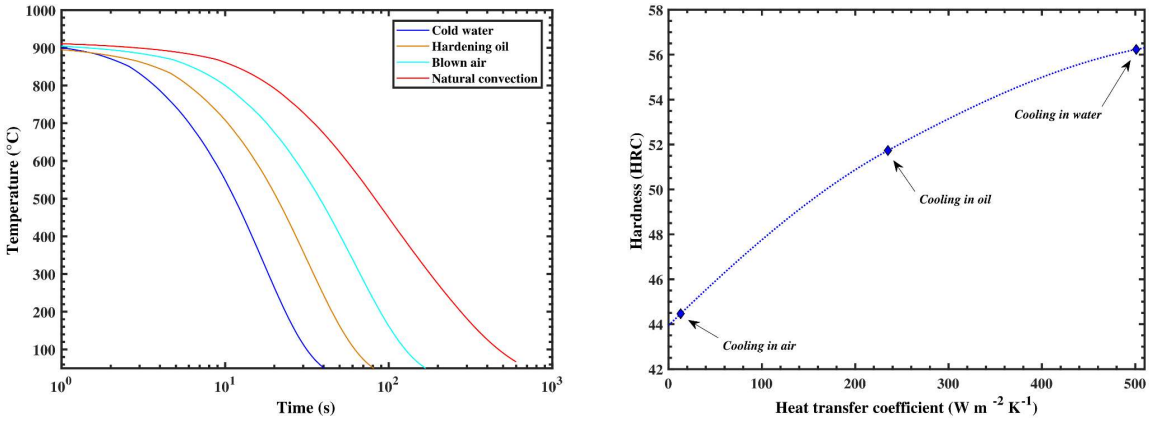

(a) (b)

Figure 1-3: Quenching medium – (a) Cooling speed, (b) Average variation in hardness

Figure 1-4 shows a microscopic visualization with magnification (×2000) of the observed microstructure. Figure 1-4a shows a completely martensitic structure with a low percentage of residual austenite observed for the majority of samples that received cooling in water and in oil. And Fig. 1-4b shows a structure composed of martensite, bainite and a small percentage of residual austenite observed for the majority of samples that received cooling in air.

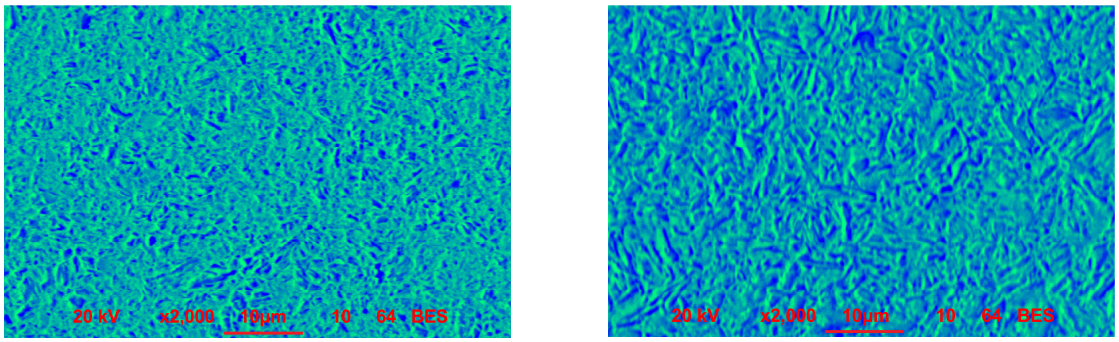

(a) (b)

Figure 1-4: Microscopic visualization – (a) Cooling in water and in oil, (b) Cooling in air

1.6.4 Measurements of Mechanical Properties

Table 2 presents the test grid with the results of the measurements of the yield strength, the ultimate tensile strength, the elongation at break, and the average hardness after tempering. The average hardness was determined by examining the cross-sectional

area of the samples by microhardness testing. Figure 1-5a–c shows the stress–strain curves of the tensile tests of the experiment planning tests in Table 1-2, according to the tempering temperature, the residence time in the oven and quenching medium. Figure 1-5d shows the values of hardness measurements, by test, before and after oven tempering.

Table 1-2: L_9 orthogonal matrix and experimental results

Tests	**Factors**			**Responses**			
	T (°C)	ORT (min)	HTC ($W.m^{-2}.K^{-1}$)	Sy (MPa)	Su (MPa)	Er (%)	$\mathscr{H}$ (HRC)
1	300	30	13	1417	1552	14.1	43.6
2	300	60	235	1497	1758	12.3	39.5
3	300	90	500	1519	1720	13.4	46.8
4	500	30	235	1143	1207	14.5	35.9
5	500	60	500	1124	1204	14.9	30.0
6	500	90	13	1027	1142	18.7	33.7
7	650	30	500	997	1059	15.0	31.9
8	650	60	13	865	996	17.5	28.1
9	650	90	235	1015	1142	22.0	30.9

We notice that, the higher the temperature of the oven, and the longer the residence time in the oven, the lower is the load corresponding to ultimate tensile strength. So for an oven temperature of 300°C and a residence time in the oven of 30-min, the maximum breaking load of our samples is 50-kN. And for an oven temperature of 650°C and a residence time in the oven of 90-min, the minimum breaking load observed is 28-kN.

It is also noted that the power of the quenching medium after austenitization has an influence on the ultimate tensile strength. This influence on the load corresponding to the tensile strength is proportional to the coefficient of heat transfer by convection of the quenching medium. Regarding the hardness, it is noted that it is inversely proportional to the temperature of the oven and the residence time in the oven. Its value changes from 45-HRC (Rockwell C) for an oven temperature of 300°C and a residence time in the oven of 30-min, to 30-HRC for an oven temperature of 650°C and a residence time in the oven of

90-min. It should also be noted that the value of the hardness is proportional to the coefficient of heat transfer by convection of the quenching medium.

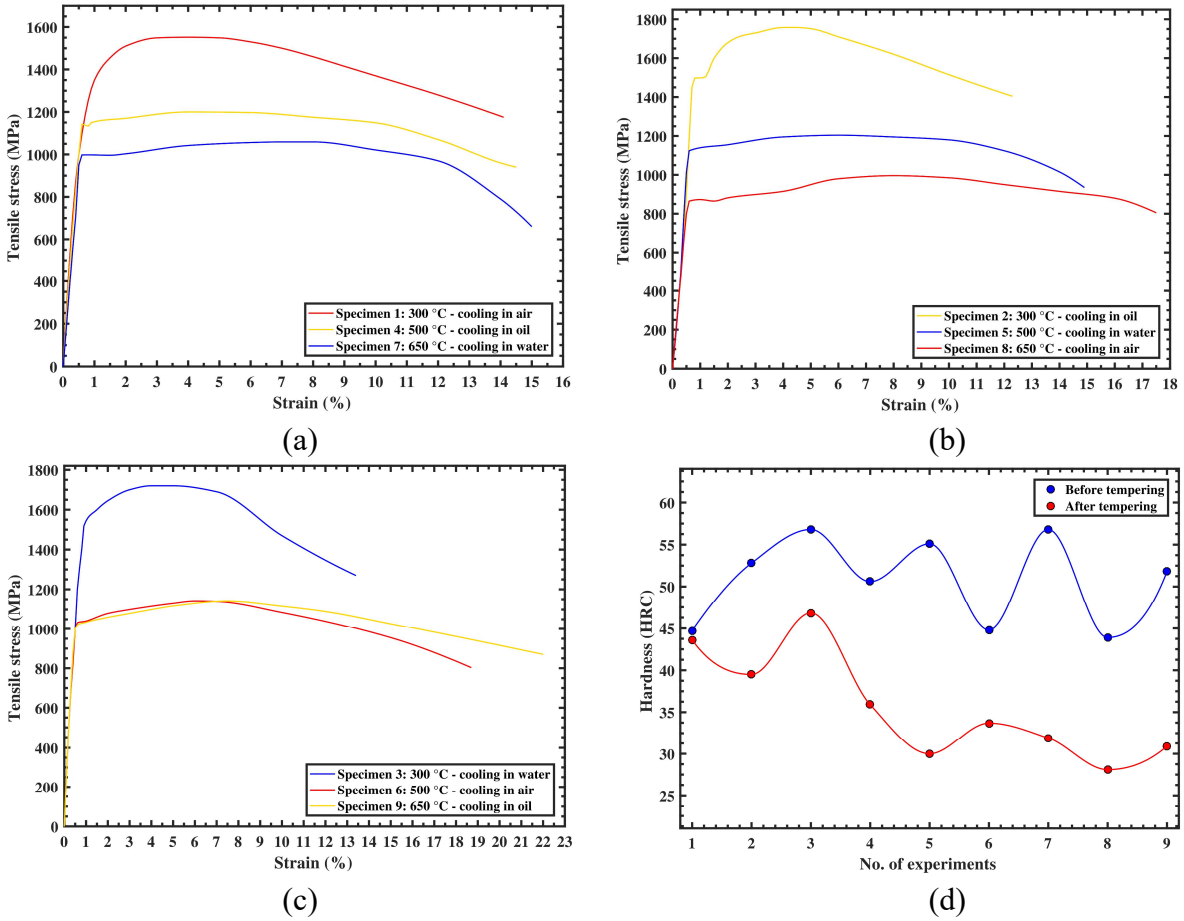

Figure 1-5: (a) Strain versus tensile stress for test 1, 4 and 7, (b) Strain versus tensile stress for test 2, 5 and 8, (c) Strain versus tensile stress for test 3, 6 and 9, (d) Hardness before and after tempering

1.6.5 Analysis of Variance (ANOVA)

To determine the influence of model input parameters (T, ORT, and HTC) on output responses (Sy, Su, Er and $\mathscr{H}$), and thus quantify the decisions using hypothesis tests to know if the variation is influenced by a single parameter, different parameters or by a combination of parameters. An analysis of variance (ANOVA) [15, 16] was performed which is a widely used calculation technique to determine which design parameter affects the variation of mechanical properties. The parameter with the lowest contribution ratio is

set to error factor to capture only the main factor affecting the final response. Generally, the ANOVA table contains the degrees of freedom, the sum of the squares, the average square, the value of P and the value of F. For each parameter studied, the value of the variance ratio F was compared with the values of the tables F standard.

Tables 1-3, 1-4, 1-5 and 1-6 present a variance analysis of the respective responses for Sy, Su, Er and $\mathscr{H}$ using the general stepwise method under the terms of order 1 for Sy, and the term order 2 for Su, Er and $\mathscr{H}$. A value of P less than 5% indicates that the corresponding factor (characteristic) has a significant effect on the model response. It is noted that the conventional elastic limit Sy is influenced mainly by the temperature of the oven (T), with a percentage of about 91.1%, and by the coefficient of heat transfer by convection (HTC) with a percentage of contribution of approximately 3.7%. The tensile strength Su, in turn, is influenced mainly by the temperature of the oven (T) with a percentage of 94%, as well as by the other parameters with a contribution percentage of about 5%.

Table 1-3: ANOVA for Sy

Characteristic	**dof**	**Contributions (%)**	**Sum of Squares**	**F-value**	**P-value**
T	1	91.14	418704	106.28	0.001
HTC	1	3.71	17062	4.33	0.083
Residual	6	5.15	23638	–	–
Total	8	100.00	459404	–	–

Table 1-4: ANOVA for Su

Characteristic	**dof**	**Contributions (%)**	**Sum of Squares**	**F-value**	**P-value**
T	1	88.28	589065	211.02	0.001
ORT	1	0.86	5766	15.48	0.029
HTC	1	1.91	12762	67.09	0.004
T^2	1	6.10	40730	109.31	0.002
HTC^2	1	2.67	17806	47.79	0.006
Residual	3	0.17	1118	–	–
Total	8	100.00	667247	–	–

Table 1-5: ANOVA for Er

Characteristic	dof	Contributions (%)	Sum of Squares	F-value	P-value
T	1	49.09	36.21	297.40	0.003
ORT	1	24.91	18.37	3389.92	0.001
HTC	1	11.42	8.42	48.95	0.020
ORT^2	1	5.19	3.82	2063.91	0.001
HTC^2	1	0.86	0.63	11.92	0.075
T x ORT	1	8.54	6.30	3397.80	0.001
Residual	2	0.01	0.01	–	–
Total	8	100.00	73.76	–	–

Table 1-6: ANOVA for $\mathscr{H}$

Characteristic	dof	Contributions (%)	Sum of Squares	F-value	P-value
T	1	79.96	265.24	249.39	0.040
ORT	1	0.00	0.01	609.74	0.026
HTC	1	0.56	1.85	43.90	0.095
T2	1	4.27	14,17	151.69	0.052
ORT2	1	12.76	42.32	598.98	0.026
T x HTC	1	2.42	8.03	77.67	0.072
ORT x HTC	1	0.01	0.02	0.30	0.680
Residual	1	0.02	0.08	–	–
Total	8	100.00	331.72	–	–

Analysis of variance showed that the total elongation at break Er is influenced mainly by oven temperature (T) and oven residence time (ORT) and a combination of temperature and residence time, with a total contribution percentage of about 87.7%.

Regarding the hardness after tempering, we note that it is influenced mainly by the oven temperature with a percentage of 81.3% and a combination of the other parameters (HTC and ORT), including their iteration, with a total percentage about 18.5%. It was concluded, within the range of parameter variation ranges that oven temperature, oven

residence time, and convective coefficient of cooling medium are significant for the 94% response value of the model.

Figure 1-6 shows the effect of all parameters on the average response value. The results obtained confirm that the value of the hardness, the Offset yield strength and the ultimate tensile strength decrease with increasing oven temperature, and that the elongation at break increases with the temperature and the residence time in the oven. And that the cooling medium has a significant effect on elongation at break.

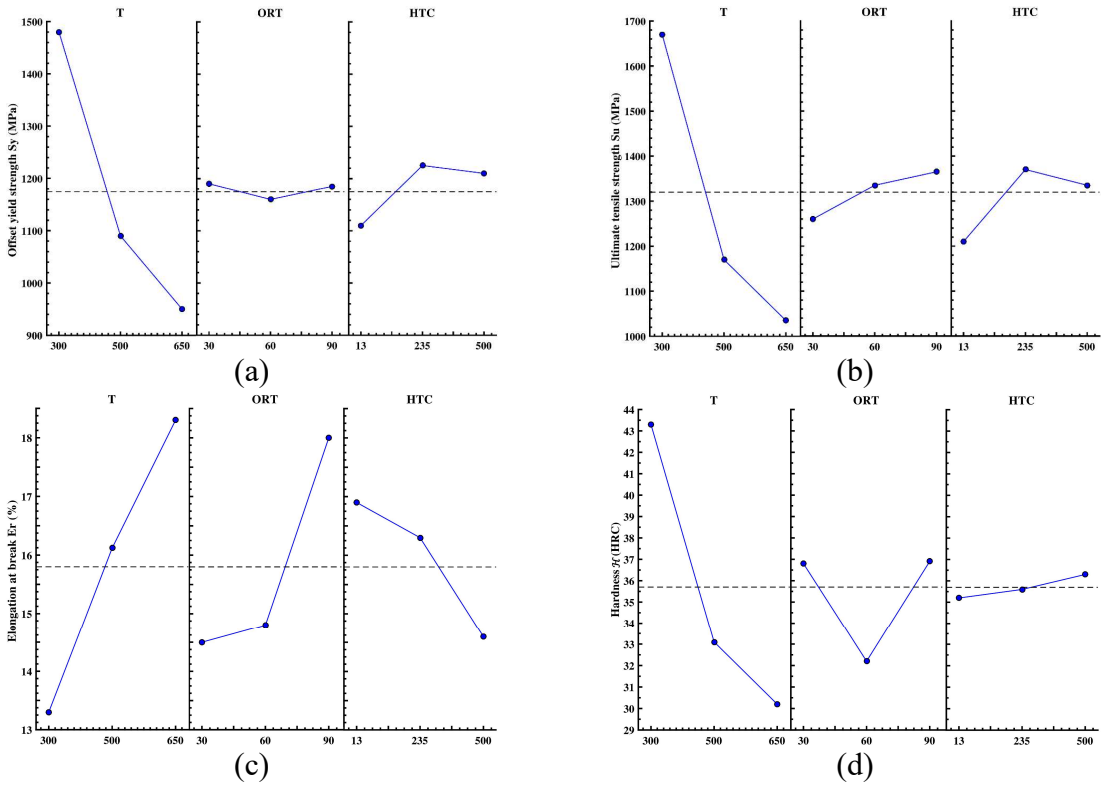

Figure 1-6: Main effects plot – (a) Offset yield strength, (b) Ultimate tensile strength. (c) Elongation at break, (d) Hardness

Equation (7) presents the formulation of the multiple linear regression model, ANOVA analysis of variance, between the parameters used in the sensitivity study (T, ORT and HTC) and the output results (Sy, Su, Er and $\mathscr{H}$). The regression model was obtained using the Minitab statistical analysis software (version 18). Table 1-7 shows the

coefficients of the multiple linear regression polynomial P of the four output responses. The residual value squared (R^2) of the regression polynomial is about 0.94, which is a value close to 1 (exact solution). Therefore, the responses of the prediction polynomial to the experimental tests are quite correct. Figure 1-7 shows the measured and predicted curves of the regression model responses.

$$P = a_0 + a_1.T + a_2.ORT + a_3.HTC + a_4.T^2 + a_5.ORT^2 + a_6.HTC^2 + a_7.T.ORT + a_8.T.HTC + a_9.ORT.HTC \quad (7)$$

Table 1-7: Coefficients of the polynomial of prediction of the mechanical properties

P	Sy	Su	Er	$\mathscr{H}$
a_0	1.85E+03	2.98E+03	2.02E+01	8.58E+01
a_1	-1.50E+00	-6.28E+00	6.23E-03	-1.12E-01
a_2	–	1.03E+00	-2.89E-01	-7.51E-01
a_3	2.19E-01	1.02E+00	- 0.001968	2.67E-02
a_4	–	4.77E-03	–	9.10E-05
a_5	–	–	1.54E-03	5.99E-03
a_6	–	1.61E-03	2.00E-06	–
a_7	–	–	3.37E-04	–
a_8	–	–	–	-4.80E-05
a_9	–	–	–	-1.80E-05

The results are displayed for the nine tests of experience planning. In the range of the parameters defined in Table 1-1, it is possible to predict the mechanical properties with an error not exceeding 6%. The predicted curves align very well with the measured curves, which explains the good agreement between the predicted values and the measured values.

1.6.6 Analysis of RSM Model

To produce contour lines with variable response intervals according to the furnace heat treatment parameters of 6-mm diameter cylindrical specimens. And in order to analyze the relationships between the parameters (T, ORT and HTC) and the mechanical properties (Sy, Su, Er and $\mathscr{H}$), the RSM experimental analysis was used, which is a technique of statistical analysis and, which has the advantage of being easy to apply [17, 18].

We chose to use the interpolation method Thin-plate-spline which gave a coefficient of determination of the order of 0.93, which is close to the value of the exact solution 1.

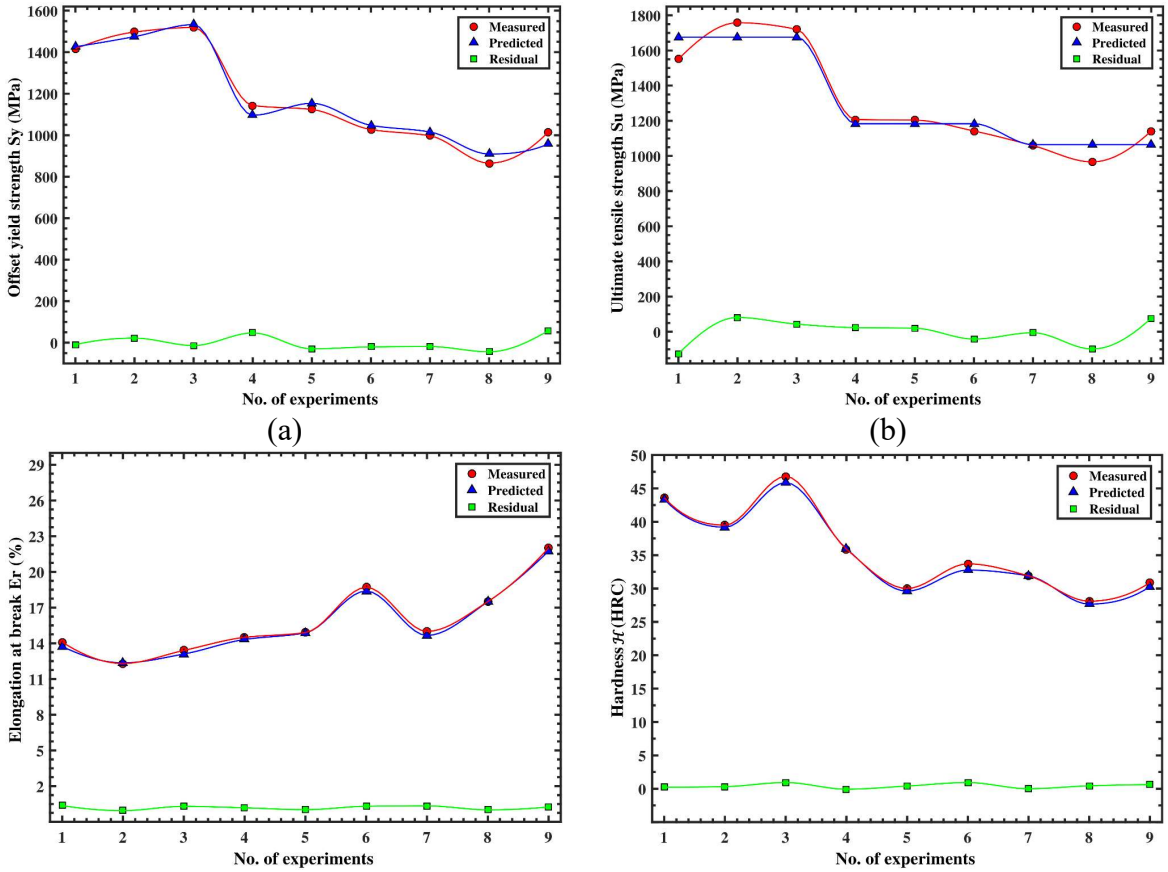

Figure 1-7: Measured versus predicted – (a) Offset yield strength, (b) Ultimate tensile strength, (c) Elongation at break, (d) Hardness

Figure 1-8a shows the estimated response area for the change in the yield strength, according to the oven temperature and the convection heat transfer coefficient. The residence time in the oven was not considered in the graphical representation because it has a small percentage contribution (about 5%) on the variation of the value of Sy. Figure 1-8b shows the estimated response surface for the variation of tensile strength, according to the oven temperature and convection heat transfer coefficient. The residence time in the oven was not considered in the graphical representation because it has a small percentage contribution (about 1%) on the variation of the value of Su.

Figure 1-8c shows the estimated response area for the change in ultimate elongation at break, according to oven temperature and oven residence time. The coefficient of heat transfer by convection was not considered in the graphical representation because it has a small percentage contribution (about 12%) on the variation of the Er value. Figure 1-8d, in turn, shows the estimated response area for the change in average hardness value according to oven temperature and oven residence time.

The coefficient of heat transfer by convection was not considered in the graphical representation because it has a small percentage contribution (about 3%) on the variation of the total value of $\mathscr{H}$. The heat treatment process engineer may use multiple linear regression polynomials to predict mechanical properties as a function of parameters (T, ORT and HTC). As it can rely on response surfaces to evaluate mechanical properties, by perpendicular intersection of the chosen value in the abscissa axis (T) and the value chosen in the ordinate axis (ORT or HTC).

1.7 DISCUSSION

From the contour lines and the analysis of variance, as shown in Figs. 1-6 and 1-8, it can easily be seen that the yield strength and the ultimate tensile strength are affected mainly by the cooling power of the quenching medium, and also the tempering temperature. And the elongation at rupture and the average hardness is influenced mainly by the residence time in the oven and the tempering temperature. The variation of the value of the average hardness before and after tempering as shown in Fig. 1-5d, can be explained by dependence on tempering temperature and cooling medium after austenitization of the material. According to stress–strain curves of tensile tests, as shown in Fig. 1-5a–c, we note that the groups of samples 7, 8 and 9, which were treated by tempering at a high temperature (650°C), have a limited resistance to traction lower compared with other samples groups that received a tempering at a lower temperature (300°C and 500°C) compared to 650°C.

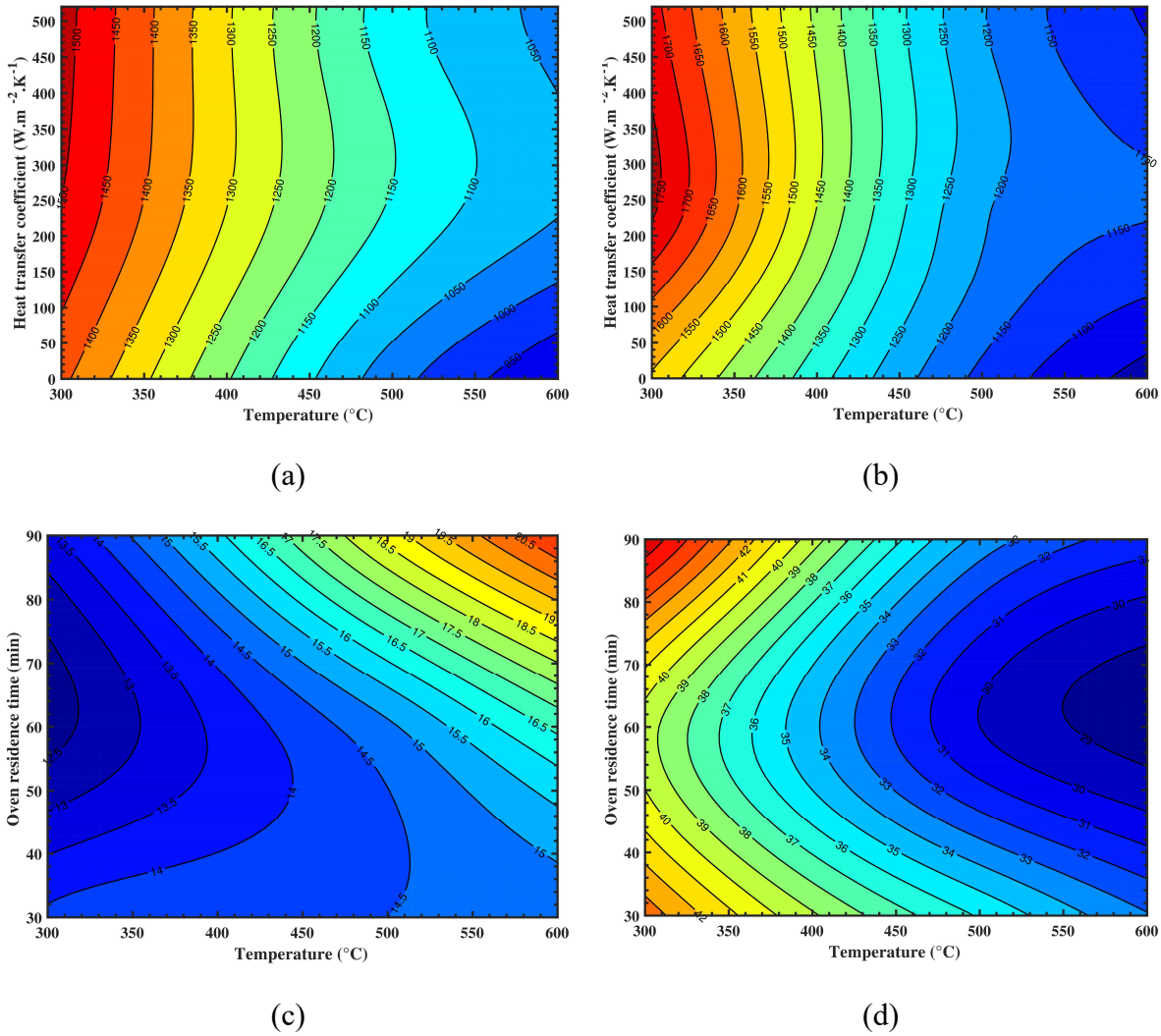

Figure 1-8: Contour plot – (a) Offset yield strength, (b) Ultimate tensile strength, (c) Elongation at break, (d) Hardness

From the point of view of ultimate elongation at break, it can be seen that a high temperature considerably increases its value to the detriment of the conventional limit of elasticity and the tensile strength limit, which is quite normal as mechanical behavior of this type of material [1, 19]. At the level of the microstructure, it is noted that a cooling in the air, after austenitization, will provide a mixture between martensite and bainite. Also cooling in oil or water will provide a completely martensitic structure, because the cooling

rate of our samples, as shown in Fig. 1-3a, is greater than the critical cooling rate which causes the formation of a completely martensitic structure.

1.8 CONCLUSIONS

In this study, we analyzed the variation of the mechanical properties of AISI 4340 steel according to three tempering temperature (300, 500 and 650 °C), three residence times in the oven (30, 60 and 90 min) and three cooling media (air, oil and water). The coefficient of heat transfer by convection of the quenching medium was evaluated for a 6-mm cylinder using empirical correlations adapted to scientific computation.

The experimental approach developed using Taguchi experience planning and analysis of variance, allowed to highlight the influence of oven temperature on the set of mechanical properties, the influence of the cooling medium on the yield strength and the ultimate tensile strength, and finally the influence of the residence time in the oven on the elongation at break and the value of the final hardness after tempering. Prediction equations for mechanical properties have been proposed according to oven heat treatment parameters of the AISI 4340. The microstructure showed a completely martensitic structure for the samples that received cooling in the oil or in the water, and a structure composed of martensite and bainite for samples cooled in air.

The main findings of this study can be used in practice for the steel industry. It would be interesting to consider completing this study by including other quenching fluids, and a thorough investigation to see the behavior of this approach in fatigue tests.

We believe that the type of approach proposed in this study is the most appropriate way to develop mechanical properties control models for simple cylindrical geometries.

References

1. W.-S. Lee, S. Tzay-Tian, Mechanical properties and microstructural features of AISI 4340 high-strength alloy steel under quenched and tempered conditions. J. Mater. Process. Technol. 87(1), 198–206 (1999).
2. T.V. Philip, T.J. McCaffrey, Properties and Selection: Irons, Steels, and High-Performance Alloys, ASM Handbook, vol. 1 (ASM International, Materials Park, OH, 1990), pp. 430–448.
3. R.K. Shiue, C. Chen, Laser transformation hardening of tempered 4340 steel. Metall. Mater. Trans. A 23(1), 163–170 (1992).
4. M. Jahazi, B. Egbali, The influence of hot rolling parameters on the microstructure and mechanical properties of an ultra-high strength steel. J. Mater. Process. Technol. 103, 276–279 (2000).
5. J.J. Kai et al., The effects of heat treatment on the chromium depletion, precipitate evolution, and corrosion resistance of INCONEL alloy 690. Metall. Mater. Trans. A 20(10), 2057–2067 (1989).
6. Hans P. Hougardy et al. Theory and Technology of Quenching: A Handbook, 1992.
7. Y.V. Murty, T.Z. Kattamis, R. Mehrabian, M.C. Flemings, Behavior of sulfide inclusions during thermomechanical processing of AISI 4340 steel. Metall. Mater. Trans. A 8, 1275–1282 (1977).
8. ASTM E8/E8M. Standard test methods for tension testing of metallic materials. ASTM International, West Conshohocken (2009).
9. K. Liu, X. Cao, X.-G. Chen, Tensile properties of Al–Cu 206 cast alloys with various iron contents. Metall. Mater. Trans. A 45(5), 2498–2507 (2014).
10. D. Shahriari, M.H. Sadeghi, A. Akbarzadeh, M. Cheraghzadeh, The influence of heat treatment and hot deformation conditions on g′ precipitate dissolution of Nimonic 115 superalloy. Int. J. Adv. Manuf. Technol. 45, 841–850 (2009).
11. J. Datsko, L. Hartwig, B. McClorv, On the tensile strength and hardness relation for metals. J. Mater. Eng. Perform. 10, 718–722 (2001).

12. Phillip J. Ross, Taguchi Techniques for Quality Engineering (McGraw-Hill, London, 1988), p. 66.

13. D.H. Kim, D.J. Kim, D.C. Ko, B.M. Kim, J.C. Choi, The application of the artificial neural network and Taguchi method to process sequence design in metal forming processes. Met. Mater. 4(3), 548–553 (1998).

14. Stuart W. Churchill, Humbert H.S. Chu, Correlating equations for laminar and turbulent free convection from a vertical plate. Int. J. Heat Mass Transf. 18, 1323–1329 (1975).

15. K. Dehnad, Quality Control, Robust Design, and the Taguchi Method (Springer, New York, 1989).

16. K. Palanikumar, L. Karunamoorthy, R. Karthikeyan, B. Latha, Optimization of machining parameters in turning GFRP composites using a carbide (K10) tool based on the Taguchi method with fuzzy logics. Met. Mater. Int. 12(6), 483–491 (2006).

17. R.H. Myers, Response Surface Methodology (Allyn and Bacon, Boston, MA, 1971).

18. K. Dehghani, A. Nekahi, Interactive effects of aging parameters of AA6056. Met. Mater. Int. 18(5), 757–767 (2012).

19. G.Y. Lai et al., The effect of austenitizing temperature on the microstructure and mechanical properties of as-quenched 4340 steel. Metall. Trans. 5(7), 1663–1670 (1974).

CHAPITRE 2

ÉTUDE DU PROCÉDÉ DE DURCISSEMENT AU LASER APPLIQUÉ À DES ÉPROUVETTES CYLINDRIQUES EN ACIER AISI 4340 À L'AIDE DE LA SIMULATION NUMÉRIQUE ET DE LA VALIDATION EXPÉRIMENTALE

Fakir, R., Barka, N., & Brousseau, J.
Université du Québec à Rimouski, Rimouski, Québec, Canada, G5L 3A1

Cet article a été publié dans le journal Case Studies in Thermal Engineering., 11, 2018, 15–25. Son identifiant numérique d'objet (DOI) est : 10.1016/j.csite.2017.12.002

Mots clés : Méthode des différences finies · Méthode des éléments finis · Simulation numérique · Durcissement au laser · Validation expérimentale · AISI 4340

2.1 RÉSUMÉ EN FRANÇAIS DU DEUXIÈME ARTICLE

Cet article présente une approche numérique qui permet de prédire la distribution de la température dans une éprouvette cylindrique en acier AISI 4340 en fonction des paramètres du processus de durcissement au laser en un point stationnaire. Le modèle développé a été construit à l'aide de la méthode des différences finies (FDM) et validé à l'aide d'un logiciel commercial spécialisé en éléments finis et à l'aide de données expérimentales. L'approche proposée a été construite progressivement par (i) une analyse de la distribution de la température à l'aide d'équations de diffusion de la chaleur, de conditions aux limites et des propriétés du matériau (ii), une discrétisation du modèle mathématique par la méthode des différences finies, (iii) une validation du modèle par des essais expérimentaux et des simulations numériques avec le logiciel COMSOL Multiphysics et (iv) une analyse et discussion des résultats. La faisabilité et l'efficacité de l'approche proposée conduisent à un modèle précis et fiable capable de prédire la distribution de la température à l'intérieur de la composante durcie au laser.

Ce deuxième article, intitulé « *Case study of laser hardening process applied to 4340 steel cylindrical specimens using simulation and experimental validation* », fut corédigé par moi-même ainsi que par le professeur Noureddine Barka et le professeur Jean Brousseau. Il

fut accepté pour publication dans sa version finale en 2017 par l'éditeur chef Huihe Qiu de la revue *Case Studies in Thermal Engineering*. En tant que premier auteur, ma contribution à ce travail fut l'essentiel de la recherche sur l'état de l'art, le développement de la méthode, l'exécution des simulations numériques et des tests expérimentaux, et la rédaction de l'article. Les professeurs Noureddine Barka et Jean Brousseau, second et troisième auteurs, ont participé à définir le projet d'article et ils ont aidé à la recherche sur l'état de l'art, au développement de la méthode ainsi qu'à la révision de l'article.

2.2 TITRE DU DEUXIÈME ARTICLE

Case Study of Laser Hardening Process Applied to 4340 Steel Cylindrical Specimens using Simulation and Experimental Validation.

2.3 ABSTRACT

This paper presents a numerical approach that can predict the temperature profile of cylindrical specimens made with AISI 4340 steel according to laser hardening process parameters. The developed model was built using the finite difference method (FDM) and validated using commercial finite element tools and experimental data. The proposed approach was constructed progressively by (i) examination of the temperature distribution using heat diffusion equations, boundary conditions and material properties (ii), discretization of the mathematical model using the finite difference method, (iii) validation of the proposed approach using experimental tests and simulation with COMSOL Multiphysics software and (iv) analysis and discussion of the results. The feasibility and effectiveness of the proposed approach led to an accurate, reliable model capable of predicting the temperature profile inside the heated component.

2.4 NOMENCLATURE

$\tilde{\boldsymbol{\alpha}}$	*Absorption coefficient of the material,*
$\boldsymbol{C_p}$	*Specific heat,* $J.kg^{-1}.K^{-1}$

$\boldsymbol{h}$	*Thermal transfer coefficient,* $W.m^{-2}.K^{-1}$
$\boldsymbol{k}$	*Thermal conductivity,* $W.m^{-1}.K^{-1}$
$\boldsymbol{\sigma}$	*Stefan-Boltzmann constant,* $W.m^{-2}.K^{-4}$
$\emptyset_{T_{laser}}$	*Diameter of the laser spot,* m
$\boldsymbol{D}$	*Diameter of the cylinder,* m
$\boldsymbol{\alpha}$	*Thermal diffusivity,* $m^2.s^{-1}$
$\boldsymbol{\varepsilon}$	*Emissivity of material surface*
$\boldsymbol{L}$	*Cylinder length,* m
$\boldsymbol{nt}$	*Number of temporal mesh nodes,*
$\boldsymbol{\rho}$	*Density,* $kg.m^{-3}$
$\boldsymbol{nr}$	*Number of mesh nodes following R,*
$\boldsymbol{nz}$	*Number of mesh nodes following Z,*
$\boldsymbol{Nu}$	*Nusselt's number,*
$\boldsymbol{Pr}$	*Prandtl's number,*
$\boldsymbol{Re_D}$	*Reynolds number,*
$\boldsymbol{\Delta r}$	*Pitch of the spatial mesh following R,* m
$\boldsymbol{\Delta z}$	*Pitch of the spatial mesh following Z,* m
$\boldsymbol{\Delta t}$	*The pitch of the temporal mesh,* s
$\boldsymbol{P_{laser}}$	*Laser power, W*
$\boldsymbol{I}$	*Efficient laser power, W*
$\boldsymbol{R}$	*Radius of the cylinder,* m
$\boldsymbol{\theta}$	*Reflectivity coefficient of the material,*
$\boldsymbol{S_{irr}}$	*Irradiated surface,* m^2
$\boldsymbol{T_\infty}$	*Ambient air temperature, K*
$\boldsymbol{AC_1}$	*Heating temperature at point A1, K*
$\boldsymbol{AC_3}$	*Heating temperature at point A3, K*
$\boldsymbol{T}$	*Temperature of the material, K*
$\boldsymbol{T_{in}}$	*Initial material temperature, K*

ϑ	*Kinematic viscosity,* $m^2.s^{-1}$
ω	*Rotation speed of the cylinder,* $rad.s^{-1}$
$\aleph$	*Distance from laser beam centre,* m
$\aleph_m$	*Laser beam radius,* m

2.5 INTRODUCTION

Laser processes are highly performing, simple and fast. They are currently used in several industries, such as automotive and aerospace, to increase productivity and quality. The flexibility and precision of laser processes justify their use in cutting [1,2], welding [3], cladding [4], cleaning and surface hardening [5]. Laser processes must be carried out with speed, minimal deformation and unequaled accuracy [6]. Heat treatment involves the use of heating and/or cooling, normally at extreme temperatures, to obtain the desired hardness profile and microstructure, including friability, hardness, ductility, brittleness, plasticity, elasticity or mechanical strength of the materials. Heat treatments by laser are divided into two types: those that generate a transformation of the solid state and those that generate a fusion. The first type includes martensitic quenching, severe tempering and tempering. The second type includes reflow, alloying, recharging and dispersion curing. In this study, a martensitic hardening treatment was applied to AISI 4340 steel. However, the hardness profile of the treated parts remains challenging to control because the effects of process parameters and material properties are difficult to predict, especially when it comes to complex geometry [7,8].

Laser heat treatment processes involve high-intensity laser radiation that rapidly heats the thin steel component surface to above Ac_3 and converts it into an austenitic phase upon cooling [9]. The temperature gradient is very high because the heating rate is also high due to the laser's ability to concentrate significant amounts of heat in a localized area. These conditions make it possible to generate an extremely fine, homogeneous, hard microstructure [10,11]. Using commercial software based on the finite element method (FEM), it is possible to solve the heat flow equation to determine the temperature

distribution for each period of time during the heating process [12,13]. This method is one of the applied mathematical tools which allows to provide a solution to a differential equation or partial differential equation, with a condition at the limits of Dirichlet when we specify the values that the solution must check on the boundary, or a boundary condition of Neumann when specifying the values of the derivatives that the solution must check on the boundary [14]. The finite element method (FEM) allows for processing of complex geometries and a more natural determination of boundary conditions, with the possibility of mathematical demonstrations of convergence study and error mapping. Even so, it remains extremely complex to implement and very consuming in terms of computation time and memory capacity [15]. The finite difference method (FDM) replaces the derivatives appearing in the continuous problem with divided differences or combinations of point values of the function in a finite number of discrete points or nodes of the mesh [16]. FDM has the advantage of being simplistic in writing and less expensive in computation time for simple geometries and calculation domains, such as for the circular cylinder treated in this study.

The finite difference method allows for understanding of the physical phenomenon studied through modeling that is independent of commercial numerical simulation software, which does not reveal the tools and mechanisms for solving system equations treated by case. For successful laser heat treatment, it is extremely important to know the temperature distribution within the processed part. The temperature distribution depends on several parameters such as laser power, irradiated zone, interaction time, thermal transfer coefficient, thermal conductivity and specific heat of the material. To better approximate the values of thermal conductivity and specific heat as a function of temperature variation, an approximation was developed with a prediction quality for thermal conductivity and specific heat with a good correlation.

The proposed approach was developed progressively using three major steps. The first step consisted of formulating the temperature distribution using heat diffusion equations, boundary conditions and material properties. The second step represented the

process of discretizing the numerical model using the finite difference method. The third step consisted of numerical and experimental validation using COMSOL Multiphysics software and testing performed using the laser process. The viability and effectiveness of the proposed approach led to an accurate and reliable model for predicting the temperature profile inside the heated component.

2.6 MATHEMATICAL FORMULATION

In this study, a AISI 4340 steel specimen with a diameter of 15 mm and a length of 50 mm was used. As illustrated in Fig. 2-1, the specimen was mounted on a rig spindle rotating at 5000 RPM. The laser beam power was adjusted to heat the component to above the austenitizing temperature (Ac_3) without exceeding the substrate's melting temperature. The heating step was followed by rapid cooling of the irradiated area using thermal conduction in the mass of the component and convection toward the ambient air. The austenitized region transformed into a fine martensitic microstructure with high hardness. To avoid overheating the treated area, it is essential to predict and know the precise temperature distribution inside the treated component.

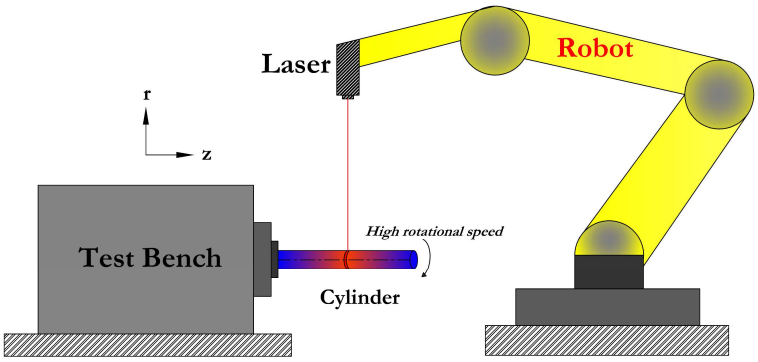

Figure 2-1: Schematic diagram of the experimental set-up

2.6.1 Thermal-conduction equation

For a revolution system with an axial temperature gradient, the indefinite equation of heat transmission via conduction in a cylindrical geometry without internal heat generation

[17,18] was written in the following form. The Fourier-Kirckhoff equation was adapted in the axisymmetric modeling form using cylindrical coordinates (Eq. (1)).

$$k(T) * \left(\frac{\partial^2 T}{\partial r^2} + \frac{1}{r}\frac{\partial T}{\partial r} + \frac{\partial^2 T}{\partial z^2}\right) = \rho * C_p(T) * \frac{\partial T}{\partial t} \quad (1)$$

2.6.2 Initial condition and boundary conditions

The cylinder temperature at the beginning of computation (t=0 s) was uniform at the studied volume and was fixed at 300 K (T_{in} = 300 K). Since the laser beam was applied in a stationary position even though the heated specimen was rotating during heating, it was assumed that beam spot diameter was fixed at 1-mm. The boundary conditions are expressed according to Eq. (2) to take into consideration the treated area of the specimen's outer surface. The points on the cylinder's outer surface (r = R) and along the Z-axis are expressed by conditions 1 and 2.

$$\begin{cases} Condition\ 1: \ 0 \leq z < \dfrac{L - \emptyset_{T_{laser}}}{2} \ ou \ \dfrac{L + \emptyset_{T_{laser}}}{2} < z \leq L \\ Condition\ 2: \ \dfrac{L - \emptyset_{T_{laser}}}{2} \leq z \leq \dfrac{L + \emptyset_{T_{laser}}}{2} \end{cases} \quad (2)$$

The boundary conditions inside and outside the laser-heated area are expressed by Eq. (3). The first term in Condition 2 represents the laser heat source, the second term represents convection loss and the third condition represents loss by radiation. The efficient laser power and the irradiated surface are calculated using Eqs. (4) and (5) respectively.

$$k\frac{\partial T}{\partial r}\Big|_{r=R} = \begin{cases} h(T - T_\infty) + \varepsilon\sigma\left(T^4 - {T_\infty}^4\right) & \text{(condition 1)} \\ \dfrac{I}{S_{irr}} - \left(h(T - T_\infty) + \varepsilon\sigma\left(T^4 - {T_\infty}^4\right)\right) & \text{(condition 2)} \end{cases} \quad (3)$$

$$I = P_{laser}\,(1 - \theta) = P_{laser}.\,\tilde{a} \quad (4)$$

$$S_{irr} = 2\pi R \emptyset_{T_{laser}} \quad (5)$$

The Gaussian beam distribution is a solution of Helmholtz's propagation equation in the framework of the paraxial approximation. A beam whose transverse amplitude profile evolution (as a function of the spatial propagation) is proportional to a Gaussian function that is written in the following form (Eq. (6)).

$$I = P_{laser} \exp(-\varkappa^2/{\varkappa_m}^2) \quad (6)$$

2.6.3 Thermal properties

Fig. 2-2 presents specific heat and thermal conductivity evolution according to heating temperature for AISI 4340 steel. Specific heat, representing a material's ability to accumulate energy in thermal form with increasing temperatures, must be considered in terms of its variation according to heating temperature. Thermal conductivity, which represents the energy transferred per surface unit and time under a temperature gradient of one unit, requires consideration of its temperature-dependent variation. It is important to note the effect of allotropic transformation of the steel on both properties.

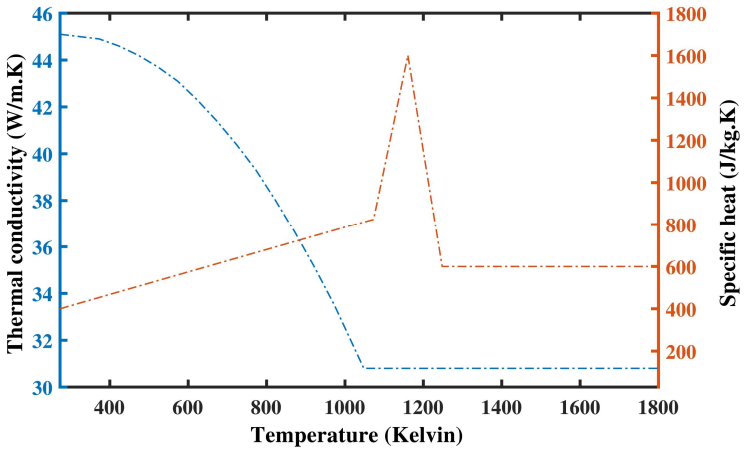

Figure 2-2: Specific heat and thermal conductivity versus heating temperature

To solve Eq. (1), a linear system of specific heat approximation was proposed based on the following equation, determined between 273 K and 1825 K with a determination coefficient of $R^2 = 1$ (Eq. (7)).

$$C_p(T) = \begin{cases} 0.5417\,T^{0.99774} + 254.5, & 273 \le T \le 1073 \\ 8.857\,T - 8679, & 1073 < T \le 1160.5 \\ -11.43\,T + 14860, & 1160.5 < T \le 1248 \\ 600, & 1248 < T \le 1825 \end{cases} \quad (7)$$

A nonlinear system (sum of sine method) is suggested for approximating the thermal conductivity and was expressed in Eq. (8) with a determination coefficient of $R^2 = 0.99$.

$$k(T) = 39.91\,sin(0.0007467\,T + 1.115) + 5.869\,sin(0.004005\,T + 0.2016) - 0.7068\,sin(0.01136\,T - 16.67) \quad (8)$$

2.6.4 Convective heat transfer coefficient h ($W.m^{-2}.K^{-1}$)

During this study, the convective heat transfer coefficient was estimated with empirical correlations adapted for scientific computation [19] using Nu (Nusselt number), R_{eD} (Reynolds number) and Pr (Prandtl number). For rotating cylinders [20], a suitable correlation for estimating the convection coefficient was developed using Eq. (9). Where $R_{eD} = \omega D^2/\vartheta$ and ω is the rotation speed of the specimen (rad/s). Eq. (9) is valid only for $R_{eD} < 4.3\times10^5$ and $0.7 < Pr < 670$. Eq. (9) can be written respecting the general form using the equation below.

$$\overline{N_{u_D}} = \frac{hD}{k} = 0.133\,{Re_D}^{2/3}\,Pr^{1/3} \quad (9)$$

$$h = 0.133\,\frac{k}{D}\,(\omega D^2/\vartheta)^{2/3}\,(\vartheta/\alpha)^{1/3} \quad (10)$$

To estimate the mean value of the convective heat transfer coefficient, the temperature mean value observed by simulation over the whole surface of the specimen (526 K) was used. The ambient temperature of the external air was assumed to be constant at 300 K. The thermo-physical properties of air at atmospheric pressure and a temperature of 413 K are summarized in Table 2-1. When Eq. (10) is applied, the convective heat transfer coefficient will be equal to 72.14 $W.m^{-2}.K^{-1}$. This coefficient was evaluated at atmospheric pressure, with a surface temperature of about 413 K and a rotational cylinder speed reaching 5000 RPM. Upon analysis of Eq. (10), it was clear that rotation speed has a

non-negligible effect on the convection heat transfer coefficient and the laser heating process. A rotation speed of about 5000 RPM is recommended in this study to ensure that coefficient h is slightly high, permitting good heat flux penetration into the heated specimen.

Table 2-1: Thermo-Physical Properties of Air

	Air (Gas) at 413 K	Value	Unit
ρ	Density	0.898	kg/m^3
C_p	Specific Heat	1.013×10^3	J/kgK
k	Thermal Conductivity	0.0328	W/mK
ϑ	Kinematic Viscosity	25.23×10-6	m^2/s
α	Thermal Diffusivity	36.05×10-6	m^2/s
Pr	Prandtl's Number	0.7	–

2.7 NUMERICAL MODEL BASED ON FDM

2.7.1 Discretization of the Fourier-Kirckhoff equation

The finite difference method [21,22], which consists of approaching the physics equation derivatives by means of Taylor's developments, is directly derived from the definition of the derivative [23,24]. The first derivation of T according to radius (r) and time (t) can be discretized with an explicit scheme using finite differences, as demonstrated in Eqs. (11) and (12) respectively.

$$\frac{\partial T}{\partial r} = \frac{T(i+1,j,t) - T(i,j,t)}{\Delta r} \tag{11}$$

$$\frac{\partial T}{\partial t} = \frac{T(i,j,t+1) - T(i,j,t)}{\Delta t} \tag{12}$$

The second derivation of T according to the radius (r) and rotational cylinder axis (Z) can be discretized with an explicit scheme using finite differences, as demonstrated in Eqs. (13) and (14) respectively.

$$\frac{\partial^2 T}{\partial r^2} = \frac{T(i+1,j,t) - 2T(i,j,t) + T(i-1,j,t)}{\Delta r^2} \quad (13)$$

$$\frac{\partial^2 T}{\partial z^2} = \frac{T(i,j+1,t) - 2T(i,j,t) + T(i,j-1,t)}{\Delta z^2} \quad (14)$$

Δr, Δz and Δt represent the mesh size according to the radial axis, the mesh size of the cylinder axis and the time step t respectively. The temperature prediction at the time step (t + dt) can be given by the explicit discretization of the finite differences of the Fourier- Kirchkoff equation (Eq. (15)).

$$k\big(T(i,j,t)\big) * \left(\frac{T(i+1,j,t) - 2T(i,j,t) + T(i-1,j,t)}{\Delta r^2} + \frac{T(i+1,j,t) - T(i,j,t)}{(R-(i-1)dr) * \Delta r} + \frac{T(i,j+1,t) - 2T(i,j,t) + T(i,j-1,t)}{\Delta z^2}\right) = \rho * C_p\big(T(i,j,t)\big) * \frac{T(i,j,t+1) - T(i,j,t)}{\Delta t} \quad (15)$$

2.7.2 Initial and boundary conditions

The temperature at the initial time (t = 0 s) was assumed constant and fixed at T(i, j, t) = 300 K. The boundary conditions inside and outside the area irradiated by the laser beam expressed by Eq. (3) can be discretized with an explicit finite difference scheme, as described in Eqs. (16) and (17).

❖ Condition 1 : $0 \le z < \frac{L - \emptyset_{T_{laser}}}{2}$ or $\frac{L + \emptyset_{T_{laser}}}{2} < z \le L$

$$-k\frac{T(R-dr,j,t) - T(R,j,t)}{\Delta r} = -\Big(h(T(R,j,t) - T_\infty) + \varepsilon\sigma\big(T(R,j,t)^4 - {T_\infty}^4\big)\Big) \quad (16)$$

❖ Condition 2 : $\frac{L - \emptyset_{T_{laser}}}{2} \le z \le \frac{L + \emptyset_{T_{laser}}}{2}$

$$-k\frac{T(R-dr,j,t) - T(R,j,t)}{\Delta r} = \frac{I}{S_{irr}} - \Big(h(T(R,j,t) - T_\infty) + \varepsilon\sigma\big(T(R,j,t)^4 - {T_\infty}^4\big)\Big) \quad (17)$$

2.7.3 Resolution algorithm

To determine surface temperature T(R, j, t) at time t, the polynomial Eqs. (16) and (17) with order 4 are solved using the numerical dichotomy method. This method consists of repeating shares of an interval in two parts and then selecting the subinterval in which there exists a zero of the solution in the function of T(R, j, t).

$$a = \epsilon\sigma\frac{dr}{k} \tag{18}$$

$$b = 1 + h\frac{dr}{k} \tag{19}$$

$$e = T(R - dr, j, t) + \frac{dr}{k}\left(\frac{P_{laser}(1-\theta)}{2\pi R\emptyset_{T_{laser}}} + \epsilon\sigma T_{\infty}^{4} + hT_{\infty}\right) \tag{20}$$

With the expression of the polynomial Eqs. (16) and (17) with the known input parameters as illustrated using Eq. (21). With P_{laser} = 0 for parameter e of Condition 1, Table 2-2 gives the physical data used during the numerical computation process, including the laser parameters and material properties.

$$\begin{cases} aT(R,j,t)^4 + bT(R,j,t) - e = 0, & Condition\ n°1 \\ aT(R,j,t)^4 + bT(R,j,t) - e = 0, & Condition\ n°2 \end{cases} \tag{21}$$

Table 2-2: Physical properties of 4340 for computation numerical parameters

Constants	Numerical values
$\boldsymbol{\rho}$	$7870\ kg.m^{-3}$
$\boldsymbol{\epsilon}$	0.7
$\boldsymbol{\sigma}$	$5.67\ 10^{-8}\ W.m^{-2}.K^{-4}$
$\boldsymbol{\theta}$	≈ 0.33
$\widetilde{\boldsymbol{a}}$	≈ 0.67
$\boldsymbol{D}$	$15\ mm$
$\emptyset_{\boldsymbol{T_{laser}}}$	$1\ mm$
$\boldsymbol{S_{irr}}$	$4.714285714 * 10^{-5}\ m^2$
$\boldsymbol{P_{Laser}}$	$2000\ Watts$
$\boldsymbol{h}$	$72.14\ W.m^{-2}.K^{-1}$
$\boldsymbol{T_{\infty}}$	$300\ K$

2.7.4 Numerical model algorithm

Fig. 2-3 resumes a summary algorithm of the mathematical model of prediction of temperature at all spatial and temporal points belonging to the cylinder. The computation is based on some initial values of laser process parameters and material properties. The steps were determined according to the dimensions r and z, and the time step was fixed.

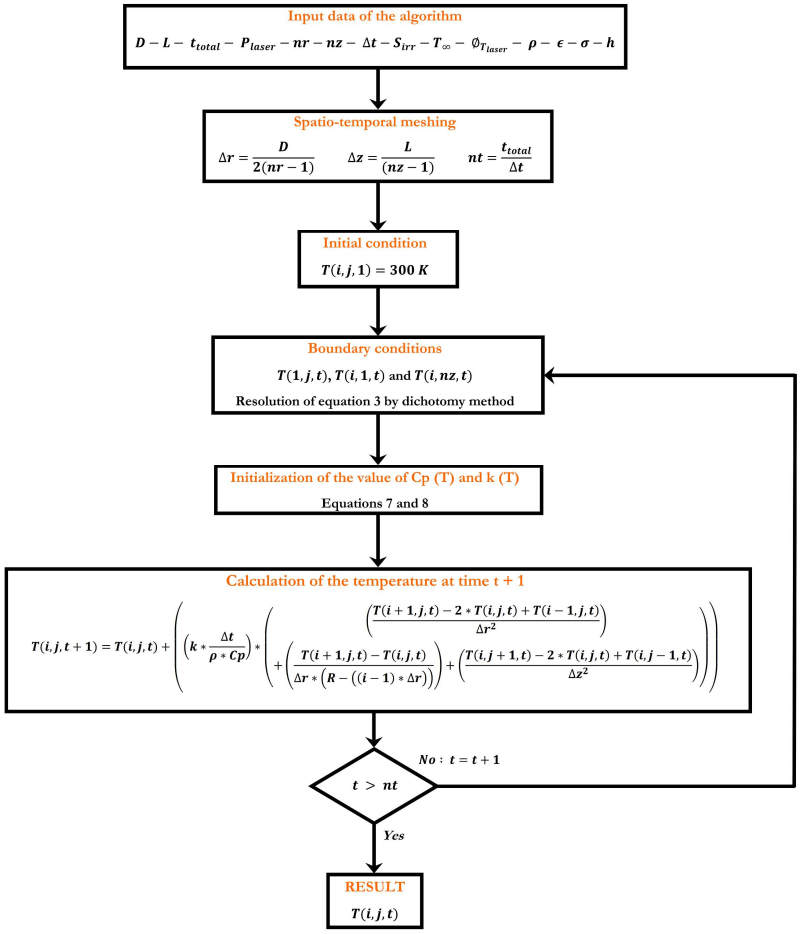

Figure 2-3: Master resolution algorithm based on finite difference methods

2.7.5 FDM convergence study

The approximate solution of the mathematical model using a finite difference numerical scheme was executed via the resolution of partial differential equations (PDE). This approximation remains unreliable if the convergence of the model has not appeared

[25]. It is essential to ensure that the difference between the numerical solution obtained and the exact solution of the discretized equations is bounded (stability), that the exact solution of the discretized equations tends to the exact solution of (Δr, Δz) and Δt tends to zero (consistency), and that the numerical solution tends to the exact solution of the continuous equations (convergence).

The Lax-Wendorff theorem states that a consistent numerical schema converges when the time and space pitches are refined, that is, when $\Delta t \rightarrow 0$, $\Delta r \rightarrow 0$ and $\Delta z \rightarrow 0$. A refined mesh provides more accurate results with considerable computation time. For an inexpensive mesh in terms of memory, it is interesting to proceed using a manual convergence study of the mesh. This process stipulates that the mesh is created using a reasonable number of elements and the model is analyzed, and that the mesh is refined using a slight increase in mesh density and the model's results are compared with the first calculation. It is suitable to optimize the mesh density by verifying that the results converge satisfactorily. This type of manual mesh convergence makes it possible to obtain a precise solution with a sufficiently dense mesh and without requiring too many computer resources. For a stable solution to Eq. (15) using an explicit finite difference scheme, the link between the time step Δt and the space steps (Δr and Δz) was advantageously exploited. The temperature versus heating time was plotted at a specific point at the surface in the cylindrical specimen center by varying the meshing step Δt and for $\Delta r = \Delta z = 10^{-4}$ m, to ensure that the condition of Eq. (22) was satisfied.

$$\Delta t < \frac{\rho C_p}{k\left(\frac{2}{\Delta r^2} + \frac{2}{\Delta z^2} + \frac{1}{r\Delta r}\right)} \tag{22}$$

This fact is intimately related to the Lax-Wendorff theorem concerning the meshing convergence ($\Delta t = 1.5\times10^{-4}$ s). The discretized mathematical model (Fig. 2-3 algorithm) converges for the time and space steps of $\Delta t = 1.5\times10^{-4}$ s and $\Delta r = \Delta z = 10^{-4}$ m.

2.8 VALIDATION

2.8.1 Finite element model

Simulations were carried out using COMSOL Multiphysics software. Numerical simulation based on the finite element method makes it possible to simulate problems related to physics and engineering applications, especially coupled phenomena or Multiphysics simulations. In this study, the cylinder used was made of AISI 4340 steel, with a 15-mm diameter and 50-mm length. The cylinder was heated using a laser beam with 1800-W power and $\emptyset_{Tlaser}$ of 1-mm spot diameter. The mesh stability study used the new functionality of mesh controlled by physics. The functionality of adapting the size and type of mesh according to the prerequisites of the physics involved, extremely fine mesh and controlled by physics. Fig. 2-4a shows a three-dimensional visualization of the mesh in the COMSOL Multiphysics software, and Fig. 2-4b shows the temperature value versus the mesh density for a point located on the surface of the cylinder and in the center of the zone that received the laser energy. Mesh convergence was obtained for about 350,000 mesh elements.

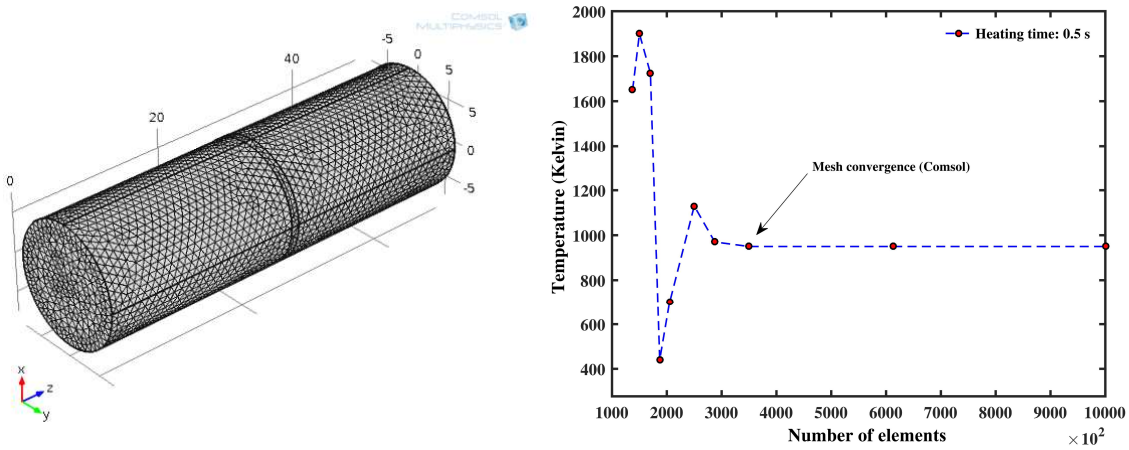

(a) (b)

Figure 2-4: (a) COMSOL mesh visualization, (b) Temperature versus number of elements at time 0.5 s and Power 1800 W for a point in the center of the laser spot

Fig. 2-5a shows the temperature distribution for the outer surface of the cylinder obtained by applying 2000 W for 1.5 s. The temperatures obtained using commercial software and the developed mathematical model were compared at various positions on the surface. In this case, four measurements were selected, as illustrated in Fig. 2-5a. Both tools gave two identical curves regardless of position. These results confirm that the mathematical model is extremely precise and accurate for predicting temperature during heating. In the same way, the temperature obtained using FEM numerical simulation software was compared to the temperature obtained using the mathematical model for four lines of points (geometric edge) that were parallel to one another (along the Z-axis) and spaced 0.5 mm apart. The 0.0 mm depth corresponds to a line of points on the outer surface of the cylinder. Fig. 2-5c to f illustrate the evolution of the temperature according to the laser beam's interaction time for t = 1.5 s. The temperature values predicted by the mathematical model based on FDM align well with the temperatures estimated by the FEM numerical simulation software, with a 3% difference in the results. The mathematical model developed therefore provides results comparable to the numerical simulation software.

2.8.2 Experimental validation

The predicted value temperature makes it possible to estimate the optimum penetration depth of the heat flux with a view to improving the specimen's mechanical performances. The steel used had a melting temperature of 1690 K, with an initial allotropic transformation temperature of 1000 K (Ac_1) and completed austenitizing temperature of 1200 K (Ac_3). Fig. 2-6a presents a visualization of the experimental set-up. To validate the developed model, a 3-kW laser power was used (IPG YLS-3000-ST2). The laser was equipped with a robot joint with a 6DoF axis. Fig. 2-6b presents the heating and cooling cycles for three seconds and for three laser beam powers. The heating time was fixed at 1.5 s and the part was cooled when the power dropped off. The laser beam was powerful and can bring the surface to more than 850 K within 1.5 s. In fact, the laser beam irradiates the fixed point on the surface between the instant t = 0 s and t = 1.5 s and then goes into stop mode.

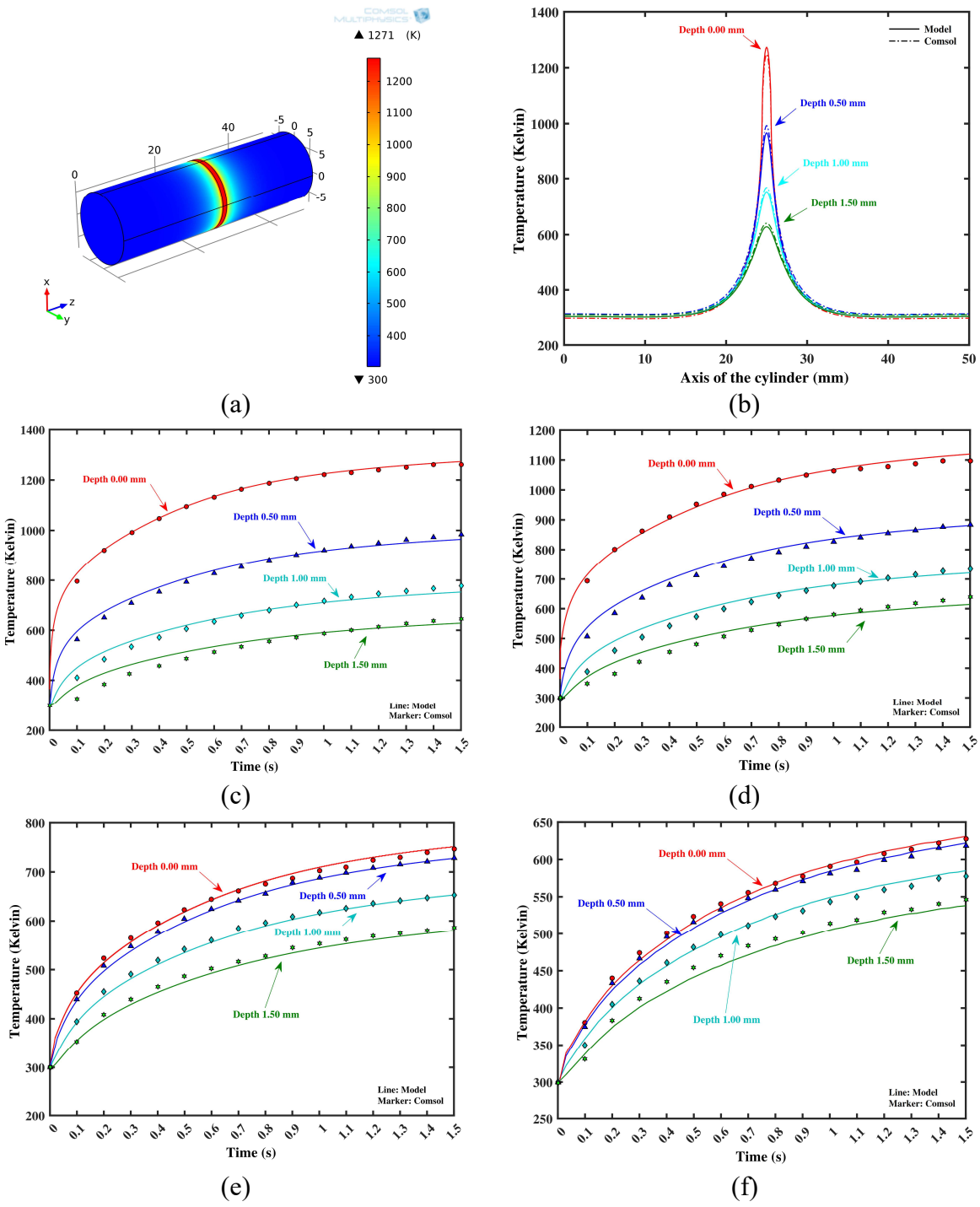

Figure 2-5: (a) Temperature distribution for 1.5 s and 2000 W, (b) Temperature versus depth for 1.5 s and 2000 W, (c) Temperature at 25 mm versus time for several depths, (d) Temperature at 25.5 mm versus time for several depths, (e) Temperature at 26 mm versus time for several depths, (f) Temperature at 26.5 mm versus time for several depths

The temperature varied from 300 K to 600 K for a point in the center of the heating zone in an interaction time of about 60 ms, for a total laser power of 3000 W. This rapid change in temperature is related to the high concentration of energy in a very small section [26,27]. Once the value of 600 K was reached, we observed a change in temperature from 600 K to 1400 K in an interaction time of 1.5 s. This evolution was slower compared to the 0–60 ms interval because the thermal properties of AISI 4340 steel change depending on the temperature (Fig. 2-1). The thermal losses in the heat transfer balance become important because the surface temperature is high compared to the initial condition of 300 K.

It is also interesting to note that the temperature dropped close to the ambient temperature during the cooling cycle due to the conduction and convection modes. It was then possible to compare the temperature curves during cooling with the TTT curves and draw conclusions as to the toughness of the treated steel. As can be seen in Fig. 2-6b, for a laser power of 2500 W after the laser interaction had been canceled (i.e. at t = 1.5 s), the surface temperature of the cylinder dropped from 1500 K to 373 K (Mf) in a time lapse of 1.0 s, which on average is a cooling rate of 1100 $K.s^{-1}$. This was because the cylinder remained in rotation (5000 RPM) between the time t = 1.5 s and t = 3 s. This cooling rate was much higher than the critical velocity (281.45 $K.s^{-1}$), as illustrated in the TTT curve of 4340 steel, which is the minimal speed of rapid cooling of AISI 4340 steel [28]. This may give rise to the formation of a fully martensitic structure when the Ms is reached during cooling. Fig. 2-6.c shows a visualization of the depth transformation by interpreting the results provided by our model, which predicts the temperature value along the X-axis and at the center of the Z-axis of the cylinder for different laser powers. Temperature value exceeds the initial transformation temperature (Ac_1) at a depth of 0.75 mm and the transformation temperature (Ac_3) at a depth of 0.50 mm for a laser power of between 2500 W and 3000 W.

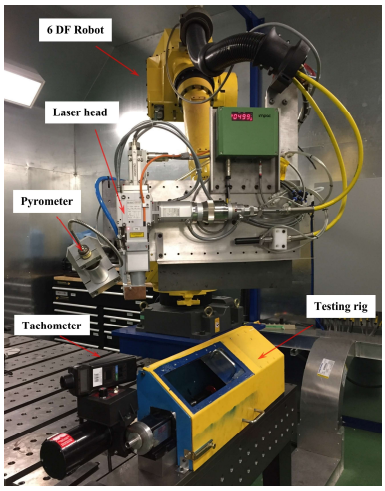

(a)

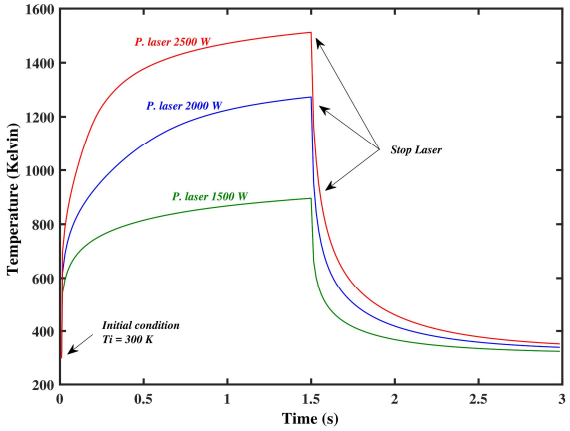

(b)

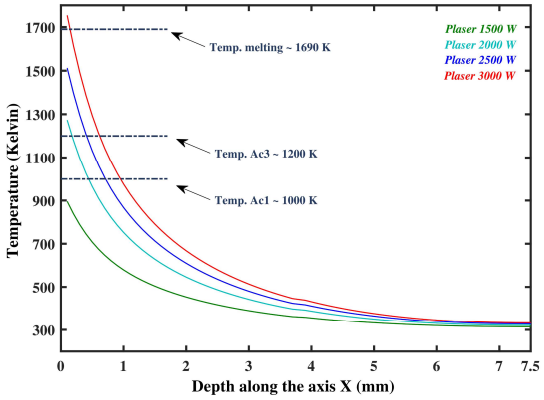

(c)

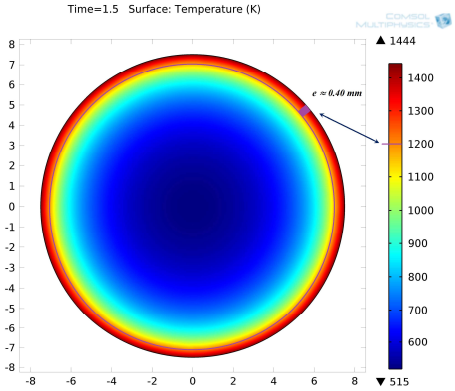

(d)

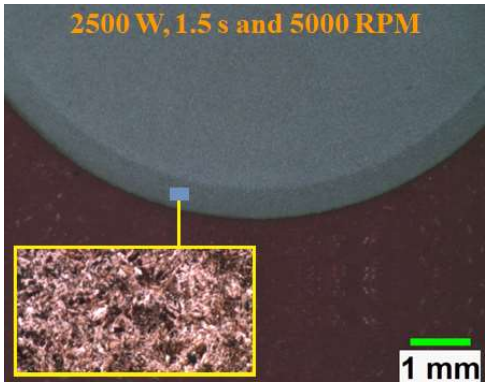

(e)

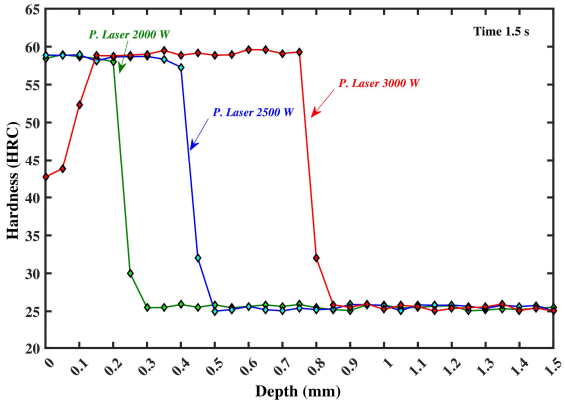

(f)

Figure 2-6: (a) Experimental setup, (b) Temperature during heating and cooling cycles for three laser powers, (c) Temperature evolution according to radial X-axis versus power for 1.5 s, (d) Cross section temperature distribution for 1.5 s and 2500 W, (e) Radial hardness profile for 1.5 s and 2500 W, (f) Hardness curves versus powers for 1.5 s

The austenitizing temperatures Ac_1 and Ac_3 can be used to obtain an approximate prediction of the hardness profile. For a laser power of 2000 W, the surface and depth temperature will be less than 1235 K, which corresponds to the initial crystallographic structure transformation of AISI 4340 steel. Fig. 2-6d shows a numerical simulation with a laser beam power of 2500 W for a processing time of 1.5 s, which can produce a martensitic transformation at a depth of about 0.4 mm. Fig. 2-6e shows a transverse section of the laser-hardened zone and a microscopic visualization with magnification (×1000) of the eutectoid transformation zone microstructure. The magnification of the zone affected by the laser heat treatment shows a completely martensitic structure. After the treatment was carried out and the samples were prepared and polished, a microhardness measurement allowed for characterization of the hardness curve as a function of depth using a Clemex CMT microhardness machine. Fig. 2-6f illustrates microhardness measurement values for different laser powers, with an interaction time of 1.5 s.

The case depth is approximately 0.43 mm for a laser power of 2500 W. On the curve of the microhardness measurement corresponding to a power of 3000 W, we observed a drop in the hardness value to a depth of 0.15 mm compared to the 2000-W and 2500-W powers. This was due to superficial melting at the surface, which corresponds to the interpretation of Fig. 2-6c.

2.9 CONCLUSIONS

In this study, the temperature distribution in a cylinder heat-treated by a laser was simulated using the finite difference method. The major findings are summarized below.

- The algorithm developed with the FDM model for AISI 4340 steel is very efficient for simulating the temperature distribution inside a cylinder heat-treated by laser. The results of the simulation correspond to theoretical predictions.
- In terms of calculation time, the proposed model reproduces the commercial software's numerical simulation results with a less expensive calculation time

and with a difference of about 3%. The thermal properties of the material have been introduced in such a way that the temperature variation does not affect the output of the model. The coefficient of heat transfer by convection has been approximated using an empirical correlation for a good evaluation of thermal losses.

- The established model can predict temperature distribution and indirectly, hardened depth, according to the parameters of laser heat treatment and the properties of the material.

- Variation in the absorption coefficient [29-31] depending on the interaction conditions between laser energy and cylinder surface influences effective penetration of the heat flow inside the cylinder. This coefficient has been estimated in the model at ~ 0.67 by means of experimental tests using the incremental variation method, which is a method for comparing the value of the temperature recorded on the surface by the pyrometer and the value of the temperature obtained by the numerical simulation.

It would be interesting to consider completing this temperature profile prediction model by integrating scanning speed and absorption coefficient for a wide range of materials. We think that this type of approach is the most accurate way to develop a hardened depth prediction model for simple cylindrical geometries.

References

1. Chin-Ping Fung, Kan-Ping Peng, Ji-Liang Doong, Int. Commun. Heat Mass Transf. 17 (1990) 147–154.
2. G. Byrne, D. Dornfeld, B. Denkena, CIRP Ann. 52 (2003) 483–507.
3. R. Kassab, H. Champliaud, V.N. Lê, J. Lanteigne, M. Thomas, Experimental and finite element analysis of a T-joint welding, J. Mech. Eng. Autom. 2 (2012) 411–421.
4. R. Vilar, J. Laser Appl. 11 (1999) 64–79.

5. Sanasam Sunderlal Singh, Prahlad Kr Baruah, Alika Khare, Shrikrishna N. Joshi, Opt. Laser Technol. 99 (2018) 107–117.

6. Abdullahi K. Gujba, Mamoun Medraj, Materials 7 (2014) 7925–7974.

7. Frederick J. Otto, Daniel H. Herring, Heat Treat. Prog. 2 (2002) 55–59.

8. Kannatey-Asibu Elijah Jr., Principles of Laser Materials Processing, 4 John Wiley & Sons, 2009.

9. E. Kennedy, G. Byrne, D.N. Collins, J. Mater. Process. Technol. 155–156 (2004) 1855–1860.

10. G. Ricciardi, M. Cantello, G.F. Micheletti, CIRP Ann. 31 (1982) 125–130.

11. Ritesh S. Lakhkar, Yung C. Shin, Matthew John M. Krane, Mater. Sci. Eng.: A 480 (2008) 209–217.

12. Rahul Patwa, Yung C. Shin, Int. J. Mach. Tools Manuf. 47 (2007) 307–320.

13. T. Mioković, V. Schulze, O. Vöhringer, D. Löhe, Mater. Sci. Eng.: A 435–436 (2006) 547–555.

14. Gartling, D.K and Reddy, J. N, The Finite Element Method in Heat Transfer and Fluid Dynamics, CRC Press, Third Edition, 2010.

15. Klaus-J.ürgen Bathe, Edward L. Wilson, Numerical Methods in Finite Element Analysis, 197 Prentice-Hall, Englewood Cliffs, NJ, 1976.

16. Bao-Lin Wang, Zhen-Hui Tian, Finite Elem. Anal. Des. 41 (2005) 335–349.

17. H.S. Carslaw, J.C. Jaeger, Conduction of Heat in Solids, 2nd ed., Clarendon Press, Oxford, 1959, pp. 1907–1979.

18. J. Vardi, Thermal Conduction in a Finite Cylinder with Boundary Radiation and a Distributed Electromagnetic Heat Source, Doctoral dissertation Publishing, 1964.

19. Bassel Assaad, Guy Friedrich, Khadija El Kadri Benkara, Stephane Vivier, Radhouane Khlissa, Antoine Michon, University of Technology of Compiègne, Symposium de Génie Électrique, 2014.

20. Theodore L. Bergman, P. Incropera Frank, Fundamentals of Heat and Mass Transfer, John Wiley & Sons, 2011.

21. Gordon D. Smith, Numerical Solution of Partial Differential Equations: Finite Difference Methods, Oxford University press, 1985.

22. John C. Strikwerda, Finite difference schemes and partial differential equations, Soc. Ind. Appl. Math. (2004).

23. Keith W. Morton, David Francis Mayers, Numerical Solution of Partial Differential Equations: An Introduction, Cambridge university press, 2005.

24. Robert D. Richtmyer, W. Morton Keith, Difference Methods For Initial Value Problems, 2nd ed., Krieger Publishing Co, Malabar, Fla., 1994, p. c1994.

25. A.K. Aziz, The Mathematical Foundations of the Finite Element Method with Applications to Partial Differential Equations, 1st ed., Academic Press, 1972, p. 796.

26. Z.H. Shen, B.Q. Xu, X. Ni, J. Lu, J. Appl. Phys. 95 (2004) 2116–2122.

27. B.Q. Xu, Z.H. Shen, X. Ni, J. Wang, J. Guan, J. Lu, Opt. Laser Technol. 38 (2006) 138–145.

28. Karl-Erik Thelning, Steel and its Heat Treatment, 2nd ed., Butterworth-Heinemann, 1984, p. 696.

29. Chun Deng, Hyungson Ki, J. Appl. Phys. 114 (2013) 164901.

30. W.M. Steen, C. Courtney, Met.Technol. 6 (2013) 456–462.

31. A.K. Gujba, M. Medraj, Laser peening process and its impact on materials properties in comparison with shot peening and ultrasonic impact peening, Materials 7 (2014) 7925–7974.

CHAPITRE 3

INVESTIGATION EXPÉRIMENTALE ET NUMÉRIQUE PAR LA MÉTHODE DES DIFFÉRENCES FINIES DU PROCÉDÉ DE DURCISSEMENT AU LASER APPLIQUÉ A L'ACIER AISI 4340

Fakir, R.[1, 2], Barka, N.[1], Brousseau, J.[1] & Caron-Guillemette, G.[2]
(1) Université du Québec à Rimouski, Rimouski, Québec, Canada, G5L 3A1
(2) Bombardier Transport Canada Inc., La Pocatière, Québec, Canada

Cet article a été publié dans le Journal of Applied Mathematics and Physics., 6, 2018, 2087–2106. Son identifiant numérique d'objet (DOI) est : 10.4236/jamp.2018.610176

Mots clés : Durcissement au laser · Vitesse de balayage · Profondeur durcie · Méthode des différences finies · AISI 4340

3.1 RÉSUMÉ EN FRANÇAIS DU TROISIÈME ARTICLE

Cet article présente une étude d'analyse numérique et expérimentale de la distribution de la température dans un échantillon cylindrique traité thermiquement par laser et refroidi dans l'air à la température ambiante. Le cylindre étudié est en acier AISI 4340 et a un diamètre de 14.5 mm et une longueur de 50 mm. La distribution de la température est discrétisée en utilisant la méthode numérique des différences finies en trois dimensions. Le gradient de température de la transformation de la microstructure est généré par une source laser fibre de 3.0 kW dont le faisceau est transmis à une tête HighYag manipulée à l'aide d'un bras robotique programmé pour contrôler les mouvements du faisceau laser dans l'espace et dans le temps. La mesure expérimentale de la température en surface et de la température de l'air au voisinage de l'échantillon permet de déterminer les valeurs du coefficient d'absorption et du coefficient de transfert de chaleur par convection, indispensables pour une prédiction numérique précise de la profondeur durcie. Malgré un régime dynamique instable au niveau des pertes de chaleur par convection et par rayonnement, l'analyse des résultats moyennés des capteurs de température montre une cohérence avec les résultats de mesures de microdureté. La faisabilité et l'efficacité de

l'approche proposée conduisent à un modèle mathématique précis et fiable, capable de prédire la distribution de la température dans une pièce cylindrique traitée thermiquement par laser.

Ce troisième article, intitulé « *Numerical Investigation by the Finite Difference Method of the Laser Hardening Process Applied to AISI 4340* », fut corédigé par moi-même ainsi que par le professeur Noureddine Barka et le professeur Jean Brousseau. Il fut accepté pour publication dans sa version finale en 2018 par l'éditeur chef Jasmyn Chen de la revue *Journal of Applied Mathematics and Physics*. En tant que premier auteur, ma contribution à ce travail fut l'essentiel de la recherche sur l'état de l'art, le développement de la méthode du modèle numérique, l'exécution des tests expérimentaux et la rédaction de l'article. Les professeurs Noureddine Barka et Jean Brousseau, et l'ingénieur Gabriel Caron-Guillemette, second, troisième et quatrième auteurs, ont participé à définir le projet d'article et ils ont aidé à la recherche sur l'état de l'art, au développement de la méthode ainsi qu'à la révision de l'article.

3.2 TITRE DU TROISIÈME ARTICLE

Numerical Investigation by the Finite Difference Method of the Laser Hardening Process Applied to AISI 4340.

3.3 ABSTRACT

This paper presents a numerical and experimental analysis study of the temperature distribution in a cylindrical specimen heat treated by laser and quenched in ambient temperature. The cylinder studied is made of AISI 4340 steel and has a diameter of 14.5-mm and a length of 50-mm. The temperature distribution is discretized by using a three-dimensional numerical finite difference method. The temperature gradient of the transformation of the microstructure is generated by a 3.0-kW fiber laser source emitting a laser beam transmitted to a HighYag laser head attached to a robotic arm programmed to control the movements of the laser beam in space and in time. The experimental

measurement of surface temperature and air temperature in the vicinity of the specimen allows us to determine the values of the absorption coefficient and the coefficient of heat transfer by convection, which are essential data for a precise numerical prediction of the case depth. Despite an unsteady dynamic regime at the level of convective and radiation heat losses, the analysis of the averaged results of the temperature sensors shows a consistency with the results of microhardness measurements. The feasibility and effectiveness of the proposed approach lead to an accurate and reliable mathematical model able to predict the temperature distribution in a cylindrical workpiece heat treated by laser.

3.4 NOMENCLATURE

Λ	*Absorption coefficient of the material,*
Cp	*Specific heat, $J.kg^{-1}.K^{-1}$*
h	*Thermal transfer coefficient, $W.m^{-2}.K^{-1}$*
k	*Thermal conductivity of the air, $W.m^{-1}.K^{-1}$*
λ	*Thermal conductivity of steel, $W.m^{-1}.K^{-1}$*
σ	*Stefan-Boltzmann constant, $W.m^{-2}.K^{-4}$*
ϕ_s	*Diameter of the laser spot, m*
D	*Diameter of the cylinder, m*
γ	*Thermal diffusivity, $m2.s^{-1}$*
ε	*Emissivity of material surface,*
L	*Cylinder length, m*
nt	*Number of temporal mesh nodes,*
ρ	*Density, $kg.m^{-3}$*
nr	*Number of mesh nodes following R,*
nx	*Number of mesh nodes following X,*
Nu	*Nusselt's number,*
Pr	*Prandtl's number,*
Re	*Reynolds number,*
ζr	*Pitch of the spatial mesh following R, m*

ζx	*Pitch of the spatial mesh following X, m*
ζt	*The pitch of the temporal mesh, s*
P	*Laser power, W*
I	*Efficient laser power, W*
SS	*Scanning speed, mm/s*
R	*Radius of the cylinder, m*
Cd	*Case depth, μm*
$l(t)$	*Spatiotemporal position of beam, m*
T_∞	*Ambient air temperature, °C*
Ac_1	*Heating temperature at point A_1, °C*
Ac_3	*Heating temperature at point A_3, °C*
T	*Temperature of the material, °C*
T_{in}	*Initial material temperature, °C*
β	*Kinematic viscosity, $m^2.s^{-1}$*
Ω	*Rotation speed of the cylinder, RPM*
r	*Distance from laser beam centre, m*
r_0	*Laser beam radius, m*

3.5 INTRODUCTION

Laser surface heat treatment, which aims to improve the properties of materials such as steel and some aluminum alloys, offers many advantages over conventional hardening processes [1] [2]. In this process, the understanding and the precise knowledge of the thermal flows absorbed and reflected by a material is a broad topic that concerns many types of industrial applications. In terms of resistance to wear, fatigue, friction and corrosion, an important part of the research is devoted to surface heat treatment and in particular to selective laser heat treatment [3]. To achieve a good performance in heat treatment, it is necessary to control the case depth generated by the heat flux transmitted by conduction through the outer surface of the workpiece [4] [5]. Several research studies to date have made it possible to present prediction approach techniques of the case depth, to

improve the longevity of mechanical parts and to improve understanding of the underlying physics.

T. Miokovic et al. presented in 2006 a study on the superficial hardening of AISI-4140, based on the effect of inhomogeneous formation of austenite due to locally different conditions of austenization and quenching, and on a dilatometry at high heating and cooling speeds during the process. Data from this study has been implemented in the ABAQUS finite element program as laws of user-defined materials for a calculation that couples temperature distribution and phase development during heating and cooling process. The results obtained in this study faithfully reproduce the evolution of the temperature as well as the value of the resulting hardness [6]. Michael K.H. Leung et al. presented in 2007 a heat transfer model with a quasi-stable interface for hardening by laser transformation of AISI-1050 steel for a rectangular beam, using IT and CCT diagrams, and with consideration of the initial workpiece temperature, the heating rate and the cooling rate of process. To obtain a customized rectangular flat-top beam from a conventional Gaussian laser beam, a diffractive optical kinoforme (DOK) was used. It has been shown that the theoretical predictions of case depth and hardness concurred perfectly with the experimental results [7]. Ritesh S. Lakhdar et al. presented in 2008 a numerical model that included heat transfer, hardening and tempering for efficient prediction of hardness and phases in tempered zones in a rectangular AISI-4140 steel part heat treated by overlapping laser beam trajectories. In this study, they combined the developed tempering model with existing models from the literature of thermal behavior and phase change kinetics for the prediction of the three-dimensional profile hardness. The model they developed has been experimentally validated by multitrack laser hardening tests, with optimized parameters providing a case depth of up to 2-mm for an overlap of 5-mm in laser beam trajectories [8].

Sen-Yung Lee et al. presented in 2014 a new method to solve temperature distribution equations in a workpiece heat treated by laser. The proposed resolution method is based on minimizing the mean squared error between the experimental data obtained and the estimated data of the analytical solution, with time-dependent boundary conditions. The

distribution of temperature and heat flux over the entire space-time domain were predicted for real cases to illustrate the simplicity, the effectiveness and the precision of the proposed method [9]. Marko Bojinovic et al. presented in 2015 a numerical model based on FEM to simulate the laser hardening process of 50CrV4 steel samples. The numerical implementation was possible thanks to the code ABAQUS for laser hardening case studies. The numerical model developed is based on austenitization temperatures (Ac1 and Ac3), on the heating and cooling rate to predict the case depth of the samples. The experimental validation proved that taking into account the kinetics of the austenite at a high temperature change rate is clearly more appropriate [10]. To determine the temperature distribution in a material, the finite element method (FEM) can be used to solve numerically the partial differential equations of heat flux in a defined domain and with boundary conditions of Dirichlet, Neumann or Robin [11]. This FEM allows using commercial software to perform simulations on complex geometries by dint of faster resolution of boundary conditions, and with a potentiality of mathematical justifications for convergence and error optimization. Despite its many qualities the FEM remains very complicated to program and requires manipulation by experienced users, because the errors of the users can be fatal for the final solution. Also, it can be very expensive in memory and in calculation time [12]. However, the finite difference method (FDM) which involves replacing the derivatives of the heat equation by divided differences or a combination of point values in a finite number of discrete points, has the advantage of being simple to write and less expensive in computing time for simple geometries like circular cylinders and plates. The FDM method allows using modeling, to facilitate control of boundary conditions for adjustment of input parameters according time [13, 14].

In the field of laser heat treatment an interesting but little studied prediction using the finite difference method to predict the temperature distribution inside of a cylindrical workpiece in rotation was developed for a stationary point by the team of R. Fakir et al. in 2018 [15]. Based on a similar and complementary approach, we developed and integrated in this study the laser beam scan parameters at the boundary conditions for efficient prediction of the case depth along the longitudinal axis of the cylinder. The mathematical

model was built and validated with experimental tests. The approach was built progressively: 1) by an analysis of the temperature distribution using the heat diffusion equations, the boundary conditions, the properties of the material which depend on the temperature, discretization of the mathematical model by the finite difference method, 2) an experimental validation with a Taguchi experimental design and 3) analysis and discussion of results. The feasibility and effectiveness of the proposed approach lead to an accurate and reliable mathematical model able to predict the temperature profile in a cylindrical workpiece heat-treated with a moving laser beam.

3.6 THERMAL MODEL

3.6.1 Methodology & Thermal Properties

In this study, a mathematical model of laser heat treatment of cylindrical workpiece was developed to predict the temperature distribution and the case depth of the transformation of the microstructure. Figure 3-1a shows the scheme of the experimental setup and Figure 3-1b shows the variation curves for thermal conductivity and specific heat according to the temperature.

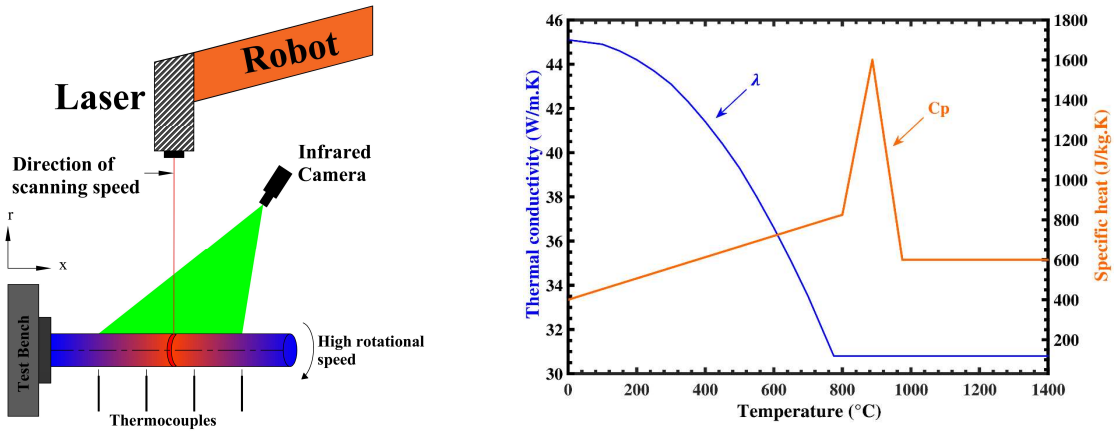

(a) (b)

Figure 3-1: Experimental setup – (a) Schematic diagram, (b) Thermal conductivity and specific heat versus temperature

The model is based on the calculation of heat flux with an adjustment, by experimental data, of the absorption coefficient of the metal and the coefficient of heat transfer by convection, for a good consideration of the variations of the thermal properties of the material according to the laser heat treatment parameters (including laser beam scanning speed). By means of temperature sensors, we measured the evolution of the surface temperature of the cylinder and the surrounding air of the workpiece, according to the laser heat treatment parameters. These temperature measurements were used to estimate the values of the absorption coefficient and the heat transfer coefficient, which are essential data for a good numerical prediction of the case depth related to the eutectoid transformation mechanism. Equations (1) and (2) present the prediction polynomials of the variation of thermal conductivity and specific heat according to the temperature.

$$\lambda(T) = \begin{cases} 45.06\,T + 0.000786\,T - 0.000025\,T^2, & T \leq 775\,°C \\ 30.8, & 775\,°C \leq T \end{cases} \quad (1)$$

$$C_p(T) = \begin{cases} 400.30 + 0.5317\,T, & T \leq 800\,°C \\ -6270 + 8.869\,T, & 800\,°C \leq T \leq 887.5\,°C \\ 11754 - 11.44\,T, & 887.5\,°C \leq T \leq 975\,°C \\ 600, & 975\,°C \leq T \end{cases} \quad (2)$$

For the evaluation of the value of the coefficient of heat transfer by convection, we used an empirical correlation adapted to scientific calculations and which groups the dimensionless number Reynolds (Re_D), Nusselt (Nu_D), and Prandtl (Pr). Equation (3) presents the expression of the empirical correlation for rotating cylinders with a constant rotation speed Ω(rad/s) [16]. Equation (4) presents the empirical correlation giving the value of the coefficient of heat transfer by convection according to the thermal conductivity of the air, the diameter of the cylinder, the rotation speed of the cylinder, the kinematic viscosity of air and the thermal diffusivity of air. This equation is valid only for $Re_D < 4.3\times10^5$ and $0.7 < Pr < 670$.

$$\overline{N_{u_D}} = (h\,D/\kappa) = 0.133\,{Re_D}^{2/3}\,Pr^{1/3} \quad (3)$$

$$h = 0.133\,(\kappa/D)\,(\Omega\,D^2/\beta)^{2/3}\,(\beta/\gamma)^{1/3} \quad (4)$$

For the estimation of the value of the heat transfer coefficient through the empirical correlation of Equation (4) it is necessary to know the exact values of the thermo-physical properties of the air (κ, β and γ) in the vicinity of the cylindrical workpiece. These properties were determined by experimental trials and are dependent of laser heat treatment parameters (laser power, scanning speed and rotational speed of the cylindrical part).

3.6.2 Heat Conduction Equation in Cylindrical Coordinates

The quantity of power density of the Gaussian beam I (x,y) transmitted by conduction in the workpiece, is modeled based on the heat conduction Equation (5) for a revolution system with an axial temperature gradient depending on the time.

$$\lambda(T)\left({}^{\partial^2 T}/_{\partial r^2} + {}^{\partial T}/_{r\,\partial r} + {}^{\partial^2 T}/_{\partial x^2}\right) = \rho C_p(T)\,{}^{\partial T}/_{\partial t} \tag{5}$$

Equation (6) presents the transversal profile in the space of the Gaussian laser beam that propagates in the direction of the z-axis [17].

$$I(x,y) = P\,exp\left({}^{-r(x,y)^2}/_{r_0}\right) \tag{6}$$

With $r(x,y) = \sqrt{(x-x_0)^2 + (y-y_0)^2}$ and x_0, y_0 the coordinates defining the center of the laser beam. P is the maximum value of I(x,y) measured at the center defined by x_0 and y_0.

3.6.3 Initial Condition and Boundary Conditions

The initial temperature of the cylinder is supposed to be uniform T_{in} = 27˚C. This initial condition makes it possible to determine the coefficients which are solutions of the equations of the system at the beginning of the laser heat treatment (at t = 0 s). The laser beam moves from the start-laser position (reference position x = 10-mm) to stop-laser position (end position of the course x = 40-mm) with a constant scanning speed SS. The sample is continuously rotating on a test bench with a fixed rotation speed Ω. The diameter

of the focal spot of the laser beam is set at 0.50-mm. Equation (7) shows the expression of the course distance of the focal spot at time t and according to the average scanning speed of the course.

$$l(t) = SS.t \tag{7}$$

Boundary conditions are expressed according to equation 8, for a good consideration of the scanning speed of the laser beam and starting and stopping positions at the outer surface of the cylinder (r = R).

$$\begin{cases} x < l(t) \quad or \quad x > l(t) + \phi_s, & Condition\ 1 \\ l(t) \leq x \leq l(t) + \phi_s, & Condition\ 2 \end{cases} \tag{8}$$

Equation (9) presents the expression of the boundary conditions outside and inside the zone irradiated by the laser beam. The first term of condition 1 represents convective heat losses and the second term represents the heat losses by radiation. The first term of condition 2 represents the amount of energy transmitted by the laser beam to the workpiece and the second term represents thermal losses by convection and radiation.

$$\left.\frac{\lambda \partial T}{\partial r}\right|_{r=R} = \begin{cases} h(T - T_\infty) + \varepsilon\sigma(T^4 - {T_\infty}^4), & Condition\ 1 \\ P\ \Lambda\ e^{-r(x,y)^2/r_0} \Big/ 2\pi R\phi_s - \left(h(T - T_\infty) + \varepsilon\sigma\left(T^4 - {T_\infty}^4\right)\right), & Condition\ 2 \end{cases} \tag{9}$$

3.7 NUMERICAL MODEL (FDM)

3.7.1 Discretization of Model Equations

Finite difference method [18] allows through Taylor developments to search the approximate solutions of partial derivatives of heat transfer equations [19]. Equations (10)-(13) present a discretization of the terms of equation 5 with an explicit schema using the finite difference method. In chronological order, the first term corresponds to the first derivation of the temperature according to the radius (r), the second term corresponds to the first derivative of the temperature according to the time (t), the third term corresponds to the second derivation of the temperature according to the radius (r) and the last term

corresponds to the second derivation of the temperature according to the x-axis of rotation of the cylinder. ζr and ζx represent respectively the mesh size along the radial axis and the axis of rotation, and ζt the pitch of the temporal mesh.

$$\partial T/_{\partial r} = \left(T(i+1,j,t) - T(i,j,t)\right)/_{\zeta r} \tag{10}$$

$$\partial T/_{\partial t} = \left(T(i,j,t+1) - T(i,j,t)\right)/_{\zeta t} \tag{11}$$

$$\partial^2 T/_{\partial r^2} = \left(T(i+1,j,t) - 2T(i,j,t) + T(i-1,j,t)\right)/_{\zeta r^2} \tag{12}$$

$$\partial^2 T/_{\partial x^2} = \left(T(i,j+1,t) - 2T(i,j,t) + T(i,j-1,t)\right)/_{\zeta x^2} \tag{13}$$

Equation (14) presents the expression of the temperature, at the moment t+dt according to the value of the temperature at time t , by means of an explicit discretization of the Fourier-Kirchkoff equation.

$$\lambda\left(T(i,j,t)\right)\left(\begin{array}{c}\left(T(i+1,j,t) - 2T(i,j,t) + T(i-1,j,t)\right)/_{\zeta r^2} + \left(T(i+1,j,t) - T(i,j,t)\right)/_{(R\zeta r - (i-1)\zeta r^2)} \\ + \left(T(i,j+1,t) - 2T(i,j,t) + T(i,j-1,t)\right)/_{\zeta x^2}\end{array}\right)$$
$$= \rho C_p\left(T(i,j,t)\right)\left(\left(T(i,j,t+1) - T(i,j,t)\right)/_{\zeta t}\right) \tag{14}$$

The initial temperature of the cylinder is assumed to be constant T(i,j,0) = 27°C. Equations (15) and (16) present a discretization with an explicit finite difference scheme of conditions 1 and 2 of Equation (9). This represents the boundary conditions outside and inside the area irradiated by the laser beam, during its course at a scanning speed SS.

Condition 1: $x < t_i.SS.\zeta t \quad or \quad x > t_i.SS.\zeta t + \phi_s$

$$\lambda\left(T(R-\zeta r,j,t) - T(R,j,t)/_{\zeta r}\right) = \left(h(T(R,j,t) - T_\infty) + \varepsilon\sigma\left(T(R,j,t)^4 - {T_\infty}^4\right)\right) \tag{15}$$

Condition 2: $t_i.SS.\zeta t \leq x \leq t_i.SS.\zeta t + \phi_s$

$$-\lambda\left(T(R-\zeta r,j,t) - T(R,j,t)/_{\zeta r}\right) = {}^{I}/_{2\pi R\phi_s} - \left(h(T(R,j,t) - T_\infty) + \varepsilon\sigma\left(T(R,j,t)^4 - {T_\infty}^4\right)\right) \tag{16}$$

Equation (17) shows a simplified writing of the 4th-order polynomials for solving the equations of conditions 1 and 2.

$$T(R,j,t) \leftarrow \begin{cases} \Psi\, T(R,j,t)^4 + \Pi\, T(R,j,t) - \Gamma = 0, & Condition\ 1 \\ \Psi\, T(R,j,t)^4 + \Pi\, T(R,j,t) - \Gamma = 0, & Condition\ 2 \end{cases} \quad (17)$$

The prediction of the value of the temperature T(R,j,t) on the surface of the cylindrical workpiece can be done by applying the numerical method of Regula Falsi, which consists of repeating the interval division to find the value of T(R,j,t) solution of conditions 1 and 2. Ψ, Π, and Γ, (Eqs. 18, 19 and 20) are the respective coefficients of the monomials of degree 4, 1 and 0.The laser energy is zero (I = 0) in the term Γ corresponding to the condition 1.

$$\Psi = {}^{\varepsilon\, \sigma\, \zeta r}\big/_{\lambda(T)} \quad (18)$$

$$\Pi = {}^{(\lambda(T) + h\, \zeta r)}\big/_{\lambda(T)} \quad (19)$$

$$\Gamma = T(R - \zeta r, j, t) + {}^{\zeta r}\big/_{\lambda(T)} \left({}^{I}\big/_{2\pi R \emptyset_s} + \varepsilon\sigma T_\infty^4 + hT_\infty \right) \quad (20)$$

Figure 3-2 shows a summary algorithm of the thermal model for predicting the distribution of the temperature at any point belonging to the cylindrical workpiece. The input data of the algorithm are: The thermal properties of the material, the dimensions of the cylinder and the parameters of the laser heat treatment (laser power, focal spot diameter, scanning speed and rotational speed of the cylindrical workpiece).

3.7.2 Mesh Stability Study

The numerical solution of the partial differential equations of the thermal model was done by the finite difference method. The method requires a convergence study of the mesh to ensure a stability of the numerical scheme, a consistency between the exact solution and the discretized solution and finally a convergence of the results of the thermal model [20]. The Lax-Wendroff theorem informs that a numerical scheme converges when the spatio-

temporal mesh is very small, that is when ζr →0, ζx→0 and ζt →0. As a refined mesh provides more accurate results with a considerable calculation time (important and not insignificant), it is necessary to carry out a manual convergence study of the mesh to optimize the parameters: computing time, data storage memory and accuracy of output results.

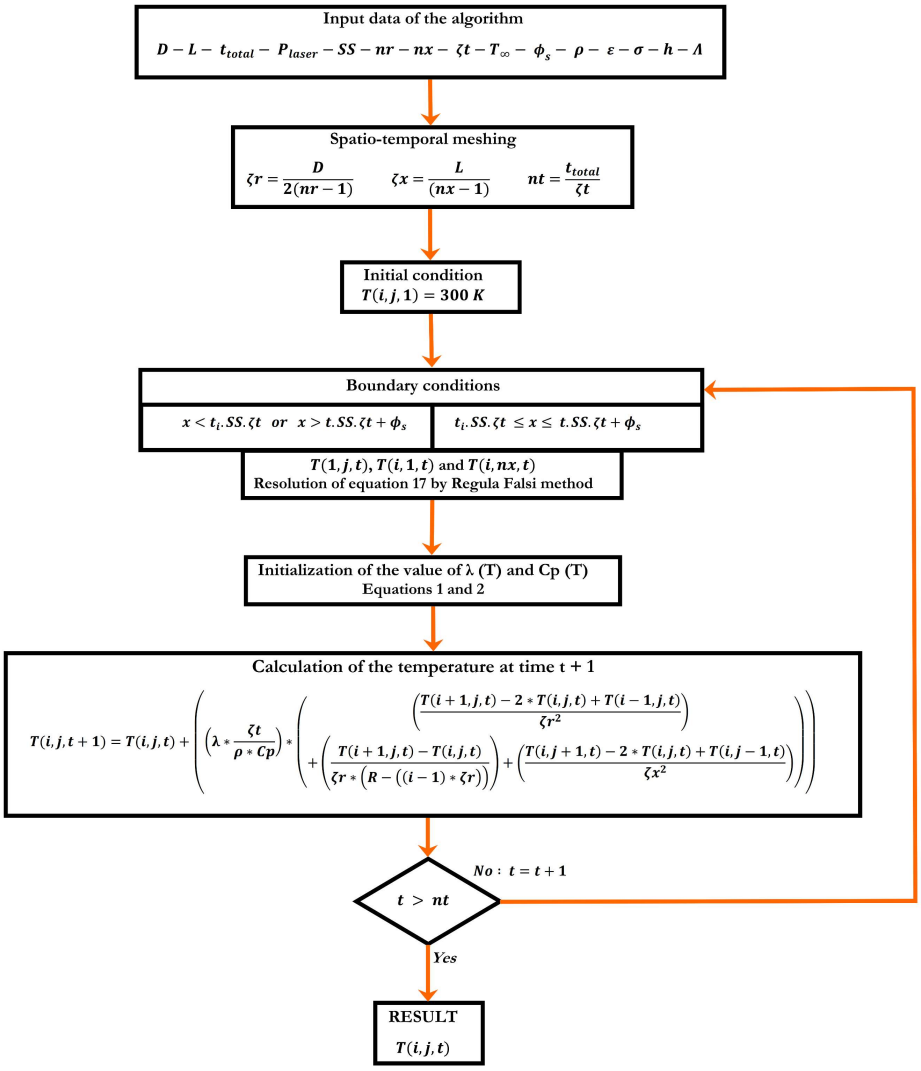

Figure 3-2: Master resolution algorithm for predicting temperature distribution according to the laser heat treatment parameters

A study that consists of creating a mesh using a reasonable number of elements, followed by an analysis of the output results, then a slight increase in the mesh density and

an analysis of the results by comparison with the results of the previous iteration. This study of manual convergence of the mesh allows us to obtain a precise and exact solution with a sufficiently dense mesh and without requiring too many computing resources. Equation (21) presents, for an explicit numerical scheme in finite differences (Equation (14)), the condition of convergence that connects the pitch of the temporal mesh ζt with the pitch of the spatial mesh ζr and ζt.

$$\zeta t < {\rho C_p}\Big/{\lambda\left({2}/{\zeta r^2} + {2}/{\zeta x^2} + {1}/{r\zeta r}\right)} \tag{21}$$

Figure 3-3 shows the value of the temperature according to the number of mesh elements, for a point on the surface of the cylinder, at a distance of 15-mm from the laser heat treatment start point, and for a scanning speed of 10-mm/s and a rotation speed of 5000-RPM. The convergence of the mesh has been obtained for approximately 37,500 mesh elements, which corresponds to a spatial-temporal mesh ζr =ζx =10^{-4} m and ζt =1.5×10^{-4} s.

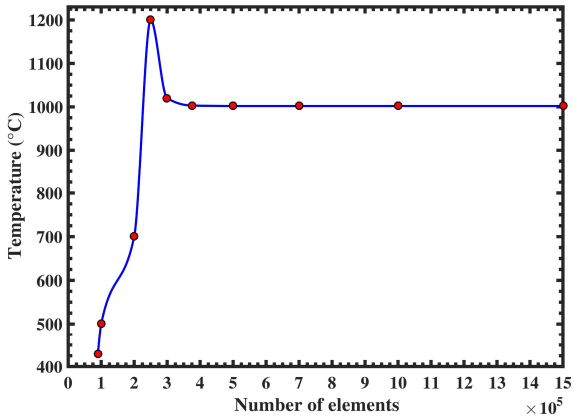

Figure 3-3: Temperature versus number of elements for P = 2800-W

3.8 EXPERIMENTAL VALIDATION

3.8.1 Experimental Setup and Experimental Design

The experimental tests were carried out on specimens of cylindrical geometry in steel AISI 4340, with a diameter of 14.5-mm and a length of 50-mm. Figure 3-4a shows a

visualization of the experimental setup, which is composed mainly of a fiber laser source (IPG YLS-3000-ST2) and an articulated 6-DOF robot supporting the laser head. The trajectory of the laser beam is perpendicular to the axis of rotation of the workpiece to harden. The specimen fixation is ensured by a rotating test rig which can reach 10,000-RPM and which is equipped with a central support with three jaws and a counter-head moving along the x-axis. To measure the surface temperature of the workpiece according to the laser heat treatment parameters, a MI-IGAR-12-LO pyrometer and a FLIR thermal infrared camera with a sensitivity of less than 5˚C, and which can cover a temperature range up to 2000˚C, have been exploited. Four J-type precision thermocouples with a sensitivity of 0.05-s were placed in the vicinity of the cylindrical part to evaluate the ambient air temperature according to the laser heat treatment parameters, by using a NI-USB-6009 which offers features data acquisition (DAQ). Before laser heat treatment, the samples were heat-treated in the oven to homogenize the hardness value. The oven heat treatment consisted of placing the samples in an oven at a 900˚C austenitization temperature for a period of 20-min, followed by cooling in the oil and tempering in the oven at a temperature of 650˚C for a period of 100-min to obtain a uniform hardness of 25-HRC (Rockwell C) [21]. After laser heat treatment, the samples were carefully prepared, cut, mounted, polished and etched using a Nital chemical solution (95% ethanol and 5% nitric acid). The hardness profiles were characterized by microhardness measurements programmed using a Clemex CMT microhardness machine.

To perform experimental modeling, it is essential to have relevant tests to adequately represent the desired results. The acquisition of validation results with a reasonable number of tests requires the definition of an ordered sequence of experimental tests using an experimental design. Experiment planning based on the Taguchi method optimizes the number of tests to be performed while maintaining the robustness, performance and statistical consistency of a factor design [22]. In the case of laser heat treatment of cylindrical workpieces, it is important to avoid the melting of the surface layer of the material while having a transformation of this same superficial layer. Experimental tests begin with the definition of the minimum and maximum values of the experimental design

factors, that are in the case of this study: laser power, scanning speed, and rotation speed. Figure 3-4b and Figure 3-4c show the results of the preliminary tests for measuring the microhardness according to the laser heat treatment parameters.

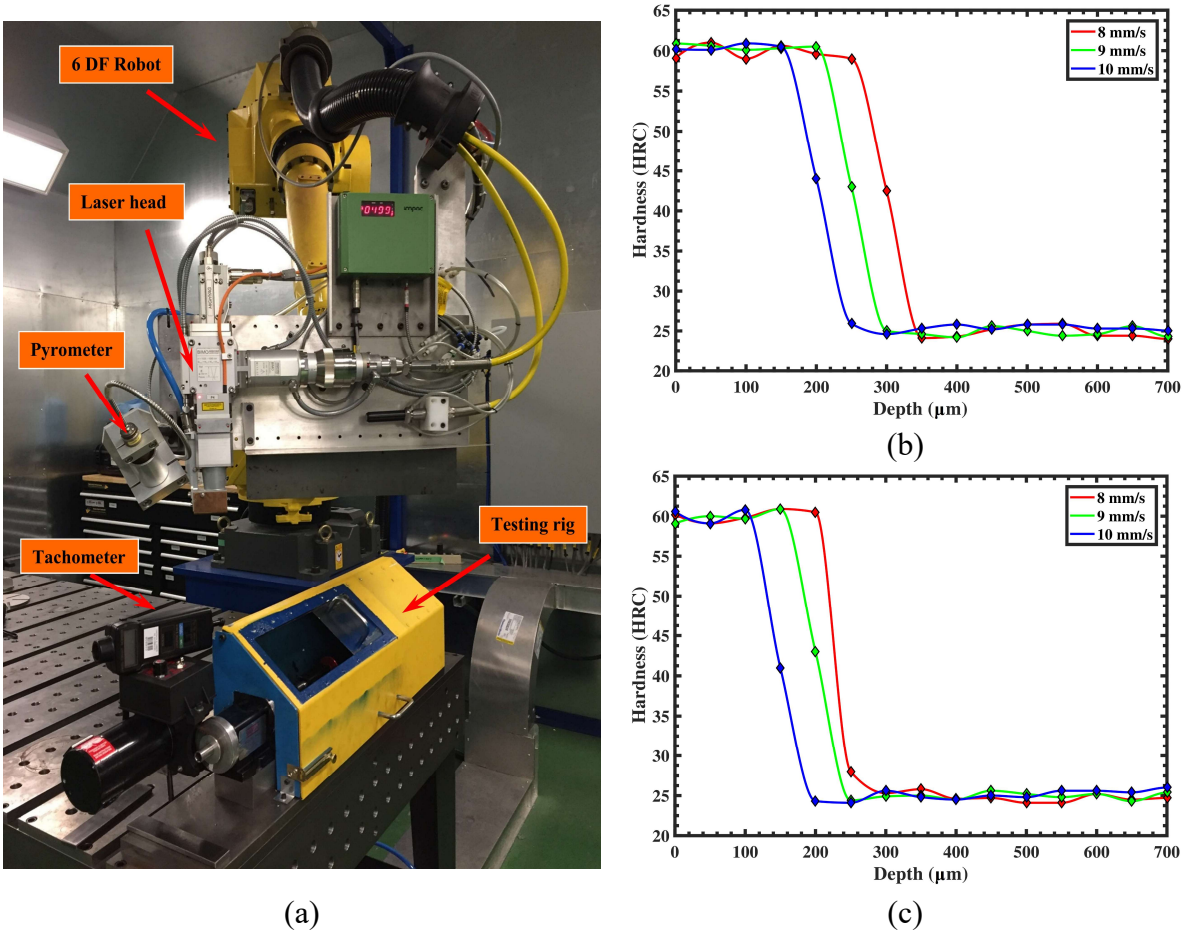

Figure 3-4: (a) Experimental setup, Hardness curve versus depth – (b) For 3000-W and 6000-RPM, (c) For 2800-W and 4000-RPM

Table 3-1 presents the 3 factors at 3 levels considered in the planning of the experiments. The levels of the experimental plan were chosen in the preliminary tests to correspond with the minimum transformation (100-µm) and the maximum transformation (250-µm) of the cylindrical workpiece, which respectively correspond to the laser hardening parameters of the test 9 (2800-W, 10-mm/s and 5000-RPM) and test 1 (3000-W, 8-mm/s and 4000-RPM). Table 3-2 shows the grid of tests according to the matrix L_9

Taguchi, with the results of measurement of the case depth, values of the dimensionless numbers (Reynolds and Prandtl), the thermal conductivity of the air and the absorption coefficient of the material. L_9 matrix output responses were determined by examining the hardness profile by measuring the microhardness, the surface temperature and the air temperature around the workpiece by using an infrared camera and air temperature sensors.

Table 3-1: Factors and levels of experience planning

Factors	**Range**
Laser power (W)	2800, 2900 and 3000
Scanning speed (mm/s)	8, 9 and 10
Rotation speed (RPM)	4000, 5000 and 6000

Table 3-2: L_9 orthogonal matrix and experimental results

	Factors				**Responses**			
Tests	P (W)	SS (mm/s)	Ω (RPM)	Cd (μm)	k (W/m-K)	Pr	Re	Λ
1	3000	8	6000	250	6.13E-02	0.718	1316.4	0.935
2	3000	9	5000	200	6.01E-02	0.716	1154.3	0.912
3	3000	10	4000	100	5.77E-02	0.710	1017.3	0.861
4	2900	8	5000	200	6.01E-02	0.716	1154.3	0.918
5	2900	9	4000	150	5.89E-02	0.713	968.5	0.905
6	2900	10	6000	100	5.77E-02	0.710	1525.9	0.890
7	2800	8	4000	200	6.01E-02	0.716	923.5	0.953
8	2800	9	6000	150	5.89E-02	0.713	1452.7	0.936
9	2800	10	5000	100	5.77E-02	0.710	1271.6	0.922

We note that the thermal conductivity of the air, the Reynolds and Prandtl numbers are proportional to the laser power and the rotation speed of the cylinder and are inversely proportional to the scanning speed of the laser beam, with a maximum difference of about 0.36E−02 W/m-K for the thermal conductivity of the air, of 347 for the Reynolds number

and a small difference of about 0.008 for the Prandtl number. Also the absorption coefficient is proportional to the scanning speed and inversely proportional to rotational speed and laser power, for a difference of about 0.074 between the maximum laser hardening configuration and the minimum configuration.

3.8.2 Analysis of Results and Discussion

To estimate the value of the convective heat transfer coefficient and the absorption coefficient according to the laser power, the scanning speed and the rotation speed, an ANOVA analysis of variance with the general step-by-step method, detailed in Table 3-3 and Table 3-4, was performed [23]. The factor with the lowest contribution rate, which corresponds to the level of significance $\alpha = 0.05$, was put in error factor compared to all the conditions of interaction between the parameters.

Table 3-3: ANOVA Table for h

Factor	DOF	Contribution (%)	Sum of squares	F-Value	P-Value
P	1	0.2	0.678	3.00	0.144
SS	1	0.5	1.752	7.76	0.039
Ω	1	98.92	324.553	1437.11	0.001
Error	5	0.34	1.129	–	–
Total	8	100	–	–	–

Table 3-4: ANOVA Table for Λ

Factor	DOF	Contribution (%)	Sum of squares	F-Value	P-Value
P	1	29.51	0.000394	4.74	0.0095
SS	1	49.20	0.000399	4.79	0.0094
P^2	1	8.02	0.000481	5.77	0.0074
P.SS	1	7.71	0.000462	5.55	0.0078
Error	4	5.56	0.000333	–	–
Total	8	100	–	–	–

For each process parameter, the value of the variance ratio F was compared with the values of the standard F tables for high statistical significance levels. It was concluded that the heat transfer coefficient is mainly linked with the rotation speed Ω, for a model response value of about 98%. And that the absorption coefficient depends mainly on the two factors P and SS , for a model response value of about 94%. Equations (22) and (23) present the empirical prediction relationships, of the heat transfer coefficient and the absorption coefficient, on the basis of a linear regression.

$$h = 19.61 - 0.00262\ P + 0.724\ SS + 0.007200\ \Omega \quad (22)$$

$$\Lambda = 11.83 - 0.00819\ P + 0.290\ SS + 0.000002\ P^2 - 0.000108\ P.SS \quad (23)$$

Figure 3-5a and Figure 3-5b show the estimated response surfaces [24] for the heat transfer coefficient and the absorption coefficient, according to the laser power, the scanning speed and the rotation speed. These response surfaces of the statistical model make it possible to reproduce the contour lines with response intervals varying according to laser heat treatment parameters. Response surfaces were represented according to dimensionless numbers: Reynolds, Prandtl and the dimensionless variable reproduced following the Buckingham approach [25] to reduce the number of response surfaces of the statistical model. The constant $\alpha = 9549$ was introduced to convert the SI system to the engineering system: the scanning speed from m/s to mm/s and the rotation speed from rad/s to RPM. It can be deduced from the figures obtained that a high rotational speed increases the convective losses but also allows to increase the value of the absorption coefficient for the levels of the factors experimental design (P, SS and Ω) presented in Table 3-1. The results obtained confirm that the value of the hardness is proportional to the laser power and the rotation speed, and is inversely proportional to the scanning speed. Figure 3-5c and Figure 3-5d show the temperature distribution along the x-axis of the cylinder for three depths and with different laser heat treatment parameters. Figure 3-5e and Figure 3-5f show the comparison values of the surface temperature at the stop-laser position (40-mm) using an infrared camera with an emittance coefficient of 0.123 and a distance between the camera lens and the cylinder surface of about 700-mm.

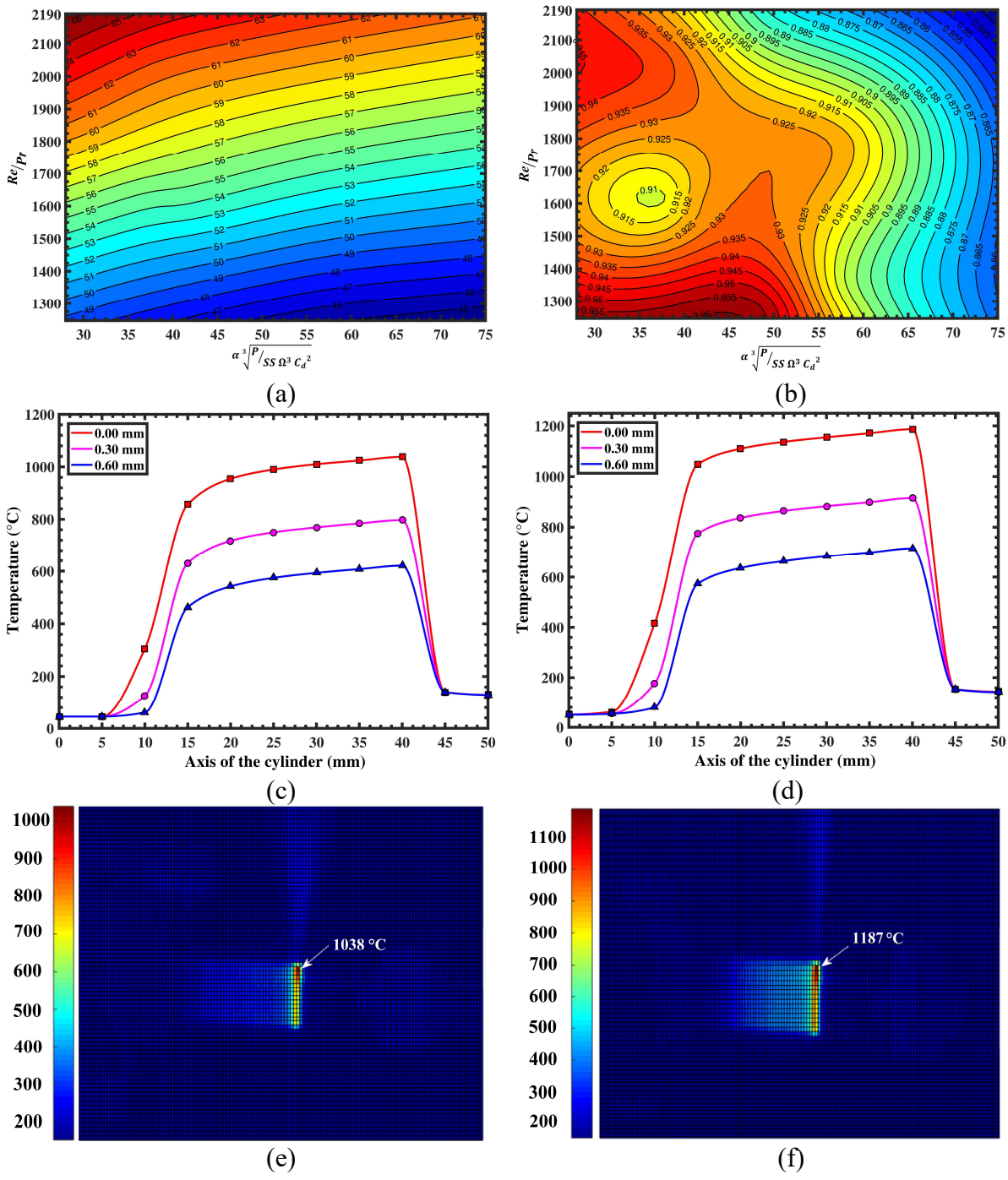

Figure 3-5: Contour plot – (a) For h, (b) For Λ, Temperature versus Axis of the cylinder – (c) For 2800-W, 10-mm/s and 5000-RPM, (d) For 3000-W, 8-mm/s and 6000-RPM, Infrared thermography for the laser parameters – (e) Configuration c, (f) Configuration d

Visualization with the thermal camera allowed us to give identical surface temperature values for a constant emissivity coefficient and this regardless of the laser heat treatment parameters. At the start position of the laser heat treatment (10-mm), the surface temperature rapidly increases from 27˚C to about 300˚C in 50-ms. Then from the 10- to 15-mm position, it rises from 300˚C to about 850˚C, followed by a slight increase every 5-mm of displacement.

This slight increase in temperature between the position 15-mm and 40-mm is due to the heating phenomenon by advancement and can be explained by the fact that the thermal properties (thermal conductivity and specific heat) change with the temperature, and that convection and radiation heat losses become more important for high temperatures. This phenomenon induces a slight modification of the case depth along the longitudinal of the cylinder. To remedy this, it is important to control the laser heat treatment parameters being processed.

The transformation start temperature allows us to estimate the case depth to improve the mechanical performance of the sample. The AISI 4340 steel used has an initial allotropic transformation temperature of 727˚C (Ac_1), a complete austenitization temperature of about 927˚C (Ac_3), and a melting temperature of about 1417˚C. To validate the developed model, it was assumed that the depth reaching a complete austenitization temperature (Ac_3) will have a martensitic microstructure if the rate of the cooling cycle is greater than 8˚C/s.

Figure 3-6a shows the heating cycle for laser heat treatment parameters corresponding to the test 9 (Table 3-2), with the values of the temperature for three depths and at the position 25-mm. It is observed for the parameters of the test 9, that the temperature Ac_3 is obtained for a depth of 100-µm. Figure 3-6b shows the heating cycle for the laser heat treatment parameters corresponding to test 1 at the same position 25-mm. It is observed for the parameters of the test 1, that the temperature Ac_3 is obtained for a depth of 250-µm. The variation of the temperature from 27˚C to 1038˚C, from the moment t = 0 s which corresponds to the position 10-mm to the moment t = 1.5 s which corresponds to the

position 25-mm for a scanning speed 10-mm/s (test 9), and from 27˚C to 1187.8˚C, from the moment t = 0 s to t = 1.857 s which corresponds to the position 25-mm for a scanning speed 8-mm/s (test 9), is related to the scanning speed of the laser beam, the variation of the thermal properties according to the temperature, the thermal losses and the high concentration of the laser energy in a very small section of the focal spot [26]. Figure 3-6c and Figure 3-6d show respectively the cooling cycles corresponding to the heating cycles of Figure 3-6a and Figure 3-6b at the same position 25-mm.

We observe that the temperature drops quite rapidly after passing the laser beam and this because of the modes of heat transfer by convection and radiation. Compared with Time-Temperature-Transformation (TTT) curves of AISI -4340 steel, we can deduce conclusions about microstructure-scale transformation. As can be seen in Figure 3-6c and Figure 3-6d, the cooling rate is of the order of 20˚C/s at the core of the workpiece. This cooling rate is higher than the critical speed (8˚C/s), which is the minimum cooling speed of steel AISI -4340 [27] requiring the formation of a completely martensitic structure. Figure 3-6e shows a cross-section of the hardened area, for two configurations of the laser heat treatment parameters, and a microscopic visualization with magnification (×1000) of the microstructure of the transformed zone. The magnification of the zone transformed by the laser heat treatment shows a completely martensitic structure. Figure 3-6f illustrates measurement values of case depth for the position 25-mm, by interpreting the results provided by our model that predicts the temperature value based on the Ac3 transformation temperature and according to laser power, scanning speed and rotation speed.

These results confirm that the mathematical model developed is accurate in predicting temperature during heating and cooling. The temperature values predicted by the model fit well with the case depth measured using the Clemex CMT microhardness machine. The developed model provides comparable results in the parameter range of Table 3-1, with a difference of less than 5% compared to the experimental tests.

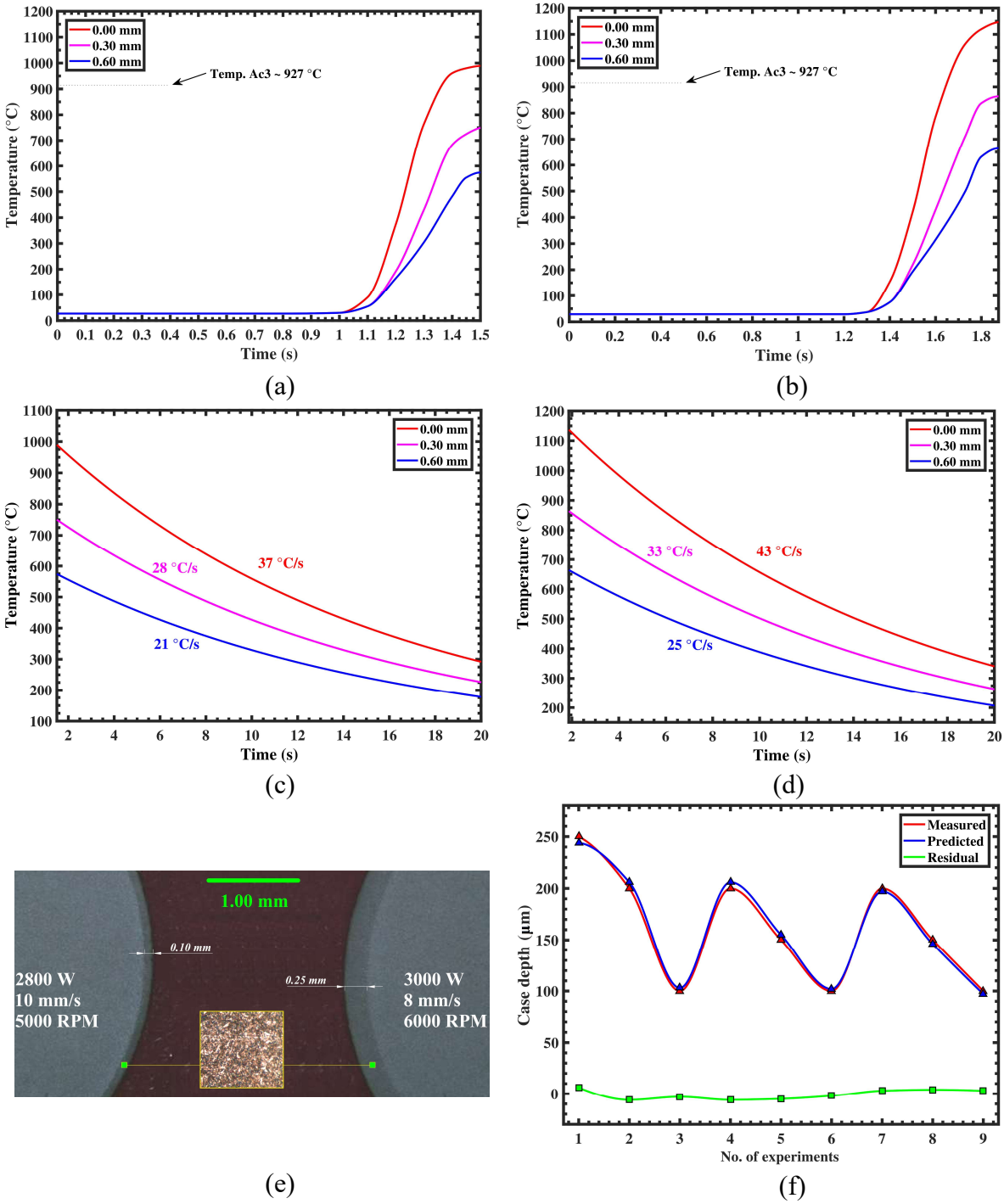

Figure 3-6: Temperature versus heating time for three depths and at x = 25-mm – (a) 2800 W, 10 mm/s and 5000RPM, (b) 3000 W, 8 mm/s and 6000 RPM, Temperature versus cooling time – (c) 2800 W, 10 mm/s and 5000 RPM, (d) 3000 W, 8 mm/s and 6000 RPM, (e) Radial hardness profile, (f) Case depth measured versus predicted

3.9 CONCLUSIONS

In this study, the temperature distribution in a cylindrical workpiece heat treated by laser was simulated using the finite difference method. The major findings are summarized below:

- The algorithm developed with the FDM model for AISI 4340 steel, by adding the displacement parameter of the laser beam, is very effective in simulating the temperature distribution in a workpiece heat treated by laser. The results of theoretical predictions correspond to the experimental tests.

- The variation of the thermal properties of the material has been integrated so as not to affect the output results of the thermal model. The coefficient of convective heat transfer has been evaluated by empirical correlations using measurements of the air temperature around the cylinder. Measurements provided by precision thermocouples that have been positioned very close to the outer surface of the cylinder.

- The variation of the absorption coefficient that influences the effective penetration of heat flux, according to interaction conditions between the laser energy and the workpiece surface was approximated using experimental tests based on Taguchi experience planning and ANOVA analysis of variance.

- Experimental validation of the model by the use of an infrared camera confirmed the values of the predicted temperature on the surface, in the range of defined parameters by the experimental design.

It would be interesting to consider completing this model of prediction of the temperature profile, by integrating a control of the laser heat treatment parameters for a uniform case depth along the longitudinal axis of the cylinder. We believe that this type of approach is the most appropriate way to develop a prediction model of the case depth for workpieces of cylindrical geometry.

References

1. Komanduri, R. and Hou, Z.B. (2001) Thermal Analysis of the Laser Surface Transformation Hardening Process. International Journal of Heat and Mass Transfer, 44, 2845-2826.
2. Senthil Selvan, J., Subramanian, K. and Nath, A.K. (1999) Journal of Materials Processing Technology, 91, 29-36.
3. Suárez, A., Amado, J.M., Tobar, M.J., Yáñez, A., Fraga, E. and Peel, M.J. (2010) Study of Residual Stresses Generated inside Laser Cladded Plates Using FEM and Diffraction of Synchrotron Radiation. Surface & Coatings Technology, 204, 1983-1988.
4. Wang, J.-T., Weng, C.-I., Chang, J.-G. and Hwang, C.-C. (2000) The Influence of Temperature and Surface Conditions on Surface Absorptivity in Laser Surface Treatment. Journal of Applied Physics, 87, 3245-3258.
5. Tobar, M.J., Álvarez, C., Amado, J.M., Ramil, A., Saavedra, E. and Yáñez, A. (2006) Laser Transformation Hardening of a Tool Steel: Simulation-Based Parameter Optimization and Experimental Results. Surface & Coatings Technology, 200, 6362-6367.
6. Miokovic, T., Schulze, V., Vohringer, O. and Lohe, D. (2006) Prediction of Phase Transformations during Laser Surface Hardening of AISI 4140 Including the Effects of Inhomogeneous Austenite Formation. Materials Science and Engineering A, 435-436, 547-555.
7. Leung, M.K.H., Manb, H.C. and Yu, J.K. (2007) Theoretical and Experimental Studies on Laser Transformation Hardening of Steel by Customized Beam. International Journal of Heat and Mass Transfer, 50, 4600-4606.
8. Lakhkar, R.S., Shin, Y.C. and Krane, M.J.H. (2008) Predictive Modeling of Multi-Track Laser Hardening of AISI 4140 Steel. Materials Science and Engineering A, 480, 209-217.

9. Lee, S.-Y. and Huang, T.-W. (2014) A Method for Inverse Analysis of Laser Surface Heating with Experimental Data. International Journal of Heat and Mass Transfer, 72, 299-307.

10. Bojinovic, M., Mole, N. and Stok, B. (2015) A Computer Simulation Study of the Effects of Temperature Change Rate on Austenite Kinetics in Laser Hardening. Surface and Coatings Technology, 273, 60-76.

11. Cheng, A.H.-D. and Cheng, D.T. (2005) Engineering Analysis with Boundary Elements. Engineering Analysis with Boundary Elements, 29, 268-302.

12. Bathe, K.-J. and Wilson, E.L. (1976) Numerical Methods in Finite Element Analysis. Vol. 197, Prentice-Hall, Englewood Cliffs, NJ.

13. Wang, B.-L. and Tian, Z.-H. (2005) Application of Finite Element–Finite Difference Method to the Determination of Transient Temperature Field in Functionally Graded Materials. Finite Elements in Analysis and Design, 41, 335-349.

14. Fakir, R., Barka, N. and Brousseau, J. (2018) Optimization of the Case Depth of a Cylinder Made with 4340 Steel by a Control of the Laser Heat Treatment Parameters. ASME 2018 International Design Engineering Technical Conferences and Computers and Information in Engineering Conference, Quebec City, 26-29 August 2018, 1-9.

15. Fakir, R., Barka, N. and Brousseau, J. (2018) Case Study of Laser Hardening Process Applied to 4340 Steel Cylindrical Specimens Using Simulation and Experimental Validation. Case Studies in Thermal Engineering, 11, 15-25.

16. Bergman, T.L. and Incropera, F.P. (2011) Fundamentals of Heat and Mass Transfer. John Wiley & Sons, Hoboken.

17. Khosrofian, J.M. and Garetz, B.A. (1983) Measurement of a Gaussian Laser Beam Diameter through the Direct Inversion of Knife-Edge Data. Applied Optics , 22, 3406-3410.

18. Smith, G.D. (1985) Numerical Solution of Partial Differential Equations: Finite Difference Methods. Oxford University Press, Oxford.

19. Richtmyer, R.D. and Morton, K.W. (1994) Difference Methods for Initial Value Problems. 2nd Edition, Krieger Publishing, Malabar.

20. Aziz, A.K. (1972) The Mathematical Foundations of the Finite Element Method with Applications to Partial Differential Equations. Academic Press, Cambridge, 796.

21. Fakir, R., Barka, N. and Brousseau, J. (2018) Mechanical Properties Analysis of 4340 Steel Specimen Heat Treated in Oven and Quenching in Three Different Fluids. Metals and Materials International, 24, 981-991.

22. Ross, P.J. (1988) Taguchi Techniques for Quality Engineering. McGraw-Hill, New York.

23. Palanikumar, K., Karunamoorthy, L., Karthikeyan, R. and Latha, B. (2006) Optimization of Machining Parameters in Turning GFRP Composites Using a Carbide (K10) Tool Based on the Taguchi Method with Fuzzy Logics. Metals and Materials International, 12, 483-491.

24. Myers, R.H. (1971) Response Surface Methodology. Allyn and Bacon, Boston.

25. Buckingham, E. (1914) On Physically Similar Systems. Illustrations of the Use of Dimensional Equations. Physical Review, 4, 345-376.

26. Soltani, P. and Akbareian, N. (2014) Finite Element Simulation of Laser Generated Ultrasound Waves in Aluminum Plates. Latin American Journal of Solids and Structures, 11, 1761-1776.

27. Thelning, K.-E. (1984) Steel and Its Heat Treatment, Butterworth-Heinemann. 2d Edition, Elsevier, New York, 696.

CHAPITRE 4

ANALYSE EXPÉRIMENTALE DE LA VARIATION DU PROFIL DE DURETÉ DANS LE CADRE DU TRAITEMENT THERMIQUE AU LASER APPLIQUÉ À DES ÉPROUVETTES CYLINDRIQUES EN ACIER 4340

Fakir, R., Barka, N., Brousseau, J. & Lepage, R.
Université du Québec à Rimouski, Rimouski, Québec, Canada, G5L 3A1

Cet article a été soumis dans le Journal of Manufacturing Processes.
Manuscript Number: SMEJMP-D-18-00224

Mots clés : Durcissement au laser · Variation du profil de dureté · AISI 4340

4.1 RÉSUMÉ EN FRANÇAIS DU QUATRIÈME ARTICLE

Cet article présente une étude expérimentale visant à étudier la variation du profil de dureté dans une composante cylindrique de diamètre 14 et 15 mm, et en acier AISI 4340. Avec des paramètres de traitement thermique au laser fixe, le profil de dureté se caractérise généralement par trois points de coordonnées (profondeur durcie et valeur de dureté) qui sont variables en fonction de la position longitudinale du cylindre. Ces coordonnées qui peuvent être exprimées en fonction de la puissance laser, la vitesse d'avance et la vitesse de rotation varient dans nos expériences sur des proportions entre $\pm \pi/2$ par rapport à l'ordre de grandeur du coefficient directeur de la pente d'interpolation et de 0 μm à 250 μm par rapport à la profondeur durcie. À l'aide d'une analyse basée sur la distribution des résidus à variance appariée et sur la puissance de prédiction des réseaux de neurones, nous avons trouvé un bon accord entre les paramètres de traitement thermique au laser et la variation du profil de dureté. La faisabilité et l'efficacité de l'approche proposée conduisent à un modèle expérimental précis et fiable, capable de prédire la variation du profil de dureté en fonction des paramètres du processus de traitement thermique au laser.

Ce quatrième article, intitulé « *Experimental analysis of the hardness profile variation in laser heat treatment applied to 4340 steel cylindrical specimens* », fut corédigé

par moi-même ainsi que par le professeur Noureddine Barka, le professeur Jean Brousseau et le professeur Richard Lepage. Il fut accepté pour vérification en 2018 dans la revue *Journal of Manufacturing Processes*. En tant que premier auteur, ma contribution à ce travail fut l'essentiel de la recherche sur l'état de l'art, le développement de la méthode du modèle numérique, l'exécution des tests expérimentaux et la rédaction de l'article. Les professeurs Noureddine Barka, Jean Brousseau, et Richard Lepage, second, troisième, et quatrième auteurs, ont participé à définir le projet d'article et ils ont aidé à la recherche sur l'état de l'art, au développement de la méthode ainsi qu'à la révision de l'article.

4.2 TITRE DU QUATRIÈME ARTICLE

Experimental analysis of the hardness profile variation in laser heat treatment applied to 4340 steel cylindrical specimens.

4.3 ABSTRACT

This paper presents an experimental study to investigate the variation of the hardness profile in a cylindrical piece, of a diameter of 14 to 15 mm and in AISI 4340 steel. With fixed laser heat treatment parameters, the hardness profile is generally characterized by three coordinate points (case depth and hardness value) which are variable according to the longitudinal position of the cylinder. These coordinates that can be expressed according to the laser power, the scanning speed and the rotation speed, vary in our experiments on proportions between ± π/2 compared to the order of magnitude of the directional coefficient of the interpolation slope and from 0 μm to 250 μm compared to the variation of the case depth. Using an evaluation based on analysis of variance, on a linear regression and on the predictive power of neural networks, we found a compatibility between the laser heat treatment parameters and the variation of the hardness profile. The feasibility and effectiveness of the proposed approach leads to a precise and reliable experimental model, able to predict the variation of the hardness profile according to the parameters of the laser heat treatment process.

4.4 NOMENCLATURE

C_i	*Case depth, μm*
a_i	*Coefficient of the prediction polynomial,*
L	*Cylinder length, mm*
D	*Diameter of the cylinder, mm*
ϕ_s	*Diameter of the laser spot, mm*
$\aleph$	*Dimensionless quantity,*
f_{logsig}	*Activation function Logsig,*
$f_{purelin}$	*Activation function Purelin,*
W	*Weight matrix,*
P	*Laser power, W*
Z_i	*Position in the longitudinal axis, mm*
Ω	*Rotation speed of the cylinder, RPM*
SS	*Scanning speed, mm/s*
Γ_i	*Slope of interpolation, degree*
H_i	*Value of hardness at depth Ci, HRC*
β_i	*Variation of the depth, μm*
b	*Basis vector,*
γ	*Input vector of laser parameters,*

4.5 INTRODUCTION

Laser heat treatment offers many advantages over other traditional processes, induction, flame or thermochemical heating. Using a precision robotic arm, the laser can obtain a speed of execution coupled with a high quality of production. During this last decade, and through great efforts in research and development, laser technology is growing continuously in many applications such as: the improvement of the wear resistance, improving fatigue resistance, aluminum engraving (QR codes, images, etc.), cutting thin stainless steels, stripping (paints, rust, oil, etc.) and laser welding [1,5]. In the field of laser

surface heat treatment [6] and more precisely that of martensitic quenching, the laser beam increases the surface temperature up to the austenization temperature, which is between the reference points Ac1 (1000 K) and Ac3 (1200 K) of the equilibrium diagram of the iron-carbon system. This eutectoid transformation of the superficial layer into austenite, followed by rapid cooling leads to a martensitic transformation of this superficial layer of steel, which shows high hardness values compared to the initial state of the material [7,8].

For a successful design process of a mechanical part, it is necessary to determine the material adapted to the needs of the design and also to choose the right heat treatment parameters to meet the mechanical stress criteria. To meet these design requirements, it is essential to have effective prediction formulas for output responses as a function of the input parameters of the model. During these last few years, several professionals and research teams specialized in the field of laser heat treatment have succeeded to develop models for predicting mechanical properties (case depth, hardness, conventional yield strength, ultimate tensile strength, number of cycles at break, etc.) for a material, a geometry, with operating conditions, and with specific prediction methods (numerical, probabilistic, statistical or based on neural networks).

R. Narayanasamy et al. presented, in 2012, a comparison study between regression and modeling with neural networks, for the prediction of the elastic return of the steel sheet during the air-bending process. It was noticed that the artificial neural network ANN modeling process was able to predict accurately the output response of the model according to the input parameters [9]. D. Yu. Pimenov et al. presented, in 2017, using neural networks, a method for predicting surface roughness deviations, according to the main driving power, taking into account the wear of the milling tools in the machining processes and the generation of flat surfaces. This approach ensures full utilization of the potential of CNC machines for real-time control of drive power. In this study, a series of neural network algorithms was tested to generate linear relationships between process parameters and roughness, and thus avoid the rapid wear of tools [10]. Within the laser heat treatment of AISI 4340 steel, an interesting small studied prediction, using the power of neural

networks as predictors of the variation of the hardness profile inside a cylindrical piece was developed in this study. The experimental analysis is built progressively by (i) a definition of experience planning, (ii) an analysis of the responses based on the ANOVA method, (iii) a development of a model of prediction of the hardness profile based on a multiple linear regression, a visual representation of the data by the use of the response surfaces and (iv) use of the prediction power of multilayer neural networks (MLPs) with an error backpropagation scheme. The feasibility and effectiveness of the proposed approach leads to a precise and reliable experimental approach capable of controlling the variation of the hardness profile as a function of the laser heat treatment process of simple cylindrical geometries.

4.6 EXPERIMENTATION

4.6.1 Experimental setup

Figure 4-1a shows a view of the experimental device which mainly consists of a Fanuc 6-axis robot, a laser source IPG YLS-3000-ST2 6 modules (each module generates 500 W) for a continuous emission up to a total power of 3000 W, with a wavelength of 1.07 µm. The setup also includes optical fibers of two diameters (200 µm and 600 µm), an DC-Scanner system for optimal control of spot size. A MI-IGAR-12-LO Pyrometer and an infrared thermal camera for surface temperature control. A test bench of rotation equipped with a motor provides a direct drive of the spindle via a belt, a self-centering chuck three-jaw which is connected to the flange of the spit for fixing parts of cylindrical geometry, and a protective cage. During the laser heat treatment operation, the fixing pin driven by the motor is maintained at a fixed rotation speed **Ω** (pre-calibrated using a tachometer). The robot that supports the laser head moves along the length of the cylinder with a horizontal movement speed SS and the laser source emits uniform laser power P, from the start point of treatment (Start laser: Z_0) at the point of cessation of treatment (Stop laser: Z_{40}), with a focal spot diameter ϕ_s= 0.52 mm. Before laser heat treatment, the samples were placed in an oven at a temperature of 1000°C for a period of 20 minutes, then cooled in an oil bath

for homogenization of the martensitic microstructure. A return to the oven at a temperature of 450°C for a period of 30 minutes was performed to obtain a uniform hardness on all samples, after quenching and tempering in the range of 40 HRC.

Figure 4-1b shows a photograph of test pieces made of AISI 4340 steel with a cylindrical geometry of a diameter of 14 and 15 mm and length L = 60 mm. Figure 4-1c shows a 3D visualization of the axis of rotation of the cylinder and the point of start and stop of emission of the laser power.

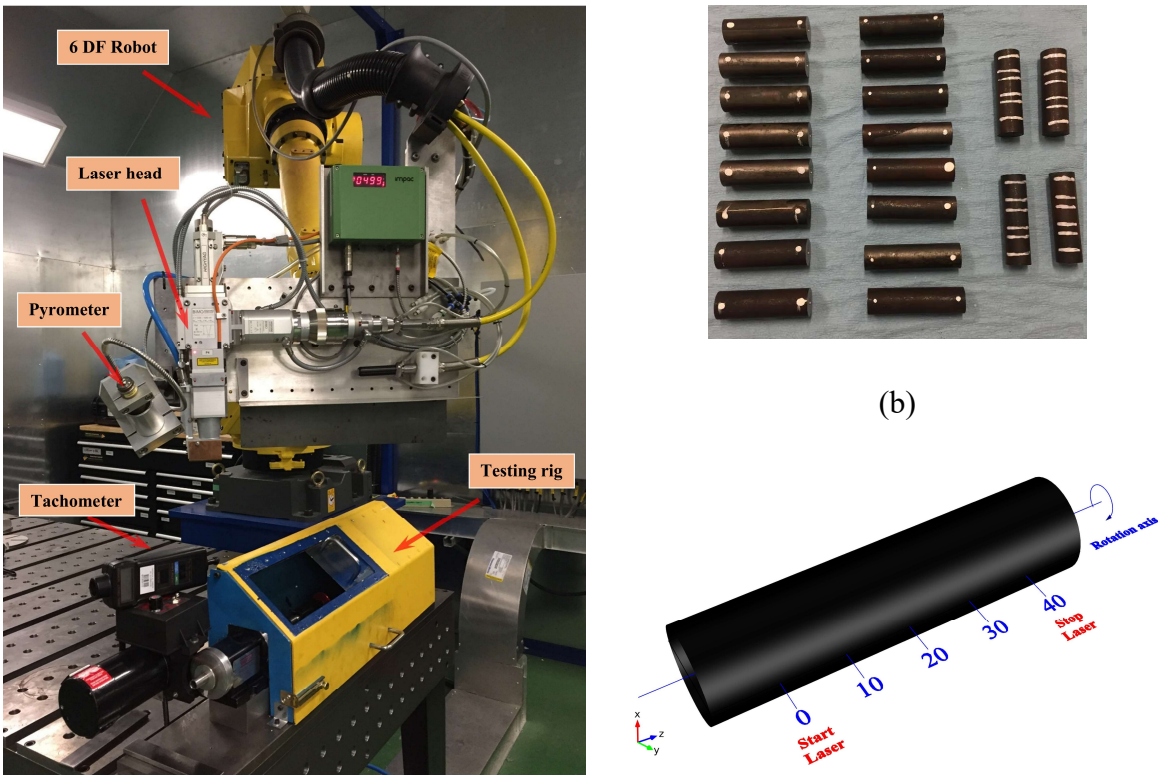

(a) (b) (c)

Figure 4-1: (a) Experimental setup, (b) Visualization of 14 and 15 mm diameter samples, (c) 3D visualization of the start and stop point of laser heat treatment

After laser heat treatment, the samples were prepared, cut to Z_{10}, Z_{20} et Z_{30}, mounted, polished and etched using a Nital chemical solution (95% ethanol and 5% nitric acid) for

characterization of the hardness profile by microhardness measurement using a Clemex CMT microhardness machine.

4.6.2 Experimental design

To calibrate prediction models in complex experimental environments, it is essential to have relevant tests to faithfully represent the output responses according to the input parameters of the model. A complete factor plan is the best tool for determining and measuring the impact of each factor on the model's final response. However, even though it has power to separate individual effects, a complete factor plan may require a lot of learning data. Nevertheless, a well-designed experiment can minimize variations around the set point for a good evaluation of the parameters of the model. The Taguchi method is one of the widely used methods to achieve, with an optimal number of tests, equally robust experimental designs and insensitive to external disturbances [11,12].

In the case of laser heat treatment, it is important to carry out preliminary tests to define the ranges of variations of the main factors that are in the case of this study: laser power, scanning speed, rotational speed, and diameter of cylindrical samples. The design that answers this problem is an L_{16} matrix that corresponds to 16 tests. Table 4-1 shows the factors and levels used in the planning of experiments. As a result, 4 factors are considered at 4 levels for laser power, scanning speed and rotational speed and at two levels for cylinder diameter. Table 4-2 presents the test grid with the measurement results of the three points of hardness, coordinates C_i (in μm) and H_i (in HRC). Hardness values were determined by examining the cross section of the samples by microhardness measurement.

Table 4-1: Factors and levels of experience planning

Factors	**Ranges**
Laser power (W)	1800, 1900, 2000 and 2100
Scanning speed (mm/s)	3, 4, 5 and 6
Rotation speed (RPM)	3000, 4000, 5000 and 6000
Diameter of the specimen (mm)	14 and 15

Table 4-2: L_{16} orthogonal matrix and experimental results

#	Factors				Responses																	
	P	SS	Ω	D	Z_{10}						Z_{20}						Z_{30}					
					C_1	H_1	C_2	H_2	C_3	H_3	C_1	H_1	C_2	H_2	C_3	H_3	C_1	H_1	C_2	H_2	C_3	H_3
1	2100	3	6000	14	200	59.3	300	35.3	500	40.9	350	59.5	450	37.1	550	40.2	450	59.5	500	37.6	600	40.7
2	2100	4	5000	14	200	59.6	250	37.5	350	40.7	250	59.9	300	36.3	450	40.3	300	59.5	350	37.6	450	40.7
3	2100	5	4000	15	200	59.7	250	38	300	40.5	200	59.7	250	36.2	350	40.4	200	59.4	250	37.6	300	40.6
4	2100	6	3000	15	150	60.0	200	36.8	300	40.2	200	59.4	250	36.8	300	40.6	200	59.3	250	37.6	300	40.6
5	2000	3	5000	15	150	59.4	300	35.3	400	40.6	200	59.6	300	35.9	450	40.5	250	59.7	300	37.2	500	40.6
6	2000	4	6000	15	150	59.2	250	37.5	300	40.8	150	59.2	250	36.5	350	40.4	200	59.5	300	37.2	400	40.6
7	2000	5	3000	14	150	59.9	250	38	300	40.3	150	59.7	250	36.5	350	40.9	200	59.5	250	37.2	300	40.5
8	2000	6	4000	14	150	59.8	250	36.8	300	40.5	150	59.5	200	36.5	300	40.9	150	59.4	200	37.2	250	40.5
9	1900	3	4000	14	150	59.6	300	35.3	350	40.5	200	60	300	35.5	350	40.7	250	59.5	300	36.8	400	40.3
10	1900	4	3000	14	100	59.8	250	37.5	300	40.4	150	59.7	250	36.2	300	40.8	200	59.5	300	36.8	350	40.3
11	1900	5	6000	15	100	59.3	200	38	250	40.6	100	59.2	150	37.8	200	40.5	100	59.4	150	36.8	250	40.6
12	1900	6	5000	15	100	59.5	200	36.8	250	40.5	100	59.6	150	36.9	200	40.7	100	59.3	150	36.8	200	40.6
13	1800	3	3000	15	100	59.7	250	35.3	300	40.4	200	59.4	250	35.8	350	40.4	200	59.7	250	36.4	350	40.5
14	1800	4	4000	15	100	59.6	200	37.5	250	40.5	100	59.7	150	35.8	200	40.3	150	59.5	200	36.4	250	40.5
15	1800	5	5000	14	100	59.5	150	38	200	40.5	150	59.9	200	36.6	300	40.4	150	59.5	200	36.4	300	40.2
16	1800	6	6000	14	100	59.4	150	36.8	250	40.5	100	59.5	200	38.1	250	40.5	100	59.4	250	36.4	300	40.2

The hardness profile in the case of laser surface hardening can be characterized in general by three coordinate points (case depth and hardness value) as well as by four regions such as the melting region (MR), the region of high hardness (HR), the transition region of a hardness lower than the initial hardness of the material (TR) and a last region that corresponds to the non-transformed region (MB). Figure 4-2 shows for three measurements each 10 mm apart (Z_{10}, Z_{20}, Z_{30}), with the value of the hardness depending on the depth. With Γ_1, Γ_2 and Γ_3 the directional coefficients of the coordinate interpolation slopes (C_i, H_i) the regions HR, TR and MB. β_1, β_2 and β_3 represent the maximum variations of the case depth within the same group of coordinates (C_i, H_i). The region characterized by a melting (MR) is evaluated at about 50 µm for the most important configuration of the matrix L_{16}. In practical applications, this region, if present, is removed from the workpiece to maintain a high surface hardness.

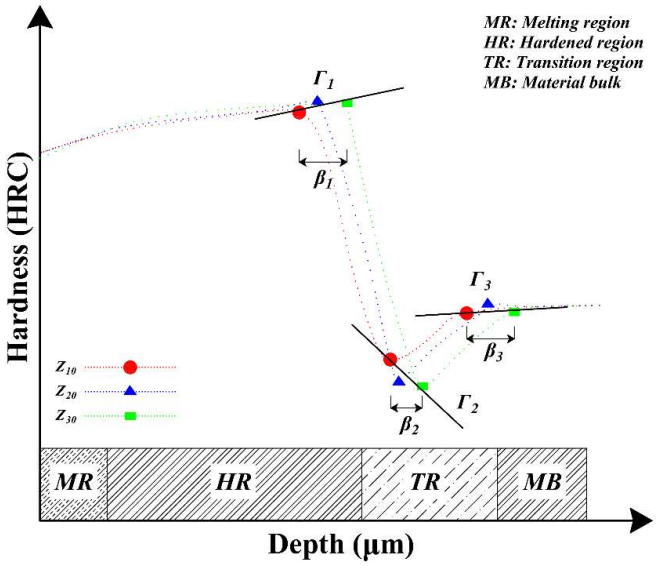

Figure 4-2: Curve representing the variation of the hardness profile according to Zi

4.7 VARIATION OF THE HARDNESS PROFILE

4.7.1 Analysis of variance (ANOVA)

Figure 4-3 presents a graphical representation of the variation of the output response (Γ_i, β_i) for all the tests of the matrix L_{16} using the Thin-plate-spline interpolation method

with a coefficient of determination of the order of 0.95. The output response is represented by the laser power and a dimensionless number which groups together the scanning speed (mm/s), the rotational speed (RPM) and the cylinder diameter (mm). The constant 30/π is introduced into the equation 1 of dimensionless number to convert the unit from the rotation speed of the engineering system to the SI system (rad/s).

$$\aleph = {}^{30.SS}/_{\pi.\Omega.D} \quad (1)$$

The maximum variation of the case depth, is represented by β_i and varies in our experiments between -50 μm, and 250 μm. This variation is maximum for the point β_1 which corresponds to the region of maximum hardness. And it is weak for the point β_3 which corresponds to the point, crossing the transition region (TR) to the region not affected by laser heat treatment (MB).

The variation of the interpolation slope which is represented by Γ_i and varies in our experiences between $-{}^{\pi}/_{2}$ and $+{}^{\pi}/_{2}$. A slope Γ_i at $\pm{}^{\pi}/_{2}$ means that there was no variation within the points β_i for positions Z_{10}, Z_{20} and Z_{30}, and may correspond to small variations in the hardness values.

To determine the influence of the input parameters of the model (P, SS, Ω, and D) on the final output response, and thus quantify decisions using hypothesis tests to know if the variation is influenced by a single parameter, different parameters or a combination of parameters, an analysis of variance (ANOVA) was performed. This calculation technique is widely used to determine which design parameter affects the variation of the hardness curve. Generally, the ANOVA table contains the degrees of freedom, the sum of the squares, the average square, the value of P and the value of F. Process parameters are ranked in terms of importance in the experiment and also to determine which parameters have significant effects on the final response [13].

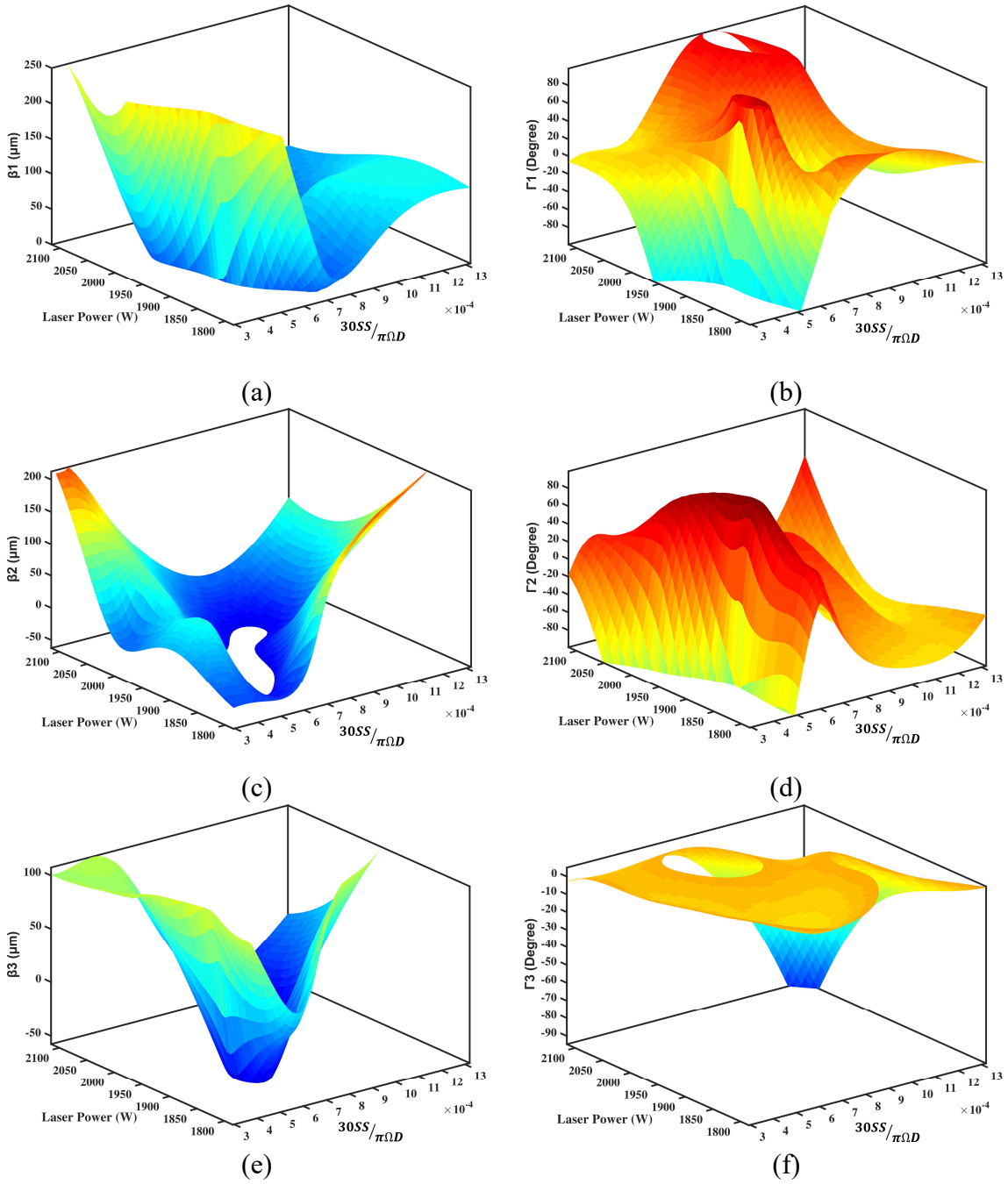

Figure 4-3: 3D-graphical representation based on laser power and adimensional number ℵ, (a) for the variation of β1, (b) for the variation of Γ1, (c) for the variation of β2, (d) for the variation of Γ2, (e) for the variation of β3, (f) for the variation of Γ3

Tables 4-3, 4-4, and 4-5 present a variance analysis of the respective responses β_1, β_2 and β_3 using the general step-by-step method under order 2. Examining the value of p (last

column) can indicate whether a term has a significant effect or not on the model's response. Terms that are not significant will be put into error factor in the model. We notice that the final answer β_1 is influenced mainly by the scanning speed of the laser beam SS with a percentage of 61%. It is also influenced by the other parameters (P, Ω and D) with a contribution percentage of 24% and by a combination of the parameters with a contribution percentage of 13%. The final response β_2 is influenced mainly by two parameters: the power of the laser beam (P) with a percentage of a contribution of 37% and the speed of rotation (Ω) with a percentage of a contribution of 22%. It is also influenced by the other two parameters (SS and D) and a combination between the parameters with a percentage of a total contribution of 31%. The final response β_3 is influenced mainly by two parameters: the scanning speed of the laser beam (SS) with a contribution percentage of 42% and by the speed of rotation (Ω) with a contribution percentage of 14%. It is also influenced by the other two parameters (P and D) and a combination between the parameters with a total contribution percentage of 19%. The coefficient of determination of the prediction quality (R^2) is mainly used to measure the relationship between the measured data and the predicted data is 98% for β_1, 90% for β_2, and 75% for β_3.

Table 4-3: ANOVA for β_1

Characteristic	**dof**	**Contributions (%)**	**Sum of Squares**	**F-value**	**P-value**
P	1	7.20	4500	14.01	0.02
SS	1	57.80	36125	0.01	0.927
Ω	1	0.20	125	9.78	0.035
D	1	9.00	5625	14.11	0.02
P^2	1	4.00	2500	15.77	0.017
SS^2	1	4.00	2500	15.77	0.017
Ω^2	1	4.00	2500	15.77	0.017
P x SS	1	2.13	1333.3	8.41	0.044
P x Ω	1	2.20	1375	8.67	0.042
SS x Ω	1	5.89	3681.8	21.16	0.01
SS x D	1	2.56	1600.8	10.1	0.034
Residual	4	1.01	634.1	–	–
Total	15	100.00	62500	–	–

Table 4-4: ANOVA for β_2

Characteristic	dof	Contributions (%)	Sum of Squares	F-value	P-value
P	1	8.14	5281	20.51	0.002
SS	1	8.14	5281	2.58	0.147
Ω	1	10.84	7031	9.87	0.014
D	1	19.52	12656	3.68	0.091
P^2	1	29.16	18906	25.43	0.001
$Ω^2$	1	11.81	7656	10.30	0.012
P x SS	1	3.21	2083	2.80	0.133
Residual	8	9.17	5948	–	–
Total	15	100.00	64844	–	–

Table 4-5: ANOVA for β_3

Characteristic	dof	Contributions (%)	Sum of Squares	F-value	P-value
P	1	0.29	125	4.61	0.057
SS	1	42.35	18000	21.30	0.001
Ω	1	14.41	6125	5.70	0.038
D	1	5.88	2500	5.00	0.049
P x D	1	11.78	5006	4.66	0.056
Residual	10	25.28	10744	–	–
Total	15	100.00	42500	–	–

4.7.2 Multi-regression model

For all longitudinal positions Z_{10}, Z_{20} and Z_{30}, we notice that the average value of hardness H_1 corresponding to the case depth C_1 is around 59.5 HRC and that the average value of hardness H_2 corresponding to the case depth C_2 is around 37 HRC and that the average value of the hardness H_3 corresponding to the case depth C_3 is around 40 HRC. As a result, and for reasons of simplification, a multiple linear regression was carried out for the prediction of the new depths of transformation C_i. Equation 2 presents the formulation of the regression model between the parameters (P, SS, W and D) and outputs responses C_i. The regression model was obtained, using the Minitab statistical analysis software [14] (version 18), with the output data of the 16 tests in Table 4-1. The residual value squared (R^2) of this regression model is 0.92. Therefore, the output results of the model are quite

adequate, since a value of 1 (for R^2) corresponds to the exact solution. Table 4-6 presents the coefficients of the prediction polynomials of the three points that define the hardness profile for the positions Z_{10}, Z_{20} and Z_{30}. Figures 4-4a and 4-4b show a graphical representation of the prediction of the polynomial of Eq. 2 for hardened depth at the position Z_{20} and Z_{30}.

$$C_i(\mu m) = a_0 + a_1\,P + a_2\,SS + a_3\,\Omega + a_4\,D + a_5\,P^2 + a_6\,SS^2 + a_7\,\Omega^2 + a_8\,D^2 + a_9\,P\,SS + a_{10}\,D\,SS + a_{11}\,P\,\Omega + a_{12}\,SS\,\Omega \quad (2)$$

Table 4-6: Coefficients of the depth prediction polynomial C_i

#	**Z_{10}**			**Z_{20}**			**Z_{30}**		
	C_1	C_2	C_3	C_1	C_2	C_3	C_1	C_2	C_3
a_0	2006	-5766	-1622	8646	5726	4248	8447	8046	836
a_1	-2.14	6.31	1.347	-8.17	-4.5	-5.51	-6.979	-6.94	4.00E-01
a_2	-7.5	-113.1	159	-171.9	-208.8	300	-60.7	-45	-236.2
a_3	5.88E-02	-6.25E-03	-1.19E-02	–	-1.08E-01	–	-2.16E-01	-1.56E-01	2.50E-02
a_4	-12.5	–	–	-31.25	-50	96.4	-106	-62.5	-50
a_5	6.25E-04	-1.56E-03	–	2.19E-03	1.25E-03	1.56E-03	1.88E-03	1.88E-03	–
a_6	–	9.38	25	15.62	18.75	15.62	12.5	–	18.75
a_7	-6.00E-06	–	–	–	1.20E-05	–	6.00E-06	1.90E-05	–
a_8	–	–	–	–	–	–	–	–	–
a_9	–	–	-2.16E-01	–	–	–	-1.25E-01	–	–
a_{10}	–	–	–	–	–	-33.9	15.22	–	–
a_{11}	–	–	–	–	–	–	1.14E-04	–	–
a_{12}	–	–	–	–	–	–	-1.52E-02	–	–

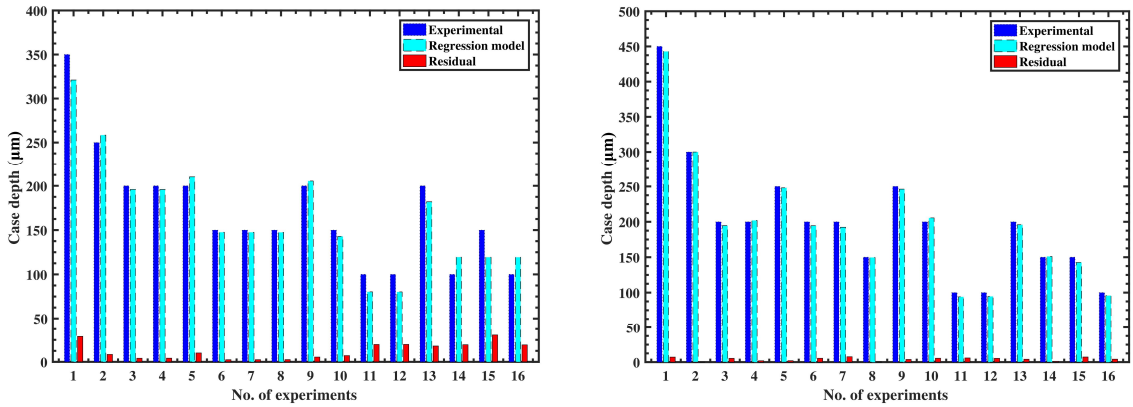

Figure 4-4: Experimental versus Regression model – (a) C_1 at Z_{20}, (b) C_1 at Z_{30}

4.7.3 Analysis of RSM Model

The RSM experimental analysis which is based on a technique of statistical analysis of the data [15] was exploited as part of this study to produce contour lines with response intervals varying according to the conditions of the laser heat treatment process of the cylindrical geometries and to examine the relationship between the response variables (β_1, β_2, β_3, Γ_1, Γ_2 and Γ_3) and all input factors (P, SS, Ω and D). Figure 4-5 shows the estimated response surfaces for variation in transformation depth (β_i) and the interpolation slope (Γ_i), depending on the laser power and the dimensionless number which includes the scanning speed, the rotation speed and the diameter of the cylinder. It can be deduced from the figures obtained that the variation of the case depth can be controlled (limited) by choosing a laser power and a combination of parameters (SS, Ω and D) by the intersection of the value selected in the abscissa axis and the value chosen in the ordinate axis corresponds to a variation $\beta_1 = \beta_2 = \beta_3 = 0$ and an angle of the interpolation slope $\Gamma_i = \pm \pi / 2$. Among the best configurations that can be chosen for a laser heat treatment without varying the hardened depth along the treated cylindrical part, we can mention the one that corresponds to a value of א = 6 and a laser power P = 1860 W (for a uniform case depth) or the one that corresponds to a value of א = 9 and a laser power P = 2100 W (for a high and uniform case depth). The laser process engineer can use to estimate the variation of the hardness profile, in a first step, the linear regression polynomials, and in a second step, the response surfaces. In a third step, the predictive power of neural networks can be used if the precision of the model is required.

4.8 ARTIFICIAL NEURAL NETWORKS

4.8.1 Neural network architecture used

The neural network used for the proposed prediction model was developed with Matlab 2017a software from MathWorks, using a multilayer neural network architecture (Multilayer perceptron) because multilayer networks are more powerful than monolayer networks. Since a number of hidden layers greater than four is rarely used and since the

majority of practical neural networks have only two or three layers, we chose in our model to use a hidden layer number equal to 2.

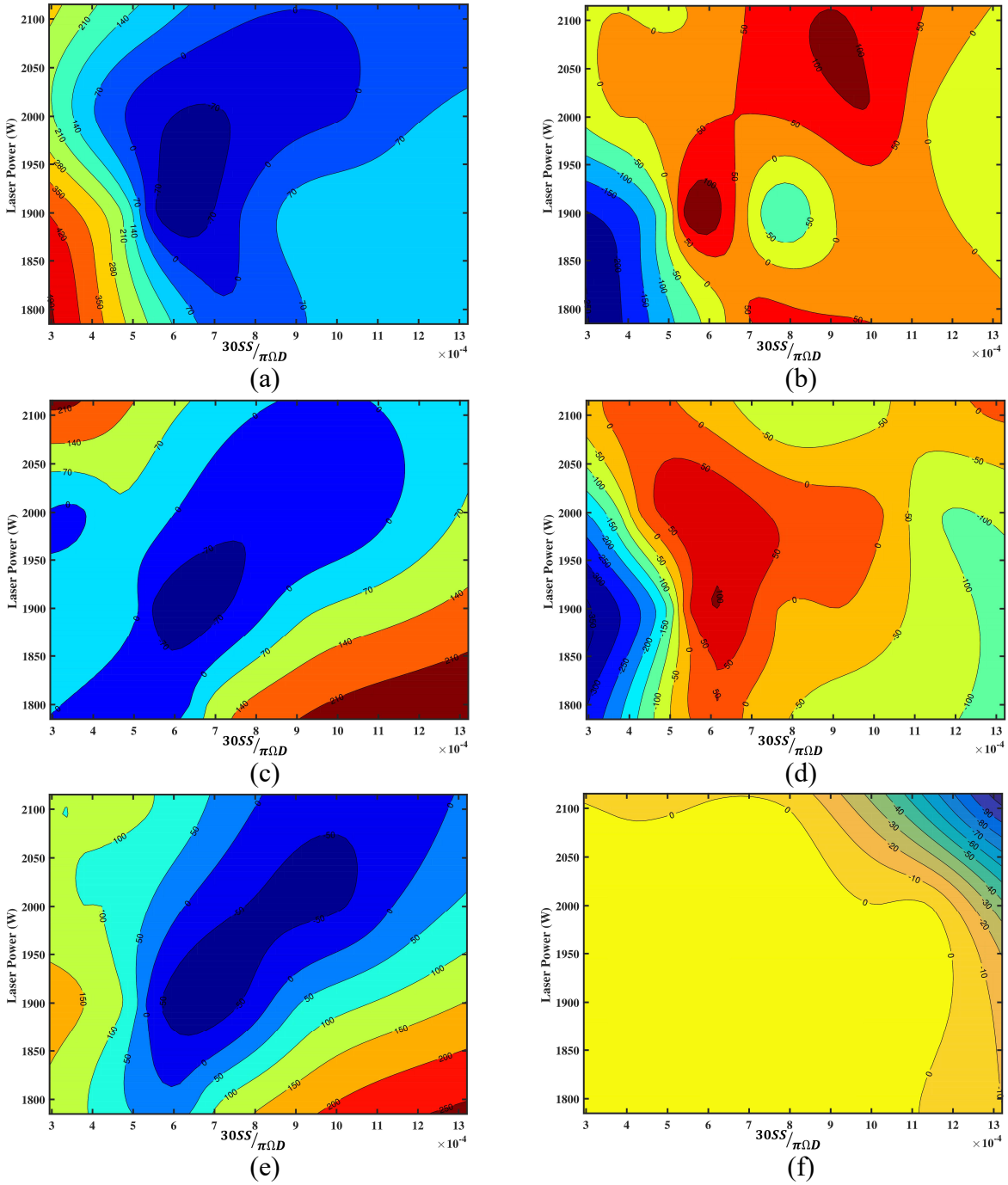

Figure 4-5: Laser power versus adimensional number א – (a) for β_1, (b) for Γ_1, (c) for β_2, (d) for Γ_2, (e) for β_3, (f) for Γ_3

The network was formed to predict the hardness profile, which is represented by three coordinate points (case depth and hardness value), according to the laser heat treatment parameters of the cylindrical geometries [16]. Using the backpropagation algorithm, we proceeded in a first phase by defining the input data (P, SS, Ω and D) and output data (C_i and H_i from Table 4-2), then an execution of a first iteration for learning the network, followed by a comparison of the output of the network with the targeted output and a calculation of the error between the outputs of each neuron. In a second phase, estimating the output value that was correct, calculating the local error, adjusting the weight of each connection for the smallest local error and then repeating this second phase until the error in network exit was very small compared to the targeted output. The number of neurons in the input layer was equal to the number of parameters (4) and the number of neurons in the output layer was equal to the number of output response (18). The optimal number of neurons needed in each hidden layer is defined by calculating and comparing the residual value between the network output and the targeted output. Figure 4-6 shows the architecture of the MLP network [16] of the model (4-9-7-2*9). This architecture was chosen because it allowed to obtain a better quality of prediction with a value of R^2 of the order of 0.96, and which is close to the exact solution evaluated at 1.

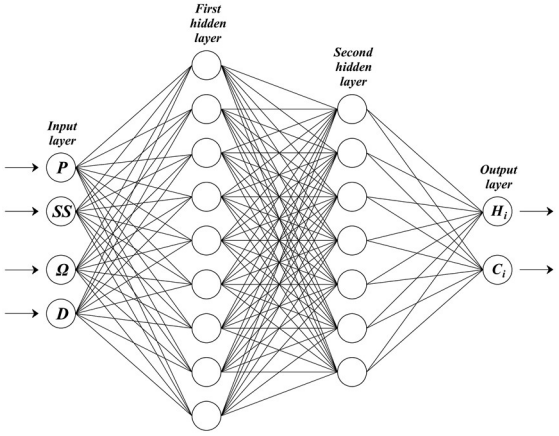

Figure 4-6: Architectural graph of a multilayer perceptron with tow hidden layers

In the first and second hidden layers, the Log-Sigmoid activation function, represented in equation 3, was applied to the output of each artificial neuron. This activation function has the particularity of receiving as input value any value between ± ∞

and returns to the output a value between 0 and 1. Equation 4 presents the Purelin activation function applied to the output of each neuron in the last network output layer. This activation function has the particularity of being linear and returns to the output the same value received at the input.

$$f_{logsig}(x) = {}^{1}/_{1 + e^{-x}} \tag{3}$$

$$f_{purelin}(x) = x \tag{4}$$

To distinguish W weight matrices, bias vectors b and activation functions of each layer, an exponent notation of each of these variables was used. Thus, the weight matrix, the bias vector and the activation function of the first hidden layer are represented by the notations W^1, b^1 and f^1. Equation 5 presents a matrix writing of the output response Y as a function of the weight matrices W, bias vectors b, activation functions f of each of the three network layers and the vector γ which represents laser heat treatment parameters.

$$Y = {f_{logsig}}^{3}\left(W^3 {f_{logsig}}^{2}\left(W^2 {f_{purelin}}^{1}(W^1\gamma + b^1) + b^2\right) + b^3\right) \tag{5}$$

4.8.2 Model performance after training

The input parameters and the output responses of the matrix L_{16} of the experiment plan, were randomly divided into three sets. A first set that consists of 70% data used for network training, a second set that consists of 15% data was used to measure network development and to stop learning when network development stops improving (Overfitting). And a last and third set that consists of 15% data, and that is totally independent of the network learning, were used to test the network once the validation phase ended. Figure 4-7 presents the summary flowchart of the Bayesian regularization backpropagation algorithm used for network learning in this study. This algorithm has the particularity to avoid overfitting [17].

Figure 4-8a shows the graphical representation of the regression that shows the relationship between network outputs and targets. Figure 4-8b shows the progress of the

network performance and shows the iteration at which the validation performance has reached a minimum. The training continued for about 30 additional iterations before the training was stopped. This number does not indicate any problem with training. The value of R, which indicates the relationship between the outputs and the targets, displays an index of 0.95 for the prediction of the case depth. This value is close to 1, which indicates the existence of a linear relationship between inputs and targets. Network results and targets seem almost perfectly aligned, this confirms that the training adopted in the MLP network is optimal for training, testing and validation.

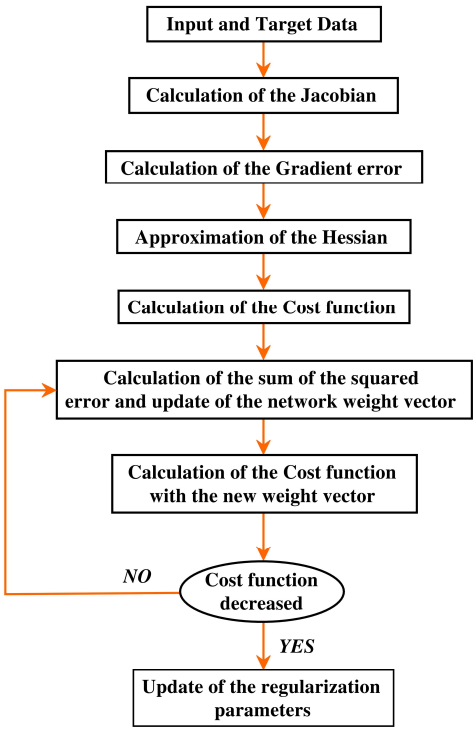

Figure 4-7: Flowchart of training process of BRANN

Figures 4-9a and 4-9b show the hardness curves according to the laser heat treatment parameters of test 1 and 9 of matrix L16 of the experimental planning (Table 4-2). These hardness curves show a good quality of prediction of the neural networks (with a Bayesian regularization backpropagation scheme) for different positions of the longitudinal axis of the cylinder. The portion corresponding to the MR region and which is about 20 to 50 µm was not been shown in the figures.

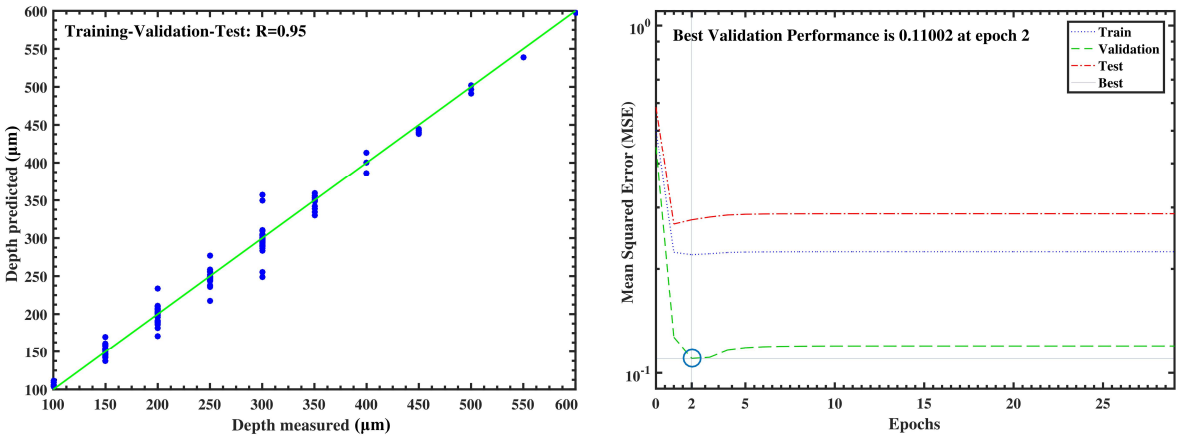

(a) (b)

Figure 4-8: (a) Case depth measured versus predicted, (b) Epochs versus MSE

Figure 4-9c presents, using the multiple linear regression polynomial (Eq. 2) and neural networks, a comparison between the experimental results and the prediction results of the variation of the hardness curves. It is noted that the neural networks offer better results of predicting the β_1 variation (in high hardness region) compared to the linear regression. This variation is zero (optimal configuration) for the laser heat treatment parameters of tests 3, 8, 11, 12 and 16.

Figure 4-9d presents the measured and predicted results of the transition region (TR) as a function of longitudinal position. This figure shows negative values for the 8, 11 and 12 tests (around 50 µm) of the variation of β_2 (in the region of low hardness). Negative values that can be explained by the exact prediction difficulty in this transition region and also by the measurement accuracy which is of the order of 50 µm. Figure 4-9e shows the measured and predicted results of the β_3 variation point, located in a region not affected by laser heat treatment (MB). There is little negative variation for tests 8 and 12, this may be by the dependency relation of the point in the MB region with the point in the TR region. Figure 4-9f shows the average value of the error by test, between the results of β_1, β_2, and β_3, measured and predicted with the multiple linear regression model and the neural network model with a BRANN scheme. It is observed that the average value of the error is less than 50 µm for the two prediction approaches, and that it is more accurate for the neural network model.

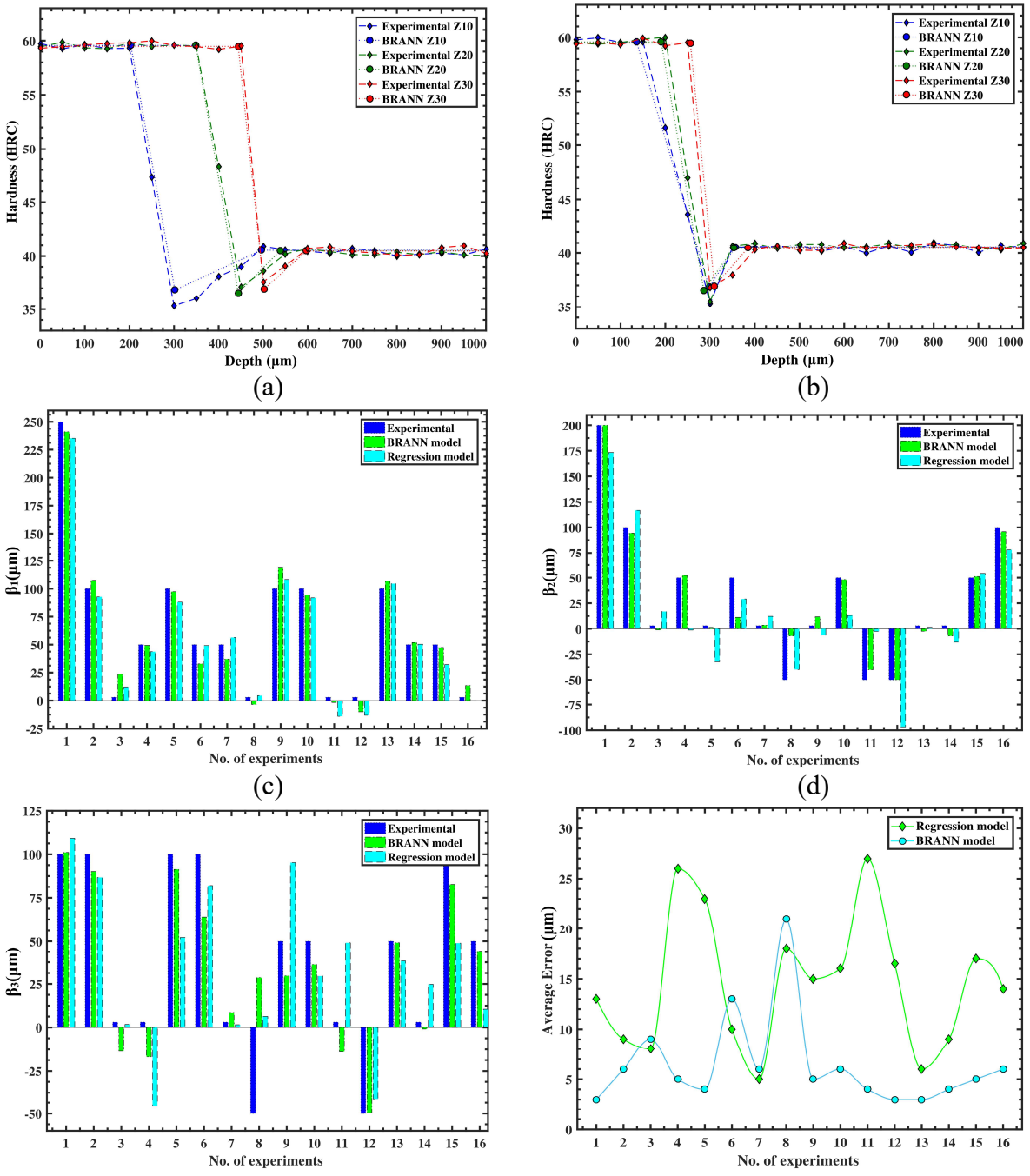

Figure 4-9: Experimental results, BRANN and Regression model – (a) Hardness versus depth for test 1, (b) Hardness versus depth for test 9, (c) Variation by test of β1, (d) Variation by test of β2, (e) Variation by test of β3, (f) Average Error by test

4.9 CONCLUSIONS

In this study, the variation of the hardness profile along a cylinder heat treated by laser, with fixed parameters, was evaluated by an experimental analysis. The major findings are summarized below:

- The experimental approach developed using rigorous experimental planning, a three-dimensional representation of the results using the Thin-plate-spline interpolation method, and an analysis of variance, allowed to highlight the influence of laser heat treatment parameters on the variation of the hardness profile along the length of the cylinder.

- The regression model developed, within the framework of the intervals defined in this study, led to represent using a semi empirical formula, the output responses as a function of the laser heat treatment parameters of the cylindrical parts. The representation of the output data by response surfaces has given the best configurations for optimal hardening without variation of the hardness profile, and allowed to estimate the variation of the case depth and the variation of the interpolation slope of the points characterizing the profile of hardness, along the longitudinal axis of the cylinder.

- The neural network architecture (multilayer perceptron MLP) with an error backpropagation scheme BRANN afforded an effective prediction of the variation of the hardness profile with a lower total average error about 25 μm.

It would be interesting to consider completing this prediction study by integrating a control on the variation of the hardness profile, by servoing during laser treatment. We believe that this type of approach is the most appropriate way to develop hardness profile control models for simple cylindrical geometries.

References

1. Chin-Ping Fung, Kan-Ping Peng, Ji-Liang Doong, Study of surface temperature on laser cutting and welding power absorption, Int. Commun. Heat Mass Transf. 17 (1990) 147-154.
2. A. Ribolla, G. L. Damoulis, G. F. Batalha, The use of Nd: YAG laser weld for large scale volume assembly of automotive body in white, Journal of Materials Processing Technology, 2005, vol. 164-165, pp. 1120-1127.
3. M. Bobby Kannan, W. Dietzel, C. Blawert, S. Riekehr, M. Koçak, Stress corrosion cracking behavior of Nd: YAG laser butt welded AZ31 Mg sheet, Materials Science and Engineering: A, vol. 444, Issues 1-2, 2007, pp. 220-226.
4. Shukri Afazov, Annestacy Okioga, Adam Holloway, Willem Denmark, Andrew Triantaphyllou, Sean-Anthony Smith, Liam Bradley-Smith, Precision Engineering, vol. 50, 2017, pp. 269-274.
5. A. Riveiroa, F. Quintero, J.del Val, M. Boutinguiza, R. Comesana, F. Lusquinos, J. Poua, Laser cutting using off-axial supersonic rectangular nozzles, Precision Engineering, vol.51, 2018, pp. 78–87.
6. Hideki Haginoab, Soichiro Shimizua, Hikaru Andoa, Hisao Kikuta, Design of a computer-generated hologram for obtaining a uniform hardened profile by laser transformation hardening with a high-power diode laser, Precision Engineering, vol. 34, Issue 3, 2010, pp. 446-452.
7. G. Ricciardi, M. Cantello, G.F. Micheletti, CIRP Ann. 31 (1982) 125-130.
8. Ritesh S. Lakhkar, Yung C. Shin, Matthew John M. Krane, Mater. Sci. Eng.: A 480 (2008) 209-217.
9. R. Narayanasamy, P. Padmanabhan, Comparison of regression and artificial neural network model for the prediction of springback during air bending process of interstitial free steel sheet, 2012, Journal of Intelligent Manufacturing, vol. 23, pp. 357-364.

10. D. Yu. Pimenov, A. Bustillo, T. Mikolajczyk, Artificial intelligence for automatic prediction of required surface roughness by monitoring wear on face mill teeth, Journal of Intelligent Manufacturing, 2017, pp. 1-17.

11. Taguchi G, Chowdhury S, WuY. Taguchi's quality engineering handbook. United States of America: Wiley &Sons, Inc; 2004.

12. Lint JHv, Wilson RM. A course in combinatorics. 2nd ed. New York, NY: Cambridge University Press; 2001.

13. Roy RK. Design of experiments using the Taguchi approach: 16 steps to product and process improvement. United Staes of America: Wiley-Interscience, 2001.

14. Ryan, Barbara F., and Brian L. Joiner. Minitab handbook. Duxbury Press, 2001.

15. Van Trees, H.L. Optimum Array Processing. New York, NY: Wiley-Interscience, 2002.

16. M.T. Hagan, H.B. Demuth, M. Beale, "Neural Network Design", PWS Publishing Compagny, 1995.

17. MacKay, Neural Computation, Vol. 4, No. 3, 1992, pp. 415-447.

CHAPITRE 5

OPTIMISATION DE LA PROFONDEUR DURCIE D'UN CYLINDRE EN ACIER 4340 PAR UN CONTRÔLE DES PARAMÈTRES DE TRAITEMENT THERMIQUE AU LASER

Fakir, R., Barka, N., & Brousseau, J.
Université du Québec à Rimouski, Rimouski, Québec, Canada, G5L 3A1

Cet article a été publié et présenté dans la conférence American Society of Mechanical Engineers, International Design Engineering Technical Conferences and Computers and Information in Engineering Conference., Québec City 2018, V01AT02A041–V01AT02A04. Son identifiant numérique d'objet (DOI) est : 10.1115/DETC2018-85574

Mots clés : Durcissement au laser · profondeur durcie · méthode des éléments finis · réseau de neurones artificiels · AISI 4340.

5.1 RÉSUMÉ EN FRANÇAIS DU CINQUIÈME ARTICLE

Cet article présente un modèle numérique capable de contrôler la distribution de la température le long d'un cylindre en acier 4340 traité thermiquement avec un laser fibre. Le modèle numérique développé à l'aide de la méthode numérique des éléments finis est basé sur une étude de la variation de la température en surface et l'ajustement de cette température par un contrôle de la puissance laser de traitement thermique. L'approche analytique proposée a été construite progressivement par (i) le développement d'un modèle numérique de traitement thermique au laser d'une pièce cylindrique, (ii) une analyse des résultats de simulations et de tests expérimentaux, (iii) le développement d'une approche d'ajustement de la puissance laser et (iv) une proposition d'un prédicteur de contrôle de la puissance laser en utilisant les réseaux de neurones. Cette approche a permis de mettre en lumière l'influence des paramètres fixes (non variables) du traitement thermique au laser sur la profondeur durcie, et a montré qu'il est possible en contrôlant les paramètres de durcissement au laser d'homogénéiser la répartition de la température maximale atteinte en

surface pour une profondeur durcie uniforme. La faisabilité et l'efficacité de l'approche proposée conduisent à un modèle fiable et précis, capable de garantir une température en surface uniforme et une profondeur durcie régulière pour une pièce cylindrique d'une longueur de 50 mm et d'un diamètre compris entre 16 mm et 22 mm.

Ce cinquième article, intitulé « *Optimization of the case depth of a cylinder made with 4340 steel by a control of the laser heat treatment parameters* », fut corédigé par moi-même ainsi que par le professeur Noureddine Barka, et le professeur Jean Brousseau. Il fut accepté en 2018 pour présentation devant public et publication dans la conférence *ASME 2018 International Design Engineering Technical Conferences and Computers and Information in Engineering Conference*. En tant que premier auteur, ma contribution à ce travail fut l'essentiel de la recherche sur l'état de l'art, le développement de la méthode du modèle numérique, l'exécution des tests expérimentaux, la rédaction de l'article et la présentation devant la communauté scientifique de la conférence. Les professeurs Noureddine Barka et Jean Brousseau, second et troisième ont participé à définir le projet d'article et ils ont aidé à la recherche sur l'état de l'art, au développement de la méthode ainsi qu'à la révision de l'article.

5.2 TITRE DU QUATRIÈME ARTICLE

Optimization of the Case Depth of a Cylinder Made with 4340 Steel by a Control of the Laser Heat Treatment Parameters.

5.3 ABSTRACT

This paper presents a numerical model able to control the temperature distribution along a 4340 steel cylinder heat-treated with laser. The numerical model developed using the numerical finite element method, was based on a study of surface temperature variation and the adjustment of this temperature by a control of the heat treatment laser power. The proposed analytical approach was built gradually by (i) the development of a numerical model of laser heat treatment of the cylindrical workpiece, (ii) an analysis of the results of

simulations and experimental tests, (iii) development of a laser power adjustment approach, and (iv) proposal of a laser power control predictor using neural networks. This approach was made possible by highlighting the influence of the fixed (non-variable) parameters of the laser heat treatment on the case depth, and has shown that it is possible by controlling the laser parameters to homogenize the distribution of the maximum temperature reached on the surface for a uniform case depth. The feasibility and effectiveness of the proposed approach leads to a reliable and accurate model able to guarantee a uniform surface temperature and a regular case depth for a cylindrical workpiece of a length of 50-mm and with a diameter of between 16 mm and 22 mm.

5.4 NOMENCLATURE

$\check{A}$	*Absorption coefficient of the material, m^{-1}*
$f_{purelin}$	*Activation function Purelin,*
f_{tansig}	*Activation function Tansig,*
Cd	*Case depth, µm*
L	*Cylinder length, mm*
ρ	*Density, $kg.m^{-3}$*
D	*Diameter of the cylinder, mm*
ϕ_s	*Diameter of the laser spot, mm*
$\aleph$	*Gaussian distribution of the laser beam,*
Ac_3	*Heating temperature at point A3, °C*
S	*Irradiated surface, mm^2*
P	*Laser power, W*
X_i	*Position in the longitudinal axis, mm*
r_{spot}	*Radius of the laser spot, mm*
Rc	*Reflectivity coefficient of the material,*
Ω	*Rotation speed of the cylinder, RPM*
SS	*Scanning speed, mm/s*

Γ	*Slope of the curve, W/mm*
Cp	*Specific heat, $J.kg^{-1}.K^{-1}$*
Ts	*Temperature of the surface, °C*
k	*Thermal conductivity, $W.m^{-1}.K^{-1}$*
t	*Time corresponding to the position Xi, s*

5.5 INTRODUCTION

The laser heat treatment is a process that offers many advantages over conventional methods for heat treatment of iron-carbon materials [1]. Allowing to guarantee a high precision of the transformed regions, at low geometric distortion and an absence of cracks after treatment, a process automation with the use of a robot arm, with a gain in speed and efficiency [2]. The laser quenching operations are carried out by the heating being very local with a cooling according to a predefined curve which is achieved by conduction in the mass with a relatively low amount of energy, brought to the piece compared to a conventional heat treatment [3]. In the case of 4340 steel, the laser beam locally heats the workpiece surface up to a certain austenitization temperature (Ac_3) which is generally between 800°C and 1000°C, without the substrate melting temperature being exceeded, then followed by a rapid cooling (quenching) to form martensite, which is the hardest form of this type of steel [4]. This alloys is the steel of choice in the aerospace and automotive industry, due to its ability to obtain a high strength and a great tenacity after heat treatment. However, despite the advantages of laser heat treatment, the optimal control of the process remains difficult to reach. Indeed, several physical factors influence the output results of the process such as the type of material, the surface finish, the angle of incidence, the absorption coefficient, the scanning speed, the rotation speed and the power of the laser. The precise knowledge of all these factors is critical to the success of the process [5].

During the last decade, several research professionals in the field of laser quenching have succeeded in developing quenching parameters for a given material, geometry and for specific operating conditions. J. Mazumder presented in 1983 a prediction technique of the hardness profile of a flat plate for evaluation of wear and fatigue properties. In this study,

we can notice, for five types of materials, the important role of the scanning speed of the laser beam on the absorptivity and on the case depth. J. Mazumder also presented a comparison between a laser treatment and an induction treatment and he detailed a theoretical model for predicting the hardness profile according to laser power, focal spot radius, reflectivity, and scanning speed [6]. J. Mackerle presented in 2002 a bibliographic review of methods applied to finite element analysis and simulation of quenching and heat treatment processes. This work included references to articles, conference posters and theses that were published between 1976 and 2001, thus grouping the processes of quenching, heat transfer, thermomechanical modeling, residual stress analysis in quenching, and superficial hardening [7]. N. Barka et al, and R. Fakir et al. presented in 2015 and 2018 two approaches, statistical and numerical, for prediction of the case depth of a 4340 steel cylinder, heat-treated using 3-kW fiber laser. In their studies, they have assumed that the case depth correlates with the parameters of the laser heat treatment process such as the laser power, the scanning speed of the laser beam and the rotation speed of the workpiece. They were able to show the effects, the contributions and the interaction between the parameters of the laser heat treatment process, to formulate prediction models capable of predicting the case depth for a 4340 steel cylinder [8, 9]. A. Jerniti et al. presented in 2016 an approach to modeling the hardness profile of a 4340 steel cylinder with a diameter of 18-mm and a length of 50-mm, based on regression equations of ANOVA analysis of variance and artificial neural networks method. The model obtained in this study was able to predict with good accuracy, the depths representing the maximum hardness zone, the hardness drop zone and the non-affected zone [10]. M. Hadhri et al. presented in 2016 an approach to predict the hardness profile according to the parameters of the laser process, for a 4340 steel cylinder of 10-mm diameter heat treated by laser. Based on the finite element method, Taguchi experience planning, ANOVA analysis and artificial neural networks, they managed to predict the hardness profile with a relative error of about 10% [11]. X. Deng et al presented in 2012 a model for predicting the structural evolution and hardness distribution during quenching and tempering of 80MnCr5 steel in cylindrical geometry. The model developed takes into account temperature parameters, carbon content,

isothermal and non-isothermal transformations, precipitation of transition carbides, decomposition of retained austenite, and precipitation of cementite [12].

As we have seen, several approaches were proposed by various research teams to predict case depth. However, none of them incorporates the irregularity of case depth and hardness profile along the length of the cylinder. Moreover, the literature reports no data on this irregularity for fixed parameters of the laser heat treatment process of AISI 4340 steel. Table 5-1 presents the chemical composition of the steel studied [13] and Fig. 5-1 shows the variation as a function of the temperature of its thermal conductivity and its specific heat [14, 15].

Table 5-1: Chemical composition of AISI 4340 steel

Composition	Content (%)
Iron	95.71
Nickel	1.83
Chromium	0.81
Manganese	0.70
Carbon	0.40
Molybdenum	0.25
Silicon	0.23
Sulfur	0.04
Phosphorus	0.03

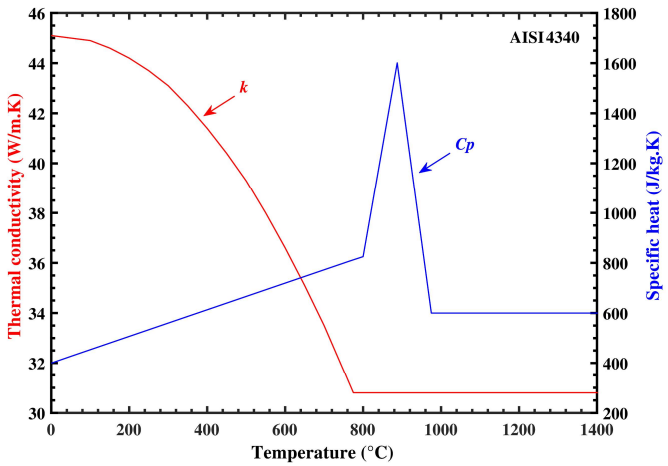

Figure 5-1: Specific heat and thermal conductivity versus temperature

The development of the model is built progressively by (i) development of a numerical model of laser heat treatment using a numerical simulation software, (ii) orderly planning of numerical simulations and experimental trials, (iii) the development of an approach to control the laser power for a uniform distribution of the temperature and for a regular case depth along the longitudinal cylindrical piece, and (iv) proposition of a predictor of control, of the laser power, using neural networks. The feasibility and precision of the proposed approach leads to an analytical model able of controlling and to guaranteeing a uniform distribution of the temperature by servo-control of the heat treatment laser power of the cylindrical geometries.

5.6 NUMERICAL SIMULATIONS

5.6.1 Numerical model (FEM)

Numerical simulations were performed with the version 4.2a of COMSOL Multiphysics software. This numerical simulation software based on the finite element method allows to simulate problems related to engineering applications and complex multiphysics phenomena [16]. The numerical model developed in the framework of this study makes it possible to predict the distribution of the temperature at any point of the cylinder according to the laser heat treatment parameters: laser beam power, cylinder rotation speed, scanning speed, cylinder diameter and thermal properties of the material. The cylinders considered in this study are made of AISI 4340 steel, with a diameter of between 16-mm and 22-mm and a length L of 50-mm. Fig. 5-2a shows the schematic diagram of the experimental set-up. The cylinder is continuously rotating on a test bench and receives a laser energy from the starting position X_{10} to the stop position X_{40} with a constant speed between the two positions. The heat flux transmitted by the laser beam to the workpiece at a Gaussian distribution TEM_{00}. Equation 1 presents the mode of transfer of heat by conduction, considered for this physical problem and, which depends on the density of the material, its specific heat, its thermal conductivity, the temperature gradient, and convective and radiation losses [17].

$$\rho C_p \, {dT}/_{dt} + \rho C_p u \nabla T + \nabla(-k \nabla T) = \beta(x, y, z) - \varphi_{conv} - \varphi_{rad} \quad (1)$$

The density of laser energy β(x, y, z) applied to the material at a given position is represented by Equation 2 [18].

$$\beta(x, y, z, t) = {P}/{S} \, \aleph(x, y, t) \check{A}(1 - R_c) e^{-\check{A}|R-z|} \quad (2)$$

With the term P which represents the laser power, S the section of the laser beam and ℵ(x,y,t) the Gaussian distribution of the laser beam, which is formulated by Equation 3 for a distribution on a cylindrical geometry [19].

$$\aleph(x, y, t) = e^{-\left({\sqrt{((x-SSt)^2+(y-R)^2)}}/{2 \, {r_{spot}}^2} \right)} \quad (3)$$

So the product θ = (1 – Rc).Ă, with Rc the reflectivity of steel and Ă the absorption coefficient which is of the order of 600-m^{-1} for AISI 4340 steel. As, it has been reported in the studies of Steen and Courtney in 1979 [20], Bradley in 1988 [21], Dausinger and Shen in 1993 [22], Pantsar and Kujanpaa in 2004 [23] and Tobar et al in 2006 [24], the absorption coefficient depends on the angle of incidence, the scanning speed, the rotation speed, the surface finish and the irradiating laser. As we would like to determine the value of the θ parameter, which is a variable function of the laser power, the scanning speed, the rotation speed, and the diameter of cylinder, a series of numerical simulations were carried out with reference to the case depth measurement results proposed by previous work on AISI 4340 steel [8-11]. Preliminary tests were carried out to determine the ranges of variation of the laser parameters with the 16-mm diameter cylinder and the 22-mm diameter cylinder. A systematic approach for selecting the parameters was based on a maximum transformation without fusion of the outer surface of the 16-mm cylinder, for the parameters 2300-W, 3-mm/s and 6000-RPM. And was also based on a minimal transformation of the 22-mm cylinder for the parameters 1700-W, 6-mm/s and 3000-RPM.

Table 5-2 shows the range of variation in our simulations of laser heat treatment parameters. Fig. 5-2b shows a graphical representation of the variation of the value of the parameter θ, in the parameters range of Table 5-2 and according to the laser power and a dimensionless number, which includes the scanning speed, the rotation speed and the diameter of the cylinder. The constant 30/π was introduced to convert the unit of the rotational speed of the engineering system to the SI system (in rad/s).

Table 5-2: Factors and levels of the numerical planning

Factors	Ranges
Laser power (W)	1700, 1900, 2100 and 2300
Scanning speed (mm/s)	3, 4, 5 and 6
Rotation speed (RPM)	3000, 4000, 5000 and 6000
Diameter (mm)	16, 18, 20 and 22

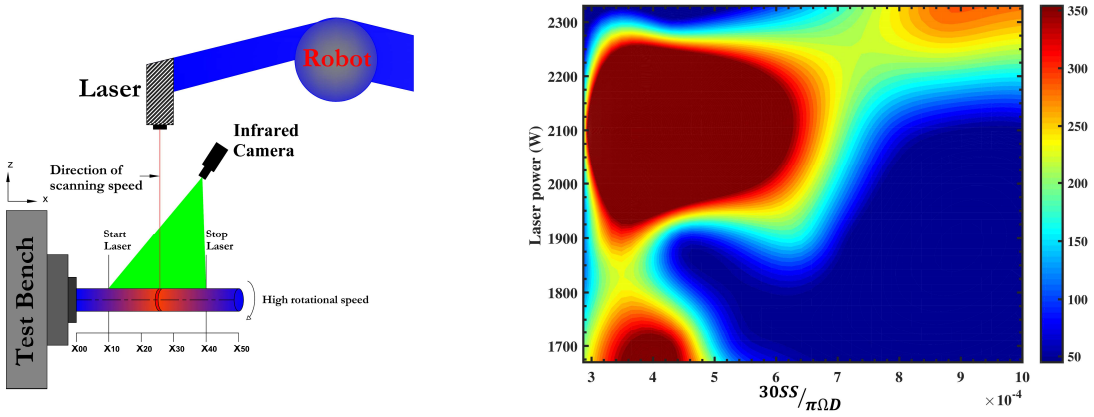

(a) (b)

Figure 5-2: (a) Schematic diagram of the experimental set-up, (b) Variation of θ according to the laser power, the scanning speed, the rotation speed and the diameter of the cylinder

5.6.2 Mesh stability study and numerical simulations

The results obtained by the numerical simulation software COMSOL (version 4.2a) remained at low credibility until the convergence of the mesh was demonstrated. A manual

convergence study was conducted to optimize the mesh [25]. This study involved creating a mesh using a number of elements, then refining the mesh, and comparing the results with the results of the previous calculation for a point in the center and on the surface of the cylinder, and for different mesh sizes.

Fig. 5-3a shows a three-dimensional visualization of the mesh of the cylindrical workpiece. Fig. 5-3b shows the temperature value for different mesh sizes. The mesh density retained is about 1.0 million elements.

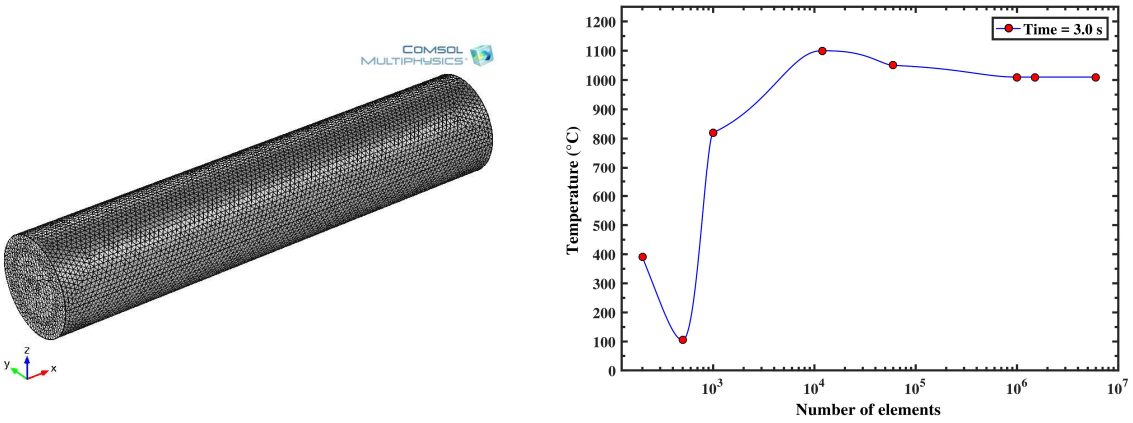

(a) (b)

Figure 5-3: (a) COMSOL mesh visualization, (b) Temperature versus number of mesh elements for P=2000W, SS=4.5mm/s, Ω=5000RPM, and D=20mm

Fig. 5-4 shows the results of the numerical simulations for sixteen configurations of varying parameters of the laser heat treatment process. The value of the temperature on surface was represented by a variation of a parameter on each configuration. We note that the temperature is proportional to the laser power and the rotation speed of the cylinder and that it is inversely proportional to the scanning speed and the diameter of the cylinder. For fixed (non-variable) parameters of laser heat treatment, an increase in temperature on surface is observed, generated by a conduction heating effect of the position x+dx compared to the previous position x. This variation of the temperature on the surface with respect to the longitudinal axis of the cylinder induces an irregularity in the case depth or even a melting (damage) of the layer surface of the workpiece.

Generally, to avoid this phenomenon, a control by servo-control of the laser power is carried out through the use of a pyrometer and a digital program of laser power adjustment depending on the desired target temperature on the surface.

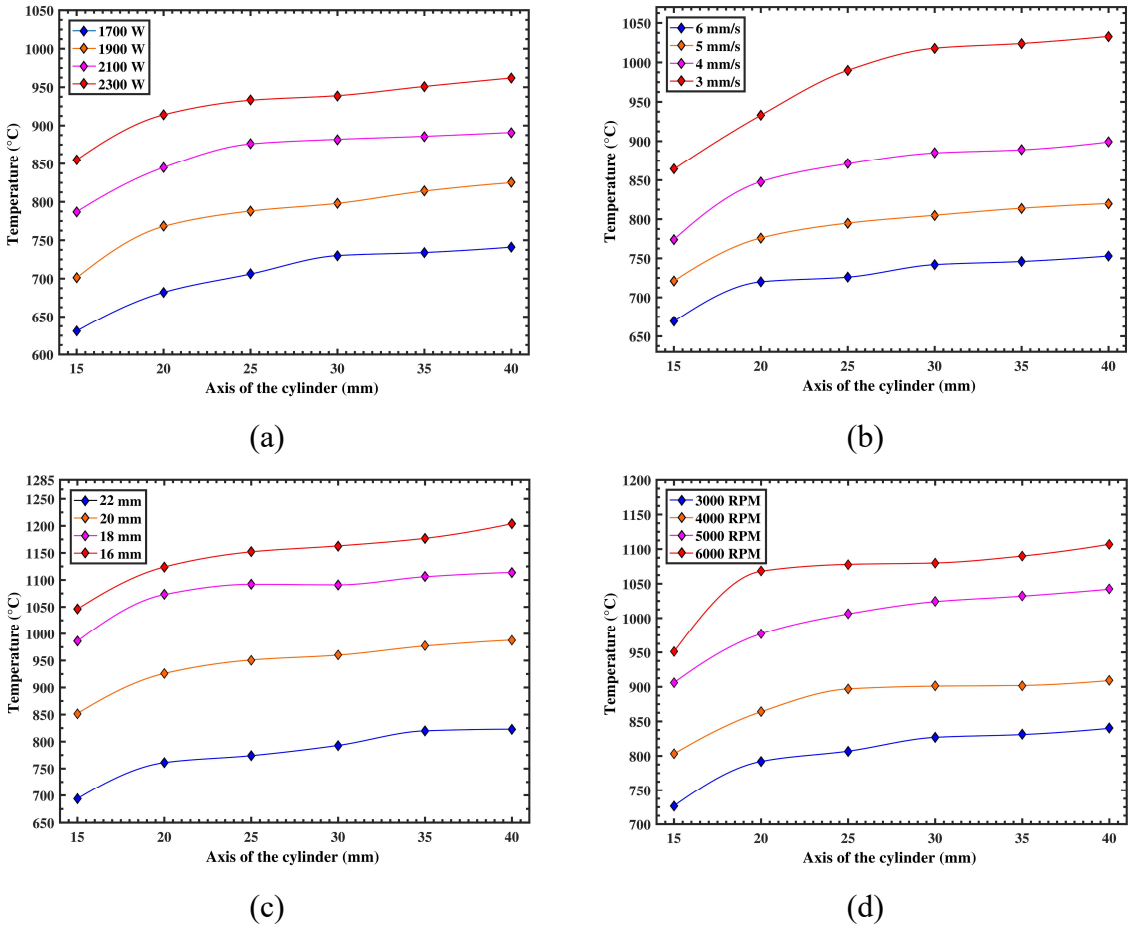

Figure 5-4: Temperature Curves – for different configurations: (a) Position versus laser power, (b) Position versus scanning speed, (c) Position versus diameter, (d) Position versus rotation speed

5.7 EXPERIMENTAL & NUMERICAL INVESTIGATION

5.7.1 Experimental setup and numerical planning

Fig. 5-5a shows the experimental device that consists of a 6 axis FANUC robot and a laser source IPG YLS-3000-ST2 with maximum transmitted power of 3000-W. This setup

also includes a pyrometer MI-RIG-12-LO and an infrared thermal camera FLIR A325sc for measuring the surface temperature of the workpiece. A rotary test bench was used for a control of the rotational speed of the samples. The focal spot diameter of the laser is adjusted using an DC-Scanner-System on ϕs=1.26-mm. The initial hardness of the samples before laser heat treatment was of the order of 25-HRC, this value was obtained after austenitization of the samples in the oven, oil cooling, and tempering at a temperature of 650°C for a period of time of 100-min [26].

After the laser heat treatment, the samples were carefully cut to X_{15}, X_{20}, X_{25}, X_{30}, X_{35}, and X_{40} using an AbrasiMatic300 automatic cutting machine, then mounted and polished for a representation of the hardness profile by measuring the microhardness using Clemex CMT microhardness machine. Fig. 5-5b shows for fixed parameters of laser heat treatment, the variation of the value of the maximum temperature reached on the surface, and the variation of the value of the case depth, according to the position of the longitudinal axis of the cylinder. Fig. 5-5c shows, for the same laser parameters, the variation in the value of the maximum temperature reached in depth and the variation of the hardness profile for three positions of the longitudinal axis of the cylinder (15, 25 and 40-mm). It was noted that the transformation of the microstructure of the steel takes place at a temperature of about 925°C and that a laser heat treatment without variation of laser power induces an irregularity in the case depth and a maximum temperature on the surface and in depth are non-uniform.

For a good analysis of the output responses of an analytical model of control of laser heat treatment parameters, it is essential to have relevant tests. The Taguchi experiment planning method is one of the best-known methods for this purpose, because it guarantees robust representation of model responses for an optimal number of tests [27]. In the range of the four factors of Table 5-2, at 4 levels for laser power, scanning speed, rotation speed and cylinder diameter. Taguchi experience design that responds to this planning of experiments is a matrix L_{16} that corresponds to 16 tests. Equation 4 presents the condition to be satisfied for a uniform surface temperature. And equation 5 shows the slope of the

interpolation line of the laser power adjustment curve depending on the position of the focal spot on the longitudinal axis of the cylinder, and to satisfy the condition of Eq. 4.

$$dT_s(x)/_{dx} = 0 \tag{4}$$

$$\Gamma = {}^{dP(x)}/_{dx} \tag{5}$$

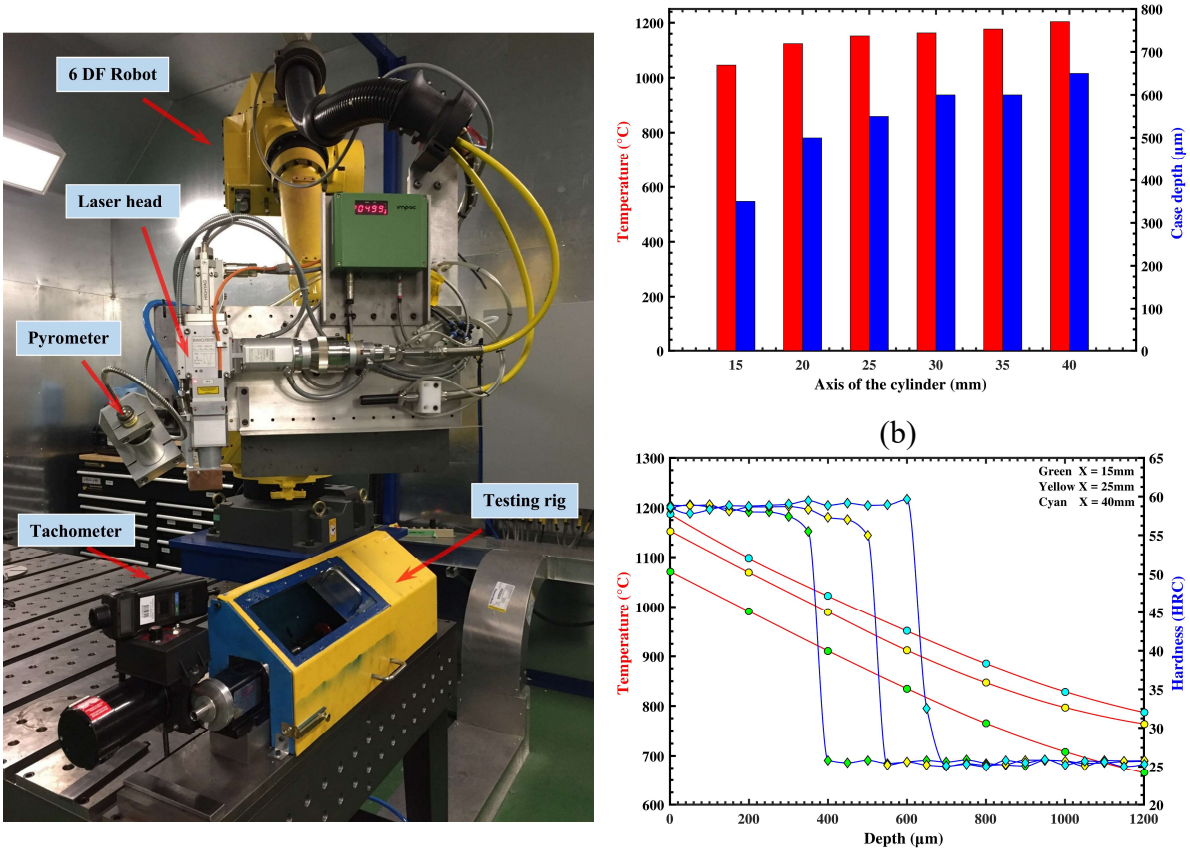

(a) (b) (c)

Figure 5-5: (a) Experimental setup. For fixed parameters – P=2000W, SS=4.5mm/s, Ω=4500RPM and D=16mm: (b) Temperature and Case depth versus Axis of the cylinder, (c) Temperature and Hardness versus depth

Equation 5-6 presents the expression of the variation of the laser power according to the initial power of laser emission, the position corresponding to the desired depth of

transformation X_{15}, the position of the focal spot x, and the slope of the interpolation line of the power curve.

$$P(x) = P_i - \Gamma(x - X_{15}) \quad (6)$$

Table 5-3 shows the test grid with the output responses for uniform surface temperature and regular case depth along the longitudinal axis of the cylinder. Fig. 5-6a shows the value of the maximum temperature reached at the surface of the cylinder for three configurations of the laser parameters of Table 5-3. This uniform temperature was achieved by a reduction in the amount of laser energy from the point X_{15} to the point X_{40}.

Table 5-3: L_{16} matrix and results of numerical simulations

Tests	**Factors**				**Responses**		
	Pi (W)	SS (mm/s)	Ω (RPM)	D (mm)	Γ (W/mm)	Ts (°C)	Cd (µm)
1	2300	3	6000	16	16.3	1246.1	800
2	2300	4	5000	18	17.9	1200.3	650
3	2300	5	4000	20	19.5	1154.6	550
4	2300	6	3000	22	21.1	1108.8	400
5	2100	3	5000	20	24.4	1140.8	550
6	2100	4	6000	22	26.0	1095.1	500
7	2100	5	3000	16	11.4	1153.7	500
8	2100	6	4000	18	13.0	1108.0	400
9	1900	3	4000	22	28.4	1061.7	350
10	1900	4	3000	20	22.0	1068.1	350
11	1900	5	6000	18	10.0	1074.6	400
12	1900	6	5000	16	9.0	1081.0	350
13	1700	3	3000	18	20.4	1060.8	300
14	1700	4	4000	16	13.9	1067.3	300
15	1700	5	5000	22	23.6	969.30	150
16	1700	6	6000	20	17.1	975.80	150

Fig. 5-6b shows the value of the uniform case depth, obtained along the axis of the cylinder after a control of the emission of the laser power. It was noted that the slope of the control curve of the laser power is influenced mainly by the diameter of the cylinder with a contribution percentage of about 65%, and by the scanning speed with a percentage of a contribution of 25%. The rotation speed, and the initial laser power of emission, have a contribution to the variation of Γ of about 10%.

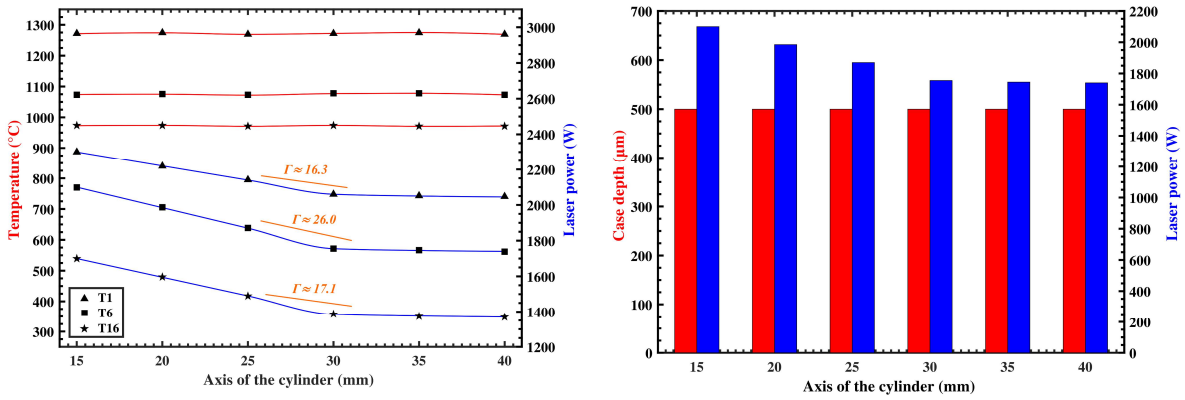

(a) (b)

Figure 5-6: (a) Temperature and Laser power versus Axis of the cylinder for T_1, T_6 and T_{16}, (b) Case depth and Laser power versus Axis of the cylinder for T_6

5.7.2 Predictor based in Artificial Neural Networks

To predict model output responses (Γ, Ts and Cd) according to the laser heat treatment parameters (P, SS, Ω and D), we used the predictive power of neural networks with a three-layer architecture (an input layer, a hidden layer and an output layer). The number of neurons in the input layer is equal to the number of parameters (four) and the number of neurons in the output layer is equal to the number of output response (three). The number of neurons needed in the hidden layer was defined by a calculation and comparison of the error. Fig. 5-7a shows the architecture of the selected neural network (4-7-3) because it allowed us to obtain a better quality of prediction with a value of R^2 of the order of 0.95, which is a value close to the exact solution evaluated at one [28]. Fig. 5-7b shows the summary flowchart of the Levenberg-Marquardt backpropagation algorithm used

in network learning. This algorithm has the distinction of automatically stopping learning when the average squared error stops improving [28, 29].

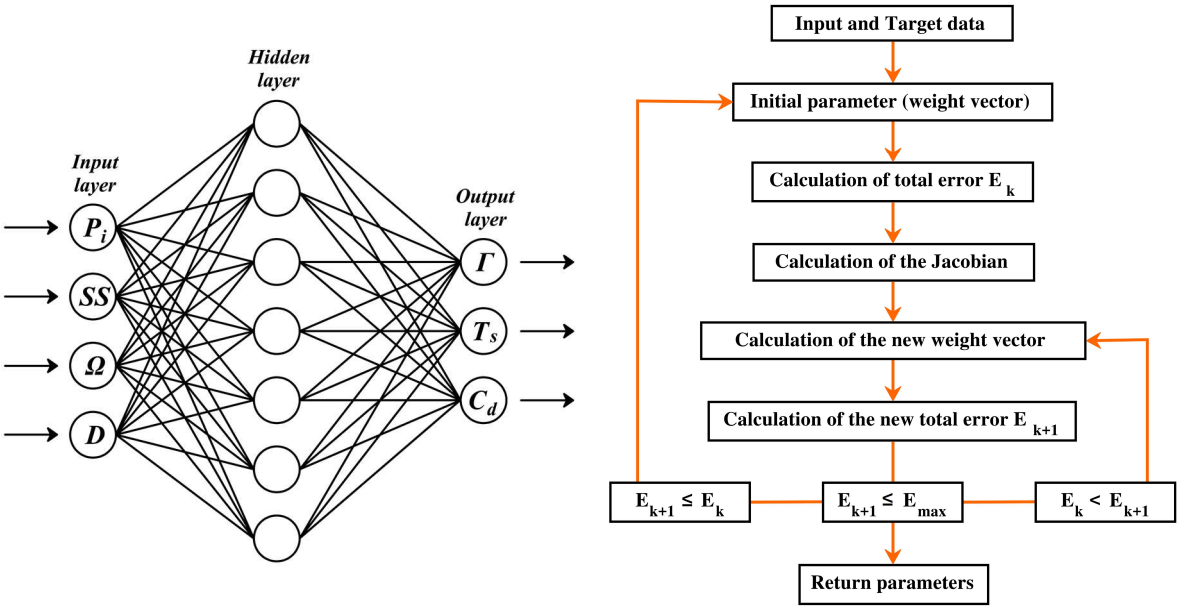

(a) (b)

Figure 5-7: (a) ANN model architecture, (b) Flowchart of training process of Levenberg Marquardt backpropagation

Equation 7 shows the Hyperbolic Tangent Sigmoid activation function applied to the output of each artificial neuron of the hidden layer. Equation 8 presents the Purelin activation function applied to the output of each artificial neuron of the output layer.

$$f_{tansig}(n) = e^{n} - e^{-n} / e^{n} + e^{-n} \quad (7)$$

$$f_{purelin}(n) = n \quad (8)$$

The L_{16} matrix data in Table 5-3 were randomly divided into three sets. To ensure that the data be used randomly, nntool the tool of Matlab MathWorks was used to oversee the division of these three groups by checking the error of the validation set during the training process [30]. It is important that the number of iterations for the error in the test set

to reach a minimum must be significantly close to the iteration number of the validation set error for an accurate distribution of data.

The function that divides data by index in nntool, and that was exploited in this study is the function dividerand [31]. A first set of 80% of the data was used for training, a second set of 10% of the data was used to measure network development (validation) and a third set of 10% of the data was used to test the network.

The data that was used in the formation of the network has made it possible to determine the weight matrix and the bias vectors of the hidden and output layers. And the data used for testing and validation confirmed a good formation of the network on the basis of the weight matrix and bias vectors calculated [32].

Figs. 5-8a, 5-8b and 5-8c show the measured and predicted values, for the slope of the interpolation line, for the maximum temperature reached at the surface, and for the value of the case depth, according to the laser heat treatment parameters of tests 1 to 16 of the L_{16} matrix of the experimental planning in Table 5-3.

These curves indicate good prediction quality of neural networks with a Levenberg Marquardt backpropagation scheme and a 4-7-3 neural network architecture. The value of R^2, which informs the prediction quality of the network, shows an index of 0.95 for the slope of the power curve, the surface temperature and the case depth.

Fig. 5-8d shows the progression of the network performance according to the number of iterations. It is observed that the learning of the network continued for about 600 iterations, and that the value of MSE and its corresponding curve does not indicate any problem with learning. Comparison of experimental results and prediction results shows that neural networks offer better prediction results with an average error for the slope value Γ of about 1.3-W/mm, an average error for the value of the maximum surface temperature of about 25°C and an average error for the value of the case depth of about 17.5-µm.

This precision in the prediction of output responses informs us of the existence of a linear relationship between the input parameters of the model and its output responses, including servo-control in the laser power.

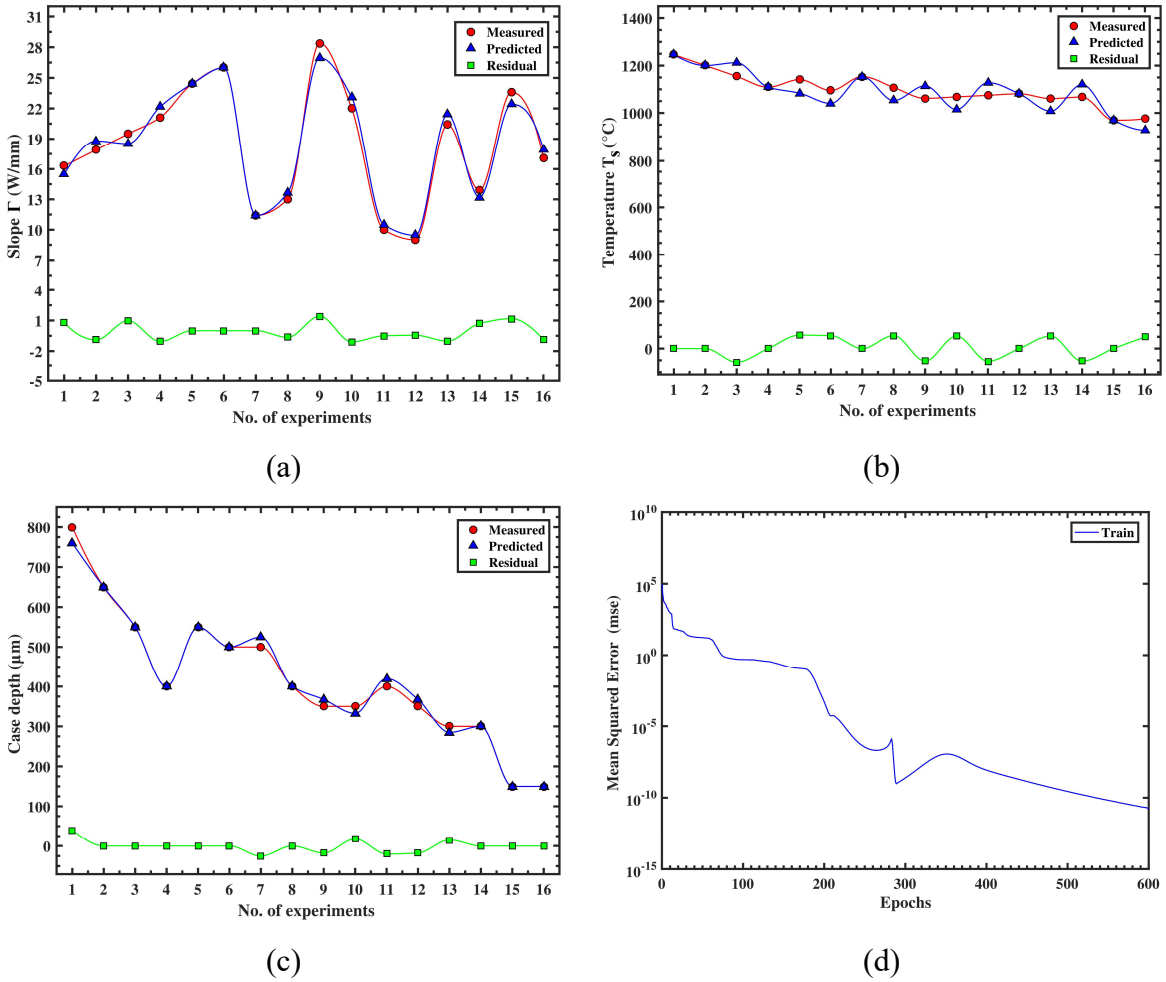

Figure 5-8: (a) Measured versus predicted Γ, (b) Measured versus predicted Ts, (c) Measured versus predicted Cd, (d) Mean squared error versus epochs

5.8 CONCLUSION

In this study, the temperature distribution in a laser heat-treated cylinder was evaluated by a numerical and experimental approach. The major findings are summarized below:

- The numerical model developed using the numerical finite element method and experimental tests, with the thermal properties of steel AISI 4340, allowed us to highlight the influence of the fixed parameters (non-variable) of the laser heat treatment, on the distribution of temperature and case depth in cylindrical workpiece.

- Through rigorous experience planning and analysis of the variation of laser power during heat treatment, it was possible to homogenize the distribution of the maximum temperature reached on the surface and thus regulate the case depth along the longitudinal axis of the cylinder.

- Analysis of laser heat treatment parameters, which led to a homogeneous case depth, allows to formulate an equation of control of the laser power according to the slope of the interpolation line, the initial power of emission and the position of course of the laser beam.

- In the range of variation of the factors in Table 5-2, a neural network architecture (4-7-3) with Levenberg-Marquardt-Backpropagation scheme was proposed for predicting output responses giving consistent case depth based on laser heat treatment parameters, with a total average error of less than 5%.

It would be interesting to complete this study using other types of materials, with other diameters of the focal spot, as well as other cylinder diameters including control in the rotational speed of the cylinder and in the scanning speed of the laser beam. We believe that this type of numerical and experimental approach is the most appropriate way to develop case depth control models for simple cylindrical geometries.

References

1. J. C. Ion, Laser transformation hardening, Surface Engineering, 2002, vol. 18, no. 1, pp. 14-31.
2. Abdullahi K. Gujba, Mamoun Medraj, Laser peening process and its impact on materials properties in comparison with shot peening and ultrasonic impact peening, Materials, 2014, vol. 7, no. 12, pp. 7925-7974.
3. E. Kennedy, G. Byrne, D.N. Collins, A review of the use of high power diode lasers in surface hardening. Journal of Materials Processing Technology, J. Mater. Process. Technol., 2004, vol. 155, pp. 1855-1860.
4. G. Ricciardi, M. Cantello, G.F. Micheletti, Technological applications of the laser beam in heat treatments. CIRP Annals-Manufacturing Technology, 1982, vol. 31, no. 1, pp. 125-130.
5. Kannatey-Asibu Elijah Jr., Principles of Laser Materials Processing, 4 John Wiley & Sons, 2009.
6. J. Mazumder, Laser heat treatment: The state of the art, Journal of Metals, 1983, vol. 35, no 5, p. 18-26.
7. Jaroslav Mackerle, Finite element analysis and simulation of quenching and other heat treatment processes A bibliography (1976–2001), Computational Materials Science, 2003, vol. 27, no. 3, pp. 313-332.
8. Barka, N., El Ouafi, A., Effects of Laser Hardening Process Parameters on Case Depth of 4340 Steel Cylindrical Specimen-A Statistical Analysis, Journal of Surface Engineered Materials and Advanced Technology, 2015, vol. 5, no. 03, pp. 124.
9. Fakir, R., Barka, N., Brousseau, J., Case study of laser hardening process applied to 4340 steel cylindrical specimens using simulation and experimental validation, Case Studies in Thermal Engineering, 2018, vol. 11, pp. 15-25.
10. Jerniti, A.G., El Ouafi, A., Barka, N., A Predictive Modeling Based on Regression and Artificial Neural Network Analysis of Laser Transformation Hardening for Cylindrical Steel Workpieces, Journal of Surface Engineered Materials and Advanced Technology, 2016, vol. 6, no. 04, pp. 149-163.

11. Hadhri, M., El Ouafi, A., Barka, N., Prediction of the hardness profile of an AISI 4340 steel cylinder heat-treated by laser-3D and artificial neural networks modelling and experimental validation, Journal of Mechanical Science and Technology, 2017, vol. 31, no. 2, pp. 615-623.

12. Xiaohu Deng, Dongying Ju, Modeling and Simulation of Quenching and Tempering Process in steels, Physics Procedia, 2013, vol. 50, pp. 368-374.

13. Metals Handbook, Howard E. Boyer and Timothy L. Gall, Eds., American Society for Metals, Materials Park, OH, 1985.

14. Engineering Properties of Steels, Philip D. Harvey, editor, American Society for Metals, Metals Park, OH, 1982.

15. Physics for Scientists and Engineers with Modern Physics, 2nd ed., Douglas C. Giancoli, Prentice Hall Publishers, Englewood Cliffs, NJ, 1989.

16. Multiphysics, Comsol. Version 4.2, COMSOL. Inc., http://www.comsol.com, 2011.

17. H.S. Carslaw, J.C. Jaeger, Conduction of Heat in Solids, 2nd ed., Clarendon Press, Oxford, 1959, pp. 1907-1979.

18. Kannatey-Asibu Jr, Elijah. Principles of laser materials processing. Vol. 4. John Wiley & Sons, 2009.

19. Ion, John. Laser processing of engineering materials: principles, procedure and industrial application. Elsevier, 2005.

20. Teen, W.M., C.H.G Courtney, Surface heat treatment of EnS 8 steel using a 2 kW continuous-wave C021aser, Metals Technology, 1979, vol. 6, no. 1, pp. 456-462.

21. Bradley, J. R., A simplified correlation between laser processing parameters and case depth in steels, Journal of Physics D: Applied Physics, 1988, vol. 21, no. 5, pp. 834.

22. Dausinger, F., & Shen, J., Energy coupling efficiency in laser surface treatment, ISIJ international, 1993, vol. 33, no. 9, pp. 925-933.

23. Pantsar, H., Kujanpää, V., Diode laser beam absorption in laser transformation hardening of low alloy steel. Journal of Laser Applications, 2004, vol. 16, no. 3, pp. 147-153.

24. Tobar, M. J., Álvarez, C., Amado, J. M., Ramil, A., Saavedra, E., Yáñez, A., Laser transformation hardening of a tool steel: Simulation-based parameter optimization and experimental results, Surface and Coatings Technology, 2006, vol. 200, no. 22-23, pp. 6362-6367.

25. Klaus-J.ürgen Bathe, Edward L. Wilson, Numerical Methods in Finite Element Analysis, 197 Prentice-Hall, Englewood Cliffs, NJ, 1976.

26. Fakir, R., Barka, N. & Brousseau, J., Mechanical Properties Analysis of 4340 Steel Specimen Heat Treated in Oven and Quenching in Three Different Fluids, Metals and Materials International, 2018.

27. Roy, Ranjit K. A primer on the Taguchi method. Society of Manufacturing Engineers, 2010.

28. Hagan, Martin T., Demuth, Howard B., Beale, Mark H., et al. Neural network design. Boston: Pws Pub., 1996.

29. Marquardt, D. W., An algorithm for least-squares estimation of nonlinear parameters, Journal of the society for Industrial and Applied Mathematics, 1963, vol. 11, no. 2, pp. 431-441.

30. MathWorks, Inc. (2018). Matlab: the language of technical computing, Divide Data for Optimal Neural Network Training.

31. MathWorks, Inc. (2018). Matlab: the language of technical computing, Divide targets into three sets using random indices, Introduced in R2008a.

32. MathWorks, Inc. (2018). Matlab: the language of technical computing, Analyze Shallow Neural Network Performance after Training.

CHAPITRE 6

ANALYSE DU COMPORTEMENT MECANIQUE D'ÉCHANTILLONS CYLINDRIQUES EN ACIER AISI 4340 TRAITÉS THERMIQUEMENT AU LASER FIBRE

Fakir, R.[1], Barka, N.[1], Brousseau, J.[1] & Caron-Guillemette, G.[2]
(1) Université du Québec à Rimouski, Rimouski, Québec, Canada, G5L 3A1
(2) Bombardier Transport Canada Inc., La Pocatière, Québec, Canada

Cet article a été soumis dans le Journal of Manufacturing Processes.
Manuscript Number: SMEJMP_2018_1401

Mots-clés : Durcissement au laser, essai de traction, essai de fatigue, ANOVA, RSM, ANN

6.1 RÉSUMÉ EN FRANÇAIS DU SIXIÈME ARTICLE

Cet article décrit une méthode d'analyse et d'amélioration du comportement mécanique d'une pièce cylindrique en acier AISI 4340, traitée thermiquement avec une source laser fibre 3.0-kW. La recherche et l'expertise acquise durant ces dernières années ont montré que l'amélioration des propriétés mécaniques de l'acier AISI 4340 par un durcissement au laser permet de réduire considérablement les dimensions nominales et optimise ainsi le poids final du produit. La compréhension de l'impact qu'un traitement thermique au laser peut avoir sur les propriétés mécaniques et la résistance à la fatigue peut permettre d'optimiser considérablement les dimensions de conception. Cette recherche investigue l'effet et le contrôle des paramètres de traitement thermique au laser afin d'optimiser le comportement mécanique d'un échantillon standard cylindrique en acier AISI 4340, qui a un diamètre de la partie calibrée de 9.00-mm. Le contrôle de la profondeur durcie et son uniformisation ont été guidés par la modélisation expérimentale et numérique. Essais de traction, essais de fatigue (boucles d'hystérésis), microdureté, microscopie optique, et microscopie électronique à balayage ont été utilisés pour évaluer chaque condition du plan expérimental. Les résultats montrent que le traitement thermique au laser

augmente la limite d'endurance en fatigue de plus de 20% par rapport aux échantillons non durcis. De plus, il est montré avec un modèle de prédiction neuronale, et une analyse de variance rigoureuse, que les valeurs numériques des propriétés mécaniques sont en accord direct avec les paramètres d'entrée de durcissement au laser.

Ce sixième article, intitulé « *Analysis of the Mechanical Behavior of AISI 4340 Steel Cylindrical Specimens Heat Treated with Fiber Laser* », fut corédigé par moi-même ainsi que par le professeur Noureddine Barka, et le professeur Jean Brousseau. Il fut accepté pour vérification en 2018 dans la revue *Journal of Manufacturing Processes*. En tant que premier auteur, ma contribution à ce travail fut l'essentiel de la recherche sur l'état de l'art, le développement de la méthode du modèle numérique, l'exécution des tests expérimentaux et la rédaction de l'article. Les professeurs Noureddine Barka et Jean Brousseau, et l'ingénieur Gabriel Caron-Guillemette, second, troisième, et quatrième auteurs, ont participé à définir le projet d'article et ils ont aidé à la recherche sur l'état de l'art, au développement de la méthode ainsi qu'à la révision de l'article.

6.2 TITRE DU SIXIÈME ARTICLE

Analysis of the Mechanical Behavior of AISI 4340 Steel Cylindrical Specimens Heat Treated with Fiber Laser.

6.3 ABSTRACT

This paper describes a method for analyzing and improving mechanical behavior of a cylindrical workpiece made of AISI 4340 steel, by its heat treatment with a 3kW fiber laser source. Research and expertise acquired in recent years have shown that improving the mechanical properties of AISI 4340 steel by heat treatment significantly reduces the design dimensions and thus optimizes the final weight of the product. Understanding the impact that a laser heat treatment can have on mechanical properties and the fatigue life can lead to significantly optimizing the design dimensions. This research investigates the effect and control of laser heat treatment parameters to optimize the mechanical behavior of an AISI

4340 steel cylindrical standard-specimen, which has a diameter of the calibrated part of 9.00-mm. The control of the case depth and its uniformization were guided by experimental and numerical modeling. Tensile tests, fatigue tests (hysteresis loops), microhardness, optical microscopy, and scanning electron microscopy measurements were used to evaluate each condition of the experimental design. Results indicate that laser heat treatment increases fatigue endurance by more than 20% compared to non-hardened samples. Moreover, it is shown with a model of neural prediction, and a rigorous analysis of variance, that the numerical values of the mechanical properties are in direct agreement with the laser hardening input parameters.

6.4 NOMENCLATURE

χ	*Absorption coefficient of the material,*
f_P	*Activation function Purelin,*
f_T	*Activation function Tansig,*
θ_∞	*Ambient air temperature, °C*
C_d	*Case depth at the calibrated zone, µm*
C_n	*Case depth at the notched zone, µm*
ρ	*Density, $kg.m^{-3}$*
D	*Diameter of the cylinder, mm*
El	*Elongation at break, $mm.mm^{-1}$*
ε	*Emissivity of material surface,*
S_e	*Endurance limit, MPa*
G	*Gaussian distribution of the laser beam,*
h	*Heat transfer coefficient, $W.m^{-2}.K^{-1}$*
Ac_1	*Heating temperature at point A_1, °C*
Ac_3	*Heating temperature at point A_3, °C*
v	*Kinematic viscosity, $m^2.s^{-1}$*
P	*Laser power, W*
Sy	*Offset yield strength, MPa*

$\boldsymbol{T}$	*Prediction polynomial,*
$\boldsymbol{R}$	*Radius of the cylinder, mm*
$\boldsymbol{s_0}$	*Radius of the laser spot, mm*
$\boldsymbol{\Omega}$	*Rotation speed of the cylinder, RPM*
$\boldsymbol{U_x}$	*Scanning speed, $mm.s^{-1}$*
$\boldsymbol{\gamma}$	*Scope of the laser beam following X, mm*
$\boldsymbol{\Gamma}$	*Slope of the curve, W/s*
$\boldsymbol{f}$	*Solicitation frequency, Hz*
$\boldsymbol{Cp}$	*Specific heat, $J.kg^{-1}.K^{-1}$*
$\boldsymbol{\sigma}$	*Stefan-Boltzmann constant, $W.m^{-2}.K^{-4}$*
$\boldsymbol{\dot{\varepsilon}}$	*Strain rate, min^{-1}*
$\boldsymbol{\sigma_a}$	*Stress amplitude, MPa*
$\boldsymbol{\theta_d}$	*Surface temperature at the calibrated zone, °C*
$\boldsymbol{\theta_n}$	*Surface temperature at the notched zone, °C*
$\boldsymbol{\theta}$	*Temperature of the material, °C*
$\boldsymbol{\sigma_m}$	*The average value of the stress, MPa*
$\boldsymbol{\sigma_{max}}$	*The maximum value of the stress, MPa*
$\boldsymbol{\sigma_{min}}$	*The minimum value of the stress, MPa*
$\boldsymbol{\lambda}$	*Thermal conductivity of air, $kg.m^{-3}$*
$\boldsymbol{k}$	*Thermal conductivity of steel, $W.m^{-1}.K^{-1}$*
$\boldsymbol{\alpha}$	*Thermal diffusivity, $m2.s^{-1}$*
$\boldsymbol{Su}$	*Ultimate tensile strength, MPa*

6.5 INTRODUCTION

The civil and military transport industry often use the laser for surface hardening, welding, assembling, cutting of parts and materials, and also for other advanced applications [1,2]. Among its advantages one can mention its high precision mobility in the workspace with the use of a robot arm, saving time with an automated production line, and its ability to direct the laser flow in an optical fiber allowing multiple treatment stations for

a single laser source [3]. For a perfect control of the process, it is essential to control all the variables of the process such as the laser power, temporal mode, spatial mode, wavelength, raw beam diameter, polarization, depth of focus, projected spot size, focal position, composition and density of the material, absorptivity, thermal conductivity, specific heat capacity, latent heats, thermal expansion coefficient, and the initial temperature of the material [4]. As part of laser hardening, we concentrate a laser energy of 7-W/mm2 at about 100-W/mm^2 for a time of interaction between 0.1-s and 10-s to bring the metal temperature up to a certain austenitization temperature and without reaching the melting temperature of the substrate. For AISI 4340 steel, the austenitization temperature is usually between 900°C and 1350°C, and the melting temperature is about 1425°C [5]. At the scale of the microstructure and at a temperature of austenitization, AISI 4340 steel undergoes eutectoïde transformation from solid cubic centered phase to another cubic solid phase with centered faces of notable mechanical characteristic (hardness, ductility, yield strength, etc.). Like the heating cycle, the cooling cycle plays a very important role in the transformation of the microstructure and is carried out in a quenching liquid (oil bath, molten lead, etc.) or using a quenching gas (nitrogen, air, etc.). If in the composition of the steel one has a enough carbon content, with the presence of alloying elements in small quantities such as chromium, nickel, and molybdenum, and if the cooling is very fast the microstructure that will result is called martensite [6].

As part of the laser heat treatment this transformation of the microstructure usually occurs at the surface level (shallow depth) and is characterized by the hardened depth. H.R. Shercliff et al, presented in 1990 a prediction model of case depth for laser hardening of steel surfaces. Based on an analysis of the dimensional relationships between process variables, they were able to formulate the prediction equations of the surface temperature of the material according to the shape of the laser beam, the laser power, the spot width and length, and the beam scanning speed. This model of approximate heat flux has been validated with a wide range of experimental data and it compares favorably with previous work in the literature that requires a more elaborate numerical calculation [7]. In a similar approach D.W. Wu et al, presented in 1990 a study to explain using a statistical analysis,

the effect of hardness on the formation of residual stresses as reported on the previous experimental studies. In this study, they experimentally examined by the analysis of mechanical and thermal stresses the effect of hardness on several factors related to the machining process, and the roles of these factors in the formation of residual stresses. The results of this study showed that the residual stress profile is related to the shear angle and that the modification of the residual stress profile is mainly due to changing the shearing angle in the chip-forming process, and that the average stress rate in the deformation zone decreases as the hardness increases, which produces a residual stress more resistant to the tensile test [8]. In a purely experimental approach R.K. Shiue et al. presented in 1991 a hardening study of a rectangular piece in AISI 4340 steel. In this study they used a CO_2 laser source with a fixed laser power of 1.8-kW, a scanning speed of the laser beam between 5 and 10-mm/s, to analyze the influence of the scanning speed on the hardness profile and on the microstructure of the hardened area. It has been observed that a fast scanning speed causes the smaller sizes of martensite, that lower scan rates cause self-tempered martensite and that the surface hardness is higher for specimens hardened with a high scanning speed [9]. In a study of cylindrical geometry, L. Orazi et al. presented in 2014 an analytical approach to laser surface hardening of large steel cylindrical components in AISI-1040 and with a diameter of 20-mm and 30-mm. The approach made it possible to obtain a very hard layer, of martensitic composition, with a uniform depth of up to 1.95-mm across the entire depth of the cylindrical workpiece. The main results of this study show that the laser heat treatment process represents an interesting alternative to induction quenching in the case of hardening of the cylindrical workpiece [10]. Using experimental data R. Fakir et al. presented in 2018 a numerical study to predict the hardened depth of a cylindrical workpiece in AISI 4340 steel thermally treated with a 3-kW fiber laser. Using the numerical finite difference method and experimental tests, they have been able to evaluate the thermal flows entering and leaving the cylindrical workpiece, to show the influence of laser power, scanning speed, and rotational speed on the case depth of the microstructure transformation [11].

To evaluate the impact of laser hardening on mechanical properties, we can use the tensile test which is a physical experiment allowing in a uniaxial stress state to characterize materials by reproducing an easy and controllable solicitation. This test consists of placing a standard-sized test piece between the jaws of a tensile test machine, whose upper jaw is fixed, and the displacement of the lower jaw is ensured by a hydraulic piston that pulls the specimen with a certain loading speed down to its break. The tensile test determines the elastic behavior of a material, allowing to measure its degree of tensile strength and provide several important values such as the Young's modulus, Poisson's ratio, yield strength, ultimate tensile strength and elongation at break [12]. To analyze the impact of laser heat treatment on the mechanical properties of AISI 4340 steel, we can use a method of analysis of experimental data (numerical, statistical, probabilistic and or based on artificial intelligence) to validate and predict future trends of material behavior. As we have seen, several approaches have been proposed by different research teams to predict the case depth and mechanical behavior of AISI 4340 steel after laser heat treatment, however we did not find a detailed study of the impact of laser hardening parameters on the mechanical behavior in static and fatigue for a specimen standardized in AISI 4340 steel hardened by fiber laser.

In this paper, the methodology proposed to analyze the mechanical behavior is built progressively by (i) the development according to the laser parameters a numerical model of prediction of the profile of temperature and the case depth, (ii) the development of a laser power adjustment function for a uniform depth of transformation along the longitudinal axis of the cylinder, (iii) presentation of the experimental setup, the experimental design and the results of the static and fatigue mechanical tests (hysteresis loops), (iv) an analysis of variance, an RSM representation of the results of the mechanical tests and a proposition of a predictor based on the predictive power of neural networks, and (v) analysis discussion of numerical results and visualization of the microstructure and the fracture surface. The feasibility and effectiveness of the proposed method leads to a precise and reliable model able to control the variation of mechanical properties according to the laser heat treatment parameters of the cylindrical workpiece.

6.6 THERMAL MODEL

6.6.1 Thermal balance

The understanding and accuracy in the development of the thermal balance in the case of laser heat treatment is very important for a precise evaluation of the heat flows transmitted by conduction in the workpiece and lost by convection and radiation in the ambient air. These heat flows (entering and coming out) that are related to the temperature and the thermal properties of the workpiece, are variable according to the laser heat treatment parameters. The difficulty in estimating these heat flows according to laser heat treatment parameters is mainly due to the variation according to the temperature of the thermal conductivity, the specific heat, the coefficient of heat transfer by convection and the absorption coefficient of the material.

Figure 6-1a presents the scheme of the experimental device which shows the start and stop position of the heat treatment of a cylindrical workpiece, in continuous rotation using a rotary test bench, the laser source moving in a path parallel to the axis of the cylinder and a thermal camera that was used to measure the value of the surface temperature. The proposed thermal model is based on the prediction of the temperature distribution by means of the numerical resolution of the conduction heat transfer equation for a system of revolution with a variable temperature gradient and time dependent. Equation 1 presents the expression of thermal conduction, for a temperature differential defined by the boundary conditions and, with the thermal conductivity and the specific heat which are temperature dependent [13,14].

$$\partial^2\theta/\partial x^2 + \partial\theta/r\,\partial r + \partial^2\theta/\partial r^2 = \left(\rho . C_p(\theta)/k(\theta)\right) . \partial\theta/\partial t \quad (1)$$

Equation 2 presents the expression of the amount of the power density of the laser beam G (x, y) which has an amplitude of evolution of the transversal profile in correlation with the spatial propagation of a Gaussian function [4,5]. With s_0 the radius of the focal spot of the laser beam and (x_0, y_0) the coordinates of the center of the laser beam whose

maximum power is P. Figure 6-1b shows the distribution in the z-axis direction of the laser beam for a diameter of 0.50-mm.

$$G(x,y) = P.exp\left(-{(x-x_0)^2 + (y-y_0)^2}/{s_0}\right) \quad (2)$$

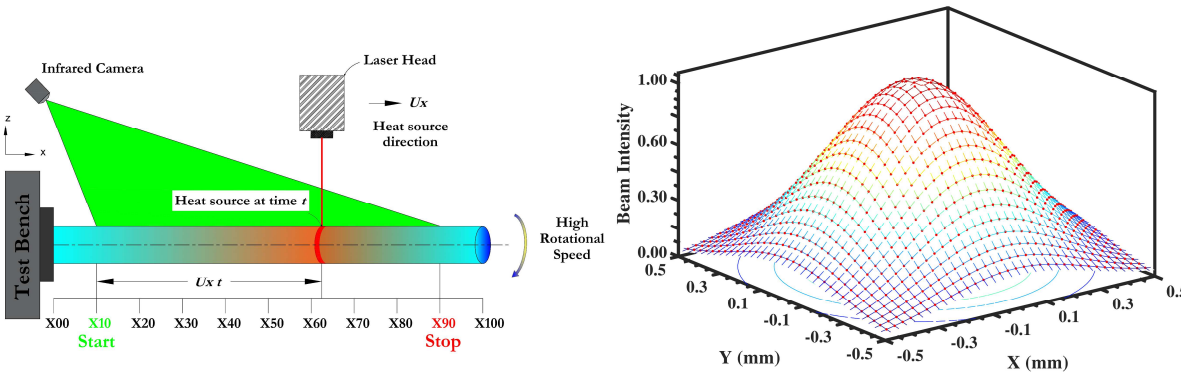

(a) (b)

Figure 6-1: (a) Schematic diagram of the experimental set-up,
(b) Gaussian distribution of the laser beam

For the resolution of the equation of thermal conduction (Eq. 1), it has been assumed that the initial temperature of the cylinder is uniform and equal to 25°C and at the level of the boundary conditions the laser beam will have as starting position X_{10} and as end of course position X_{90}. The rotation speed of the cylinder and the diameter of the focal spot were respectively fixed at 3000-RPM and 0.50-mm (non-variable factors). Equation 3 presents the expression of the position of the laser beam according to the time and the scanning speed U_x.

$$p(t) = U_x.t \quad (3)$$

Equation 4 and 5 present the boundary conditions for a laser beam of length γ and width d, which moves at a constant speed along the outer surface of the cylinder. The first condition (Eq. 4) corresponds to the surface of the cylinder which is outside the range of the laser beam and the second condition (Eq. 5) corresponds to the surface of the cylinder which is under the range of the laser beam.

$$x < p(t) \quad \text{or} \quad x > p(t) + \gamma \tag{4}$$

$$p(t) \leq x \leq p(t) + \gamma \tag{5}$$

Equation 6 presents the expression of the boundary conditions outside the zone irradiated by the laser beam. In this zone outside the range of the laser beam, only the convective losses represented by the first term and the radiation losses represented by the second term of equation 6 will be considered at the level of the boundary conditions. Equation 7 presents the expression of the boundary conditions within the zone irradiated by the laser beam. In this zone under the range of the laser beam we will have at the level of the boundary conditions the first term that corresponds to the laser energy transmitted by condition to the workpiece, the second term which corresponds to convective thermal losses and the third term which corresponds to radiation thermal losses. The absorption coefficient of the metal is represented by the symbol χ in the first term of equation 7.

$$k(\theta).{\partial\theta}/{\partial r}\Big|_{r=R} = h.(\theta - \theta_\infty) + \varepsilon.\sigma.(\theta^4 - {\theta_\infty}^4) \tag{6}$$

$$k(\theta).{\partial\theta}/{\partial r}\Big|_{r=R} = {G.\chi}/{2\pi.r.\gamma} - \left(h.(\theta - \theta_\infty) + \varepsilon.\sigma.\left(\theta^4 - {\theta_\infty}^4\right)\right) \tag{7}$$

6.6.2 Thermal properties and heat transfer coefficient

The knowledge of the precise variation of the thermal properties of AISI 4340 steel makes it possible to model efficiently the thermal transfers at the level of the cylindrical workpiece, for a control of the temperature profile that allows to predict the case depth. Figure 6-2 shows the variation of thermal properties of AISI 4340 steel according to the temperature [15-17].

The thermal conductivity, which quantifies the ability of the material to conduct heat, is inversely proportional to the heating temperature and it reaches a plateau for temperatures above the temperature Ac1. The specific heat that measures the material's ability to absorb heat, is proportional to the temperature between the interval 0-900°C,

inversely proportional to the temperature between the interval 900-1000°C with a peak in the eutectoid transformation region of AISI 4340 steel and not temperature dependent for temperatures above 1000°C. At a constant pressure, the specific heat is related to the constant volume heat capacity by the molar volume, the volume expansion coefficient and the coefficient of isothermal compressibility. The magnetic permeability, which makes it possible to characterize the faculty of the material to modify lines of magnetic flux (magnetic field) is inversely proportional to the heating temperature of AISI 4340 steel and reaches a plateau at a temperature close to the temperature Ac_1. Electrical conductivity that characterizes the ability of the material to let electrical charges move freely in order to allow the passage of an electric current, is inversely proportional to the heating temperature of AISI 4340 steel and it reaches a plateau for a temperature close to the temperature of 1000°C. Magnetic permeability and electrical conductivity are physical quantities that are essential data for numerical simulation of induction heat treatment of AISI 4340. Moreover, for laser heat treatment, the thermal conductivity, the specific heat, the absorption coefficient of the material and the coefficient of heat transfer by convection are the data necessary for the resolution of the differential equations of the heat balance.

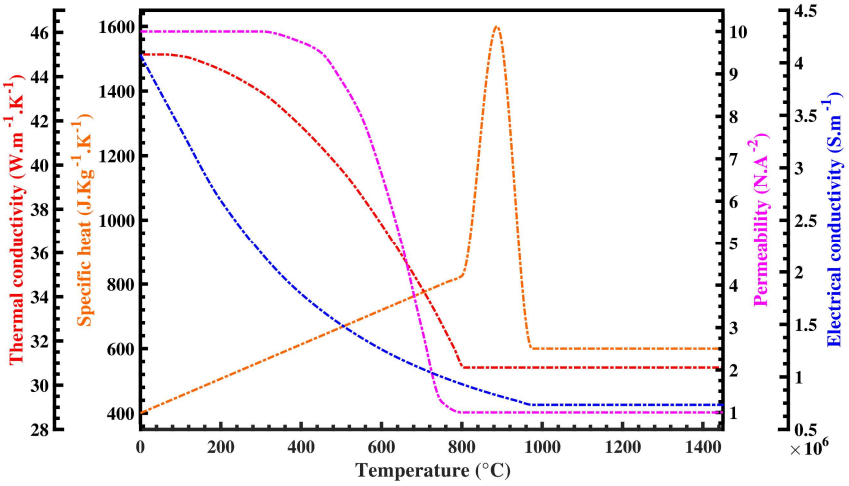

Figure 6-2: Thermal properties of AISI 4340 steel versus temperature

The rotation of the cylinder generally contributes to increasing the thermal losses by forced convection. This forced convection occurs between the outer surface of the cylinder

and the environment fluid when they are not at the same temperature. The coefficient that governs the heat transfer by convection near an exchange surface is the coefficient of thermal convection h. Equation 8 presents its expression according to the rotational speed of the cylinder, the diameter of the cylinder, and the thermo-physical properties of the air. This equation is valid only for a Reynolds number less than 4.3×10^5 and a Prandtl number between the interval 0.7-670 [18].

$$h = 0.133\left(\lambda/_D \,.\, (\nu/_\alpha)^{1/3}\right)\left(\Omega.D^2/_\nu\right)^{2/3} \quad (8)$$

6.6.3 Numerical simulations

The simulations were performed with the 4.2a version of COMSOL Multiphysics software. This multiplatform numerical simulation software can simulate many physics and engineering applications, using the finite element method. It also allows the user to define his own systems of partial differential equations, ordinary derivatives and algebro-differentials. The cylindrical workpiece considered in our simulations is a cylinder with a diameter of 9.6 mm and a length of 100-mm.

The variation of the thermal properties of the material according to the temperature was defined in the simulation using interpolation function which faithfully reproduces the thermal properties of Figure 6-2. The heat flow transmitted by conduction to the cylindrical workpiece by the laser beam was introduced into the numerical model to represent the heat source according to the equation 1 and 2. All the faces of the cylinder were considered in convective-forced heat exchange and in radiative exchange according to the equations 6 and 7 of boundary conditions. The average duration of the simulations is about 70-s and depends mainly on the scanning speed of the laser beam and the cooling time of the part.

The mesh used is triangular, regular and refined on the whole cylinder. Several sizes of meshes have been tested to ensure stability, consistency and convergence of the mesh [19]. The convergence of the mesh was carried out for the configuration of laser hardening which allows to provide a maximum case depth without melting of the surface of the part,

and for the configuration of laser hardening which allows to provide a minimum case depth. Figure 6-3a shows the value of the temperature at the surface and in the center of the cylinder according to the mesh density for both laser heat treatment configurations. The retained mesh density is about 1.5-million elements.

Experimental tests have shown that a 9.6-mm diameter cylinder made of AISI 4340 steel, and which is rotated relative to its axis with a rotation speed of 3000-RPM, can reach a maximum case depth of 1100-µm for a scanning speed of 3-mm/s and a laser power of 1300-W, and a minimum case depth of 350-µm for a scanning speed of 4-mm/s and a laser power of 1200-W. Figure 6-3b shows the variation of the absorption coefficient according to the laser heat treatment parameters [20-24]. This coefficient was validated using surface temperature measurement, by means of an infrared thermal camera, and microhardness measurements that were correlated with the results of the numerical simulations.

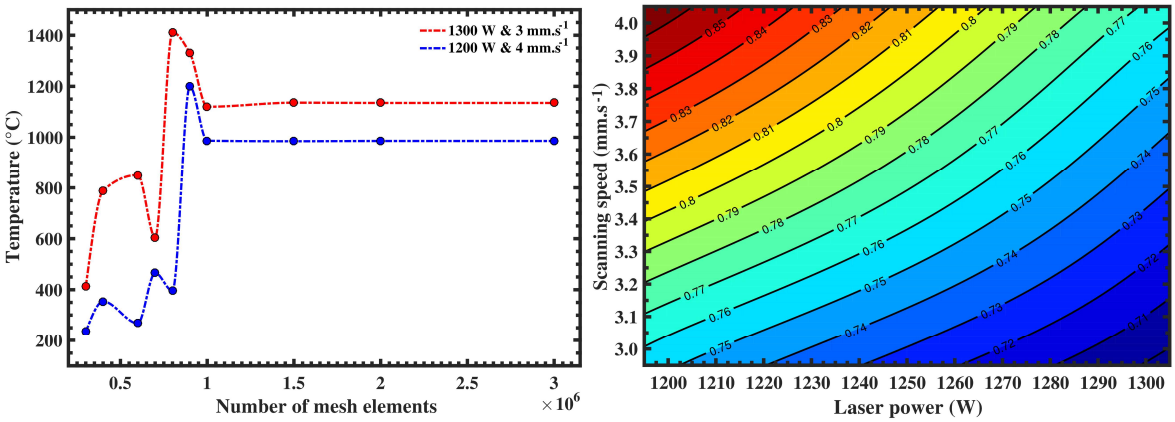

(a) (b)

Figure 6-3: (a) Temperature versus number of mesh elements, (b) Variation of χ according to the laser power and the scanning speed of laser beam

Table 6-1 presents the numerical values of the main variables and constants used in the numerical model of prediction of the temperature distribution in a steel cylinder AISI 4340, of 9.6-mm diameter, and heat treated by laser.

Table 6-1: Numerical values of variables and constants

Symbol	Expression	Value	Unit
ρ	Density of the material	7870	Kg/m^3
λ	Thermal conductivity of the air	0.0551 to 0.0653	W/m.K
D	Diameter of the cylinder	9.60	mm
Ω	Cylinder rotation speed	3000	RPM
ν	Kinematic viscosity	7.39×10^{-5} to 1.08×10^{-4}	m^2/s
α	Thermal diffusivity	9.67×10^{-5} to 1.55×10^{-4}	m^2/s
γ	Laser beam length	2.50	mm
ε	Emissivity of material surface	0.7	–
σ	Stefan-Boltzmann constant	5.67×10^{-8}	$W.m^{-2}.K^{-4}$
θ_∞	Ambient air temperature	20	°C
χ	Absorption coefficient	0.70 to 0.86	–

6.7 EXPERIMENTAL PROCEDURE

6.7.1 Experimental setup and preliminary tests

In our experiments, a robotic laser heat treatment cell was used which is mainly equipped with an industrial robot FANUC M710iC/70 comprising a manipulator, a controller and a system software (R-J3) to perform tasks described in the programming language KAREL or through TPP (Teach Pendant Programming).

The robot has six rotating joints, which are powered by brushless AC motors, for repeatability with a precision of about 0.07-mm and a maximum linear velocity of the order of 250-mm/s. A cooler LC71-01.A-2.5/6 and a fiber laser system (IPG YLS-3000-ST2) class 4 with a total power of 3-kW for a wavelength between 1070-nm and 1080-nm. The focal distance between the reference line and the surface of the part is 310-mm. The laser beam has a variable diameter between 0.33- to 0.52-mm for a fiber diameter of 200-µm, and between 1.00- to 1.53-mm for a 600-µm fiber diameter. By using the DC-Scanner

System for laser surface treatment applications (transformation hardening) and according to the focal lengths of the focusing mirror, it is possible to obtain scan amplitudes up to 30-mm.

We used a spot diameter of 0.50-mm, an amplitude of the DC-Scanner of 30% and a frequency of 140-Hz for a scan length of 2.5-mm. The rotary test bench used, is equipped with a clamping jaw to secure the test sample on the rotating bench. A FLIR A325sc infrared thermal imaging camera was used to continuously measure the temperature value at the outer surface of the specimens.

The initial temperature of the laboratory was set at 20°C for an ambient air control. The path of the laser beam was programmed so that it is in focus relative to the outer surface of the cylinder (along the moving distance of 80-mm) according to the experimental setup diagram of Figure 6-1a which shows the start and stop position of the laser heat treatment. The rotational speed of the cylinder is fixed, and the scanning speed of the laser beam and the laser power are controllable parameters from the TPP. Figure 6-4a shows a visualization of the experimental setup and Figure 6-4b shows the dimensions of the sample studied according to ASTM E8. An extra 0.3-mm allowance was added at the outer surface and will be removed after laser heat treatment for a smooth surface finish. A 0.5-mm radius notch is made at the center of the specimen (red zone) to introduce a stress concentration that will provide a controlled rupture zone in mechanical tests. Figure 6-4c shows the experimental curves of hardness measurements and the results of numerical prediction of the temperature, according to the depth of the workpiece and the measuring position in the main axis of the specimen (x-axis), for a laser power of 1300-W, a scanning speed of 3-mm/s and a rotation speed of 3000-RPM.

We noted that the case depth was greater at the x=70-mm position relative to the x=30-mm position and was even greater for the position x=50-mm because of the presence of the notch which induced a diameter smaller than that of the calibrated part. The curve of hardness has a first region of low hardness (Melting region) less than 0.3-mm deep, a

second region of high hardness (Hardened region) and a third region of initial hardness (Material bulk). This initial hardness of 35-HRC was obtained after austenitization in the oven, followed by a cooling in the quench oil and a tempering at a temperature of 500°C for a period of 30-min [25].

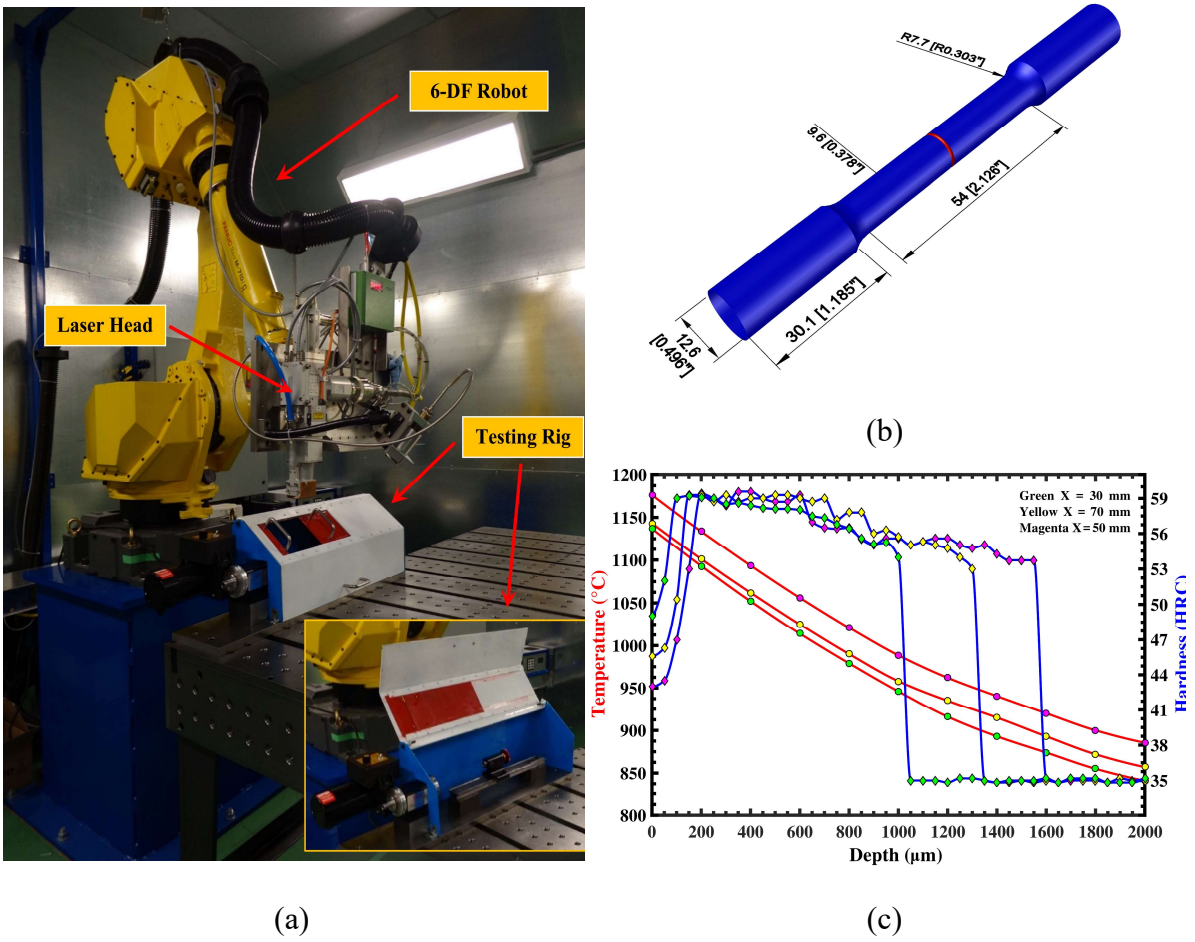

Figure 6-4: (a) Experimental setup, (b) 3D visualization of the specimen, unit Millimetre [Inch], (c) Temperature and Hardness versus depth

6.7.2 Homogenisation of the hardness profile

To homogenize the distribution of the case depth along the axis of the cylinder, it is essential to carry out a control in the laser power as a function of time, or a control on the scanning speed, or in the rotation speed of the cylinder [26]. As part of this work, we chose

to control the laser emission power as a function of time and following a first-order control function. Equation 9 presents the expression of the servo function of the laser energy which depends on the initial power of emission, the control coefficient Γ, the position of the laser beam at the outer surface of the cylinder and its scanning speed.

$$P(t) = P_i - \Gamma\left({}^{p(t)}/_{SS}\right) \tag{9}$$

Before the laser heat treatment, a notch with a radius of 0.5-mm was made at the outer surface of the test specimen in order to obtain an adequate distribution of case depth in the notched zone. Table 6-2 provides a full factorial design with two factors and two levels, define 4 experimental conditions programmed to vary simultaneously and in a balanced way throughout the experiment. The fifth experimental condition of the experiment matrix corresponds to the center value between the maximum configuration (1300-W and 3-mm/s) and the minimum configuration (1200-W and 4-mm/s) of laser hardening. With the numerical values of surface temperature and case depth at the region outside notch (θ_d, C_d) and at the level of the notch region (θ_n, C_n). The case depth was uniformed along the longitudinal axis of the test specimen through a control in the laser power, via the coefficient Γ introduced in Eq. 9.

Table 6-2: Experimental design and results for uniform case depth

Tests	**Factors**		**Responses**				
	P (W)	Ux (mm/s)	θd (°C)	Cd (µm)	θn (°C)	Cn (µm)	Γ (W/s)
1	1300.0	3.0	1114.7	1100.0	1170.6	1550.0	16.87
2	1300.0	4.0	1047.1	500.0	1053.4	600.0	12.70
3	1200.0	3.0	1064.3	800.0	1141.7	1350.0	7.58
4	1200.0	4.0	1018.4	350.0	1044.3	500.0	6.50
5	1250.0	3.5	1060.2	750.0	1092.2	950.0	8.14

This power servo control coefficient, which represents the slope of the 1st order interpolation line, was adjusted using numerical simulations and experimental validation, between the position 20-mm and 60-mm from the beginning of the laser heat treatment. We noted that this coefficient is mainly influenced by laser power with a percentage contribution in the final response of about 75% and that the scanning speed contributes on its variation with a percentage of contribution in the final response of about 25%.

Figures 6-5a to -5e shows the servo values of the laser power and the uniform case depth obtained along the longitudinal axis of the cylinder. At the notch (position that corresponds to 40-mm of the position of the beginning of heat treatment) we got a case depth greater compared to the untouched zone, and this because we had a reduction of the diameter of the cylinder in this zone. The melting region was completely removed just to keep only a high surface hardness. Figure 6-5f shows a detailed sketch of the cut made to the test pieces after heat treatment in order to remove 0.3-mm from the outer surface.

6.7.3 Experimental design and measurements of mechanical properties

To analyze the impact of heat treatment (case depth) on the mechanical behavior of AISI 4340 steel, specimens of dimensions corresponding to Figure 6-4b were carefully prepared and machined after laser heat treatment to match the dimensions of a standard specimen according to the ASTM E8 standard.

Since the specimen was hardened, it is then made of a material in two different states. The crown is hard and fragile and the core is less hard and more tenacious. The stress at the transition point between the elastic zone and the plastic zone S_y^* represents the contribution in terms of yield strength of the crown and the core of the specimen at which 0.2% plastic deformation occurs. The ultimate stress S_u^* represents the contribution in terms of tensile strength limit of the crown and the core of the specimen. The stress corresponding to the fatigue endurance limit S_e^* represents the contribution in terms of fatigue endurance limit of the crown and the core of the specimen. The elongation at break E_l^* represents the contribution in terms of ultimate elongation at break of the crown and the core of the

specimen. The mechanical properties considered in this performance analysis are S_y^*, S_u^*, S_e^* and E_l^*. To measure the numerical values of these mechanical properties, an automatic tensile testing machine (MTS 810 Material Test System) which has a total tensile load of 100-kN was used. The flexibility of the configuration of this tensile testing machine, which serves to develop and qualify the use of materials, allows a variety of applications including performing fatigue tests. Once the specimen is placed and tightened between the grips of the machine with a pressure of approximately 10.0-MPa, a displacement of the lower part is made by a hydraulic piston device in order to stretch the test piece.

The stretching force is measured by a force sensor inserted into the loading machine and the deformation is measured by an extensometer placed at the center of the specimen, which is suitable for general use in testing axial traction, compression and cyclic fatigue. For an effective analysis of the impact of laser heat treatment parameters on the mechanical behavior of AISI 4340 steel, experimental modeling based on relevant experimental tests was used. The arrangement and ordered sequence of these experimental tests are essential for a fair representation of the mechanical properties according to the parameters of the test. Due to its efficiency and simplicity a complete two-level and three-factor factorial design was used to measure the mechanical responses of all possible combinations of factor levels. The tests matrix required in the context of a complete two-level and three-factor factorial plan is an L_8 matrix.

Table 6-3 presents the factors that will be studied to analyze their effects on the process. The first factor is the initial laser emission power, the second factor is the scanning speed of laser beam and the third factor corresponds to the strain rate.

Table 6-3: Factors and levels of experience planning

Factors	**Levels**
Laser power (W)	1200.0 and 1300.0
Scanning speed ($mm.s^{-1}$)	3.0 and 4.0
Strain rate (min^{-1})	0.005 and 0.015

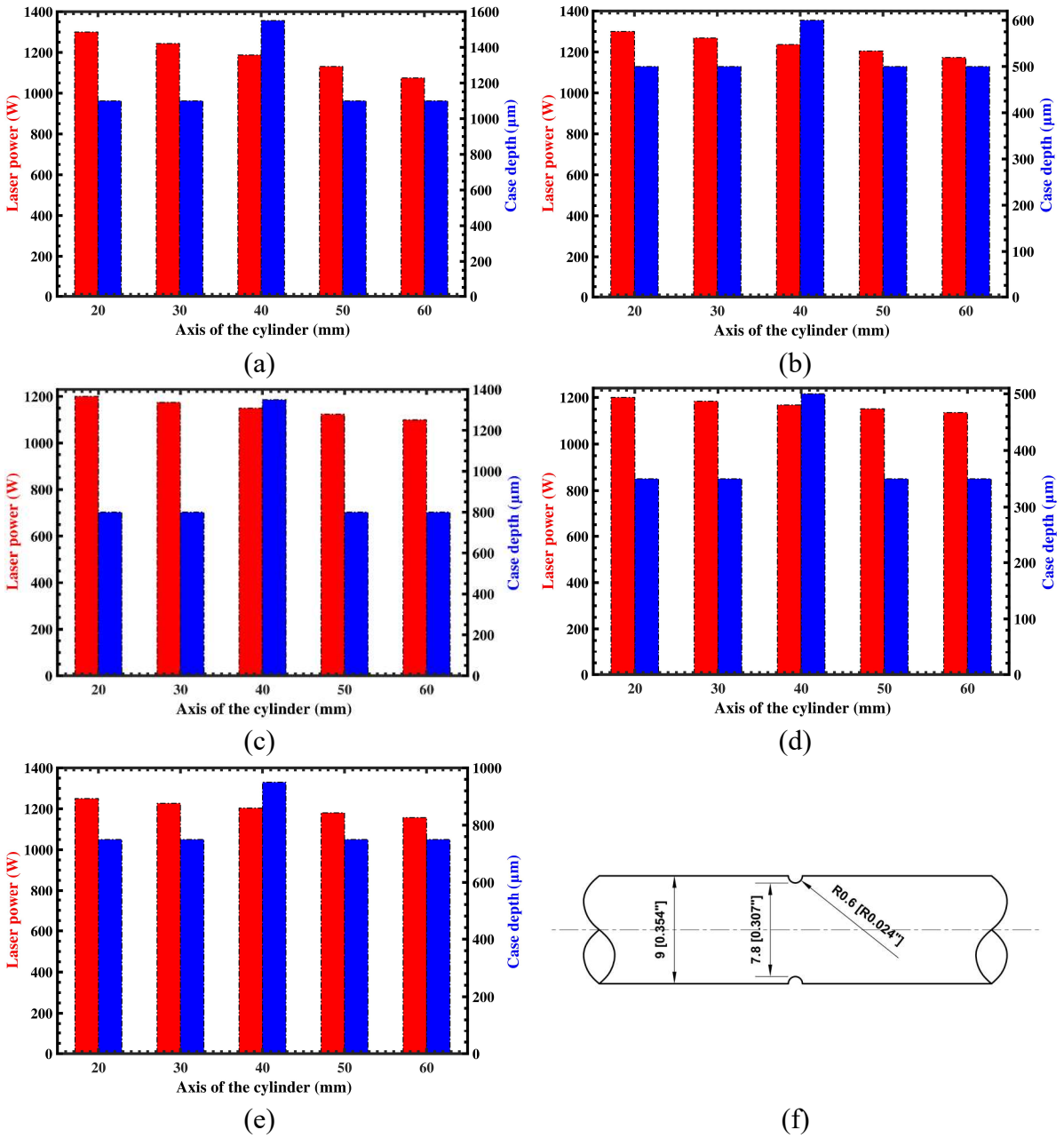

Figure 6-5: Laser power and Case depth versus Axis of the cylinder – (a) 1300-W & 3-mm/s, (b) 1300-W & 4-mm/s, (c) 1200-W & 3-mm/s, (d) 1200-W & 4-mm/s, (e) 1250-W & 3.5-mm/s, (f) Sketch of the material removed from the specimen, unit Millimetre [Inch]

Each L_8 full factor plan test of the tensile tests was repeated three times to ensure precise statistical significance of the data. Figures 6-6a-b show stress-strain curves for

different combinations of laser power and scanning speed, and for two respective strain rates of 0.005-min^{-1} and 0.015-min^{-1}. We noted that S_y^* and S_u^* were proportional to the high parameters of laser heat treatment and that E_l^* is inversely proportional to the laser parameters (case depth). For laser heat treatment parameters of 1300.0-W and 3.0-mm.s^{-1} S_u^* of the samples is approximately 1515.0-MPa, knowing that it was 1129.0-MPa for untreated specimens, with an improvement of about 34% in the value of S_u^*. Moreover, E_l^* decreases from 6.7-mm.mm^{-1} for samples not hardened with laser to 2.1-mm.mm^{-1} for samples hardened with the highest laser parameters. We also noted that the strain rate had an influence on the mechanical properties of the samples. A high strain rate gives a high S_u^* and a lower E_l^*. The ultimate strength S_u^* of samples hardened with laser parameters 1300.0-W and 3.0-mm.s^{-1} varies from 1515.0- to 1559.0-MPa for respective strain rates of 0.005-min^{-1} and 0.015-min^{-1}, for a slight variation of about 3%. On the other hand E_l^* of the samples not hardened with laser varies from 6.72 to 6.01-mm.mm^{-1} for respective strain rates of 0.005-min^{-1} and 0.015-min^{-1}, for a net variation of about 12%. To study the fatigue behavior of laser-hardened specimens, a uniaxial tensile stress cyclically variable was used according to a sinusoidal modeling. Equation 10 presents the expression of the applied stress, which depends on the average stress (σ_m), the amplitude of the stress (σ_a) and the frequency of the solicitation (f). At the beginning of the tests, the average stress was set to be reached in 60-s with a linear loading speed, followed by a sinusoidal variation with a frequency of 20-Hz between the minimum and maximum values of the applied stress. Equation 11 presents the expression of the stress ratio (R) which relates the extreme values that the applied stress can take. In our experiments, this ratio was close to zero ($\approx 8.3\times10^{-3}$), for sinusoidal solicitations of tensile ($\sigma_{min} > 0$).

$$\sigma(t) = \sigma_m + \sigma_a.\sin(2\pi f t) \tag{10}$$

$$R = {}^{\sigma_{min}}/_{\sigma_{max}} = {}^{\sigma_m - \sigma_a}/_{\sigma_m + \sigma_a} \tag{11}$$

The fatigue endurance limit S_e^* which is the stress that can be applied to the material without causing fatigue failure, at least not before 1.0-million cycles, is an essential data for

the design and dimensioning of mechanical workpiece. It usually corresponds to the value of the stress which represents the straight line in the Wöhler graph. To determine this limit of endurance zone which generally exceeds the expected lifetime of the workpiece, in many cases, we can draw an asymptote at this part of the curve which corresponds to the limit of endurance or fatigue (generally true for steels but not for aluminum where there is no asymptote). The endurance limit is always determined with some error (probability of reaching the endurance limit). A just estimate of endurance limit requires to use a large number of specimens (twenty), solicited at the same level of stress. Break is determined based on a network of endurance curves each corresponding to a given probability of failure. Many methods exist, which can be classified into two types, approximate estimation methods requiring few specimens and methods that lead to a good approximation but which also require a larger number of specimens. As part of this research, the staircase method with a small number of test pieces (3 to 4) was used, at different levels of stress, close to a number of cycles of 10^6. Each level of stress is different from an increment value relative to the previous level of stress.

Figure 6-6c shows the fatigue curves (S-N) according to the model of Wöhler, for three laser heat treatment configurations and one without laser heat treatment. It is noted that the laser heat treatment has a positive impact on the fatigue strength of the cylindrical workpiece made of AISI 4340 steel. This impact on the improvement of the endurance limit is proportional to the case depth of the transformation of the microstructure. The samples, which received a heat treatment with laser parameters 1300-W and 3-mm/s, and which have a case depth in the calibrated part of 800-µm, had an endurance limit of around 609-MPa which is a significant improvement in 53% compared to samples that have not been laser hardened and which have a basic endurance limit of about 397-MPa. We noticed that S_e^* depends mainly on the S_u^* and that it is close to the empirical formulation that represents it with a ratio of 2 [27]. The plot of the S-N curve gives a representation similar to the S-N curve plot obtained during induction heat treatment of steel AISI-4340 [28].

Equation 12 presents the expression of S_y^*, S_u^*, S_e^* and E_l^* according to the laser heat treatment parameters. Table 6-4 shows the values of the coefficients of the multiple linear regression polynomial (T), obtained using the Minitab statistical analysis software (version 18). The residual value squared (R^2) of multiple linear regression is about 0.94, which means that the prediction is very close to the exact solution ($R^2 \approx 1.0$) corresponding to the results of the experimental tests.

$$T = \alpha_0 + \alpha_1.P + \alpha_2.U_x + \alpha_3.P^2 + \alpha_4.{U_x}^2 + \alpha_5.P.U_x \quad (12)$$

Table 6-4: Coefficients of the polynomial prediction

T	S_y^*	S_u^*	S_e^*	E_l^*
α_0	1.024E+03	1.129E+03	3.966E+02	6.726E+00
α_1	-3.066E+00	-3.088E+00	5.651E-01	3.205E-02
α_2	1.117E+03	1.340E+03	-1.752E+02	-1.431E+01
α_3	1.631E-03	1.947E-03	–	-1.300E-05
α_4	-1.193E+02	-1.545E+02	–	2.249E+00
α_5	-2.300E-01	-3.900E-01	–	-4.600E-04

Figure 6-6d shows the variation curves of the mechanical properties according to the laser heat treatment parameters. We note that S_y^*, S_u^* and S_e^* are proportional to the laser power and are inversely proportional to the scanning speed of the laser beam. We also note that the elongation at break E_l^* is proportional to the scanning speed and inversely proportional to the laser power.

6.7.4 Analysis of variance (ANOVA) & RSM representation

To study the percentage of contribution and the impact of each parameter of the laser heat treatment process on the mechanical properties of AISI 4340 steel, an analysis of variance was used [29-30]. The percentage of contribution of a factor on the final response indicates its degree of influence on the total variation observed in the experiment, and the

diagram of the average effects of each factor level groups the main effects with their interaction to designate the variation of the average response. In general, there is interaction between factors if the effect of one factor depends on the level of the other factor.

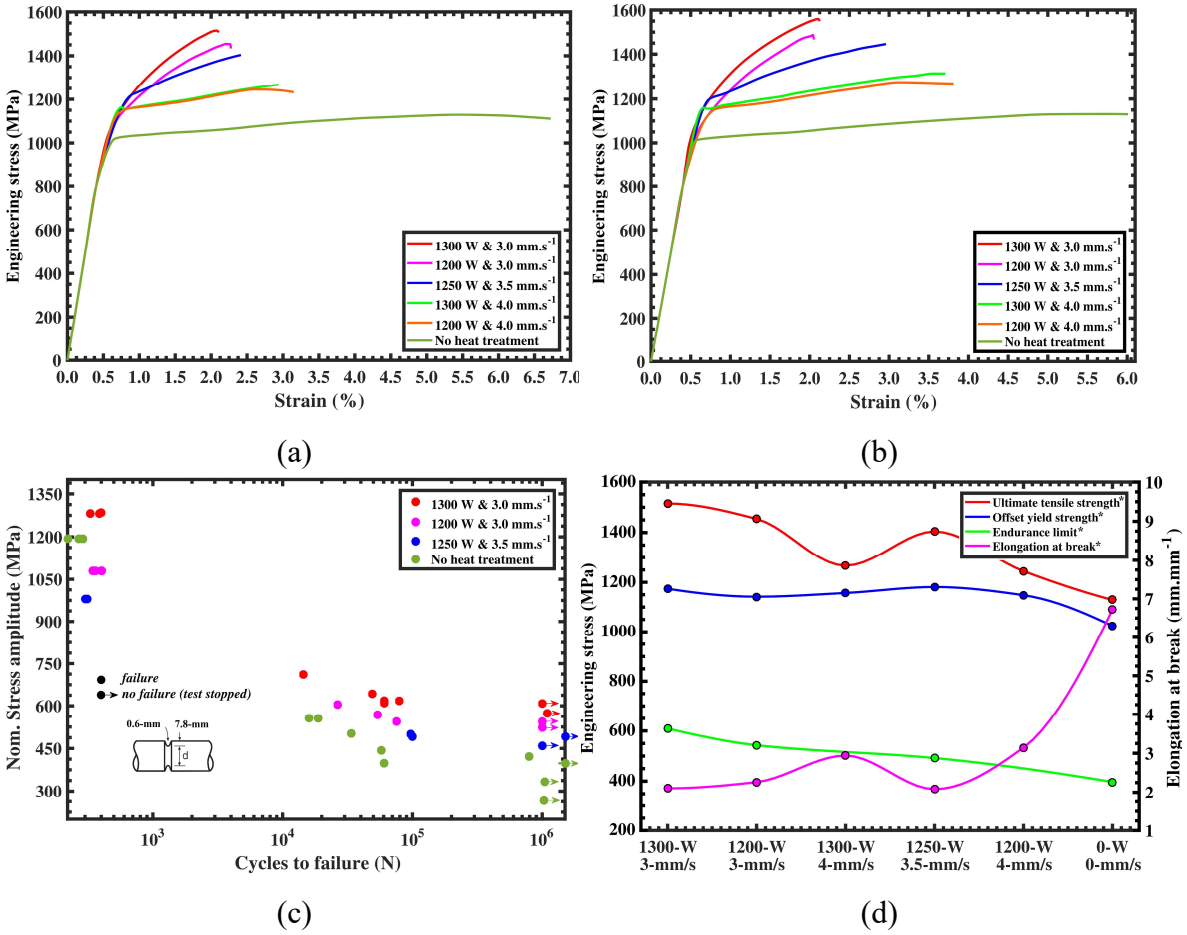

Figure 6-6: Stress strain versus Laser parameters – (a) for $\dot{\boldsymbol{\varepsilon}}$ = 0.005 mm/mm/min, and (b) for $\dot{\boldsymbol{\varepsilon}}$ = 0.015 mm/mm/min, (c) Nom. Stress amplitude versus Cycles to failure, (d) Three stress values and elongation at break versus Laser parameters

Tables 6-5, 6-6, 6-7 and 6-8 present an analysis of variance of the parameters P and Ux on the respective responses S_y^*, S_u^*, S_e^* and E_l^*, using the stepwise method (backward elimination of terms with an alpha to remove equal to 0.1) of order 2 for S_y^*, S_u^*, and E_l^*, and order 1 for S_e^*. These tables contain degrees of freedom, the sum of the squares, the average square, the value of P and the value of F for each parameter studied. In general, a

significance level of P-value of approximately 5% allows to confirm that differences between averages are statistically significant for values of the variance ratio F comparable to the values of the standard tables.

Table 6-5: ANOVA for S_y^*

Characteristic	df	Contributions (%)	Sum of squares	F-value	P-value
P	1	91.05	15125.50	56.5793	0.0151
U_x	1	0.37	61.80	0.2299	0.0645
P^2	1	0.32	53.20	0.1989	0.0534
U_x^2	1	3.23	536.90	2.0072	0.0619
$P \times U_x$	1	0.80	132.20	0.4971	0.0137
Error	2	4.23	707.70	–	–
Total	7	100.00	16617.30	–	–

Table 6-6: ANOVA for S_u^*

Characteristic	df	Contributions (%)	Sum of squares	F-value	P-value
P	1	49.10	52494.6	859.71	0.022
U_x	1	47.92	51029.0	317.57	0.036
P^2	1	1.59	1695.0	14.48	0.067
U_x^2	1	0.81	866.0	7.37	0.048
$P \times U_x$	1	0.36	380.0	3.27	0.056
Error	1	0.22	15.4	–	–
Total	7	100.00	106479.0	–	–

Table 6-7: ANOVA for S_e^*

Characteristic	df	Contributions (%)	Sum of squares	F-value	P-value
P	1	74.35	17831.20	180.09	0.047
U_x	1	25.42	6097.60	113.10	0.060
Error	1	0.22	53.90	–	–
Total	3	100.00	23982.70	–	–

Table 6-8: ANOVA for E_l^*

Characteristic	df	Contributions (%)	Sum of squares	F-value	P-value
P	1	93.49	14.81	1046.93	0.019
U_x	1	3.90	0.61	43.67	0.004
P^2	1	0.95	0.15	10.63	0.012
U_x^2	1	1.38	0.21	15.45	0.001
$P \times U_x$	1	0.10	0.01	1.11	0.094
Error	2	0.18	0.02	–	–
Total	7	100.00	15.81	–	–

It is noted that the laser power and scanning speed of the laser beam have a great impact on the four mechanical properties (S_y^*, S_u^*, S_e^* and E_l^*) of AISI 4340 steel, with an average contribution percentage of about 76% for laser power (P) and about 19% for the scanning speed (Ux). There also is a slight contribution of about 5% from other uncontrolled factors, including the experimental error. The ANOVA analysis shows that the endurance limit S_e^* is influenced mainly by laser power with a 74% contribution percentage and by scanning speed for a percentage of about 25%. Concerning the ultimate strength S_u^* we noted that it is influenced by laser power and scanning speed, with an equal percentage of about 49%, and that the elongation at break E_l^* is influenced mainly by laser power with a total contribution percentage of about 93%, and a combination of power and scanning speed for a percentage of 7%. It was concluded, in the range of variation of the studied parameters, that the laser power (P) and the scanning speed (Ux) are significant for a response value of 94% of the statistical model.

Figure 6-7 shows the average effects of laser power and scanning speed on the response values of S_y^*, S_u^*, S_e^* and E_l^*. The results confirm that laser power has a positive and proportional effect on S_y^*, S_u^*, S_e^*, with an inverse effect on E_l^*. Also, the scanning speed has an inversely proportional effect on S_y^*, S_u^*, and S_e^*, with an positive and proportional effect on E_l^*.

Figures 6-8a to 6-8d show the estimated response surfaces for a representation of the variation of the mechanical properties according to the laser power and the scanning speed [31]. We used the Thin-plate-spline interpolation method to represent the response surfaces because it allowed to obtain a better representation of the experimental measurements, with a R^2 value of 0.97 which is a value close to the exact solution 1. These contour lines correspond to the intervals of the parameters in Table 6-3, and they can be used in practice by model users for predicting the mechanical properties of AISI 4340 steel as part of laser heat treatment. We notice explicitly of the contour lines (Fig. 6-8a) that the S_y^*, is maximum (1180-Mpa) for a laser power of 1260-W and a scanning speed of 3.5-mm/s.

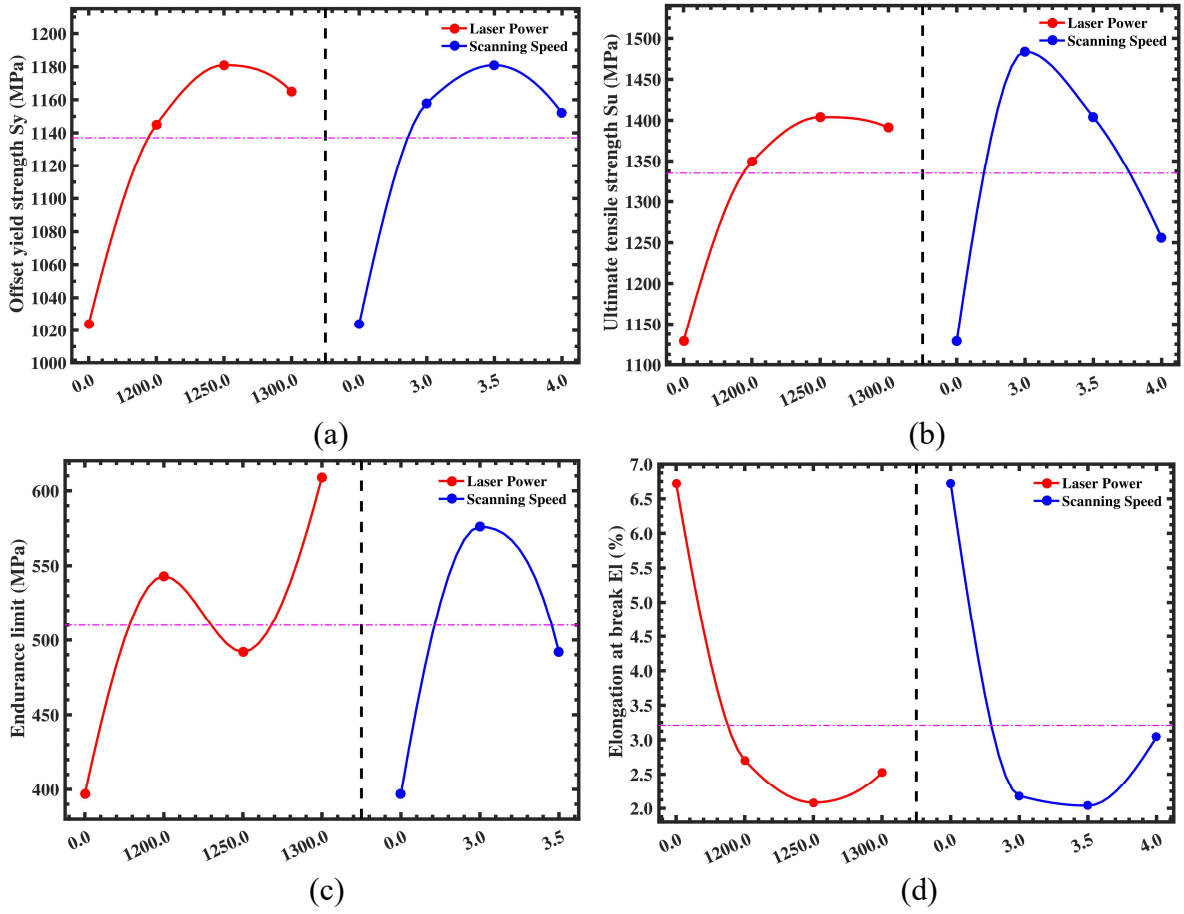

Figure 6-7: Main effects plot – (a) Offset yield strength, (b) Ultimate strength, (c) Endurance limit, and (d) Elongation at break

This overall variation in the value of S_y^* is between 1145-MPa and 1180-MPa, a variation not exceeding 5% in the experiment planning interval of Table 6-3, and a variation compared to the unhardened samples of the order of 15%. We observe from the contour lines (Fig. 6-8b and 6-8c) that the ultimate strength S_u^* and the fatigue endurance S_e^* have a quasi-linear variation which is proportional to the laser power and inversely proportional to the scanning speed. Maximum value for S_u^* is of the order of 1515-MPa and maximum for S_e^* is about 609-MPa for the same laser heat treatment parameters (1300-W and 3-mm/s). We observe from the contour lines (Fig. 6-8d) that E_l^* is maximum (3.14%-mm/mm) for a laser power of 1200-W and a scanning speed of 4.0-mm/s. This overall variation in the value of E_l^* is between 2.08 and 3.14%-mm/mm, a significant variation of about 51% in the range of the parameters defined in Table 6-3.

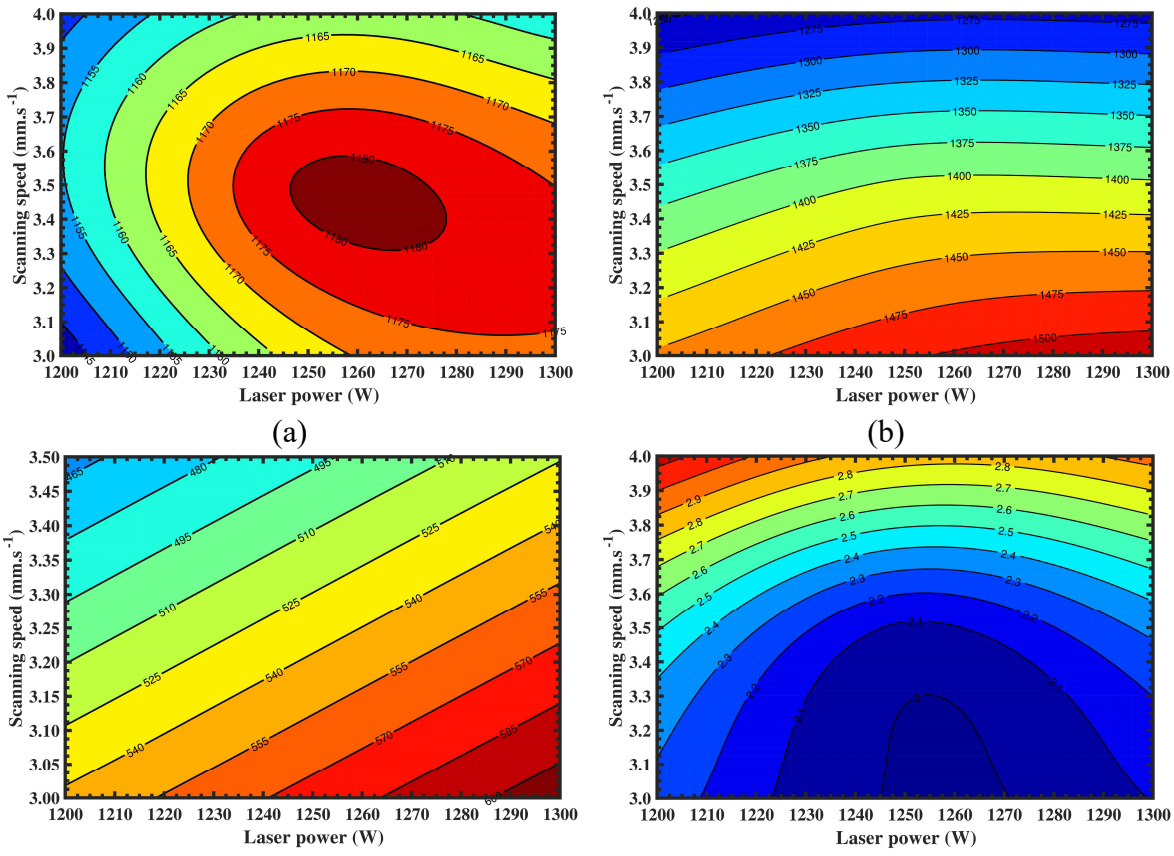

Figure 6-8: Contour plot – (a) Offset yield strength, (b) Ultimate strength, (c) Endurance limit, and (d) Elongation at break

6.7.5 Artificial neural network predictor

For the prediction of model output responses (Γ, S_y^*, S_u^*, S_e^* and E_l^*) according to the laser heat treatment parameters (P_i and SS), a network of artificial neurons inspired by the functioning of biological neurons was introduced using the Matlab MathWorks library (Neural Network Toolbox) for a automatic learning and processing capable of storing experiential knowledge and makes them usable later in practice for prediction. Arbitrary validations with center values of laser parameters were performed to confirm the robustness and effectiveness of the prediction model, which can be exploited in practice by model users in the form of an external routine that execute a task described in the programming language.

Figure 6-9a shows the architecture of the selected neural network (2-10-5) which consists of an input layer, a hidden layer and an output layer. The number of neurons in the input layer is the number of input parameters, the number of neurons in the output layer is the number of output parameters and the number of neurons in the hidden layer is determined by incrementing the number of neurons in the hidden layer and an estimate and comparison of the generalization error with the previous iteration. The architecture of the neural network (2-10-5) was chosen because it allowed us to obtain a better quality of prediction with a R^2 value of 0.98 which is a value close to the exact solution 1. Figure 6-9b shows the summary flowchart of the Bayesian regularization backpropagation algorithm used in network learning. This algorithm usually requires more time than other learning algorithms, but provides a good generalization for difficult, small or noisy datasets. The training of the network stops according to the adaptive weight reduction (regularization) [32]. Equation 13 presents the TANSIG transfer function (Hyperbolic Tangent Sigmoid) applied to the output of each artificial neuron for the hidden layer. This transfer function is generally preferred to the LOGSIG transfer function because it produces outputs centered and close to zero while LOGSIG produces only positive outputs. Equation 14 presents the transfer function PURELIN (Linear) applied to the output of each artificial neuron from the output layer. The output of this linear transfer function is equal to its input.

$$f_T(n) = e^n - e^{-n} / e^n + e^{-n} \quad (13)$$

$$f_P(n) = n \quad (14)$$

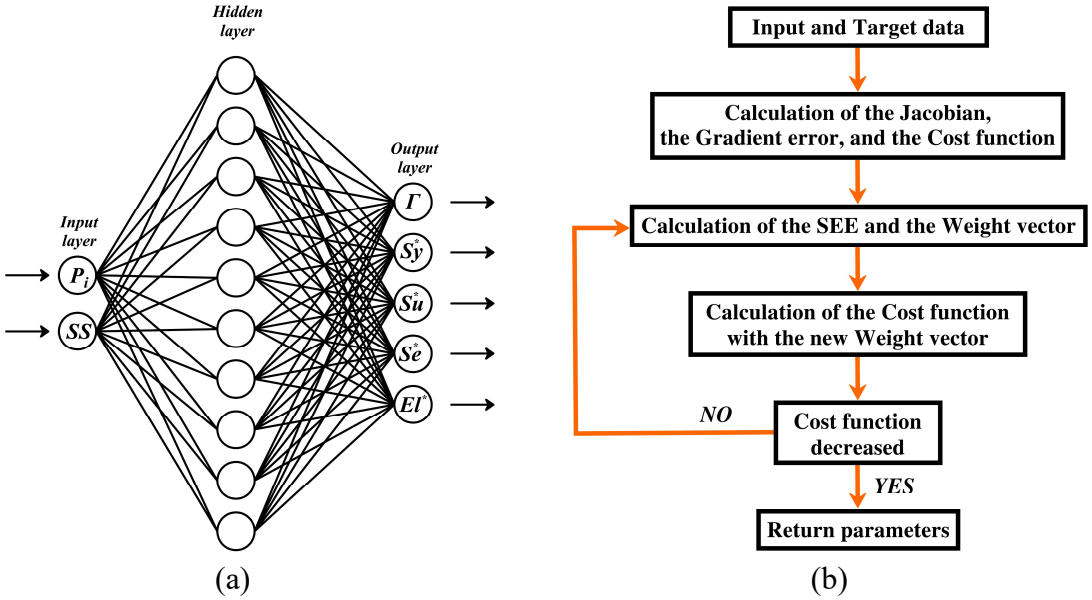

(a) (b)

Figure 6-9: (a) ANN model architecture, (b) Flowchart of training process of Bayesian regularization backpropagation algorithm

Figures 6-10a to 10c show the curves measured and predicted by the neural network architecture (4-10-5) using the Bayesian regularization algorithm backpropagation, for the slope of the laser power curve Γ, S_y^*, S_u^*, S_e^* and E_l^*. Results are displayed for all six laser heat treatment configurations, including both configurations of the center validation. We observe that the predicted responses align very well with the measured data, which shows the good prediction agreement of the ANN model and which informs of the existence of a good relation between the nonlinear input parameters of the model. Equation 15 presents the expression of the mean absolute error (MAE), and equation 16 presents the expression of the mean relative error (MRE), for comparison and quantification of the differences between the number n of measured data (Xi) and the number n of predicted data (Yi) by the neural network. The relative error was introduced in this analysis because it allows to compare the prediction responses for different units [33].

$$MAE = \sum_{i=1}^{n} |Y_i - X_i| / n \quad (15)$$

$$MRE = \sum_{i=1}^{n} \left(|Y_i - X_i| / |X_i| \right) / n \quad (16)$$

Figure 6-10d shows the value of the mean absolute error (in SI unit) and the mean relative error (in %), for S_y^*, S_u^*, S_e^*, E_l^*, and Γ the slope of the laser power curve. We notice that the mean absolute error does not exceed 10-MPa for S_y^*, S_u^* and S_e^*, and is close to zero for E_l^* and Γ, and that the mean relative prediction error does not exceed 3.5% for its maximum in E_l^*.

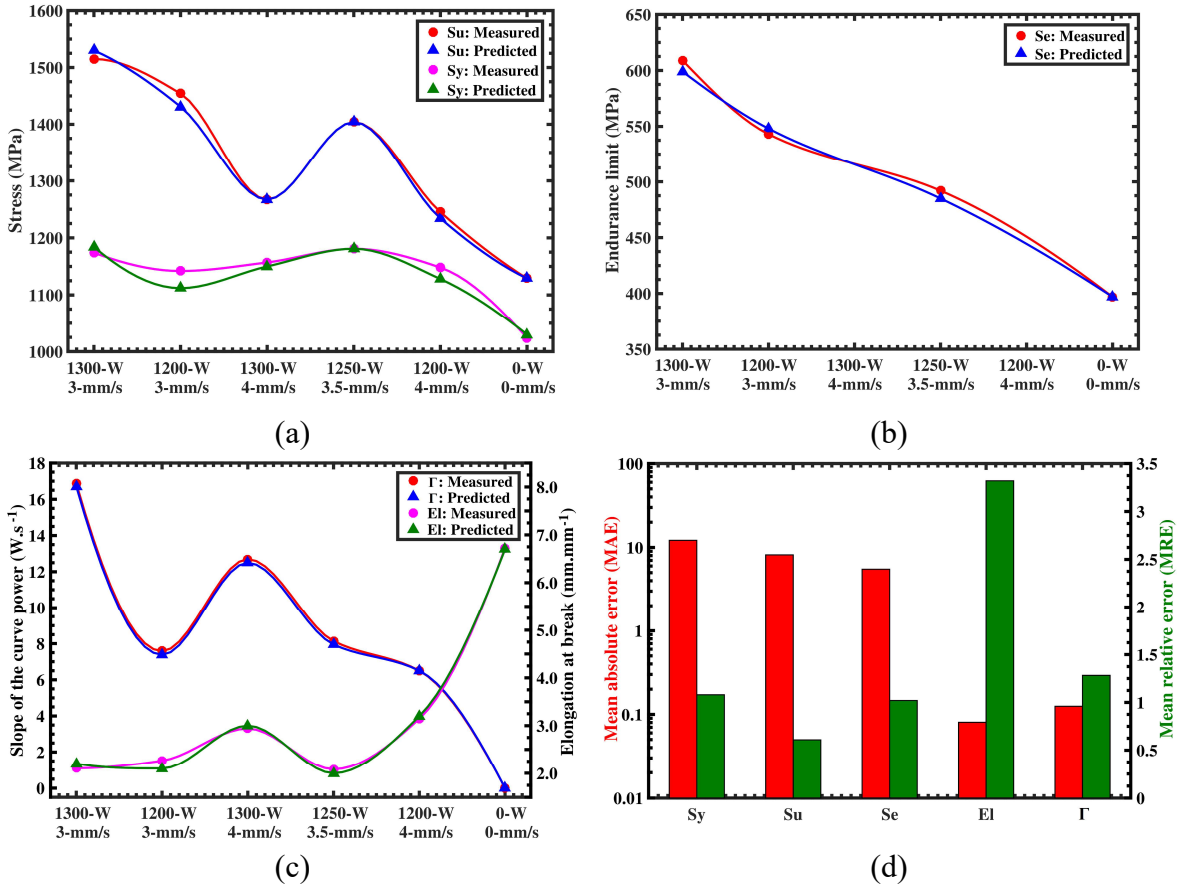

Figure 6-10: Measured versus predicted – (a) Offset yield strength and Ultimate strength, (b) Endurance limit, (c) Slope of the curve power and Elongation at break, (d) Mean absolute error and Mean relative error for output responses of model

6.8 DISCUSSION

From the results of the numerical simulations we can notice that the thermal losses by convection and radiation, are proportional to the laser power and are inversely proportional to the scanning speed of the laser beam. According to the balance of thermal exchanges at the level of the circumference of the cylinder and at the position of the laser beam at a fixed moment of time, we note that the average energy that will be transmitted by conduction to the workpiece is about 76% of the total energy emitted by the source, for convective thermal losses of about 1% and radiation heat losses of about 23%. The variation in the percentages of the thermal balance (thermal flow transmitted by conduction, lost by convection and lost by radiation) compared to experimental planning is about 7% for conduction and radiation, and is almost stable for convection. After stopping the laser emission (end of the heating cycle), begins the cooling phase in the air of the cylindrical workpiece (cooling cycle). This cooling cycle is as important as the heating cycle, because it allows if it is well controlled to control the formation of the microstructure of steel after austenitization. In our experiments, we maintained after the laser heat treatment the cylindrical workpiece in rotation for 10-min continuous cooling up to the ambient temperature. This condition has ensured a cooling rate greater than the critical cooling rate (8-°C/s) which allows the formation of a completely martensitic structure.

When a high-density laser beam is irradiated on the surface of steel AISI 4340, the initially formed structure of tempered martensite with medium carbides (tempering made at a temperature of 500°C for 30 min of time) reaches the temperature of austenite in a very short time. Which allows, in the austenitic state (Temperature Ac3) the carbide dissolution after a very short period of time, and if it is cooled quickly the structure becomes strengthened as martensite is formed [9]. Figures 6-11a and 6-11b show a microscopic visualization with magnification (× 2500) of the AISI 4340 steel microstructure observed in hardened zone (depth of 100 µm) and in zone not affected by laser heat treatment (2000 µm). The microstructure has a martensitic structure in the hardened zone (Fig. 6-11a) with a small percentage of retained austenite that did not change during fast quenching. In the

zone not affected by the heat treatment (Fig. 6-11b) a mixture of hardened martensite, bainite and untransformed austenite is observed. Figures 6-11c and 6-11d show the results of X-ray spectroscopy for Spectrum 1 and 2, respectively at the hardened zone and in the zone not affected by the heat treatment. We note a slight (almost zero) change in the chemical composition between the hard crown and the core of the specimen (zone not affected by laser heat treatment).

From the point of view of breaking strength, we noticed a brittle type break in tensile tests for all specimens that were heat treated with the laser parameters in Table 6-1. The rupture in tensile test takes place in most cases at the notch (stress concentration zone), except for specimens that were heat-treated with the highest laser parameters (1300-W and 3-mm/s). The latter had a break in tensile test at the position X_{20} of Figure 6-1a. This brittle fracture in static out of the notch zone is due mainly to the hardened depth that is not equal (smaller) at the case depth between the positions X_{40} and X_{80}. This difference of about 100-µm between hardened depths requires a laser power control curve of order 2 to ensure wide servo range and regular case depth.

Furthermore, all test pieces had a fatigue failure at the position of the notch, including specimens that were heat-treated with the highest laser parameters. This break in fatigue at the notch, as shown in Fig. 6-6c, is due mainly to the stress concentration that are higher than the nominal stress. The concentration of stress can be evaluated by a multiplication of the nominal stress with the coefficient of stress concentration. The coefficient of stress concentration can be estimated according to the geometry of the piece, the geometry of the notch and the nature of the solicitation. This coefficient is of the order of 2.4 for the notch studied in this work. In terms of hardened transverse surface and transversal surface unaffected by laser heat treatment for a cylinder of 9-mm diameter and in AISI 4340 steel, we note a maximum hardening of about 51% of the cross section for the highest laser parameters (1300-W and 3-mm/s). This allowed to improve the value of S_y^* by 150 MPa, the value of S_u^* by 386 MPa, and the value of S_e^* by 212 MPa compared to non-hardened samples.

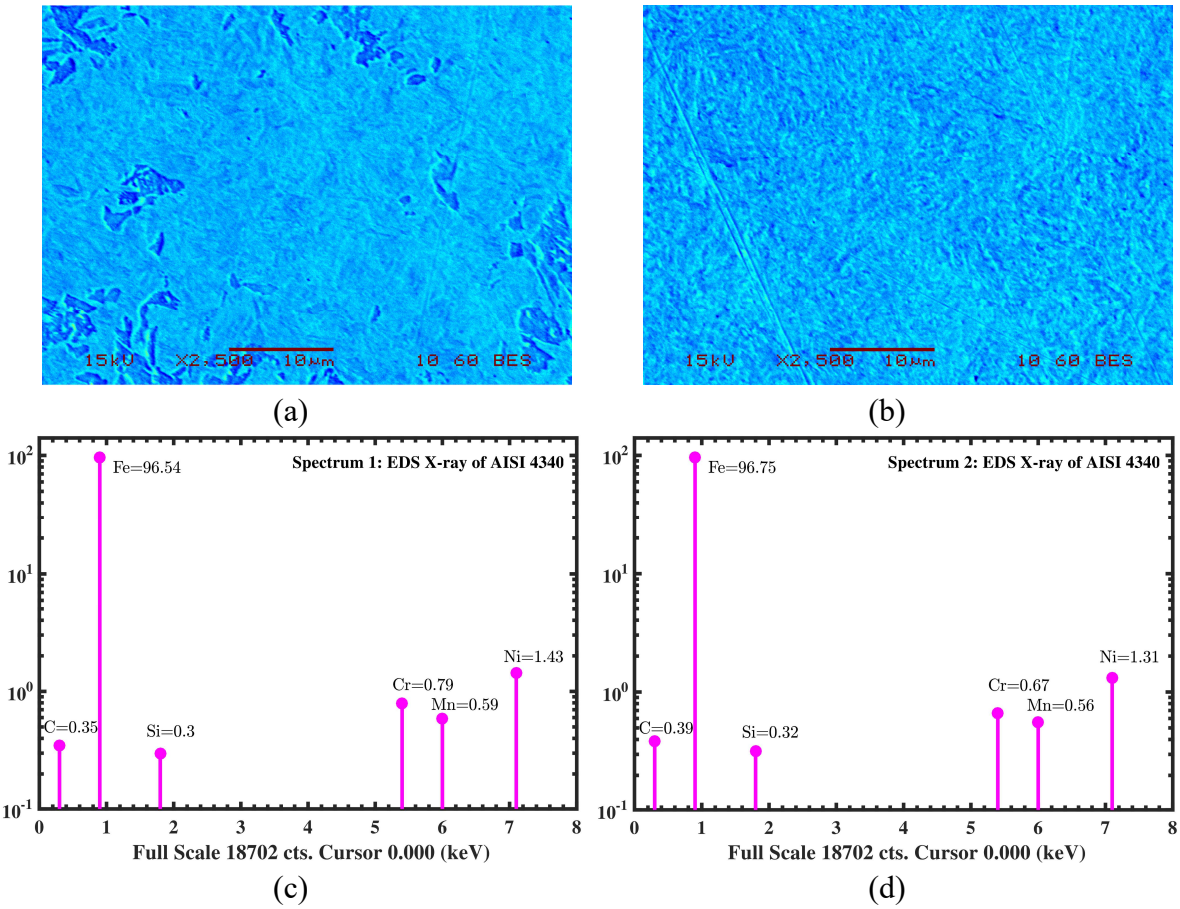

Figure 6-11: Microscopic visualization – (a) For the hardened zone, (b) For the unhardened zone. Energy dispersive X-ray spectroscopy (EDS) spectra acquired in scanning electron microscopy (SEM): (c) Spec. 1 of the hardened zone, (d) Spec.2 of the unhardened zone

To show the mechanical behavior of steel AISI 4340, in fatigue, in cylindrical geometry and after its laser heat treatment, a hysteresis loops with repeated sinusoidal stress in tensile were studied for an oligocyclic fatigue failure (ruin in less than 50 000 cycles) and conventional fatigue failure (ruin beyond 50 000 cycles). Figure 6-12 shows stress-strain hysteresis loops for non-hardened specimens and for specimens hardened with laser parameters 1250-W and 3.5-mm/s (case depth of 550-µm), with two stress ranges 1143-MPa and 525-MPa which are respectively about 0.87 and 0.51 of the tensile strength limit (Su). These hysteresis loops observed for untreated and laser heat-treated samples are almost similar for the two loading conditions in Figure 6-12, and this because of the small

deformation that occurs by sliding of the dislocations. However, despite this similarity, there are differences in the final response of the material according to the laser heat treatment and the value of the load of the repeated tensile stress.

Firstly, the profile of hysteresis loops which can be analyzed by a simple comparison of the value of variation of the slope of each cycle of fatigue, present in all the studied configurations a value of slope at the end of life by approximately 20% smaller compared to the value of the slope of the first cycles. This same slope value is proportional to the high parameters of laser heat treatment and also at the high values of the repeated tensile stress. This flattening phenomenon confirms the results reported in the work of Hidayetoglu et al. [34], and inflections begin to develop after the first cycles of life and grow strongly towards the end of life to reach their maximum values.

Secondly, the strain ranges present in all the configurations studied show a large variation for the two stress conditions σmin and σmax. We note that the strain ranges are proportional to the amplitude of strain, and are inversely proportional to the case depth. We notice at the level of the last cycle before the break (Fig. 6-12a et Fig. 6-12b) a failure strain of about 0.63% for samples hardened and unhardened with laser and solicited with a stress of 1143-MPa. For a stress of 525 MPa, a failure strain of about 0.25% is noted for hardened and unhardened samples (Figs 6-12c and Fig. 6-12d). However, for both stress 525 MPa and 1143 MPa, there is a marked improvement in fatigue life for hardened samples by laser compared to unhardened samples. The variation in the strain range between the cycles closest to the break is very small for samples that have received laser heat treatment compared to untreated samples. This variation in the strain range shows the ability of the material to respond to deformation under various stress conditions.

Thirdly, we note that the elongation at break is maximum for samples that did not receive laser heat treatment, and this occurs whatever the applied stress. As shown in Figure 6-12, it is noted that a high relative value of the elongation at break does not mean that the cylindrical workpiece will have a higher fatigue cycle number. According to hysteresis loops, as shown in Figures 6-12a to -12b, we note that this group of samples,

which has been evaluated at a stress of 1143-MPa in fatigue stress, has an elongation at break of about 2.05% for untreated samples and approximately 1.19% for thermally laser treated samples. Also that the group of samples, which was evaluated at a stress of 525-MPa has an elongation at break of about 0.39% for untreated samples and approximately 0.30% for thermally laser treated samples, which corresponds to a decrease in the deformation of about 76% and a net improvement of a ratio of 5 in the lifetime of specimens. This analysis supports the hypothesis that increasing resistance reduces mobility of dislocations [35].

Figure 6-13 shows the fracture surfaces of AISI 4340 steel, in tensile tests and fatigue tests, under the conditions of laser heat treatment of test T_5 (1250-W and 3.5-mm/s), which corresponds to a case depth of 550-µm. Condition without laser heat treatment (case depth of 0-µm) is also shown. A color delineation code has been introduced to delimit the case depth, the initiation region of crack, the propagation region of crack and the region of fast fracture.

We can see in Figures 6-13a and 6-13c, which correspond to a solicitation in standardized tensile tests, that a brittle failure occurred because of a loading force greater than the ultimate tensile strength. The fracture surface of Figure 6-13a corresponds to a laser hardened specimen which has an elongation at break of 2.08% and an ultimate tensile strength of 1181-MPa. The region outlined by a yellow color corresponds to the laser case depth. The fracture surface of Figure 6-13c corresponds to an unhardened specimen (initial hardness of 35-HRC, in Rockwell C unit) which has an elongation at break of 6.72% and an ultimate tensile strength of 1024-MPa. Figures 6-13b, 6-13c, 6-13e and 6-13f show the fracture surfaces in fatigue stress it can be seen from these images that the fatigue cracks appeared mainly at the surface of the cylinder. These cracks created in fatigue service, which propagates radially towards the center of the cylinder, are caused mainly by micro-defects close to the outer surface (fragile particles and porosity) [36]. Figures 6-13b and 6-13e which correspond to the large load (1143-MPa) of fatigue solicitation (low life) show a

rapid crack propagation, with a rapid break like a tensile test failure, and this for hardened and unhardened laser samples.

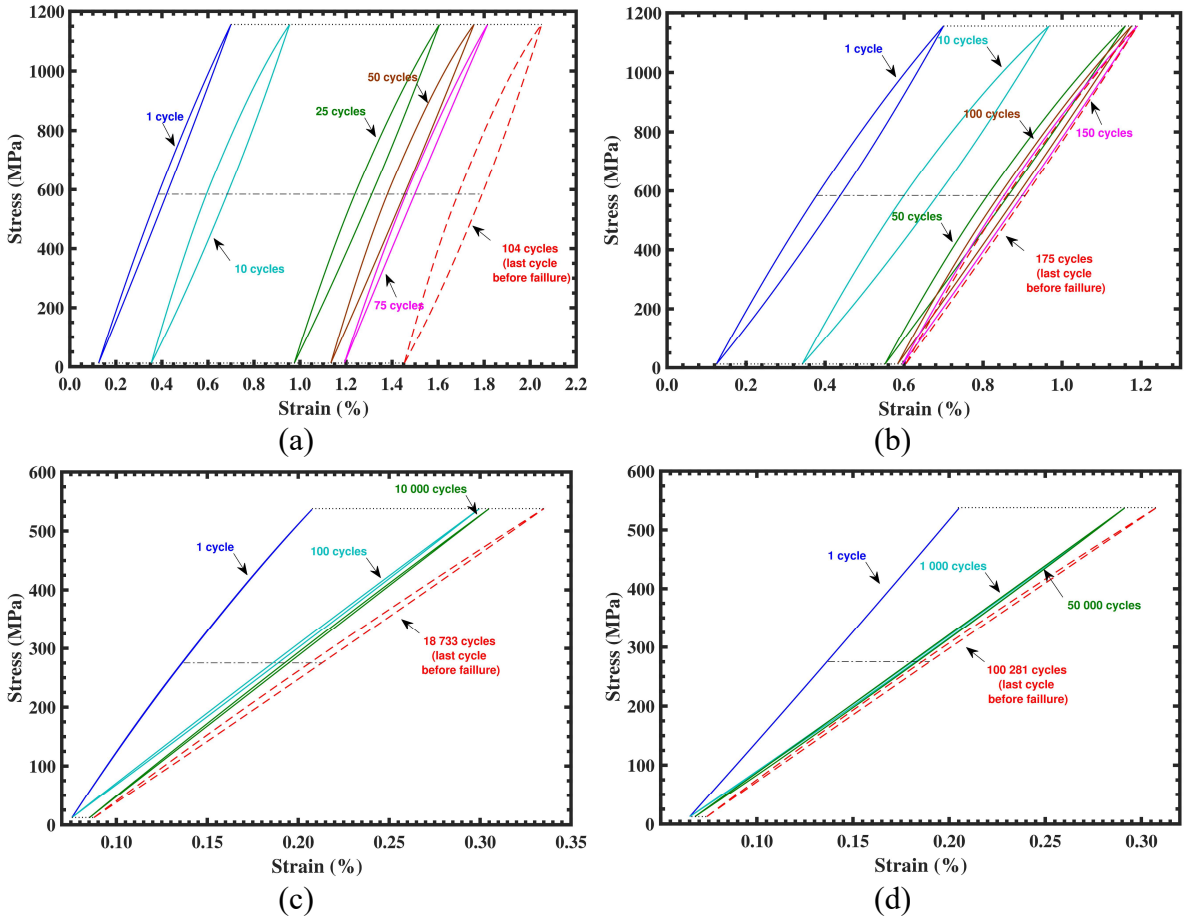

Figure 6-12: Stress-strain hysteresis loops according to the Case depth (Cd) and the Stress range (Δσ) – (a) 0-µm & 1143-MPa, (b) 550-µm & 1143-MPa, (c) 0-µm & 525-MPa, (d) 550-µm & 525-MPa

Figures 6-13c and 6-13f which correspond to the low load (525-MPa) of fatigue solicitation (conventional life) show a different crack initiation region, with a region of propagation of the crack delimited by the blue-sky color, and a region of rapid propagation delimited by the red color and this for both hardened and un hardened laser samples. With a deformation range of 0.30% for samples heat-treated with laser (Fig. 6-13c) and of 0.39% for samples not heat-treated with laser (Fig. 6-13f).

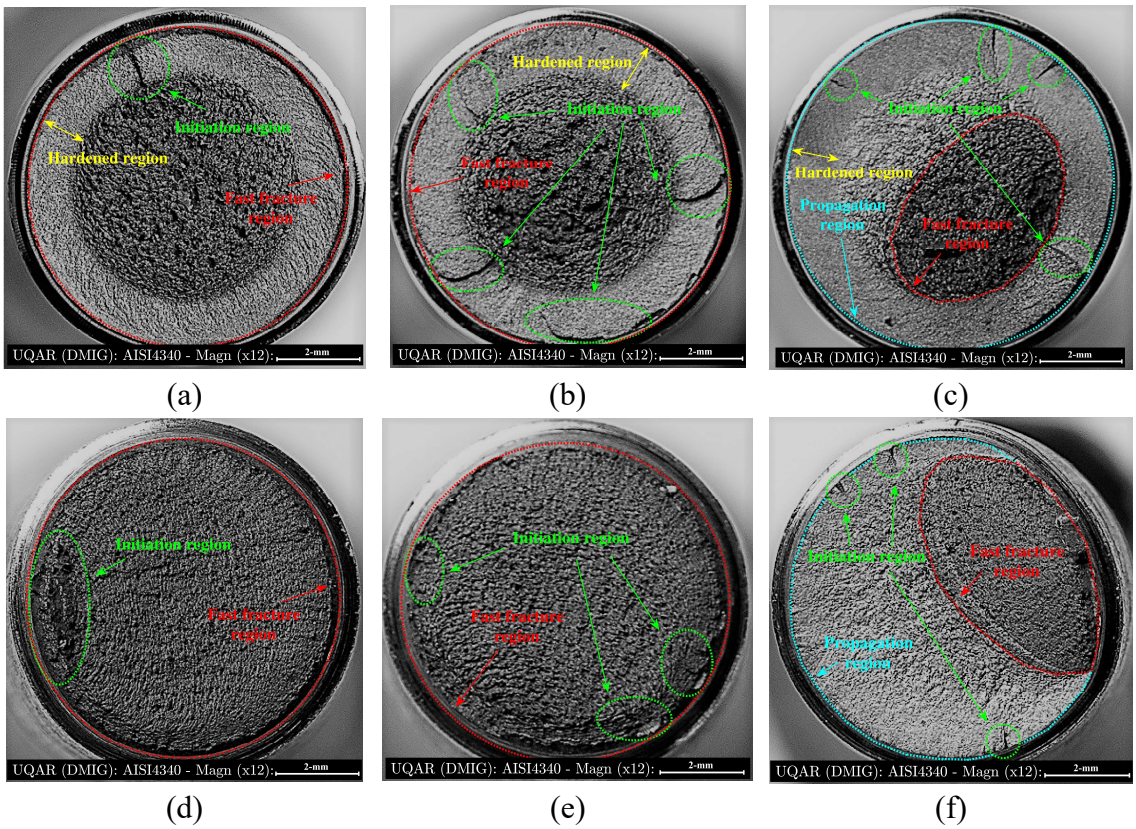

Figure 6-13: Fracture surface with laser heat treatment – (a) Tensile test, (b) Low cycle fatigue, (c) High cycle fatigue. Fracture surface without laser heat treatment: (d) Tensile test, (e) Low cycle fatigue, (f) High cycle fatigue

At the level of engineer calculations, and according to the needs of the design, we note that it is important to define the parameters of heat treatment, the amount of energy that can be absorbed the material before rupture (his tenacity), tolerances, the ultimate stress and the precise dimensions of the mechanical workpiece in order to avoid any plastic deformation in service which can render the workpiece inoperative. As part of a cylindrical workpiece in AISI 4340 and with 9-mm diameter we have seen that a laser heat treatment can significantly improve the mechanical properties, as shown in Figure 6-10b, including fatigue endurance limit for a lifetime up to 5 times higher. This is due to a high surface hardness that prevents the breaking of atomic bonds that can create free surface (surface tension) and thus spread the microcracks.

6.9 CONCLUSIONS

In this study, we analyzed the mechanical behavior in static and fatigue of AISI 4340 steel according to the laser power (1200-, 1250-, and 1300-W), the scanning speed of the laser beam (3.0-, 3.5-, and 4.0-mm/s), the rotation speed of the cylinder (3000-RPM), the strain rate in standard tensile tests (0.005- and 0.015-mim^{-1}) and several amplitude of undulating sinusoidal tensile stresses for specimens of cylindrical geometry. Thermal flow analysis transmitted by conduction in the cylindrical workpiece and lost by convection and radiation allowed us to set up a numerical model able to predict and control, according to the laser heat treatment parameters, the temperature distribution in the specimen for a uniform case depth. The experimental approach developed using a design of experiments and an analysis of variance has highlighted the influence of the laser hardening in the mechanical proprieties. Prediction relationships of mechanical properties (regression and ANN) according to laser parameters have been proposed with contour lines (RSM, Thin-plate-spline) in the range of the parameters of Table 6-3 to facilitate the exploitation of the results by the users of the model. Microstructure and X-ray spectroscopy (for the respective chemical composition of each Spectrum) showed a completely martensitic structure in hardened region, and a mixture of martensite, bainite and residual austenite beyond hardened depth. Fatigue tests, hysteresis loops and analysis of fracture surfaces revealed an increase in the fatigue endurance limit of more than 40%, with an average strain range of not more than 0.30%, due to laser hardening. The main findings and results of this study can be used in practice by the laser heat treatment industry and by mechanical part designers. It would be interesting to consider completing this study including a 2nd order control function of laser power, for a wide uniform distance of case depth (greater than 80-mm), and studying the impact of torsion torque combined with the normal tensile effect on the fatigue life. We believe that the type of approach proposed in this study is the most appropriate way to develop models for improving the performance of mechanical parts of cylindrical geometry.

References

1. Fung, Chin-Ping, Peng, Kan-Ping, and Doong, Ji-Liang. Study of surface temperature on laser cutting and welding power absorption, International communications in heat and mass transfer, 1990, vol. 17, pp. 147-154.
2. Ribolla, Adriano, Damoulis, Gleiton Luiz, and Batalha, Gilmar Ferreira. The use of Nd: YAG laser weld for large scale volume assembly of automotive body in white. Journal of materials processing technology, 2005, vol. 164, pp. 1120-1127.
3. Gujba, Abdullahi K. and Medraj, Mamoun. Laser peening process and its impact on materials properties in comparison with shot peening and ultrasonic impact peening. Materials, 2014, vol. 7, no 12, pp. 7925-7974.
4. Kannatey-Asibu JR, Elijah. Principles of laser materials processing. John Wiley & Sons, 2009.
5. Ion, John. Laser processing of engineering materials: principles, procedure and industrial application. Elsevier, 2005.
6. Gourgues A.-F., Flower, H. M., and Lindley, T. C. Electron backscattering diffraction study of acicular ferrite, bainite, and martensite steel microstructures. Materials Science and Technology, 2000, vol. 16, no 1, pp. 26-40.
7. Shercliff, Hugh R. and Ashby, M. F. The prediction of case depth in laser transformation hardening. Metallurgical Transactions A, 1991, vol. 22, no. 10, pp. 2459-2466.
8. Wu, D. W. and Matsumoto, Y. The effect of hardness on residual stresses in orthogonal machining of AISI 4340 steel. Journal of Engineering for Industry, 1990, vol. 112, no. 3, pp. 245-252.
9. Shiue, R. K. and Chen, C. Laser transformation hardening of tempered 4340 steel. Metallurgical Transactions A, 1992, vol. 23, no. 1, pp. 163-170.
10. Orazi, Leonardo, Liverani, Erica, Ascari, Alessandro, and al. Laser surface hardening of large cylindrical components utilizing ring spot geometry. CIRP annals-manufacturing technology, 2014, vol. 63, no. 1, pp. 233-236.

11. Fakir, R., Barka, N., and Brousseau, J. Case study of laser hardening process applied to 4340 steel cylindrical specimens using simulation and experimental validation. Case studies in thermal engineering, 2018, vol. 11, pp. 15-25.

12. ASTM E8/E8M. Standard test methods for tension testing of metallic materials. ASTM International, West Conshohocken (2009).

13. Carslaw, H. S. and Jaeger, J. C. Conduction of heat in solids: Oxford Science Publications. Oxford, England, 1959.

14. J. Vardi, Thermal Conduction in a Finite Cylinder with Boundary Radiation and a Distributed Electromagnetic Heat Source, Doctoral dissertation Publishing, 1964.

15. Metals Handbook, Howard E. Boyer and Timothy L. Gall, Eds., American Society for Metals, Materials Park, OH, 1985.

16. Engineering Properties of Steels, Philip D. Harvey, editor, American Society for Metals, Metals Park, OH, 1982.

17. Physics for Scientists and Engineers with Modern Physics, 2nd ed., Douglas C. Giancoli, Prentice Hall Publishers, Englewood Cliffs, NJ, 1989.

18. Theodore L. Bergman, P. Incropera Frank, Fundamentals of Heat and Mass Transfer, John Wiley & Sons, 2011.

19. Klaus-J.ürgen Bathe, Edward L. Wilson, Numerical Methods in Finite Element Analysis, 197 Prentice-Hall, Englewood Cliffs, NJ, 1976.

20. Teen, W.M., C.H.G Courtney, Surface heat treatment of EnS 8 steel using a 2 kW continuous-wave C021aser, Metals Technology, 1979, vol. 6, no. 1, pp. 456-462.

21. Bradley, J. R., A simplified correlation between laser processing parameters and case depth in steels, Journal of Physics D: Applied Physics, 1988, vol. 21, no. 5, pp. 834.

22. Dausinger, F., & Shen, J., Energy coupling efficiency in laser surface treatment, ISIJ international, 1993, vol. 33, no. 9, pp. 925-933.

23. Caron-Guillemette, Gabriel. Modélisation du procédé de trempe au laser appliqué à des composantes mécaniques complexes. Université du Québec à Rimouski, 2013.

24. Tobar, M. J., Álvarez, C., Amado, J. M., Ramil, A., Saavedra, E., Yáñez, A., Laser transformation hardening of a tool steel: Simulation-based parameter optimization and experimental results, Surface and Coatings Technology, 2006, vol. 200, no. 22-23, pp. 6362-6367.

25. Fakir, R., Barka, N., Brousseau, J., Mechanical Properties Analysis of 4340 Steel Specimen Heat Treated in Oven and Quenching in Three Different Fluids, Metals and Materials International, 2018, Volume 24, Issue 5, pp 981–991.

26. Fakir, R., Barka, N., Brousseau, J., Optimization of the case depth of a cylinder made with 4340 steel by a control of the laser heat treatment parameters, In : ASME 2018 International Design Engineering Technical conferences and Computers and Information in Engineering Conference, 2018.

27. Beer, Ferdinand P., Johnston, E. Russell, Dewolf, John T., et al. Mechanics of materials. In SI Units, McGraw-Hill, UK, App, 1992.

28. Howard E. Boyer, Atlas of Fatigue Curves, Senior Technical Editor American Society for Metals,1986, pp 112.

29. Montgomery, D. C., Runger, G. C., & Hubele, N. F. (2009). Engineering statistics. John Wiley & Sons.

30. Fowlkes, W. Y., Creveling, C. M., & Derimiggio, J. (1995). Engineering methods for robust product design: using Taguchi methods in technology and product development (pp. 121-123). Reading, MA: Addison-Wesley.

31. R.H. Myers, Response Surface Methodology (Allyn and Bacon, Boston, MA, 1971).

32. Hagan, Martin T., Demuth, Howard B., Beale, Mark H., and al. Neural network design. Boston: Pws Pub., 1996.

33. Tofallis, Chris. A better measure of relative prediction accuracy for model selection and model estimation. Journal of the Operational Research Society, 2015, vol. 66, no 8, pp. 1352-1362.

34. Hidayetoglu, T.K.; Pica, P.N.; Haworth, W.L. Aging dependence of the bauschinger effect in aluminum alloy 2024. Mater. Sci. Eng. 1985, 73, pp. 65–76.

35. Vander Voort, G. F., Metallography, Principles and Practice, ASM International, Materials Park, OH, 1984.

36. Tian, D. D., Liu, X. S., He, G. Q., and al. Low cycle fatigue behavior of casting A319 alloy under two different aging conditions. Materials Science and Engineering: A, 2016, vol. 654, pp. 60-68.

CONCLUSION GÉNÉRALE

Dans le but d'effectuer une étude de sensibilité du profil de dureté, d'extrapolation des résultats numériques et expérimentaux, et d'évaluation des performances mécaniques d'une composante de géométrie cylindrique en fonction des paramètres de traitement thermique au laser. Ce mémoire a présenté une étude approfondie appliquée à l'acier allié 4340, qui est apte au traitement thermique et qui contient une teneur en carbone entre 0.37 à 0.43-%.

Au cours de la première étape, une étude d'un traitement thermique au four d'une composante cylindrique en acier AISI 4340 a été réalisée pour une mise en lumière de l'effet de la température du four, du milieu de refroidissement, et de la température de revenu sur les propriétés mécaniques. Cette étude qui précède généralement toute opération de traitement thermique au laser a permis de tracer des courbes de niveau pour un meilleur contrôle des propriétés mécaniques. Une étude numérique utilisant la méthode des différences finies et des éléments finis, ainsi qu'une analyse expérimentale ont permis de proposer des modèles numériques et statistiques de prédiction de la profondeur de la transformation de la microstructure de l'acier. Les deux algorithmes développés avec la méthode numérique des différences finies, pour un faisceau laser stationnaire et pour un faisceau laser en mouvement, ont été validés par des résultats expérimentaux en laboratoire et ont permis d'ajuster les coefficients physiques (coefficient d'absorption, et de pertes de chaleur par convection et par rayonnement). En termes de temps de calcul, les deux algorithmes développés reproduisent les résultats de simulation numérique du logiciel commercial COMSOL avec un temps de calcul moins long et avec une précision dans les résultats d'environ 3% d'écart. Le modèle développé peut prédire la distribution exacte de la température et indirectement la profondeur durcie, en fonction des paramètres de traitement thermique au laser et des propriétés physiques du matériau. La variation du profil de dureté le long d'un cylindre traité thermiquement au laser, avec des paramètres fixes, a été évaluée par une analyse expérimentale. Cette approche expérimentale développée à l'aide d'une planification expérimentale rigoureuse a permis de mettre en

évidence l'influence du traitement thermique au laser avec des paramètres fixes sur la variation du profil de dureté le long de la longueur du cylindre. La profondeur durcie est croissante entre la position de début du traitement thermique et le la position d'arrêt. L'architecture du réseau neuronal (MLP) avec un schéma de rétropropagation d'erreurs BRANN a permis de proposer une prédiction efficace de cette variation du profil de dureté le long de l'axe du cylindre, avec une erreur moyenne totale inférieure à 25-µm. À l'aide d'une approche numérique et expérimentale, la variation du profil de dureté le long de l'axe du cylindre a été homogénéisée par un asservissement de la puissance laser via un contrôle de la température maximale atteinte à la surface du cylindre.

La deuxième étape de cette étude portait sur l'analyse de l'effet de la profondeur durcie sur les propriétés mécaniques en statique (traction simple) et en fatigue (sollicitation sinusoïdale) dans le cadre du traitement thermique au laser d'éprouvettes cylindriques en acier AISI 4340 de diamètre de la partie calibrée de 9.0-mm, ainsi que l'analyse et les recommandations pour résoudre les problèmes techniques rencontrés. Dans cette deuxième étape, nous avons analysé le comportement mécanique en statique et en fatigue de l'acier AISI 4340 en fonction de la puissance du laser (1200, 1250 et 1300 W), de la vitesse de balayage du faisceau laser (3.0, 3.5, et 4.0 mm/s), de la vitesse de rotation du cylindre (3000 RPM), de la vitesse de déformation dans les essais de traction standard (0.005 et 0.015 mim^{-1}) et de plusieurs amplitudes de contraintes de sollicitations en fatigue. Il a été nécessaire d'analyser, par des calculs numériques et des essais expérimentaux, le flux thermique transmis par conduction dans la pièce cylindrique et perdue par convection et rayonnement, pour une distribution uniforme de la température en surface et une profondeur durcie régulière. Cette analyse a permis de montrer qu'il est possible par contrôle de la puissance laser d'éviter une fusion de la couche extérieure des échantillons. L'approche expérimentale développée à partir d'un plan d'expérience et d'une analyse de variance a permis de mettre en évidence l'influence des paramètres de durcissement au laser sur les propriétés mécaniques. Les tests de fatigue, les boucles d'hystérésis et l'analyse des surfaces de rupture ont révélé une augmentation de la limite d'endurance en fatigue jusqu'à 40% pour une éprouvette cylindrique de diamètre de 9-mm constituée d'un

matériau dans deux états différents. Une couronne dure et fragile et un cœur moins dur et plus tenace. La microscopie a montré une structure complètement martensitique dans la région durcie et un mélange de martensite, de bainite et d'austénite résiduelle au-delà de la profondeur durcie. Des relations de prédiction des propriétés mécaniques (régression et ANN) en fonction des paramètres laser ont été proposées avec des courbes de niveau RSM afin de faciliter l'exploitation des résultats par l'industrie du traitement thermique au laser et par les concepteurs de pièces mécaniques en acier AISI 4340 pour améliorer les performances des pièces mécaniques de géométrie cylindrique de 9.00 mm de diamètre.

RECOMMANDATIONS POUR LES TRAVAUX FUTURS

Cette section présente d'autres aspects du sujet qui pourront faire l'objet d'une investigation plus approfondie à l'avenir.

- Investigation de l'effet que peut avoir la température du four, le temps de revenu et le milieu de trempe (air, huile ou eau) sur le comportement mécanique en fatigue. Cette investigation sera très bénéfique pour l'industrie sidérurgique.

- Proposition d'un algorithme numérique fondé sur la méthode des différences finies capable de fournir des résultats de prédiction de la profondeur durcie, en fonction des paramètres laser, avec un temps de calcul jusqu'à 5 fois plus rapide par rapport aux deux algorithmes proposés dans le chapitre 2 et 3. Parmi les pistes à investiguer nous proposons : (1) une optimisation de la résolution de l'équation aux conditions limites par la méthode aux coefficients indéterminés de Descartes, (2) une division du domaine de calcul par tranche en moyennant les résultats comptés pour une libération de la mémoire de calculs tout en assurant une bonne précision dans la prédiction. Cette investigation sera très bénéfique pour le calcul prédictif rapide.

- Étude de l'asservissement de la vitesse de balayage du faisceau laser ou de la vitesse de rotation du banc d'essai pour une température en surface uniforme et une profondeur durcie régulière le long de la composante cylindrique, dans le cadre d'une émission laser en continu. Cette investigation permettra de comparer l'asservissement de l'énergie laser (chapitre 5) avec l'asservissement en termes de vitesse de balayage et de rotation.

- Étude de l'effet du durcissement au laser distribué par matrice de points (émission laser en pulsé) sur les propriétés mécaniques en statique et en

fatigue de l'acier AISI 4340. Cette investigation sera très bénéfique pour l'industrie du traitement thermique au laser.

LISTE DES RÉFÉRENCES BIBLIOGRAPHIQUES

- William M. Steen PhD, MA, CEng (auth.) Laser Material Processing-Springer London (2003).
- ASTM E8/E8M. Standard test methods for tension testing of metallic materials. ASTM International, West Conshohocken (2009).
- Phillip J. Ross, Taguchi Techniques for Quality Engineering (McGraw-Hill, London, 1988).
- K. Dehnad, Quality Control, Robust Design, and the Taguchi Method (Springer, New York, 1989).
- R.H. Myers, Response Surface Methodology (Allyn and Bacon, Boston, MA, 1971).
- Kannatey-Asibu Elijah Jr., Principles of Laser Materials Processing, 4 John Wiley & Sons, 2009.
- Klaus-J.ürgen Bathe, Edward L. Wilson, Numerical Methods in Finite Element Analysis, 197 Prentice-Hall, Englewood Cliffs, NJ, 1976.
- J. Vardi, Thermal Conduction in a Finite Cylinder with Boundary Radiation and a Distributed Electromagnetic Heat Source, Doctoral dissertation Publishing, 1964.
- Theodore L. Bergman, P. Incropera Frank, Fundamentals of Heat and Mass Transfer, John Wiley & Sons, 2011.
- Gordon D. Smith, Numerical Solution of Partial Differential Equations: Finite Difference Methods, Oxford University press, 1985.
- John C. Strikwerda, Finite difference schemes and partial differential equations, Soc. Ind. Appl. Math. (2004).

- Keith W. Morton, David Francis Mayers, Numerical Solution of Partial Differential Equations: An Introduction, Cambridge university press, 2005.
- Richtmyer, R.D. and Morton, K.W. (1994) Difference Methods for Initial Value Problems. 2nd Edition, Krieger Publishing, Malabar.
- Thelning, K.-E. (1984) Steel and Its Heat Treatment, Butterworth-Heinemann. 2nd Edition, Elsevier, New York, 696.
- Taguchi G, Chowdhury S, WuY. Taguchi's quality engineering handbook. United States of America: Wiley &Sons, Inc; 2004.
- Metals Handbook, Howard E. Boyer and Timothy L. Gall, Eds., American Society for Metals, Materials Park, OH, 1985.
- Engineering Properties of Steels, Philip D. Harvey, editor, American Society for Metals, Metals Park, OH, 1982.
- Hagan, Martin T., Demuth, Howard B., Beale, Mark H., et al. Neural network design. Boston: Pws Pub., 1996.
- MathWorks, Inc. Matlab: the language of technical computing, 2018.
- Carslaw, H. S. and Jaeger, J. C. Conduction of heat in solids: Oxford Science Publications. Oxford, England, 1959.
- Physics for Scientists and Engineers with Modern Physics, 2nd ed., Douglas C. Giancoli, Prentice Hall Publishers, Englewood Cliffs, NJ, 1989.